4-25-2016 12:00 AM

The Inner Gaseous Disks Of Herbig Be Stars

Parshati Patel
The University of Western Ontario

Supervisor
Dr. Aaron Sigut
The University of Western Ontario Joint Supervisor
Dr. John Landstreet
The University of Western Ontario

Graduate Program in Astronomy
A thesis submitted in partial fulfillment of the requirements for the degree in Doctor of Philosophy

Recommended Citation

Patel, Parshati, "The Inner Gaseous Disks Of Herbig Be Stars" (2016). *Electronic Thesis and Dissertation Repository*. 3692.
https://ir.lib.uwo.ca/etd/3692

Abstract

Herbig Ae/Be stars are intermediate mass ($\sim$ 2 to 20 $M_{\odot}$) pre-main sequence stars that inherit a circumstellar disk of dust and gas from their formation phase. The region of this disk closest to the star is entirely gaseous because dust evaporates at the high temperatures there, and this gaseous region is currently poorly understood. Using non-LTE circumstellar disk codes to model the optical and near-infrared spectra of five, early-type (B0Ve to B2Ve) Herbig Be stars obtained with the Canada-France-Hawaii telescope ESPaDOnS instrument, the density structure of each inner gaseous disks was determined and estimates of the disk masses and sizes were obtained. In the modeling, the photoionizing radiation of the central B star was assumed to be the disk's sole source of energy input.

For the four Herbig B2e stars, BD+65 1637, HD 76534, HD 114981 and HD 21669, reasonable matches were found for all emission line profiles considered individually; however, for each star, no disk density model based on a single power law for the equatorial density was able to simultaneously fit all of the observed emission lines in the spectrum. For BD+65 1637, the equatorial disk density law was estimated to fall as $10^{-10}(R_*/R)^3$ g cm^{-3} in a 50 R$_*$ disk, and this model provided a reasonable match to the overall line shapes and strengths. The stars HD 76534, HD 114981 and HD 216629 required a similar density model to that of BD+65 1637, but in a smaller, 25 R$_*$ disk. The overall implied masses of these inner gaseous disks are in the range of $\sim 5.7 \times 10^{-8}$ to $1.2 \times 10^{-9}\, M_*$.

For BD+65 1637, the metal lines, Fe II and especially the Ca II IR triplet lines, required higher disk densities than implied by the hydrogen Balmer lines, with the disk density falling more slowly as $10^{-10}(R_*/R)^2$ g cm^{-3}. In general for all stars, the metal lines of Ca II and Fe II required higher disk densities than the Balmer lines to match the observed line profiles. A more complex disk density distribution is likely required to reconcile this difference and refine the match to the spectra of these stars.

The spectrum of the Herbig B0e star MWC 137 is dominated by very strong emission lines in comparison to the Herbig B2e stars. Preliminary results show that the models require extended disks to reproduce the observed Ca II and Fe II metal emission line profiles. For hydrogen Balmer lines, no disk models extending up to 200 R_* were capable of reproducing the observed line strengths, indicating that even larger disks are required and/or the observed hydrogen lines are contaminated by hydrogen recombination emission from the surrounding H II region.

Taken as a whole, the analysis of these five, early-type HBe stars suggest that the optical and near-IR emission lines in their spectra can be adequately accounted for by an inner, entirely gaseous, disk in Keplerian rotation, heated solely by the photoionizing energy input of the central star, and requiring only a tiny fraction ($<\sim 10^{-7}$) of the central star's mass.

Keywords: accretion, accretion disks - line: profiles - stars: emission-line, Be - stars: individual (BD+65 1637, HD 76534, HD 114981, HD 216629, MWC 137) - stars: pre-main-sequence - stars: variables: T Tauri, Herbig Ae/Be

Acknowledgements

To my supervisors:

First and foremost, I offer my sincerest gratitude to my supervisors from the bottom of my heart, *Aaron Sigut* and *John Landstreet*. Your dedication and constant encouragement have led to where I am today, and I am forever in debt of all the knowledge, guidance and support you have provided me. Thank you for pushing me outside my comfort zone when necessary, and providing me with strength in all my endeavours. You have not only bettered me as a scientist but also an individual, empowering me with life-long skills.

To my mentors:

I would also like thank *Jan Cami*, who has been my advisory committee member ever since I arrived at Western, in providing me with constructive advice and constant support. Additionally, I would like to show my gratitude to *John Lester*, who was a constant mentor during my undergraduate program. I would not have been where I am today, if it was not for your support, guidance and encouragement.

To my friends:

My best friend *Nivedita Chandrashekhar*, thank you for always being there for me and providing me with your expertise in editing. *Ghazal Farhani*, *Sahar Rahmani*, *Feresthe Rajabi*, *Maryam Tabeshian*, and *Dilini Subasinghe*, thank you for always lending a shoulder to cry on, hugs and advice when needed. You guys have made this journey easier and more memorable.

To my family:

Last but not least, I would like to thank my family: my mother, *Neeta Patel*, father, *Paresh Patel* and brother, *Dhrumil Patel* for everything. Without your everlasting, unwavering support and encouragement in all my ventures, I would never be who I am today. Thank you for the compromises you made to help me achieve my dream. Your love and confidence in me has helped me go through the difficult times with ease. Thank you for always having my back. I would like to thank my husband *Nandish Patel* for standing by me through thick and thin. I cannot thank you enough for moving halfway around the world for me and being always by my side. I would not have been able to achieve this without your constant encouragement, love and support. You kept me calm, patient and sane in this journey, thank you! I would also like to thank my late grandfather, *Ramanlal Patel*, my grandmothers, *Kamala Patel* and *Shanta Patel*, my mother-in-law, *Ami Patel* and father-in-law, *Bhishma Patel*, for providing me with so much love, support and encouragement. My special thanks to my cousin *Nisha Patel*, who was always just a phone call away to provide me with support and guidance when need be.

Dedication

I would like to dedicate this thesis to my late grandfather, *Manilal Patel*, whose dedication and enthusiasm towards education and learning has empowered me to be what I am today. Thank you instilling the thirst of knowledge in me and supporting me in this endeavour.

Contents

List of Figures

List of Tables

List of Symbols and Abbreviations

Table 1: List of Symbols

Symbol	Definition
Å	Angstroms (10^{-8} cm)
α	Viscosity parameter
Δ_{ji}	Transition Probability (s^{-1})
ζ	Microturbulent contribution to line width
η_ν	Emissivity ($\mathrm{erg\,s^{-1}\,cm^{-3}\,sr^{-1}\,Hz^{-1}}$)
λ	Wavelength (Å)
μ	Mean molecular weight
ν	Frequency (Hz^{-1})
ρ	Mass Density ($\mathrm{g\,cm^{-3}}$)
ρ_0	Initial mass density
τ_ν	Optical Depth
χ_ν	Gas opacity (cm^{-1})
ϕ_ν	Line profile
Ω	Solid angle
c	Speed of light ($2.99 \times 10^{10}\,\mathrm{cm\,s^{-1}}$)
c_S	Local sound speed ($\mathrm{cm\,s^{-1}}$)
D	Distance to the source
E	Energy level
F_c	Continuum flux ($\mathrm{erg\,s^{-1}\,cm^{-2}}$)
F_λ	Flux per unit wavelength ($\mathrm{erg\,s^{-1}\,cm^{-2}}$ Å^{-1})
F^{Mod}	Synthetic model flux
F^{Obs}	Observed flux

Continued on next page

Table 1 – *Continued from previous page*

Symbol	**Definition**
$\mathcal{F}$	Figure-of-merit
G	Gravitational constant (6.67×10^{-8} cm^3 g^{-1} s^{-2})
g	Surface gravity (cm s^{-2})
H	Disk scale height
I_ν	Specific intensity (erg s^{-1} cm^{-2} sr^{-1} Hz^{-1})
i	Angle between line-of-sight and rotation axis or inclination angle (°)
J_ν	Mean intensity
k	Boltzmann constant (1.38×10^{-16} erg K^{-1})
L_* or L	Stellar luminosity (erg s^{-1})
$L_\odot$	Solar luminosity (3.84×10^{33} erg s^{-1})
$log\,g$	Logarithmic of gravity
$M_\odot$	Solar mass (1.99×10^{33} g)
M_*	Stellar mass (g)
m_H	mass of hydrogen atom (1.67×10^{-24} g)
N	Level population
n	Power law index
P	Pressure (dyne cm^{-2})
$R_\odot$	Solar radius (6.96×10^{10} cm)
R_*	Stellar radius (cm)
R_{subl}	Sublimation Radius
R_{disk}	Disk Radius
S_ν	Source function (erg s^{-1} cm^{-2} sr^{-1} Hz^{-1})
T_{eff}	Effective temperature (K)
T_{HE}	Hydrostatic equilibrium disk temperature
V_K	Keplerian velocity (cm s^{-1})
$v\,sini$	Project rotational velocity

Table 2: List of Abbreviations

Abbreviation	**Definition**
AU	Astronomical Unit ($\sim\ 1.46 \times 10^{13}$ cm)
Ap/Bp	Chemically peculiar A or B-type star
Br γ	Brackett γ line ($2.1655\,\mu m$ or 21655 Å)
CFHT	Canada-France-Hawaii Telescope
CQE	Central Quasi Emission
ESPaDOnS	an **E**chelle **S**pectro**P**olarimetric **D**evice for the **O**bservatio**n** of **S**tars
EW	Equivalent Width
HAeBe	Herbig Ae/Be stars
HAe	Herbig Ae stars
HBe	Herbig Be stars
HR Diagram	Hertzsprung - Russell diagram
HJD	Heliocentric Julian Date
IR	Infrared
LTE	Local Thermodynamic Equilibrium
Ly α	Lyman α line (1216 Å)
MIR	Mid-infrared
MS	Main Sequence
μm	Micron (10^{-4} cm)
nm	Namometer (10^{-7} cm)
NIR	Near-Infrared
PC	Parsec (3.08×10^{18} cm)
PMS	Pre-Main Sequence
SEDs	Spectral Energy Distributions
SNR	Signal-to-Noise Ratio
UV	Ultra-Violet
UT	Universal Time
V/R	Violet-to-Red
YSO	Young Stellar Object
ZAMS	Zero-Age Main Sequence

List of Appendices

Chapter 1

Introduction

The formation of stars and planets is one of the most intriguing mysteries the universe has to offer. Giant molecular clouds that contain gas and dust are the cradle of stars and planets, and sometime called Stellar Nurseries.

The material in the molecular clouds is rich in not only hydrogen and helium but also trace amounts of heavy elements, which resulted from the collapse of stars. These molecular clouds collapse to form cores, either when the cloud is massive enough, i.e. above Jeans mass, and undergoes gravitational collapse; or when an external event generates shock waves and triggers gravitational collapse. The size of the cloud collapses from $\sim 10^4$ AU to $\sim 10^3$ AU. An illustration of this process can be seen in Figure 1.1. The collapse results into accretion of dust and gas towards the core and the core further shrinks in size to a few solar radii. While the core still accretes material via infalling gas, it is called a protostar. This phase is accompanied by bipolar outflows and jets. Once the infalling of gas has stopped, the protostar becomes optically visible and is called pre-main sequence star. By now, the remaining dust and gas has settled into a disk around the young star with a system size of ~ 100 AU, while the central star is still gaining material via the disk but at a very slow rate.

The circumstellar disk of dust and gas around the pre-main sequence star will be the site of planet formation. The circumstellar material in the disk contains dust, which coalesces to

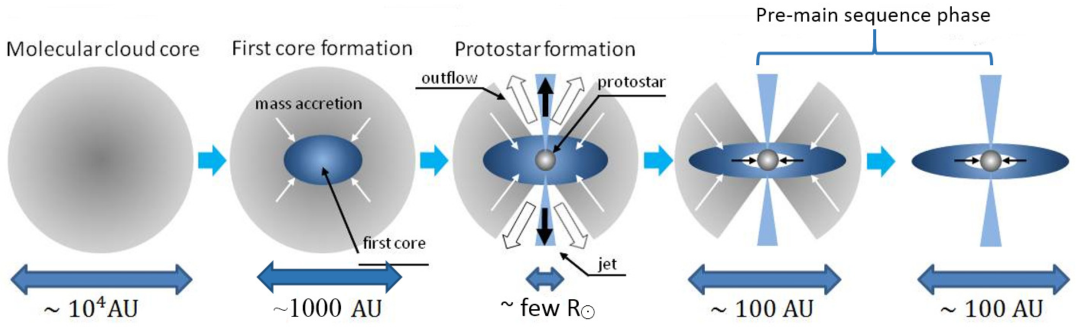

Figure 1.1: This illustration represents the formation of a star from a core in a molecular cloud. The molecular core collapses from a giant molecular cloud and shrinks to a size of ~ 10^3 AU from ~ 10^4 AU. The core accretes more material from the surroundings to form a protostar a few solar radii in size, which also exhibits bipolar outflows and jets. Once the accretion of the surrounding gas and dust dies down, the protostar becomes optically visible and is called a pre-main sequence star. Figure credit: Yusuke Tsukamoto, RIKEN (modified version).

form centimeter/meter grains and kilometer sized boulders. These grains and boulders collide to form bigger planetesimals. If the disk is massive, these planetesimals accrete material from their surroundings to eventually form planets. Even with a clear overall understanding of how the planets and star form, details of the processes are still far from clear, and are subjects of active research.

The star's mass is a fundamental property that drives star formation and eventually planet formation in its surroundings. Because the lower mass objects spend more time in each phase, a great strides have already been made in understanding their formation process. As the stellar masses increases, the amount of time a protostar spends in each phase decreases, making it harder to find high mass objects to fill in the void for understanding the star formation process. High mass stars, such as O-type stars, have already started burning hydrogen in their cores when they become optically visible, thus denying us of any optical observational evidence about their formation process. This is where intermediate mass stars, such as the Herbig Ae/Be stars, which become visible just before they start burning hydrogen in the core, can play an important role and provide us with a peek into the process of their formation. In addition, these stars are precursor to Vega-type debris disk and hence make interesting test beds for planet formation and disk physics.

1.1 Definition of Herbig Ae/Be Stars

In 1960, George Herbig (Herbig, 1960) proposed that there should exist stars that are the higher mass counterparts of the pre-main sequence (or still contracting) T Tauri stars [1]. He studied a small group of objects that met the three following conditions:

1. They are spectral type A or earlier, with emission lines in their spectra;
2. They are located in an obscured regions or inside a molecular cloud and
3. They illuminate bright nebulosity in the vicinity.

These criteria allowed him to eliminate many other types of stars that would resemble the young stellar objects. For example, the second criterion excludes objects surrounded by ejected envelopes such as the planetary nebula or an old novae. The third criterion excludes the classical Ae/Be stars. To honor G. Herbig's work in the field, these stars are now known as Herbig Ae/Be (hereafter HAeBe) stars. After their discovery, a large number of these stars were added to the catalogs by several studies, such as Finkenzeller & Mundt (1984); Herbig & Bell (1988); Thé et al. (1994).

The definition has, however, been modified as new observations and surveys identified more of these HAeBe stars. New studies, such as those of Hu et al. (1991); Oudmaijer et al. (1992); Hillenbrand et al. (1992), revealed that not all HAeBe stars are associated with a molecular cloud or star forming region and some were present in isolated regions. Based on the new studies and after noticing that the previous definition included many objects that share similar properties to HAeBe stars, Davies et al. (1990); Malfait et al. (1998); van den Ancker

---

[1] T Tauri stars are pre-main sequence stars, with masses less than 2.5 $M_{\odot}$, which show Balmer emission lines in their spectra and an excess in their infrared (hereafter IR) spectral energy distributions (hereafter SEDs), interpreted as gas and dust in the form of a circumstellar disk. The most massive T Tauri stars will later become main-sequence A-type stars.

et al. (1997); Waters & Waelkens (1998) revised the working definition of HAeBe stars to the following:

HAeBe stars are

1. Stars of spectral type A or B with emission lines,
2. Stars that have an infrared excess, attributed to hot or cool circumstellar dust or both,
3. Stars are of luminosity class III to V.

Like Herbig's criteria, these criteria allow exclusion of Classical Ae/Be stars, B[e] supergiants and other stars such as the post-main sequence stars with disks. Circumstellar dust separates the HAeBe stars from the Classical Ae/Be stars[2].

In our galaxy, less than 4% of A and B-type pre-main sequence (PMS, hereafter) stars are HAeBe stars (Böhm & Balona, 2000). The HAeBe phenomenon gives a rare opportunity and glimpse into the young star's PMS phase. At this stage, they are governed by gravitational contraction at this stage.

The protostellar objects enter the HR diagram[3] from the right of the main sequence (MS), starting with low effective temperature and luminosity and moving to higher values of both along the "birth line". While the object is still accreting strongly, it increases substantially in luminosity and increases moderately in effective temperature as it gains more mass. If the object stops accreting rapidly (that is, the supply of new mass is largely exhausted) while it has less than $\sim\ 2\,M_\odot$ of mass, it will become a T Tauri star and evolve during some tens of millions of years to become a low-mass MS star, increasing in effective temperature but not changing much in luminosity as it approaches the MS. For objects that end rapid accretion with mass somewhat above $\sim\ 2\,M_\odot$, the star may become a T Tauri star for a while, then evolve into a Herbig Ae star (hereafter HAe) star, and eventually become an MS A-type star. For a still more massive protostar, the object will become a Herbig Be (hereafter HBe) star and evolve

---

[2] Classical Ae/Be stars are A/B-type main sequence (hereafter MS) stars that have emission lines and an IR excess due to free-free emission from the ionized gas in a circumstellar gaseous *decretion* disk.

[3] The HR diagram is a plot of luminosity vs. effective temperature or observational proxies for these quantities.

Table 1.1: Stellar Parameters for Main Sequence A and B-type Stars (Cox, 2000).

Stellar Class	Teff (K)	R ($R_\odot$)	M ($M_\odot$)	log (g) (cgs)
B0	30,000	7.4	17.5	3.94
B5	15,200	3.9	5.9	3.44
A0	9790	2.4	2.9	4.14
A5	8180	1.7	2.0	4.29

to become a MS B-type star. As higher mass stars are more luminous, these stars evolve more rapidly towards MS than low mass T Tauri stars do. Many of the more massive stars, such as O-type stars, do not emerge visibly from their birth clouds until they have become MS stars.

As these stars are deeply embedded in circumstellar dust and gas, their spectra include emission lines, making it harder to determine the stellar parameters such as effective temperature, surface gravity and luminosity (Folsom et al., 2012). Normally, the wings of the observed upper hydrogen Balmer spectral lines are fitted with synthetic Balmer line profiles (Kurucz, 1979) to determine stellar parameters, which assumes that emission is negligible. The stellar parameters for MS A and B-type stars can be found in Table 1.1. The effective temperatures of MS A-type stars range from 7500 K to 10,400 K and from 11,000 K to 33,000 K for B-type stars (Cox, 2000).

1.2 Observational Properties

HAeBe stars have a wide range of observed characteristics. Some of the important properties relevant to this study include emission lines, evidence of magnetic fields and accretion, spectral energy distributions (SEDs, hereafter) and polarization. Other properties include bipolar/optical outflows, photometric variations, stellar winds, and high rotation rates.

1.2.1 Optical and Near-Infrared Emission Lines

HAeBe Stars show both permitted and forbidden emission lines. These emission lines seen in the spectrum provide important information not only about the regions from which the emission originates, but also about the composition and structure of the region. The presence of emission lines is a feature that separates the HAeBe stars from the normal, MS A/B type stars (Herbig, 1960) and is denoted by 'e' in the name HAeBe stars.

Garrison & Anderson (1977) studied 14 HAeBe stars and discovered that the Hα emission line shows three different kinds of line profiles: single-peaked, double-peaked, and P-Cygni or inverse P-Cygni. Examples of these different kinds of line profiles is demonstrated in Figure 1.2. Later studies, such as those of Finkenzeller & Mundt (1984), Catala (1989), Grinin et al. (1994), Reipurth et al (1996), Waters & Waelkens (1998), confirm this variety of Hα line shapes. Finkenzeller & Mundt (1984) found that 50% of the HAeBe stars in their sample showed a doubled-peaked profile for Hα, while ~25% showed single-peaked profile and ~20% showed either P-Cygni or inverse P-Cygni[4] line profile. The rest of ~5% the profiles showed complex structure which do not fit the above mentioned kinds of line profiles. An example of all the four different kinds of profiles can be seen be Figure 1.2. Finkenzeller & Jankovics (1984) noted that all Balmer lines exhibit the same line shape as Hα, with the strength of the line decreasing from Hα to Hγ. Hα has been widely used for wind diagnostics studies of HAeBe stars (Finkenzeller & Mundt, 1984; Corcoran & Ray , 1998) and polarization studies (Vink et al., 2002; Vink, 2015).

In addition to Balmer lines, O I, Ca II, Si II, Mg II and Fe II lines are also seen in emission in HAeBe stars (Waters & Waelkens, 1998). Studies, such as those of Cohen & Kuhi (1979); Finkenzeller & Mundt (1984); Hamann & Persson (1992a) and Böhm & Catala (1995), investigated emission lines such as Hα, the Ca II IR triplet (λ 8498, λ 8542 & λ 8662)[5] and several Fe II lines and interpreted them as revealing chromospheric and wind activity in these stars. Cauley & Johns-Krull (2014) studied He I (λ 10830) emission line as a tracer of mass flow activity.

Hamann & Persson (1992a) and Hamann & Perrson (1992b) investigated the Ca II infrared (IR) triplet in HAeBe stars and found 84% of the HAeBe stars show emission in the triplet lines.

---

[4] A P-Cygni profile is a spectral feature in which there is red-shifted emission and blue-shifted absorption component to the spectral line, indicating the expansion of a gaseous envelope away from the star. An inverse P Cygni is attributed to infalling gas.

[5] All wavelengths are in Å unless otherwise stated.

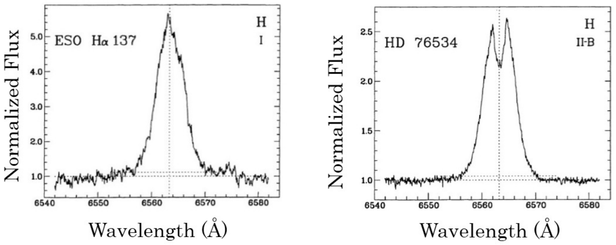

(a) Single-Peaked Profile (b) Double-Peaked Profile

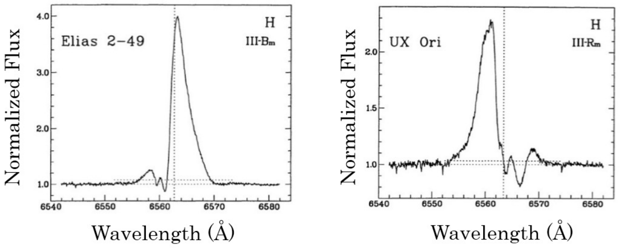

(c) P-Cygni Profile (d) Inverse P-Cygni Profile

Figure 1.2: These plots of Normalized Flux vs Wavelength (Å) show different Hα profiles seen in HAeBe stars (Reipurth et al, 1996). When a star+disk is seen pole-on, a single-peaked Hα profile is seen, while a double-peaked profile is produced when the star is seen at intermediate angles. P Cygni or Inverse P Cygni profile is seen when the material in the disk is either expanding away from the star or falling on the star (away from the observer).

Out of these, 71% of their HBe stars showed the Ca II IR triplet lines in emission. They showed that if the excitation is the same in all the stars, Ca II requires denser and/or thicker regions in hotter stars. They also noted that due to the high stellar temperatures and the double-peaked line profiles, the formation of the Ca II lines would happen away from the stellar surface in a disk, like those possessed by Classical Be stars and in a very small, ring-like structure close to the star. They also showed that there is a correlation between the Ca II luminosity and the IR excess in these stars and concluded that Ca II emission lines are somehow related to the presence of a disk. Böhm & Catala (1995) studied non-photospheric lines such as the Hα, the Ca II IR triplet, and He I (λ 5876) and concluded that the energy fluxes for these lines increase with the effective temperature and suggests that the origin of the emission in the lines is further away from the stellar surface. Heŕnandez et al. (2004) found that 33% of their sample showed emission in Fe II multiplets and also noticed that the equivalent width (EW, hereafter) of one of the Fe II lines, Fe II multiplet (42) (λ 5169), is correlated with the EW of Hα and seems to be present only when [O I] (λ 6300) also appears in the spectrum.

There are several emission lines outside the optical and NIR regions, such as Ly α (1215 Å) and Brackett γ (2.166 μm), have been used to trace several features of the disk such as the accretion, mass flow as well as rotation of the disk (Cauley & Johns-Krull, 2014; Ababakr et al., 2015; Mendigutía et al., 2015).

In addition to the permitted emission lines, HAeBe stars also show forbidden emission lines (Herbig, 1960; Finkenzeller, 1985; Böhm & Hirth, 1997; Waters & Waelkens, 1998), which are spectral lines emitted from metastable states that have a very low probability of radiative decay. These lines can only appear strongly in low density regions. They are important in characterizing the circumstellar environments around HAeBe stars. Many forbidden emission lines from different elements such as [C I], [Si I], [O I], [N II], [Ca II], [Cr II], [Fe II], [O II] and [Ni II] are seen in HAeBe stars (Hamann, 1994). The forbidden line [O I] (6300 Å) is seen to be highly blue-shifted and is thought to be an evidence of outflow. [Si II] (6717/6731 Å) is detected in HAeBe stars with jets (Corcoran & Ray, 1997).

1.2.2 Polarization

HAeBe stars show linear polarization, which can occur both in the continuum and in the spectral lines. HAeBe stars are seen to have variable polarizations varying on timescales from ~1 month to 1 year (Jain & Bhatt, 1995; Yudin & Evans, 1998). Jain & Bhatt (1995) measured 24 HAeBe stars for polarization and found that the percentage of polarization ranges from 0.1% to ~6%. Several studies, such as those of Vink et al. (2002, 2005); Mottram et al. (2007), and Vink (2015), have shown that there exists a difference in polarization between HAe and HBe stars, especially early B-type stars. It was noticed that the continuum emission from the HBe stars is more polarized than the spectral lines, an effect known as depolarization. Vink et al. (2002, 2005) showed that while all HAe stars show intrinsic linear polarization consistent with magnetospheric accretion, most HBe stars show line-depolarization which is consistent with classical disk accretion[6].

1.2.3 Magnetic Fields

Only a very small fraction of HAeBe stars are known to have magnetic fields, with the first detection by Donati et al. (1997). Alecian et al. (2009) and Alecian et al. (2013) found that less than 10% of HAeBe stars in their sample of HAeBe stars have large scale magnetic fields.

HAeBe stars, being intermediate mass stars, have small convective cores and large radiative envelopes (Alecian et al., 2009). Given that they have small convective cores, they might generate core fields, but it does not seem that such fields could appear on the surface. For this reason, the magnetic fields seen in HAeBe stars might be large scale fossil fields. The fossil field model proposes that the magnetic fields are remnants of the star formation phase or from the T Tauri stage, when the star would possess convective envelope (Alecian et al., 2009). The primodial origin of these fields in HAeBe stars aids us in understanding the evolution of these stars in the HR diagram. For lower mass counterparts of HAeBe stars, the T Tauri stars, magnetic fields play an important role in formation and evolution of the star. Whether the same applies to the HAeBe stars is still a matter of debate. A small fraction (~5%) of MS A and B type stars are known to have large scale, global magnetic fields. All the magnetic MS A and late B stars show quite specific chemical peculiarities, often termed as Ap/Bp stars (Alecian et al., 2009).

1.2.4 Accretion

The lower mass counterparts to the HAeBe stars, T Tauri stars, are known to accrete magnetospherically (see reviews by Bouvier et al. (2007) and Gómez de Castro (2013)). The large surveys of intermediate mass stars, such as those of Alecian et al. (2009, 2013), have yielded that less than 10% of HAeBe stars show magnetic fields, and hence it is appropriate to say these

---

[6] In classical disk accretion, the material is supplied to the areas very close to the star by gravitational instability or due to viscous heating (Lynden-Bell & Pringle, 1974) in the disk; this material finally settles onto the stars equatorial region by a process of sporadic accretion.

stars may not accrete material magnetospherically (Alecian et al., 2009). Whether or not these stars accrete via magnetic field lines is currently one of the mysteries in the field of HAeBe stars.

Several tracers, such as Brackett γ, Lyα, He I λ 10830 lines, balmer discontinuity, and emission lines, are used to detect the accretion amongst these objects. Hamann & Persson (1992a) used emission lines to study accretion close to the stars, and they suggested that the magnetospheric accretion disk models (normally applied to the T Tauri stars) cannot be applied to the HAeBe stars because stellar radiation plays an important role in the excitation of ionized lines such as Fe II, Ca II IR triplet etc.

Blondel et al. (1993) derived accretion rates for HAe stars to be $\sim 10^{-8}$ $M_{\odot}$/year using the Lyα (1216 Å) emission line. The emission line was not found in HBe stars in their study. Other studies, for example Donehew & Brittain (2011); Mendigutía et al. (2011a); Fairlamb et al. (2015), have used the veiling of the Balmer discontinuity, luminosity of Brγ (2.166 μm) emission line and UV-excess to derive accretion rates. These studies, however, have found differences in HAe and HBe stars, and have not been able to apply the magnetospheric accretion model to the HBe stars. Cauley & Johns-Krull (2014) studied He I (λ 10830) in a sample of HAeBe stars and noticed that HBe stars show blue shifted absorption features while HAe stars show both blue and red shifted absorption features. This difference indicates that HBe stars show little evidence of infalling material, while HAe stars show a higher level of mass flow activity, suggesting different mechanisms. Cauley & Johns-Krull (2015) studied various Balmer, iron and calcium emission lines to detect mass flows in optical data. The study confirmed the findings of Cauley & Johns-Krull (2014) that HBe stars lack the red-shift absorption features which means they show little evidence of magnetospheric accretion, meanwhile, the HAe stars show both absorption features which is evidence of magnetospheric accretion. However, it was noted that the velocities of these lines are not as large as seen in their lower mass counterparts of T Tauri stars. The observed statistics amongst their sample of the 78 stars suggest a transition of magnetospheric accretion to classical disk accretion between HAe and HBe stars.

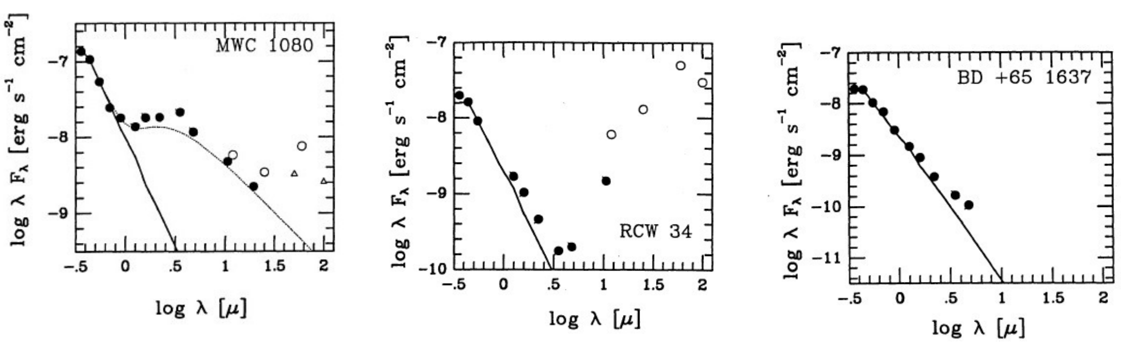

(a) Group I- MWC 1080 (b) Group II- RCW 34 (c) Group III- BD+65 1637

Figure 1.3: The Spectral Energy Distribution (SED) of the HAeBe stars of different characteristic groups. Solid circles are ground based observations; open circles are IRAS observations and triangles are observations taken at the Kuiper Airborn Observatory (KAO). The solid line is SED for a standard star of the same spectral type and dotted line (in (a)) is the 'best fit' model, where the model consists of a central star with optically thick circumstellar accretion disk (Hillenbrand et al., 1992).

Inverse P Cygni profiles are seen both in the T Tauri and HAeBe stars. For the T Tauri stars, they can be explained using magnetospheric accretion. In HAeBe stars, however they could be understood as accretion of clumpy material (Mora et al., 2004).

1.2.5 Spectral Energy Distribution

The spectral energy distribution (hereafter SED) of HAeBe stars differs from normal stars as it shows an IR excess (between 1 to $10^3 \mu$m) and an ultraviolet (hereafter UV) excess (between 10 to 300 nm). The IR excess is interpreted to be from circumstellar dust, while the UV excess is thought to be from the circumstellar gas. Warm gas near the star, whose temperature exceeds the stellar effective temperature, could result in the UV excess of HAeBe stars (Meeus et al., 1998). The UV excess is less dramatic when compared to the low mass counterparts, the T Tauri stars (Catala, 1989).

Hillenbrand et al. (1992) studied 47 HAeBe stars and noticed that the stars can be grouped into three broad groups based on the slope of the IR continuum. This classification scheme helps to understand the existence and geometry of material based on the type of IR excess seen in the SED of these stars. HAeBe stars are classified in the following groups:

Group I: Stars in this group have large IR excesses at wavelengths $\lambda \geq 2.2\,\mu m$ with spectral slope given by $\lambda F_\lambda \sim \lambda^{-4/3}$. Figure 1.3a shows the SED of one such B0e type star, MWC 1080.

Group II: Stars in this group have large IR excesses with flat or rising spectra at longer wavelengths, out to $\lambda = 100\,\mu m$. Figure 1.3b shows SED for a B3 type star, RCW 34, in which a sharp onset of IR excess is seen at 1 μm.

Group III: Stars in this group have very small IR excess, similar to those of Classical Be stars. Figure 1.3c shows SED of BD+65 1637, which is an excellent example of a B2 type star with very small IR excess.

Group I's SED resembles those of T Tauri stars which are known to have accretion disks that are geometrically flat and optically thick. The stars in this group show a decrease in IR excess as the wavelength increases. Group II is best explained as a disk+envelope system. Objects in this group show either a flat or rising spectra with a sharp onset of IR excess between 1μm and 2μm. This wavelength corresponds to a temperature of ~3000 K to ~1500 K. The approximate temperature at which the dust evaporates is ~1500 K (more on this in section 1.3). Group III's small IR excess is similar to that of the Classical Be stars, suggesting the excess is due to free-free emission from a gaseous circumstellar disk. Hillenbrand et al. (1992) suggest these stars could be higher-mass analogs of the disk-less (naked) T Tauri stars. Alonso-Albi et al. (2009) noted that most of the HAe stars show SED characteristics of Group I, and HBe stars show that of Group II.

In addition to Hillenbrand's classification, Meeus et al. (2001) studied 14 HAeBe stars and classified them into two groups based on the extended SED emission.

Group I: Stars in this group showed a rising or strong flux in the far-IR (20-100$\,\mu m$) region of the SED, and

Group II: Stars in this group had the flux fall off strongly in the far-IR region of the SED.

Meeus et al. (2001) suspected and Dullemond & Dominik (2004) confirmed, using SED modeling that the two groups can be interpreted as a flaring (group I) and flat or self-shadowed (group II) geometry of the disk.

For the remainder of the study, we will be using the Hillenbrand's classification as we are only concerned with the optical and NIR part of the SED.

1.2.6 Other properties:

HAeBe stars show photometric variability ranging from days to months to years (Herbig, 1960; Finkenzeller & Mundt, 1984; Friedemann et al., 1992; Shevchenko et al., 1997), and various models such as non-radial pulsation, accretion, etc, have been suggested for their occurrence (Catala, 1994; Waters & Waelkens, 1998; Mora et al., 2002). van den Ancker et al. (1998) and Mendigutía et al. (2011) have shown that HAe stars show large to moderate variations in magnitude (>2^m.5) while HBe stars show low to moderate variations (<0^m.5). Herbst & Shevchenko (1999) studied 230 HAeBe stars and found that the large amplitude variations are mainly seen in stars with spectral type later than B8. The differences seen in the variations have been suggested to be due to different accretion mechanisms in high mass and low mass stars amongst the HAeBe stars.

Finkenzeller (1985) studied a large group of HAeBe stars and found that HAeBe stars have higher projected rotational velocities than T Tauri stars but lower than Classical Be stars. Alecian et al. (2013) show that the HAeBe stars that possess magnetic fields rotate much slower than MS A and B type stars. In addition, HBe stars seem to rotate faster than HAe stars. Böhm & Balona (2000) find that the average projected rotational velocity for HBe stars is 110 km/s and 90 km/s for HAe stars. Böhm & Catala (1995) and Finkenzeller (1985) show that the projected rotational velocities can range from 60 km/s to 200 km/s.

Molecular outflows, sometimes bipolar in nature, have been seen in ~15-20% of HAeBe stars (Mundt & Ray, 1994; Waters & Waelkens, 1998). Bachiller (1996) shows that the outflows are correlated with the jets, which are highly collimated outflows. The origin of the outflows and the jets are not well understood but are generally associated to be a by-product of accretion. The jets and molecular outflows illuminate neighboring regions, generally known as Herbig-Haro objects (Waters & Waelkens, 1998).

1.3 Circumstellar Environment

HAeBe stars inherits dust and gas from its parent molecular cloud while it is still undergoing formation to achieve MS star status. Over time, the dust and gas settle into an equatorial disk. Remarkable progress has been made in the field of understanding the settling of this dust and gas into a disk as well as its evolution from initial dust and gas phase to final planetesimals phase. In addition to the disk, a halo of low density material surrounds the star+disk system and is generally described as an extended envelope.

The spatial distribution of this circumstellar material is still being debated, and hence the interest in these disks have grown over the last two decades. In addition to the methods mentioned in the Section 1.2, these disks can be studied using millimeter, sub-millimeter, IR spectroscopic (e.g. Mannings & Sargent (1997); Meeus et al. (2001); Dent et al. (2005)) and interferometric observations (see the review by Kraus (2015) and references therein), IR and millimeter imaging techniques (e.g. Marinas et al. (2011); Wilner et al (2011)) and SED modeling (e.g. Dullemond et al. (2007)). Each of these methods traces a different region of the disk, thus providing valueable information of the distribution as well as the kind of material in the disk.

Even with the details of the structure being the matter of debate for these stars, one can assume these young stellar objects will follow a general structure, similar to those of their lower mass counterparts, the T Tauri stars. As dust evaporates above $\sim$1500 K, the portion of the disk closest to the star is likely to be completely gaseous due to high temperatures resulting from the star's UV radiation. As one goes away from the star, the temperature is lower and the cooler conditions allow molecular gas to be present. Once the temperature is cool enough for dust to exist, one either finds a thick wall of dust, sometimes called a dust rim, or a smooth transition to a dusty disk at the dust sublimation radius (see Dullemond & Monnier (2010) for review on *The inner regions of protplanetary disks.*). At larger distances and cooler temperatures, molecular gas and dust can be found.

Thus, depending on the distance from the central star and the stellar radiation, HBe disks can be divided into atomic gas, molecular gas, and dust. The expected structure of such a disk is illustrated in Figure 1.4, with the emphasis on the inner regions of the disk. The size of the circumstellar disk can range anywhere from few tens of AUs to up to 100s of AUs, while the temperature in these disks can range from 10s K in the far distance to 1000s of K in regions closer to the stellar surface.

Optical and NIR atomic lines are used to study the hot, atomic gaseous region. The disk region beyond the gaseous disk receiving direct radiation from the star is expected to have a thin surface layer with atomic gas; hence, the emission seen in the spectrum can arise from a large extended area. The atomic gaseous region can range from 0.01 to a few AUs in size depending on the intensity of the stellar radiation. In the region beyond the atomic gaseous disk, where the temperatures are cooler, molecular gas is expected. As the temperature decreases, thee conditions are viable for the dust to exist and a mixture of warm dust and molecular gas is expected. NIR molecular emission lines and NIR/Mid-IR (MIR, hereafter) interferometry is used to understand the structure of this region. Beyond this region, cooler gas and dust are detected using millimeter and submillimeter interferometry. The region beyond the atomic gaseous disk can range anywhere in size from 0.1 to 100s of AUs, including the dusty disk (Dullemond & Monnier, 2010). The outer, dusty region of the disk is comparatively well studied, but currently very little is known about the inner, gaseous region.

There are a few theories about how the atomic gaseous region might have formed, and the characteristics of its structure. Catala (1989) proposed that there should exist a region close to the star, where the heat from the star would evaporate the dust creating a hollow region. The presence of an inner hole or dust free zone in many of the HAeBe stars can be inferred from the IR excess that starts at 1-2 μm which suggests the presence of a dust rim. As the effective

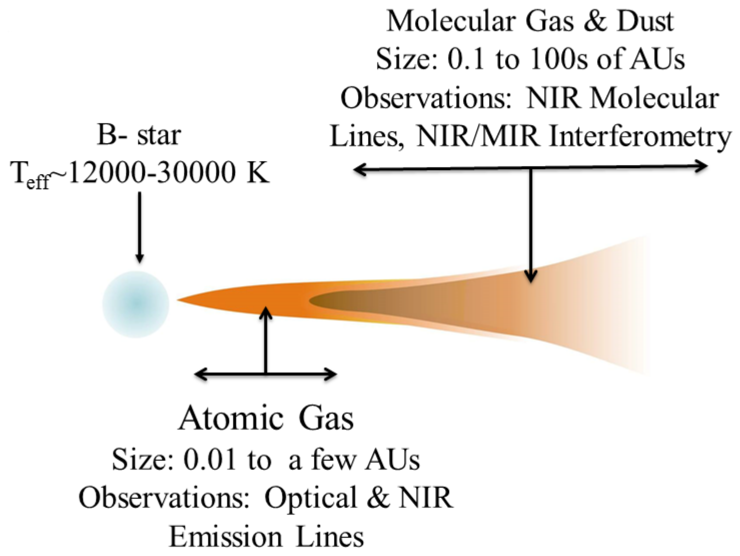

Figure 1.4: Inferred structure of the disk around HBe stars. Close to the star, partially ionized, atomic gas is expected, represented by orange color. The size of this region may extend anywhere from 0.01 AU to a few AUs. This region can be studied using optical and near-infrared spectral lines. As the temperatures cool outward in the disk, molecular gas and dust are expected. The size of this outer disk ranges from 0.1 to 100s of AUs. The transition between atomic and molecular gas occurs at around a few AUs. The molecular gas and dust found beyond the atomic gaseous disk is represented by brown, and this region can be studied using a variety of different methods such as molecular lines and NIR/MIR interferometry. It is important to note that this image is not to scale. Image Credit: Ami Patel

temperature of the HBe stars is higher than HAe stars, the higher radiation would essentially photoevaporate the circumstellar material close to the star. The gaseous disk present very close to the star, spans from ~ 0.1 AU (~ 4 R_*) to ~ 1 AU (~ 40 R_*) in size, the latter distance likely the dust sublimation radius (Dullemond & Monnier, 2010). Using optical emission lines of Mg II and O I as well as the forbidden emission lines of [O I] and the corresponding surface brightness profiles of the HBe star MWC 147 (B6e), Bagnoli et al. (2010) notes that the emission features are consistent with a flat, inner, gaseous disk. Some of the important atomic line used to study the gaseous disk are highlighted in Section 1.2.1.

Dullemond et al. (2007) suggests that young stellar objects (YSOs, hereafter) not only photoevaporate the material close to the star, but also regions beyond the dust sublimation radius. Gaseous material still exists on the outer layers of the dusty disk of the YSOs that are exposed to direct stellar radiation. Since HAeBe stars are hot, they are expected to have somewhat similar gaseous layers present in the extended disk. Molecular hydrogen (H_2) and carbon monoxide (CO) are the two most abundant molecules in the circumstellar disk. Lower transition probabilities along with high excitation temperatures make it difficult to trace molecular hydrogen. So CO is frequently used to trace molecular gas in the inner regions of the disk, especially regions inside the dust sublimation radius. A large number of studies, van der Plas et al. (2015); Eisner et al. (2014); Ilee et al. (2014, 2013) to name a few, have detected and studied CO overtone emission ($2.3\,\mu m$) amongst HAeBe stars, and found it to originate from areas inside the dust sublimation radius. There are a few examples of T Tauri stars and HAe stars whose spectra are matched to models with small inner dust free, gaseous disks using NIR and MIR interferometry (e.g. Akeson et al. 2005; Isella et al. 2008; Tannirkulam et al. 2008). A review of the molecular gases used to trace the disk at a variety of distances can be found in Carmona (2010).

Between the inner dust-free zone and the dusty disk, there exists an optically thick wall of dust normally called the dust inner rim (Dullemond et al., 2001). There is a lot of interest in trying to understand the inner rim's formation and structure. Near-IR and mid-IR interferometry have been used to trace the structure of the dusty, inner rim. Using K-band ($2.2\,\mu m$) observations, the size of the dust sublimation radius around early type HBe stars is estimated to be smaller than expected from the usual $R_{subl} \propto L_*^{1/2}$, which has been confirmed for HAe stars (Monnier & Millan-Gabet, 2002; Millan-Gabet et al., 2007; Monnier et al., 2005; Kraus et al., 2007). Monnier & Millan-Gabet (2002); Eisner et al. (2004) and Monnier et al. (2005) suggested that the smaller disk size might be explained by an optically thick gaseous disk closer to the stellar surface, which shields the dust from stellar radiation, hence allowing for cooler temperatures closer to the star than expected, and for dust to form. Disk models with optically thin gas surrounded by a dust wall have been successfully fit to the SED of HAe and late-type HBe stars (Eisner et al., 2004).

Using K-band (2.2 μm) observations, Monnier et al. (2005) suggests that if an optically thin gas exists in the dust-free zone, a wall of dust is expected as direct radiation from the star will enhance the scale height of the dust rim or puff up the inner disk wall. If an optically thick gas exists, then the transition to dust is smooth. The puffed up rim has been modeled by Dullemond et al. (2001), who successfully matched it to the SEDs of HAe stars.

Dust has been detected around YSO stars using various techniques and the structure of the dusty disk is comparatively well understood. As the temperature of the disk decreases away from the star, small dust grains are found in the disk, which are thought to later coalesce into planetesimals and planets. The temperature below $\sim 1500\,K$ is said to be ideal for dust to exist, however in rare cases, dust can exist at somewhat higher temperature of up to 1800K (Dullemond & Monnier, 2010; Tannirkulam et al., 2008). The near-IR bump seen at $\sim 2\,\mu$m corresponds to the temperature of around ~ 1500 K, which is an average temperature of dust evaporation. The IR excess at longer wavelengths is an indicator of the dust present in the disk and at distances away from the star.

For an isothermal disk to be in vertical hydrostatic equilibrium, the disk has to flare at larger radii. Combining the puffed up rim and flared disk, there may be regions where the puffed up rim will cast a shadow on the disk. The shadow on the disk creates a region with different temperatures in the disk than in the surroundings, changing the mechanism of the dust formation and condensation. Dullemond & Dominik (2004) propose that the flaring disk and self-shadowed disks are an evolutionary sequence, and that flaring disks occur in young stars while self-shadowed disks occur in comparatively older stars as the dust grains settle down over a long period of time. This has been confirmed by several studies of HAeBe stars (e.g. Acke et al. (2004)).

Studies, like that of Waelkens et al. (1996), have shown that there exist molecules and dust components that are rich in carbon and oxygen. These disks have been studied extensively at MIR, far-IR and millimeter wavelengths for molecules and dust species such as PAHs (Polycyclic Aromatic Hydrocarbons), iron oxide grains, and crystalline and amorphous silicate, to understand the evolution of these species in the disk (Waters & Waelkens, 1998; Malfait et al., 1998; Acke & van den Ancker, 2004). Nearly 50% of the HAeBe stars show PAHs in their spectrum (e.g. Meeus et al. (2001); Acke & van den Ancker (2004)), while their lower mass counterparts T Tauri stars only ~ 8% show PAH emission (Geers et al. 2006).

Using interferometric observations, one can detect disks by investigating the CO rotational lines/velocity fields. Many studies show evidence of disk's Keplerian rotation using the millimeter observations and CO J=2->1 rotational lines (e.g. Mannings et al. (1997); Pietu, Dutrey & Kahane (2003); Raman et al. (2006)). As the disks are remnants of the star formation phase, the disks are thought to be centrifugally supported, and hence Keplerian rotation is expected.

In addition to the disk, several HAeBe stars are known to have extended envelopes found beyond the disk (Waters & Waelkens, 1998). At longer wavelengths (far-IR), there is an extended emission in the spectrum of these stars which cannot be explained by disk-only models. Models with disk plus envelope match well to the SEDs of Hillenbrand's Group II stars (Hillenbrand et al., 1992). Including the envelope that is present beyond the disk for some of these stars, the circumstellar environment spans from ~ 0.1 to ~ 1000 AU using the variety of data acquired from observations (e.g. Eisner et al. (2003); Okamoto et al. (2009)).

Hillenbrand et al. (1992) derived disk masses from millimeter continuum measurements for 47 HAeBe stars and they found that the disk masses ranged from $0.1\,M_\odot$ to $6\,M_\odot$. Alonso-Albi et al. (2009) showed that the disk masses of HBe stars are 5 to 10 times lower than that of the HAe and T Tauri stars and found an average mass for gas+dust disk in HBe star was $< 0.01\,M_\odot$ and $\sim 0.04\,M_\odot$ for HAe stars. They proposed that the lower mass of the disk in HBe stars might be caused by photoevaporation of the extended disk and envelope as the star evolves. Pietu, Dutrey & Kahane (2003) observed that the disks of HAeBe stars are similar to their lower mass counterparts, but are hotter and more massive than the disks of T Tauri stars.

1.4 Comparison to Classical Be stars

Several studies have suggested that HBe stars can be compared to Classical Be stars (see Hamann & Persson (1992a); Mottram et al. (2007)) in their circumstellar disk and structure. HBe stars show many similarities with Classical Be stars in observational properties. As mentioned earlier, the SEDs of HAeBe stars in Group III of Hillenbrand's classification resemble the SEDs of Classical Be stars (Hillenbrand et al., 1992). Both show weak IR excess. Most HBe stars are known to show Group III type SEDs (Böhm & Balona, 2000). Like early-type HBe stars, Classical Be stars are known to show line depolarization (see Rivinius et al. (2013)). In addition, similarities such as the Hα equivalent width distribution, fast rotation speeds (i.e. high *v sini*), photometric variability, and slow outflow velocities further connect the Classical Be and HBe stars (Böhm & Balona, 2000). These similarities hint that maybe the same phenomenon is responsible for the emission line profiles. In addition to Hα, Classical Be stars (Briot, 1981; Jaschek et al., 1988, 1991; Apparao & Tarafdar, 1988) are known to show Ca II triplet lines in their spectrum, similar to the HBe stars (Hamann & Persson, 1992a). For Classical Be stars, Briot (1981) and Jaschek et al. (1988) noticed that the stars with the Ca II IR triplet emission lines show a slightly larger IR excess than stars without the Ca II IR triplet. Böhm & Balona (2000) note that the emission lines of HBe stars show velocities of few tens of km/s which are similar to those found in Classical Be stars. As we have seen, the disks of HAeBe stars (Mannings et al., 1997; Pietu, Dutrey & Kahane, 2003; Raman et al., 2006) are known to show Keplerian motion, similar to those of Classical Be stars (Porter & Rivinius, 2003). HAeBe stars are not such rapid rotators as Classical Be stars, but HAeBe stars are PMS stars and hence they will be spinning faster as they evolve and try to conserve the angular momentum while on their way to becoming MS stars, as suggested by Böhm & Balona (2000).

1.5 Significance of HAeBe Stars

1.5.1 Relation to the Massive & Intermediate Mass Star Formation

HAeBe stars, being intermediate mass stars, are an important link between low and high mass star formation. The evolution of their low mass counterparts, T Tauri stars, is fairly well understood as they spend a long time on the PMS phase and can be easily detected and studied. High mass, O-type stars form at the centers of very dense clusters and involve complex environments. The formation of such stars is currently poorly understood (Larson, 2003). In addition, such stars spend their pre-main sequence life in a deeply embedded state before becoming optically visible as main-sequence objects, hence depriving us of the opportunity to observe the early phase of star formation (Zinnecker & Yorke, 2007). In contrast, HBe stars, despite forming in complex and dense environments, may become optically visible just before they reach the Zero Age Main Sequence (ZAMS hereafter) as they spend comparatively longer in the PMS phase compared to their higher mass counterparts.

High mass stars are formed in Giant Molecular Clouds (GMCs) while low mass stars can not only form in GMCs but also in less massive clouds (Waters & Waelkens, 1998). Given that there is a lot of uncertainty about the structure and mass of the disks around these stars, the implications of such uncertainty can affect our understanding the evolution of these stars. Understanding disks at different stages of star formation can help us derive how the disks can change the course of a star's evolution.

1.5.2 Relation to Planetary Systems

The HAeBe stars are precursors of Vega-type systems, which are MS stars with excess IR radiation attributed to large grains of dust in the form of debris disks. Some well-known examples of such systems are β Pictoris, Fomalhaut, HR 5999, HD 100546 and Vega (Thé et al., 1996; Pérez & Grady, 1997; Grady et al., 1997; Waters & Waelkens, 1998). Deleuil et al. (1993) detected unexpected variation in the spectral lines of Fe II, Mg II and Al III in spectra of a cool star

(A5V), β Pictoris, and suggested that the spectral lines arise from the tail of a cometary like body that is being bombarded by radiation from the central star. β Pictoris has been studied and imaged extensively and is known to have a Jupiter mass planet amongst the debris.

Hernández et al. (2008) studied PMS stars in the $\sim$ 5 Myr old γ Vel star cluster and found that the gaseous disks around HAeBe stars have already dissipated, leaving only the dust debris disks which can be detected and imaged. Stars such as Vega and β Pictoris are known to show debris disks with gaps in them (Su & Rieke, 2013; Janson et al., 2013). Gaps can be a result of photoevaporation, planets/planetesimals, or a companion star. Deriving the timescale of the evolution of the disk will help us understand the overall picture of the formation of planetesimals and planets in these disks and can be used to compare the formation process in low and intermediate mass stars. Understanding HAeBe stars and their disks, thus, make an important contribution to the overall understanding of the formation and evolution of planetary systems in intermediate and high mass stars.

1.6 Summary

HAeBe stars are pre-main sequence A- or B-type stars with emission lines and SEDs with IR excess. The emission lines, particularly the Balmer series of hydrogen, and the IR excess can be attributed to circumstellar dust and gas, the likely remnants of the star-formation phase. In addition to Balmer lines, HAeBe stars also show emission lines of metals such as Ca II, Fe II, O I, Si II and Mg II.

Several observational methods, such as interferometric observations, IR and millimeter imaging techniques, have been used to establish the presence of circumstellar disks surrounding these stars along with circumstellar envelopes around some stars. Even with advancement in the understanding of these disks, the detailed spatial distribution within such disks is still a matter of debate. However, it can be assumed that the disk hosts gas and dust, with the gaseous region closer to the star and molecular and dust gas present in the more distant cooler regions.

Further away from the star, where the temperature has cooled to $\sim 1500\,\mathrm{K}$, the dust condenses. These disks host a very interesting set of dust species such as iron oxide grains, crystalline and amorphous silicate , which are thought to eventually coalesce to form planetesimals and planets. The similarities of circumstellar disks of HBe stars with those of Classical Be stars allow us an avenue to explore and test the applicability of the successful Classical Be stars' circumstellar disk models to gain more understanding of disks around HAeBe stars.

Being intermediate mass stars, these stars provide a bridge between the low-mass and high-mass star formation. Whether or not these stars accrete magnetospherically, is still a matter of debate, as large-scale magnetic fields have only been detected around $\sim 7\%$ of these stars. Magnetospheric accretion has successfully been modeled in HAe stars and late-type HBe stars but not in early-type HBe stars. Studies have hinted at the transition of mode of the accretion amongst the HBe stars, making them ideal candidates to study star formation and providing an invaluable insight in the star formation of high-mass stars. This poses interesting questions about the similarities and differences between these intermediate mass stars and their higher and lower mass counterparts.

A great deal of progress has been made in past few decades to understand the formation and evolution of these stars and their circumstellar disks. Nevertheless, HAeBe stars are mysterious in many ways, and some of the unanswered, open-ended questions include:

- When does the method of accretion transition from magnetospheric to classical disk accretion?
- Could HBe stars, the higher mass Herbig stars, host large-scale magnetic fields?
- What are the implications of classical disk accretion on the formation and evolution of the star as well as the disk?
- What is the spatial distribution and structure of the gaseous disk?
- How does the gaseous disk affect formation and evolution of the protoplanetary disk as well as the debris disk?

- How does the stellar mass affect the size of these gaseous disks?

These unanswered questions make them ideal test beds for disk physics and theory of star formation. Being young, bright and optically visible makes them great targets for such studies.

In this thesis, we present three journal articles that explore gaseous disks around early-type HBe stars. We compare the emission lines profiles seen in the observed spectra with synthetic spectra generated using non-LTE, radiative transfer circumstellar disks codes to constrain the physical properties of the inner gaseous disk. In Chapter 2 of the thesis, we describe the non-LTE radiative transfer circumstellar disk codes, BEDISK and BERAY, used to model the synthetic line profiles of gaseous disks around these stars as well as the process to generate the observables. We also look at the success of these codes in understanding the disks around Classical Be stars. In Chapter 3, we investigate the gaseous disk around one HB2e star, BD+65 1637, using Balmer and metal lines. In Chapter 4, using the same methods as in Chapter 3, we investigate the inner, gaseous region around three HB2e stars, HD 76534, HD 114981 and HD 216629. We compare the disks of these stars to that of BD+65 1637 in order to derive an overall understanding of disks around HB2e stars. In Chapter 5, we explore the disk around MWC 137, a HB0e star using the Balmer and the metal lines as well as compare the disk of this HB0e star with those of HB2e stars. In Chapter 6, we revisit the conclusions of each chapter and derive an overall understanding of inner gaseous disks amongst early-type HBe stars and note on what more needs to be done that could be helpful in understanding of the overall structure of these disks.

Bibliography

Ababakr, K. M., Fairlamb, J. R., Oudmaijer, R. D. & van den Ancker, M. E. 2015, MNRAS, 452, 2566A.

Acke, B., van den Ancker, M. E., Dullemond, C. P., van Boekel, R. & Waters, L. B. F. M. 2004, A&A, 422, 621A.

Acke, B. & van den Ancker, M. E. 2004, A&A, 426, 151A.

Akeson, R. L., Walker, C. H., Wood, K., Eisner, J. A., Scire, E., Penprase, B., Ciardi, D. R., van Belle, G. T., Whitney, B. & Bjorkman, J. E. 2005, ApJ, 622, 440.

Alecian, E., Catala, C., Wade, G. A., Bagnulo, S., Boehm, T., Bouret, J. C., Donati, J. F., Folsom, C., Grunhut, J., Landstreet, J. D., Marsden, S. C., Petit, P., Ramirez, J. & Silvester, J. 2009, EASPC, 39, 121.

Alecian, E., Wade, G. A., Catala, C., Grunhut, J. H., Landstreet, J. D., Bagnulo, S., Böhm, T., Folsom, C. P., Marsden, S. & Waite, I. 2013, MNRAS, 429, 1001.

Alonso-Albi, T., Fuente, A., Bachiller, R., Neri, R., Planesas, P., Testi, L., Berne, O. & Joblin, C. 2009, A&A, 497, 117.

Apparao, K. M. V. & Tarafdar, S. P. 1988, A&A, 192, 255.

Bachiller, R. 1996, ARAA, 34, 111.

Bagnoli, T., van Lieshout, R., Water, L. B. F. M., van der Plas, G., Acke, B., van Winckel, H., Raskin, G., Meerburg, P. D. 2010, ApJL, 724, L5.

Blondel, P. F. C., Talavern, A. & Tjin A Dije, H. R. E. 1993, A&A, 268, 624.

Böhm, T. & Balona, L. A. 2000, ASPC, 214, 103B.

Böhm, T. & Catala, C. 1995, A&A, 301, 155B.

Böhm, T. & Hirth, G. A. 1997, A&A, 324, 177.

Bouvier, J., Alencar, S. H. P., Harries, T. J., Johns-Krull, C. M. & Romanova, M. M. 2007, Protostars and Planets V, 479B.

Briot, D. 1981, A&A, 103, 1.

Carmona, A., 2010, EM&P, 106, 71C.

Catala, C. 1989, ESOC, 33, 471C.

Catala, C. 1994, ASPC, 62, 91C.

Cauley, P. W. & Johns-Krull, C. M. 2014, ApJ, 797, 112C.

Cauley, P. W. & Johns-Krull, C. M. 2015, ApJ, 810, 5C.

Cohen, M. & Kuhi, L. V. 1979, ApJS, 41, 743C.

Corcoran, M. & Ray, T. P. 1997, A&A, 321, 189.

Corcoran, M. & Ray, T. P., 1997, A&A, 331, 147C.

Cox, A. N. 2000, ”Allen’s Astrophysical Quantities”, 4th edition, Springer, ISBN 0-387-98746-0.

Davies, J. K, Evans, A. Bode, M. F. & Whittet, D. C. B. 1990, MNRAS, 274, 51722.

Deleuil, M., Gry, C., Lagrange-Henri, A. M., Vidal-Madjar, A., Beust, H., Ferlet, R., Moos, H. W., Livengood, T. A., Ziskin, D., Feldman, P. D. 1993, A&A, 267, 187.

Dent, W. R. F., Greaves, J. S., Coulson, I. M. 2005, MNRAS, 359, 663D.

Donati, J. F., Semel, M., Carter, B. D., Rees, D. E. & Collier Cameron, A. 1997, MNRAS, 291, 658.

Donehew, B. & Brittain, S. 2011, ApJ, 141, 46.

Dullemond, C. P., Dominik, C. & Natta, A. 2001, ApJ, 560, 957.

Dullemond, C. P. & Dominik, C. 2004, A&A, 417, 159.

Dullemond, C. P., Hollenbach, D., Kamp, I. & D'Alessio, P. 2007, arXiv:astro-ph/0602619.

Dullemond, C. P. & Monnier, J. D. 2010, ARAA, 48, 205.

Eisner, J. A., Lane, B. F., Hillenbrand, L. A., Akeson, R. L., & Sargent, A. I. 2004, ApJ, 613, 1049.

Eisner, J. A., Lane, B. F., Akeson, R. L., Hillenbrand, L. A. & Sargent, A. I. 2003, ApJ, 588, 360.

Eisner, J. A., Hillenbrand, L. A. & Stone, J. M. 2014, MNRAS, 443, 1916E.

Fairlamb, J. R., Oudmaijer, R. D., Mendigutía, I., Ilee, J. D. & van den Ancker, M. E., 2015, MNRAS, 453, 976F.

Finkenzeller, U. & Mundt, R. 1984, A&AS, 55, 109.

Finkenzeller, U. & Jankovics, I., 1984, A&AS, 57, 285F.

Finkenzeller, U. 1985, A&A, 151, 340.

Folsom, C. P., Bagnulo, S., Wade, G. A., Alecian, E., Landstreet, J. D., Marsden, S. C. & Waite, I. A. 2012, MNRAS, 422, 2072.

Friedemann, C., Reimann, H. G. & Guertler, J. 1992, A&A, 255, 246.

Garrison, L. M. & Anderson, C. M. 1977, ApJ, 218, 438.

Gómez de Castro, A. I. 2013, Planets, Stars and Stellar Systems. Volume 4: Stellar Structure and Evolution, 279.

Grady, C. A. Sitko, M. L. Bjorkman, K. S., Prez, M. R., Lynch, D. K., Russell, R. W., Hanner, M. S. 1997, ApJ, 483, 449G.

Grinin, V. P., The, P. S. de Winter, D., Giampapa, M., Rostopchina, A. N., Tambovtseva, L. V., van den Ancker, M. E. 1994, A&A, 292, 165.

Hamann, F. & Persson, S. E. 1992a, ApJS, 82, 285H.

Hamann, F. & Persson, S. E. 1992b, ApJS, 394, 628.

Hamann, F. 1994, ApJSS, 93, 485.

Herbig, G. H. 1960, ApJS, 4, 337H.

Herbig, G. H. & Bell, K. R. 1988, Third Catalogue of Emission-Line Stars of the Orion Population, Lick Obs. Bull. 1111:1.

Hernández, J., Calvet, N., Briceño, C., Hartmann, L. & Berlind, P., 2004, AJ, 127, 1682H.

Hernández, J. Hartman, L., Calvet, N., Jeffries, R. D., Gutermuth, R., Muzerolle, J. & Stauffer, J. 2008, ApJ, 686, 1195.

Herbst, W. & Shevchenko, V. S. 1999, AJ, 118, 1043H.

Hillenbrand, L. A. Strom, S. E., Vrba, F. J. & Keene, J. 1992, ApJ, 397, 613.

Hu, J. Y., Thé, P. S., DeWinter, D., 1991, A&A, 208, 21318.

Isella, A., Tatulli, E., Natta, A. & Testi, L. 2008, ApJ, 483, 13.

Ilee, J. D., Wheelwright, H. E., Oudmaijer, R. D., de Wit, W. J., Maud, L. T., Hoare, M. G., Lumsden, S. L., Moore, T. J. T., Urquhart, J. S., Mottram, J. C. 2013, MNRAS, 429, 2960I.

Ilee, J. D. Fairlamb, J. Oudmaijer, R. D., Mendigutía, I., van den Ancker, M. E., Kraus, S., Wheelwright, H. E. 2014, MNRAS, 445, 3723I.

Jain, S. K. & Bhatt, H. C. 1995, A&AS, 111, 399.

Janson, M., Brandt, T. D., Moro-Martn, A. 2013, ApJ, 773, 73.

Jaschek, C., Andrillat, Y., Jaschek, M. & Egret, D. 1988, A&A, 192, 285.

Jaschek, M., Andrillat, Y. & Jaschek, C. 1991, A&A, 250, 127.

Kraus, S., Preibisch, Th. & Ohnaka, K. 2007, Star-Disk Interaction in Young Stars, Proceedings of the International Astronomical Union, IAU Symposium, Volume 243, p. 337-344.

Kraus, S. 2015, Ap&SS, 357, 97K.

Kurucz, R. L. 1979, ApJS, 40, 1.

Larson, R. B. 2003, RPPh, 66,1651L.

Lynden-Bell, D. & Pringle, J. E. 1974, MNRAS, 168, 603L.

Malfait, C., Waelkens, C., Waters, L. B. F. M., Vandenbussche, B., Huygen, E. & de Graauw, M. S. 1998, A&A, 332, L25.

Mannings, V., Koener, D. W. & Sargent, A. I. 1997, Nature, 388, 6642, 555.

Mannings, V. & Sargent, A. I. 1997, ApJ, 490, 792M.

Marinas, N. Telesco, C. M. Fisher, R. S. & Packham, C. 2011, ApJ, 737, 57.

Meeus, G., Waelkens, C. & Malfait, K. 1998, A&A, 329, 131M.

Meeus, G., Waters, L. B. F. M., Bouwman, J., van den Ancker, M. E., Waelkens, C., Malfait, K. 2001, A&A, 365, 476M.

Mendigutía, I., Eiroa, C., Montesinos, B., Mora, A., Oudmaijer, R. D., Merín, B. & Meeus, G. 2011, A&A, 529A, 34M.

Mendigutía, I., Calvet, N., Montesinos, B., Mora, A., Muzerolle, J., Eiroa, C., Oudmaijer, R. D. & Mer´n, B. (2011a), A&A, 535, A99.

Mendigutía, I., de Wit, W. J., Oudmaijer, R. D., Fairlamb, J. R., Carciofi, A. C., Ilee, J. D. & Vieira, R. G. 2015, MNRAS, 453, 2126M.

Millan-Gabet, R., Malbet, F., Akeson, R., Leinert, C., Monnier, J. & Waters, R. 2007, Protostars and Planets V, B. Reipurth, D. Jewitt, and K. Keil (eds.), University of Arizona Press, Tucson, 951 pp., p.539-554.

Monnier, J. D., & Millan-Gabet, R. 2002, ApJ, 579, 694.

Monnier, J. D., Millan-Gabet, R., Billmeier, R., Akeson, R. L., Wallace, D., Berger, J.-P., Calvet, N., D'Alessio, P., Danchi, W. C., Hartmann, L., et al., 2005, ApJ, 624, 832.

Mottram, J. C., Vink, J. S., Oudmaijer, R. D. & Patel, M., 2007, MNRAS, 377, 1363M.

Mora, A., Natta, A., Eiroa, C., Grady, C. A., de Winter, D., Davies, J. K., Ferlet, R., Harris, A. W., Montesinos, B., Oudmaijer, R. D., Palacios, J. et al. 2002, A&A, 393, 259.

Mora, A. Eiroa, C. Natta, A. Grady, C. A. de Winter, D., Davies, J. K., Ferlet, R., Harris, A. W., Miranda, L. F., Montesinos, B., Oudmaijer, R. D. et al. 2004, A&A, 419, 255M.

Mundt, R. & Ray, T. P. 1994, ASPC, 62, 237.

Okamoto, Y. K., Kataza, H., Honda, M., Fujiwara, H., Momose, M., Ohashi, N., Fujiyoshi, T., Sakon, I., Sako, S., Yamashita, T., Miyata, T., Onaka, T. 2009, ApJ, 706, 665.

Oudmaijer, R. D., van der Veen, W. E. C. J., Waters, L. B. F. M., Trams, N. R., Waelkens, C. & Engelsman, E. 1992, A&AS, 96, 625.

Pérez, M. R. & Grady, C. A. 1997, SSR, 82, 407.

Pietu, V., Dutrey, A. & Kahane, C. 2003, A&A, 398, 565.

Porter, J. M. & Rivinius, Th. 2003, PASP, 115, 1153-1170.

Raman, A., Lisanti, M., Wilner, D. J., Qi, C. & Hogerheijde, M. 2006, AJ, 131, 2290.

Reipurth, B., Pedrosa, A. & Lago, M. T. V. T. 1996, A&AS, 120, 229.

Rivinius, T., Carciofi, A. C. & Martayan, C. 2013, A&ARv, 21, 69R.

Shevchenko, V. S. Ezhkova, O., Tjin A Djie, H. R. E., van den Ancker, M. E., Blondel, P. F. C. & de Winter, D. 1997, A&AS, 124, 33.

Su, K. Y. L. & Rieke, G. H. 2013, arXiv:1307.1735.

Tannirkulam, A., Monnier, J. D., Harries, T. J., Millan-Gabet, R., Zhu, Z., Pedretti, E., Ireland, M., Tuthill, P., Ten Brummelaar, T., McAlister, H., Farrington, C., Goldfinger, P. J., Sturmann, J., Sturmann, L. & Turner, N. 2008, ApJ, 689, 513.

Thé P. S., DeWinter D., Perez M. R. 1994, A&AS, 104, 31539.

Thé, P. S., Perez, M. R., Voshchinnikov, N. V. & van den Ancker, M. E. 1996, A&A, 314, 233T.

van den Ancker, M. E., Thé, P. S., Feinstein, A., Vásquez, R. A., DeWinter, D., Pérez, M. R. 1997, A&AS, 123, 6382.

van der Plas, G., van den Ancker, M. E., Waters, L. B. F. M. & Dominik, C. 2015, A&A, 574A, 75V.

van den Ancker, M. E., de Winter, D. & Thin A Djie, H. R. E. 1998, A&A, 330, 145.

Vink, J. S., Drew, J. E., Harries, T. J., Oudmaijer, R. D. 2002, MNRAS, 337, 356V.

Vink, J. S., Drew, J. E., Harries, T. J. & Oudmaijer, R. D., 2005, ASPC, 343, 232V.

Vink, J. 2015, Ap&SS, 357, 98V.

Waelkens, C., Waters, L. B. F. M., de Graauw, M. S., Huygen, E., Malfait, K., Plets, H., Vandenbussche, B., Beintema, D. A., Boxhoorn, D. R. et al. 1996, A&A, 315, 245.

Waters, L. B. F. M. & Waelkens, C. 1998, ARAA, 36, 233.

Wilner, D. J., Andrews, S. M. & Meredith Hughes, A. 2011, ApJL, 727, L42.

Yudin, R. V. & Evans, A. 1998, A&AS, 131, 401.

Zinnecker, H. & Yorke, H. W. 2007, ARAA, 45, 481.

Chapter 2

Circumstellar Disk Modeling

2.1 The BEDISK Circumstellar Disk Code

To calculate the thermal structure of an equatorial, rotationally-supported, gaseous disk surrounding a central B star, the BEDISK code (Sigut & Jones, 2007) was used. This code calculates the temperature structure of the disk, given a user-defined density structure, by enforcing radiative equilibrium in a gas of solar composition. The energy input to the disk was assumed to be solely from the photoionizing radiation field of the central star, and no wind from the central star was included in the calculations. The microscopic rates of heating and cooling were balanced to determine the temperature at many grid points in the disk. The disk was assumed to be axisymmetric and in Keplerian rotation,

$$V_K = \sqrt{\frac{GM_*}{R}} \,, \tag{2.1}$$

where G is the gravitational constant, M_* is the stellar mass and R is the radius. BEDISK includes the nine abundant elements H, He, C, N, O, Mg, Si, Ca and Fe over many ionization stages in the determination of the radiative equilibrium temperatures. The atomic level populations, required for the calculation of the heating and cooling rates, as well as for use later in computing emission lines, were obtained by solving the statistical equilibrium equations in

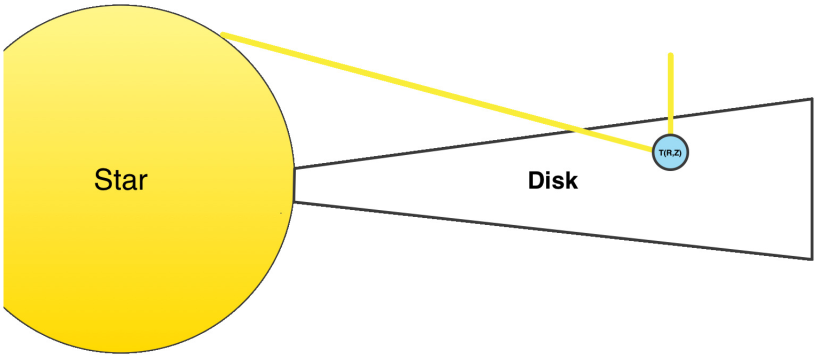

Figure 2.1: The enforcement of radiative equilibrium by BEDISK. For a given volume element in the disk (shown as the blue circle), rays are traced back to the stellar surface, and the photospheric intensity is used as the initial intensity for a radiative transfer solution along the ray. Only one ray is shown, but BEDISK includes ∼ 400 rays back to the stellar surface so that the mean intensity, J_ν, in each element can be accurately computed. This mean intensity is the sole energy source assumed for the disk. To determine photon losses, the optical depth to the upper and lower edges of the disk are computed, and the losses computed in an escape probability formalism based on these optical depths. Balancing the rates of energy gain and loss in each volume element defines the local radiative equilibrium temperature, $T(R,Z)$.

an escape probability formalism (see Sigut & Jones (2007) for details). An illustration of the basic computational principle of BEDISK can be seen in Figure 2.1.

The user defined density structure of the inner gaseous disk, $\rho(R,Z)$, in $\mathrm{g\,cm^{-3}}$, was taken to be specified by two parameters: ρ_0 (the base disk density) and n (the radial power law index) in the equation

$$\rho(R,Z) = \rho_0 \left(\frac{R_*}{R}\right)^n e^{-(Z/H)^2} \; . \tag{2.2}$$

Here R and Z are cylindrical co-ordinates in the disk, R_* is the stellar radius, and H is the disk scale height, which is a function of R as shown below. In all models, the disk is assumed to extend from the stellar photosphere at R_* out to a radius of R_{disk}, which is typically in the range of 10 to 100 R_*.

The vertical density structure of the disk is assumed to be determined by gravitational equilibrium,[1] and the scale height in this case has the form

$$H = \beta(T_{\rm HE})\left(\frac{R}{R_*}\right)^{3/2}, \tag{2.3}$$

where

$$\beta(T_{\rm HE}) = \sqrt{\frac{2kT_{\rm HE}R_*^3}{GM_*\mu m_H}}\,. \tag{2.4}$$

Here, M_* is the mass of the star, μ is the mean molecular weight of the gas in the disk (taken to be 0.68), m_H is the mass of hydrogen, and $T_{\rm HE}$ is a hydrostatic equilibrium temperature assumed for the disk. This hydrostatic temperature is used solely for setting the vertical scale height of the disk, and typically in classical Be stars, one finds $T_{\rm HE} \approx 0.6\,T_{\rm eff}$. A self-consistent treatment, in which the radiative equilibrium disk temperatures are used in the calculation of the vertical hydrostatic equilibrium, is possible (Sigut et al., 2009), but that has not been used here. In the present work, varying $T_{\rm HE}$ allowed the scale height of the disk to be varied. Note that vertical gravitational equilibrium predicts a flaring disk with $H \propto R^{3/2}$.

An example BEDISK calculation for the thermal structure of a disk surrounding a B2V star ($5.3\,R_\odot$, $9.1\,M_\odot$) is shown in Figures 2.2 through 2.5. In Figure 2.2, the computational grid (R_i, Z_{ij}) is shown. The upper envelope of the Z_{ij} grid points reflects the $R^{3/2}$ flaring of the disk predicted by vertical gravitational equilibrium.

The density structure of the disk surrounding this B2V star, assuming parameters $\rho_0 = 7.5\times10^{-11}\,{\rm g\,cm^{-3}}$ and $n = 3.0$ in Eqn. 2.2, is shown in Figure 2.3. Given this density structure, the BEDISK code enforces radiative equilibrium at each computational grid point in order to determine the disk temperature at that location using the procedure illustrated in Figure 2.1. The final balance between the heating and cooling rates in the gas (expressed as a ratio of heating to cooling) at each point in the disk is shown in Figure 2.5. As can be seen, the maximum im-

---

[1] The disk is rotationally supported in the R direction.

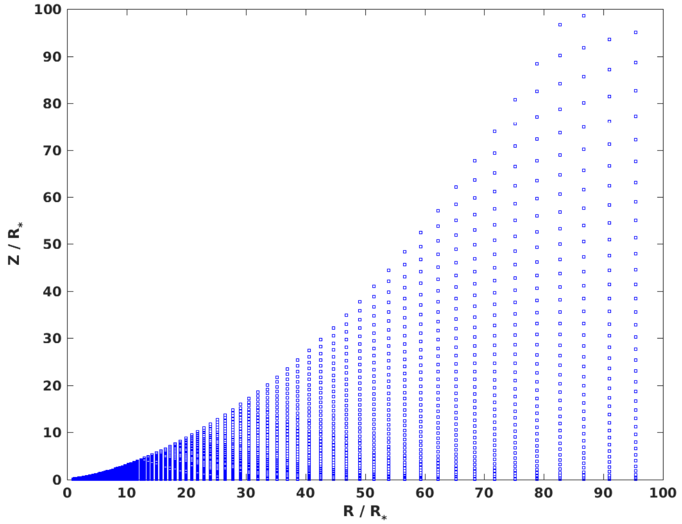

Figure 2.2: The computational grid for a BEDISK calculation for a disk surrounding a central B2V star (not shown). The grid flares with radius in order to account for the increase in the disk scale height with *R*. The disk is axisymmetric about the rotation axis and symmetric above and below the disk mid-plane.

balance is typically ±1%, although errors as large as 6% occur in the upper envelope far from the central star. As shown in Figure 2.4, the disk is far from isothermal, with a cool inner zone close to the central star. This cool zone occurs in dense disks where all lines of sight back to the central star are optically thick, thus significantly reducing the photoionization radiation from the central star reaching these regions. Moving further out in the disk, some lines of sight back to the central star (initially those terminating at high stellar latitudes) become optically thin, and the input heating rate increases. In addition, far from the star and/or far above the central plane of the disk, the low gas density reduces the cooling rate, resulting in higher temperatures. This cool inner zone, with hot “shealths” above and below, is a feature of all sufficiently dense disks heated by photoionization from a central star.

In addition to providing the basic thermodynamic state of the disk gas (T, P, and ρ), the BEDISK code also computes the atomic level populations of all of the included bound energy levels of the atoms and ions included in the calculation. All of this information is used by the BERAY code to predict observables, such as line profiles and spectral energy distributions

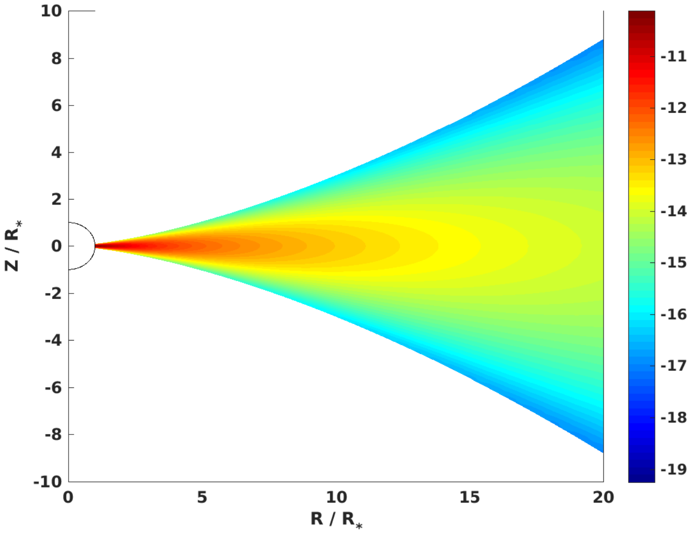

Figure 2.3: The disk density structure surrounding a B2V star with disk density parameters $\rho_0 = 7.5 \times 10^{-11}\,\mathrm{g\,cm^{-3}}$ and $n = 3.0$. The central star is shown as an outline only. The colour bar to the right is in $\log_{10}\rho$.

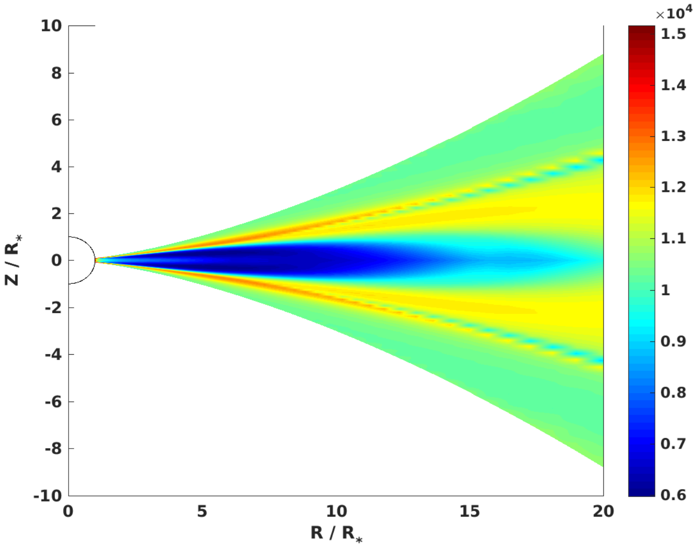

Figure 2.4: The disk radiative equilibrium temperatures corresponding to the density distribution shown in Figure 2.3. The energy input to the disk comes from the central stars photionizing radiation field. The colour bar to the right is temperature in degrees K.

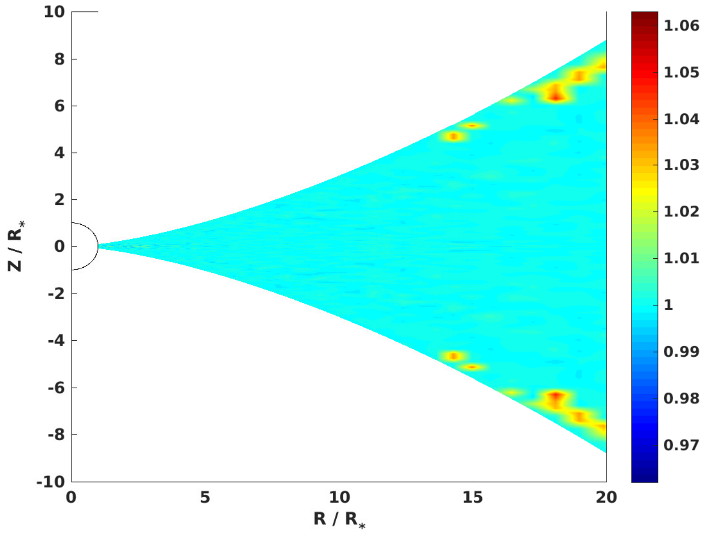

Figure 2.5: The ratio of the heating to cooling rate at each location in the disk which reflects the error in the enforcement of radiative equilibrium at that location. The colour bar to the right is the heating to cooling ratio.

(SEDs), as discussed in the next section.

The assumption of vertical hydrostatic equilibrium produces a very thin disk near the star. From Eq. 2.4, it is easy to see that the ratio H/R can be expressed as

$$\frac{H}{R} = \frac{c_S}{V_K}, \tag{2.5}$$

where $c_{\rm S}$ is the local sound speed and $V_{\rm K}$ is the Keplerian orbital velocity, Eq. 2.1. As the orbital velocity is typically hundreds of km s^{-1} while the sound speed is on the order of 10 km s^{-1} for the disk temperature, the disk is predicted to be geometrically thin with $H/R \ll 1$. Such thin disks have been successful in interpreting observables in classical Be stars, although there has been some evidence in the support of larger disk scale heights (see Arias et al. (2006); Zorec et al. (2007); Sigut & Patel (2013)). However, the application of such thin disks to HBe stars is less clear. For this reason, we also considered disk density models with an enhanced scale height, achieved by setting the $T_{\rm HE}$ temperature to be $5\,T_{\rm eff}$, a factor of nearly 10 over the gravitational equilibrium value. We will refer to these models as *thick disk* models. Note that for the same disk density parameters, ρ_0, n, and R_{disk}, the thick disk models are a factor of $\sqrt{5/0.6}$ more massive, as the total disk mass is proportional to the scale height.

2.2 The BERAY Radiative Transfer Code

The temperature structure and atomic level populations computed by BEDISK are input into the code BERAY (Sigut, 2011), which can compute observables such as line profiles, SEDs, and monochromatic images in the sky. This is done by solving the equation of radiative transfer along a series of rays ($\approx 10^5$) that pass through the star+disk system directed at the observer. Thus the BERAY calculation adds an additional parameter, namely the viewing inclination of the system: from $i = 0°$ for a pole-on star (face-on disk) to $i = 90°$ for an equator-on star (edge-on disk).

Examples rays are shown in Figures 2.6 and 2.7, in the co-ordinate system (X_s, Y_s, Z_s) where (X_s, Y_s) define the plane of the sky and the Z_s direction points at the observer, assumed to be located at $Z_s = +\infty$. In Figure 2.6, the disk is viewed at an inclination angle of 30° and the ray shown has $X_s = 0$ and $Y_s = 100\,R_*$. This ray intersects the top and bottom edges of the disk and passes through the equatorial plane of the disk. A series of grid points is created along the ray between the disk intersections, and the radiative transfer equation is formally solved for the emergent intensity by computing

$$I_\nu = I_\nu^0\, e^{-T_\nu} + \int_0^{T_\nu} S_\nu\, e^{-\tau_\nu}\, d\tau_\nu \;, \tag{2.6}$$

where T_ν is the total optical depth along this ray at frequency ν. For this ray, the incident intensity at the start of the ray is $I_\nu^0 = 0$. The optical depth scale, τ_ν, and source function, S_ν, are defined in terms of the gas opacity (χ_ν) and emissivity (η_ν) as

$$\tau_\nu \equiv \int_{Z_1}^{Z} (\chi_\nu^c + \chi_\nu^l)\, dZ_s \;, \tag{2.7}$$

and

$$S_\nu \equiv \frac{\eta^l_\nu + \eta^c_\nu}{\chi^l_\nu + \chi^c_\nu} \;, \tag{2.8}$$

respectively. The opacity and emissivity have both line (superscript l) and continuum (superscript c) contributions. Contributions to the continuum opacity include radiative bound-free (photoionization) and free-free (bremsstrahlung) processes, while the continuum emissivity includes radiative recombination and free-free emission. For the line contributions, the opacity and emissivity for a transition from atomic energy level E_i with level population N_i and to atomic energy level E_j with level population N_j are

$$\chi^l_\nu = \frac{h\nu_0}{4\pi}\left(N_i\,B_{ij} - N_j\,B_{ji}\right)\phi_\nu \;, \tag{2.9}$$

and

$$\eta^l_\nu = \frac{h\nu_0}{4\pi} N_j\,A_{ji}\,\phi_\nu \;, \tag{2.10}$$

respectively. Here, $h\nu_0 = E_j - E_i$, N_i and N_j are the atomic level populations, A_{ji}, B_{ji} and B_{ij} are the Einstein constants for spontaneous emission, stimulated emission, and photoabsorption respectively, and ϕ_ν is the line absorption profile. The required level populations N_i and N_j are found by interpolating in the level populations computed by bedisk. The line profile, ϕ_ν, which gives the probability of either absorption or emission of a line photon of frequency ν was taken to be a (unit normalized) Gaussian of the form

$$\phi_\nu = \frac{1}{\sqrt{\pi}\Delta}\, e^{-\left(\frac{\nu-\nu'_0}{\Delta}\right)^2} \;, \tag{2.11}$$

where Δ is the line width defined as

$$\Delta = \left(\frac{2kT}{A\,m_H} + \zeta_t^2\right)^{1/2} \;. \tag{2.12}$$

Here A is the atomic weight of the atom or ion and m_H is the hydrogen mass. In the compu-

Table 2.1: Atomic data for the lines used in this work. (Source: NIST Atomic Spectra Database)

Atom/Ion	Air Wavelength (Å)	g_i	g_j	E_i (eV)	A_{ji} (s^{-1})
H I (Hα)	6562.7	8	18	10.2	4.41e+07
H I (Hβ)	4861.3	8	32	10.2	8.42e+06
H I (Hγ)	4341.4	8	50	10.2	2.53e+06
He I	6678.1	3	5	21.2	6.37e+07
Ca II	8542.1	6	4	1.7	9.90e+06
Fe II	5169.0	6	8	2.9	4.20e+06
Fe II	5316.6	12	10	3.1	3.90e+05

tation of the thermal line width, a microturbulent contribution of ζ_t km s^{-1} was allowed (see discussion below). As the transfer equation is solved in the observer's frame, it is necessary to include the Doppler shift of the line centre frequency as

$$\nu_0' \equiv \nu_0 - \frac{\hat{z} \cdot V_K \hat{\phi}}{c} \, , \tag{2.13}$$

Here ν_0 is the rest frequency of the line, $h\nu_0 = E_j - E_i$, V_K is the Keplerian velocity at that point in the disk (assumed rotating in the direction specified by the unit vector $\hat{\phi}$) and $\hat{z}$ is a unit vector in the direction of the observer (assumed to be at $Z_s = +\infty$).

Atomic data for the lines of hydrogen, helium, calcium and iron considered in this work (air wavelength, excitation energy, and Einstein A_{ji} value) are given in Table 2.1.

A microtubulent contribution to the line width was included in some models as there is some evidence in classical Be stars that the α viscosity parameter required in hydrodynamical models of disk formation and dissipation is $\approx$ 1 (Carciofi et al., 2012). One possible interpretation of this result is that of sonic turbulence in the disk, i.e. $\nu = \alpha c_S H \sim c_S H$. For this reason, we have also considered models in which the disk is assumed to have a microtuburbulent velocity equal to the local sound speed. Microturbulence is a concept from classical stellar atmospheres that represents the dispersion of an assumed Gaussian distribution of turbulent velocities on scales smaller than unit optical depth. In this case, the turbulence acts to broaden

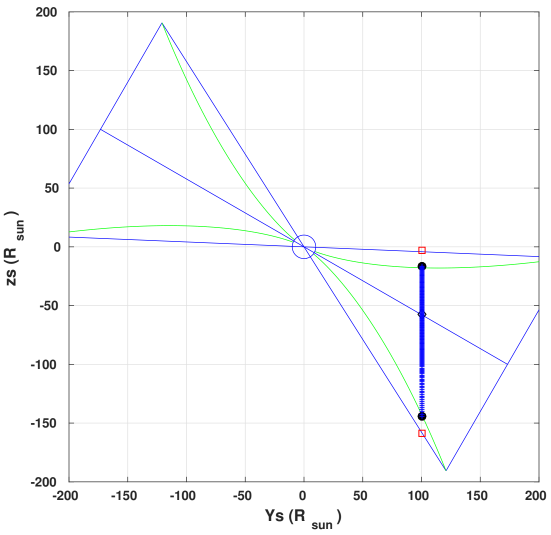

Figure 2.6: A single example ray (assumed in the Y_s, Z_s plane) passing through the circumstellar disk. Blue lines show the limits of the disk while the green lines shown the upper and lower edges of the disk. The ray along which the transfer equation is solved is shown by the thick blue line, directed at the observer, assumed to be at $Z_s = +\infty$. The inclination angle of the disk, the angle between the disk and star's common rotation axis and the line of sight is 30°. In this case, an $I_\nu = 0$ boundary condition is used for the intensity.

the atomic absorption profile and hence is easily incorporated as an increase in the Doppler widths of radiative transitions. In our models, we assumed that the microturbulence value was either zero or equal to the local sound speed. These models will be referred to as *turbulent disks*.

Another example ray is shown in Figure 2.7. Here the disk is viewed at a larger inclination angle, $i = 80°$, nearly edge one, and in this case, the ray terminates on the stellar surface. Rays that terminate on the stellar surface use a Doppler-shifted photospheric (LTE) line profile for the initial boundary condition, I_ν^0, while rays that pass entirely through the disk, like that shown in Figure 2.6, assume no incident radiation with $I_\nu^0 = 0$.

The main use of BERAY in this work is to compute line profiles for hydrogen, helium, and ionized metals, such as Ca II and Fe II, for the star+disk system. As the systems are unresolved on the sky, the emergent intensities along each of the rays are combined to form the monochromatic flux following

$$F_\nu \equiv \int I_\nu d\Omega = \int\int I_\nu(X_s, Y_s)\,\frac{dX_s\,dY_s}{D^2}\ , \tag{2.14}$$

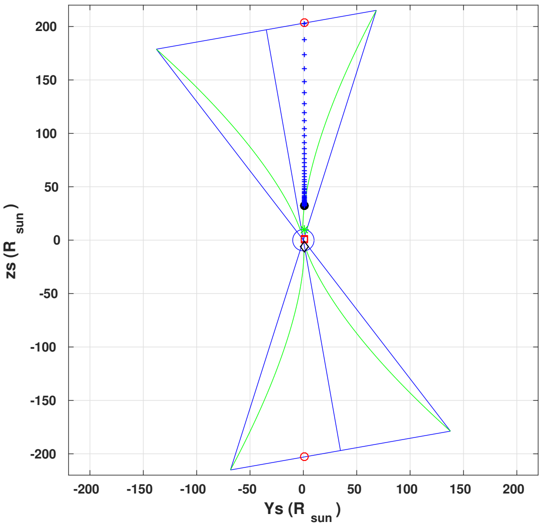

Figure 2.7: A second example ray, similar to Figure 2.6 but for a disk viewed at $i = 80°$. In this case, a photospheric intensity is used for the initial condition.

where D is the distance to the source, and the integration is over the plane of the sky containing the system. If F_c is the continuum flux outside of the line, the relative flux F_ν / F_c can be compared to continuum normalized spectra. In addition, the total strength of a line can be expressed in terms of the line equivalent width, defined as

$$\mathrm{EW} \equiv \int \frac{F_\nu - F_c}{F_c}\, d\nu \ , \tag{2.15}$$

where the integral is taken over the width of the line, and emission lines (emission above the local continuum) are defined as positive equivalent widths. Equivalent widths are usually measured in Angstroms (1 Å= 10^{-8} cm) and represent the "width" of continuum flux required to give the same emission as the line.

The stellar rotation rate was considered to be $V_{\mathrm{eq}} = 0.8\, V_{crit}$ for all the models, where

$$V_{crit} = \sqrt{\frac{2\, G\, M_*}{3\, R_*}} \ , \tag{2.16}$$

is the critical rotation rate at the equator in which the centrifugal force balances gravity. Note that in this notation, the projected stellar rotation rate, usually called $v \sin i$, is equal to $V_{\mathrm{eq}} \sin i$.

Such high rotation rate generally deforms the star and gravitationally darkens them; however, as the emission from the disk is the subject of the study here, and not the star, the star is taken to spherically symmetric.

2.3 Classical Be Stars and the BERAY and BEDISK Codes

BEDISK and BERAY are non-LTE radiative transfer codes constructed specifically for classical Be stars and their ionized, gaseous decretion disks. Many studies, such as Silaj et al. (2010, 2014), have been able to successfully model the structure of the gaseous disk by comparing synthetic and observed Hα lines. Sigut (2011) has shown that such models based on Hα are also able to correctly predict observed Fe II lines in the spectra of these stars. These models have also been able to reproduce the observed correlation seen between Hα and long-term variations in visual magnitude, which are interpreted as formation and dissipation of the disk over long periods of time in classical Be stars (Sigut & Patel, 2013). Observed IR line fluxes (Halonen et al., 2008; Jones et al., 2009) as well as optical and near-IR interferometry (Jones et al., 2008; Tycner et al., 2008; Mackay et al., 2009; Grzenia et al., 2013; Sigut et al., 2015) computed with BEDISK and BERAY models, have been used to put constraints on the several classical Be star disks.

Several authors, such as Carciofi et al. (2006, 2007, 2009), studied the classical Be stars α Eri, ζ Tau and δ Sco by fitting viscous decretion disk models to the observed Balmer lines, SEDs, and polarization measurements. Silaj et al. (2010) studied 56 classical Be stars and successfully fit the observed Hα profiles to BEDISK models. Many individual stars, such as χ Oph (Tycner et al., 2008), κ Dra, β Psc, υ Cyg (Jones et al., 2008), and o Aqr (Sigut et al., 2015), have been studied spectroscopically as well as interferometrically and are found to match a density model similar to the one adopted in this study. All of these mentioned studies, as well as several others, have fit the observed line profiles well with a power law index (n) ranging from 2.0 to 4.0, typically 3.5, and the disk base density (ρ_0) varying between 10^{-10} and 10^{-12} g cm^{-3} (Rivinius et al., 2013).

Given the noted similarities between HBe and Classical Be stars (Hamann & Persson, 1992a; Böhm & Balona, 2000; Mottram et al., 2007), a good starting point for the modeling of the emission spectra of HBe stars is using codes that have successfully been able to reproduce emission lines from the gaseous disks of classical Be stars. The analysis can give insights on the regions where the lines are being formed, the mass of the disk, and the temperature and density structure of the emitting regions.

Bibliography

Arias, M. L., Zorec, J., Cidale, L. & Ringuelet, A. E. 2006, A&A, 460, 821.

Böhm, T. & Balona, L. A. 2000, ASPC, 214, 103B.

Carciofi, A. C., Miroshnichenko, A. S., Kusakin, A. V., Bjorkman, J. E., Bjorkman, K. S., Marang, F., Kuratov, K. S., García-Lario, P., Calderón, J. V. Perea, Fabregat, J., Magalhães, A. M. 2007, ApJ, 2006, 652, 1617C.

Carciofi, A. C., Bjorkman, J. E., Miroshnichenko, A. S., Magalhães, A. M. & Bjorkman, K. S. 2007, ASPC, 631, 242C.

Carciofi, A. C., Okazaki, A. T., Le Bouquin, J. -B., Štefl, S., Rivinius, Th., Baade, D., Bjorkman, J. E. & Hummel, C. A. 2009, A&A, 504, 915C.

Carciofi, A. C., Bjorkman, J. E., Otero, S. A., Okazaki, A. T., Štefl, S., Rivinius, T., Baade, D. & Haubois, X. 2012, ApJ, 744L, 15C.

Grzenia, B. J., Tycner, C., Jones, C. E., Rinehart, S. A., van Belle, G. T. & Sigut, T. A. A. 2013, AJ, 145, 141G.

Halonen, R. J., Jones, C. E., Sigut, T. A. A., Zavala, R. T., Tycner, C., Levine, S. E., Luginbuhl, C. B., Vlieg, N. & Vrba, F. J. 2008, PASP, 120, 498H.

Hamann, F. & Persson, S. E. 1992a, ApJS, 82, 285H.

Jones, C. E., Tycner, C., Sigut, T. A. A., Benson, J. A. & Hutter, D. J. 2008, ApJ, 687, 598J.

Jones, C. E., Molak, A., Sigut, T. A. A., de Koter, A., Lenorzer, A. & Popa, S. C. 2009, MNRAS, 392, 383J.

Mackay, F. E., Elias, N. M., II, Jones, C. E., & Sigut, T. A. A. 2009, ApJ, 704, 591M.

Mottram, J. C., Vink, J. S., Oudmaijer, R. D. & Patel, M. 2007, MNRAS, 377, 1363M.

Rivinius, T., Carciofi, A. C. & Martayan, C. 2013, A&ARv, 21, 69R.

Sigut, T. A. A. & Jones, C. E. 2007, ApJ 668, 481.

Sigut, T.A.A., McGill, M. A. & Jones, C.E. 2009, ApJ, 699, 1973-1981.

Sigut, T. A. A., 2011, in IAU Symposium 272: Active OB Stars: Structure, Evolution, Mass Loss, and Critical Limits, ed. C. Neiner, G. Wade, G. Meynet, & G. Peters (Cambridge: Cambridge Univ. Press), 426.

Sigut, T. A. A & Patel, P. 2013, ApJ, 765, 41S.

Sigut, T. A. A., Tycner, C. T., Jansen, B. & Zavala, R. T., 2015, ApJ, 814, 159S.

Silaj, J., Jones, C. E., Tycner, C., Sigut, T. A. A. & Smith, A. D. 2010, ApJS, 187, 228S.

Silaj, J., Jones, C. E., Sigut, T. A. A. & Tycner, C. 2014, ApJ, 795, 82.

Tycner, C., Jones, C. E., Sigut, T. A. A., Schmitt, H. R., Benson, J. A., Hutter, D. J. & Zavala, R. T. 2008, ApJ, 689, 461T.

Zorec, J., Arias, M. L., Cidale, L. & Ringuelet, A. E. 2007, A&A, 470, 239.

Chapter 3

Herbig B2e Star: BD+65 1637

This chapter is adapted from the article: Patel, P., Sigut, T. A. A. & Landstreet, J. D., *'Photoionization Models of Inner Gaseous Disk of Herbig Be Star: BD+65 1637'*, 2016, ApJ, 817, 29.

3.1 BD+65 1637

BD+65 1637 (V* V361 Cep) is a B2e star of visual magnitude 10.83 in the young cluster NGC 7129 (Straižys et al. , 2013; Dahm & Hillenbrand, 2015). BD+65 1637 was identified as a HBe star by George Herbig in his first paper on Herbig stars (Herbig, 1960) and was noted to have a spectrum very much like that of a classical Be star. Hillenbrand et al. (1992) studied the star's SED which showed a small infrared excess, and they classified it as very similar to classical Be stars. The assigned spectral type has varied in the literature from B2 to B5 (see Herbig (1960); Strom et al. (1972); Finkenzeller & Mundt (1984); Finkenzeller (1984); Hillenbrand (1995)). Here, we will adopt the stellar parameters and their uncertainties from Alecian et al. (2013), reproduced in Table 3.1.

Table 3.1: Stellar parameters for BD+65 1637

Parameter	Value
Spectral Type	B2e
T_{eff} (K)	19000
log g (cgs)	4.0
Radius ($R_\odot$)	6.7±0.7
Mass ($M_\odot$)	$8.11^{+0.24}_{-0.23}$
Distance (pc)	1250±50
$v\,sini$ (km s^{-1})	278±27

Note. All of the values for the parameters as well as their uncertainties are taken from Alecian et al. (2013). The value of T_{eff} = 19000 K is within the error 1000 K obtained by Alecian et al. (2013).

3.1.1 Observations

The observational data were obtained in 2006 (HJD 2453898) using the high-resolution spectropolarimeter ESPaDOnS at the Canada-France-Hawaii Telescope (CFHT, hereafter). Additional spectra are also available from the Narval spectropolarimeter at the Télescope Bernard Lyot, obtained in 2009 (HJD 2455099). Both spectropolarimeters cover the wavelength range from 3700 to 10500 Å with a spectral resolution of 65,000. The peak Signal-to-Noise ratio (SNR, hereafter) per CCD pixel at 7300 Å was 237 for ESPaDOnS spectrum and 276 for Narval spectrum.

The CFHT spectrum of BD+65 1637 can be seen in Figure 3.1. A high resolution version of the spectrum can be found in Appendix A, Figure A.1. The spectrum not only contains strong Balmer line emission, Hα and Hβ, but also emission in many metal lines, such as those from calcium, oxygen and iron. In addition to the two strong Balmer lines, we will investigate one of the three Ca II infrared triplet lines (λ 8542), two Fe II lines (λ 5169 of multiplet 42 and λ 5317 of multiplet 49) and one He I line (λ 6678). The He I line is seen in absorption and is used to estimate stellar properties such as the *v sini* of the star. A detailed profile of each line

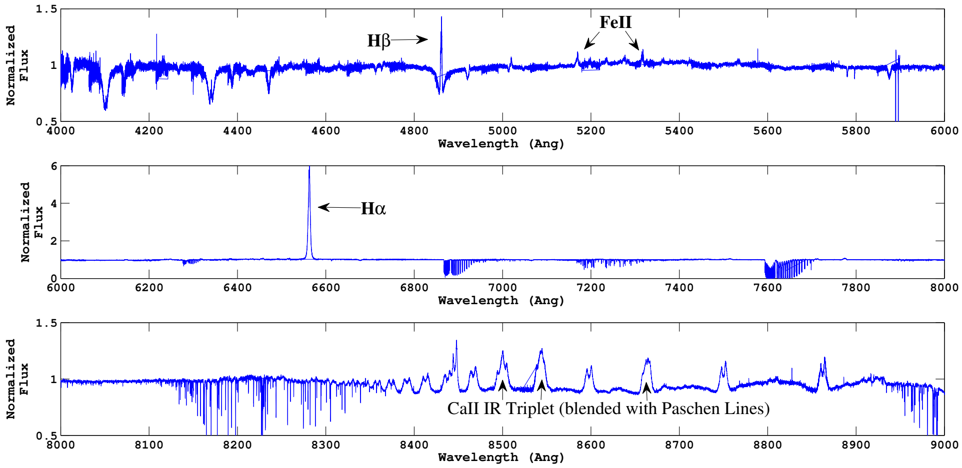

Figure 3.1: CFHT ESPaDOnS spectrum for BD+65 1637 (Alecian et al. , 2013). The spectrum shows many emission lines, such as the hydrogen Balmer lines, Hα (λ 6563) and Hβ (λ 4861), the Ca II IR-triplet lines (λ 8498, λ 8542 and λ 8662) and the Fe II lines (λ 5169 of multiplet 42 and λ 5317 of multiplet 49). The strengths of the lines vary over a large scale, particularly for Hα, as seen in the vertical scale of each subplot.

can be found in Figure 3.2.

The Balmer lines, Hα and Hβ, are the strongest emission lines in the optical/NIR spectrum of BD+65 1637, as illustrated in Figure 3.1. For BD+65 1637, the equivalent width (EW, hereafter) of the Hα lines has been noted to vary from 45 Å to 28 Å[1] (Garrison & Anderson, 1977; Heŕnandez et al. , 2004; Fernández et al. , 1995; Finkenzeller & Mundt, 1984). In the 2006 CFHT spectrum, the EW measured for Hα is 26.2 Å and for Hβ, 0.92 Å. The EW for Ca II IR Triplet (λ 8542) is measured to be 4.0 Å. The two Fe II lines, λ 5169 and λ 5317, were chosen for this study as they are in different multiplets, and their EWs were measured to be 0.58 Å and 0.40 Å. Fe II λ 5169 is in multiplet 42 ($a^6S - z^6P^\circ$) and Fe II λ 5317 is in multiplet 49 ($a^4G - z^4F^\circ$), although it is blended with a weaker line from multiplet 48.[2] Both of these lines have low excitation energy. He I (λ 6678) is in absorption, and the EW was measured to be -0.33 Å.

---

[1] Emission in EW is represented by a positive value and absorption is represented by a negative value in this as well as the following chapters.

[2] While both multiplets arise from the a^4G lower level, the transition probability (Δ_{ji}) value of the multiplet 48 component is 6.5 times smaller than the multiplet 49 component.

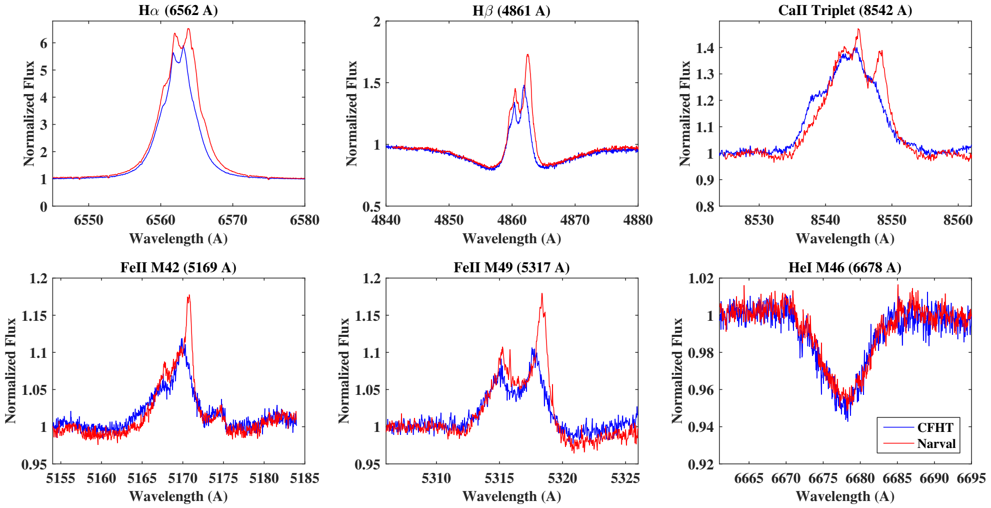

Figure 3.2: The ESPaDOnS observations (blue) are overplotted with the Narval observations (red) for each individual line. The ESPaDOnS observation was obtained in 2006 (HJD-2453898) at CFHT, and the Narval observations were taken in 2009 (HJD-2455099) at the Télescope Bernard Lyot. Except for He I (λ 6678), all the lines show variations with time.

A comparison between the CFHT and Narval spectra, taken approximately three years apart, can be seen in Figure 3.2. Some variation in the spectral lines is seen, most notably in the metal lines and V/R ratio, with a strong red component in the Narval (2009) observations. The similarity in the He I (λ 6678) absorption line, in contrast to variations in the Balmer and metal lines, confirms that the Balmer and metal emission lines arise from material outside the star and that the disk structure varies over time. For the analysis of this study, only the 2006 CFHT ESPaDOnS data was used.

Hα, Hβ, and both the Fe II lines (λ 5169 and λ 5317) show double-peaked profiles, with a stronger red component (R) when compared to the blue component (V). All the nonphotospheric lines included in this study show changes in the V/R ratio over time (see Figure 3.2). Classical Be stars are known to show V/R line variability, which is interpreted as being caused by a one-armed, global disk oscillation (for details see the review by Rivinius et al. (2013)). This effect has not been included in the model here, and hence the synthetic line profiles cannot fit both peaks of a line profile simultaneously.

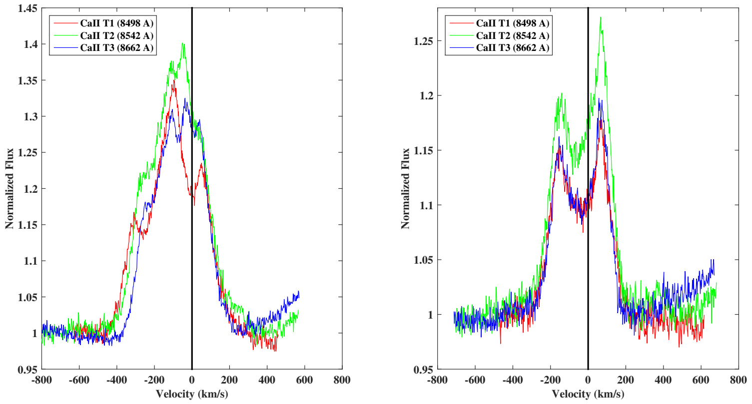

Figure 3.3: *Left:* All Ca II IR Triplets before the subtraction of Paschen lines. *Right:* The Ca II IR Triplets after subtraction of Paschen lines. The black solid line denotes 0 km s^{-1} radial velocity.

3.1.2 Reduction of Spectra

In order to compare the observed and modeled line profiles, the observed spectra needed to be continuum normalized. The unnormalized data obtained from CFHT (and Narval) were separated into specific wavelength windows that included the emission lines of interest. Each wavelength window was continuum normalized using IRAF [3]. The function and order used for normalization varied from one spectral window to another; ‘Legendre’ and ‘cubic spline’ functions and low-order polynomials were generally used in the process.

The Ca II infrared triplet lines (λ 8498, λ 8542 and λ 8662) are blended with the hydrogen Paschen series. In order to compare with synthetic line profiles, the Paschen line must be subtracted from the Ca II line. This was done by taking an average of the two nearest, unblended Paschen lines and then subtracting the average from the Ca II line. Figure 3.3 illustrates all three lines before the process of subtraction (on the left) and after subtraction (on the right) in the CFHT spectrum. It can be seen that the subtraction process decreases the strength of the Ca II line, and the resultant line profile is double-peaked with a stronger red peak.

An example of the subtraction process is illustrated in Figure 3.4, where the average of

---

[3] IRAF is distributed by the National Optical Astronomy Observatories, which are operated by the Association of Universities for Research in Astronomy, Inc., under cooperative agreement with the National Science Foundation.

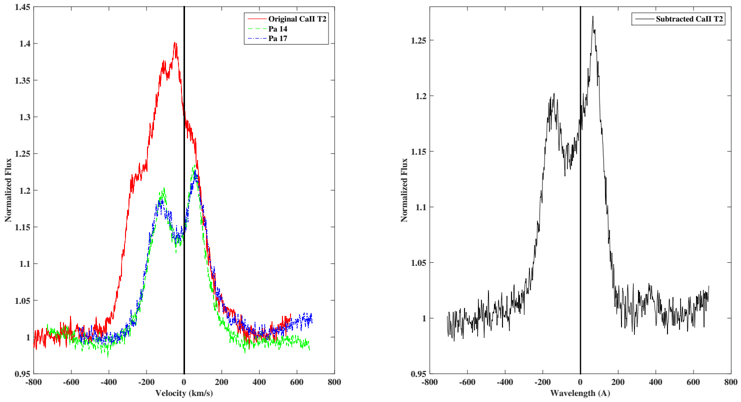

Figure 3.4: *Left*: One of the Ca II triplet lines (λ 8542), seen in red, along with the Paschen 14 (P14, λ 8596) in green and Paschen 17 (P17, λ 8467) in blue. *Right*: The resultant Ca II line profile after subtraction of the average of the Paschen lines. The different scales on the y axes should be noted. The black solid line denotes 0 km s^{-1} radial velocity.

Paschen 14 (P14, λ 8596) and Paschen 17 (P17, λ 8467) is subtracted from the blended Ca II λ 8542 line to extract the unblended Ca II profile. For the rest of the paper, the resultant Ca II line profile (seen in the right-hand panel of Figure 3.4) will be used. All the lines are adjusted for the stellar radial velocity. The radial velocity required for the line shifts was measured using the center of He I (λ 6678), which was measured to be -17.1 km s^{-1} for the CFHT spectrum and -4.1 km s^{-1} for the Narval spectrum. Both the values are within the range of -26 ± 20 km s^{-1} measured by Alecian et al. (2013).

3.2 Results

Large libraries of synthetic line profiles were calculated for Hα, Hβ, the Ca II IR triplet (λ 8542), Fe II (λ 5169, λ 5317)[4], and He I (λ 6678) for disks surrounding a B2 star using combinations of the disk density parameters listed in Table 3.2. Values of the base disk density parameter, ρ_0, ranged from 10^{-13} to 10^{-8} g cm^{-3}, and the power-law index n ranged from 0.5 to 3.0. Three different-sized disks were considered, R$_{disk}$=25, 50 and 100 R$_*$; thus, the largest disk considered has an outer diameter of 3.1 AU. This range of disk density parameters and disk sizes includes

---

[4] For Fe II 5317, only the multiplet 49 component was included.

the range of values typically found for classical Be stars, as noted above, but with an extension to more massive disks (i. e. higher ρ_0 and/or lower n). All synthetic line profiles were calculated at viewing inclinations of 18°, 45°, 60° and 75°, which represent the centers of the first four bins of five equal-area bins in a random sin i distribution.

Each observed line profile was compared to its synthetic library by computing a figure-of-merit, $\mathcal{F}$, defined as

$$\mathcal{F} \equiv \frac{1}{N} \sum_{i=1}^{N} \frac{|F_i^{\rm Mod} - F_i^{\rm Obs}|}{F_i^{\rm Obs}}, \tag{3.1}$$

where $F_i^{\rm Obs}$ is the observed relative flux, $F_i^{\rm Mod}$ is the model relative flux, and the sum is over the N wavelength points spanning the line. In performing this sum, a range of small shifts to the observed wavelength scale was also tried, within the errors of the star's radial velocity. The smallest value of $\mathcal{F}$ was deemed to define the best-fit model for that feature, although all profiles with small values of $\mathcal{F}$ were visually inspected. These top 9 best-fit lines, along with the model parameters (illustrated using $\log_{10}\rho_0$ vs n) for BD+65 1637 can be found in Appendix B, from Figure B.1 to Figure B.10. In addition, the disk density parameters of profiles that fit the observed profiles almost as well as the best-fit model were also examined, and this point, concerning the uniqueness of the fits, will be discussed in Section 3.3.

While the minimum of $\mathcal{F}$ for a given line, say $\mathcal{F}^{\rm H\alpha}$, defines the best fit for that particular line, it is not guaranteed that the best-fit model for all lines will result in the same set of disk density parameters. A figure-of-merit defined by Eqn. 3.1 can be obtained for each line

Table 3.2: Explored Model Parameters for the Disk of HBe stars.

Parameter	Range
Base Disk Density, ρ_0 (g cm^{-3})	10^{-8}...10^{-13}
Power Law Index, n	0.5...3.0
Inclination, i (°)	18...75
Disk Radius, R_{disk} (R_*)	25...100

considered: $\mathcal{F}^{\mathrm{H}\alpha}$, $\mathcal{F}^{\mathrm{H}\beta}$, and so on. Therefore, it is possible to search for the best set of disk parameters that minimizes the sum of all of the line figures-of-merit, i.e. the global, best-fit model.

For all the line profile matches performed in this study, the effort was made to fit to the blue peak of the emission line. When a reasonable fit was not found for the blue peak, the fit was computed for the red peak instead.

We will now first discuss the best-fit models for each line individually and then consider the best global model.

3.2.1 Individual Fits

The best-fit models for all individual lines are listed in Table 3.3, and the best synthetic line profile fits to the individual observed emission lines are shown in Figure 3.5. With the freedom to chose the density model independently for each line, the observed line profiles can be reproduced quite well in strength, shape, and equivalent width by the models.

The best fit for Hα is a $50\,\mathrm{R}_*$, thin disk model with the base disk density parameter ρ_0 of $3.2 \times 10^{-12}\,\mathrm{g\,cm^{-3}}$ and power-law index n of 2.0 seen at an inclination of 60°. The observed and synthetic profiles are compared in Figure 3.5. The width of Hα at its base is underestimated, and a better fit might be possible by refining the viewing inclination, however, we have not attempted this.

For Hβ, the best match to the observed profile was found for a model with slightly smaller, thin disk of $25\,\mathrm{R}_*$ seen at 45° with the base disk density parameter ρ_0 of $1.0 \times 10^{-11}\,\mathrm{g\,cm^{-3}}$ and power-law index n of 2.0. The overall strength and width of Hβ (including its absorption wings) are well reproduced by the model. We note that the V/R asymmetry cannot be reproduced by our assumed axisymmetric disk models.

At this point, we immediately see that the best-fit models for Hα and Hβ differ. Nevertheless, it should be kept in mind that in addition to the best-fit model, there is a range of other disk models that fit each profile nearly as well. For example, there will be **N** models that fit

Table 3.3: Best-fit Model Parameters for Individual Emission Lines and the Global Models with and without Ca II.

Emission Line	Disk Density ρ_0 (g cm^{-3})	Power Law Index n	Inclination i (°)	Disk Radius R_{disk} (R_*)	Model Type
Hα (6562 Å)	3.2×10^{-12}	2.0	60	50	Thin
Hβ (4861 Å)	1.0×10^{-11}	2.0	45	25	Thin
Ca II IR-triplet (8542 Å)	1.0×10^{-10}	2.0	60	25	Thin & Turbulent
Fe II (5169 Å)	1.0×10^{-10}	3.0	45	25	Thick & Turbulent
Fe II (5317 Å)	1.0×10^{-9}	1.5	75	25	Thin & Turbulent
Global	1.0×10^{-10}	2.0	45	50	Thin
Global (w/o Ca II)	1.0×10^{-10}	3.0	45	50	Thin & Turbulent

Note. No best-fit model for He I (λ 6678) absorption line is given because it is of photospheric origin.

Hα with a figure-of-merit within 25% of the best fit model, and for Hβ, there will be **M** such models. We will return to the question of the number of such models and how the disk density parameter ranges compare in Section 3.3.

For Ca II λ 8542, the best-fit model to the observed line has a disk density parameter ρ_0 of 1.0×10^{-10} g cm^{-3} and power-law index n of 2.0 seen at 60° for a 25 R$_*$ thin and turbulent disk. We again note that the width and overall strength of the line are well reproduced.

For the two Fe II lines, the figure of merit $\mathcal{F}$ was computed by using only the red half of the line, i.e. the blue peak was ignored in the fit. The Fe II multiplet (42) λ 5169 line requires the base disk density parameter ρ_0 of 1.0×10^{-10} g cm^{-3} and a power-law index n of 3.0 seen at 45° for a 25 R$_*$ thick and turbulent disk. The Fe II multiplet (49) λ 5317 line requires a model with disk density parameter ρ_0 of 1.0×10^{-9} g cm^{-3} and a power law index n of 1.5 seen at 75° for a 25 R$_*$ thick and turbulent disk. We note that the lines of Ca II and Fe II prefer the turbulent disk model, as these models tend to produce broader and stronger lines.

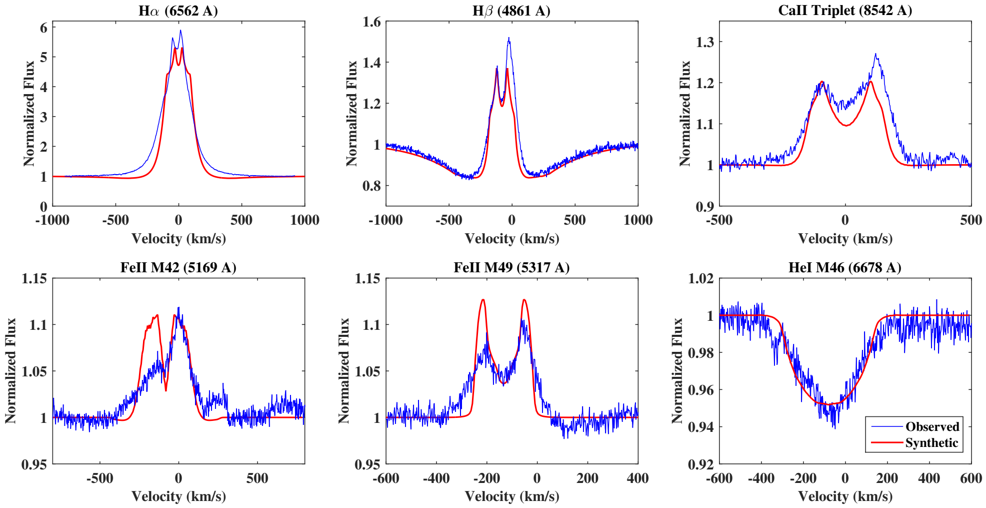

Figure 3.5: The best-fit profile (red) for observed emission line (blue) of Hα (λ6562), Hβ (λ4861), Ca II IR Triplet (λ8542), Fe II multiplet (42) (λ5169), Fe II multiplet (49) (λ5317), and He I (λ6678) for BD+65 1637, which were modeled using BERAY. The fit parameters for each model can be found in Table 3.3, with the exception of He I because it is fit by a photospheric profile.

To investigate what range of disk radii contribute to the formation of the lines considered, the cumulative intensity produced by each emission line was plotted against the radius of the disk for the models listed in Table 3.3, as shown in Figure 3.6. To do this, a face-on synthetic image ($i = 0°$) was produced using the best-fit disk density model for each line. For each $i = 0°$ image, the intensity was integrated over the total width of the line. Then, the integrated intensity out to a disk radius of R can then be defined as

$$C(R) = 2\pi \int_{R_*}^{R} I(R')\, R'\, dR' \,, \tag{3.2}$$

where $I(R)$ is the wavelength integrated line intensity at distance R, and R_* is the stellar radius, assumed to be the inner edge of the disk. Then $C(R)/C(R_{disk})$ can be plotted versus R to determine how the line intensity is accumulated by the disk. In the Figure 3.6, a dashed black line shows the cumulative fraction of 0.9. It is important to keep in mind when looking at this figure that the disk density model particular to each transition has been used and not a single disk density model. This explains, for example, why C=1 is reached at 50 R$_*$ for Hα but 25 R$_*$

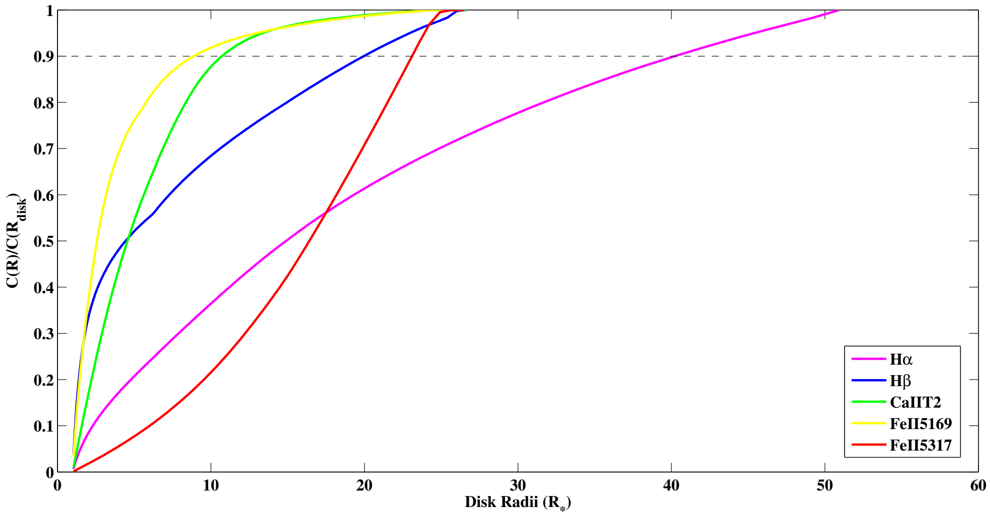

Figure 3.6: The cumulative line emission (Equation 3.2) as a function of distance from the star for each observed line using the best-fit disk density model. The model parameters that produced each individual line can be found in Table 3.3. The black dashed line represents a cumulative emission fraction of 0.9.

for the remaining lines. In order to reproduce the strength of the Hα emission, an extended emission region is required, reaching 90% of the emission at 40 R_*. However, 90% of the emission for Ca II, and Fe II (λ 5169) originates from the innermost 10 R_* of the disk, and Hβ and Fe II (λ 5317) are intermediately reaching 90% complete at ~20 R_*.

This figure also illustrates how the disk might be structured in order to produce all the line profiles by having the disk's equatorial density vary in a more general way than as a single power-law (see Section 3.4).

3.2.2 Global Fits

Given that different disk density models are required to best fit each observed profile for BD+65 1637, the next logical step was to see if a single disk density model could fit all the lines in a reasonable (as opposed to optimal) manner. This will also assist us in deciding how to move forward in looking for a more general density model that would better describe the structure of the disk. To find the single best model, we minimized the sum of all the individual

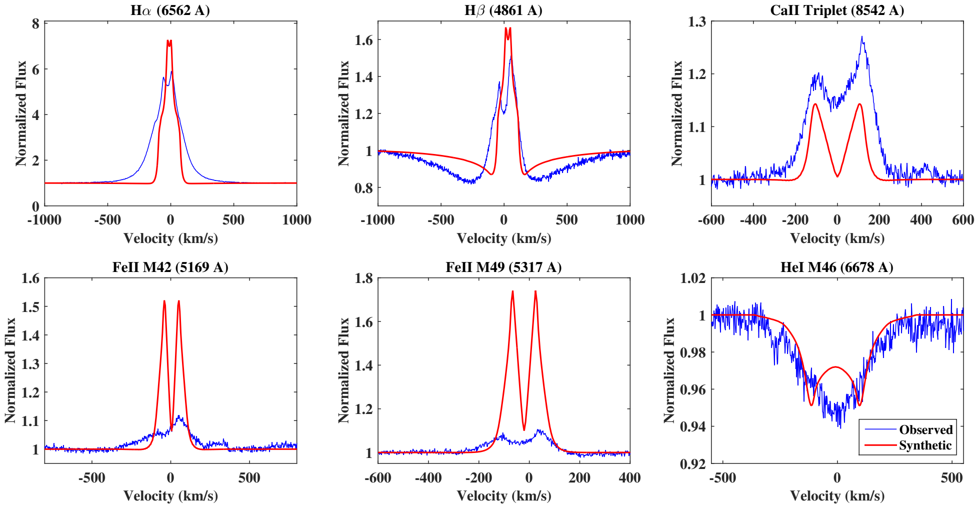

Figure 3.7: The global best fit of all the synthetic line profiles (red) for the observed emission lines (blue) of Hα (λ 6562), Hβ (λ 4861), Ca II IR Triplet (λ 8542), Fe II multiplet (42) (λ 5169), Fe II multiplet (49) (λ 5317), and He I (λ 6678) for BD+65 1637, which were modeled using BERAY. The global best-fit model parameters used for this Figure can be found in Table 3.3.

$\mathcal{F}$, i.e.

$$\mathcal{F}^{\text{total}} = \sum_{i=1}^{6} w_i F^{\text{i}} \tag{3.3}$$

where i ranges over the six lines considered. Initially, we set w_i=1 for all i to weigh all six lines equally. The model that was found to best reproduce all the observed line profiles in this manner is listed in Table 3.3.

Figure 3.7 shows all six synthetic emission lines produced for this model as compared to the observed line profiles. The disk parameters are a power-law index n of 2.0, the base disk density parameter ρ_0 of $1.0 \times 10^{-10}\,\mathrm{g\,cm^{-3}}$ with a $50\,\mathrm{R}_*$, thin disk seen at 45°. As illustrated in the figure, the Balmer lines can be reproduced approximately in strength, but are too narrow at the base; the metal lines are either too strong (Fe II lines) or too weak (Ca II IR Triplet) compared to the observed emission lines. The mismatch of the shape of the Balmer line profiles, particularly in the wings, indicates that that the material is not distributed correctly in the disk by a single power-law. The synthetic line profile for Ca II IR triplet (λ 8542) is weaker in strength, as well as narrower in velocity, than the observed line profile. It does, however, produce a double-

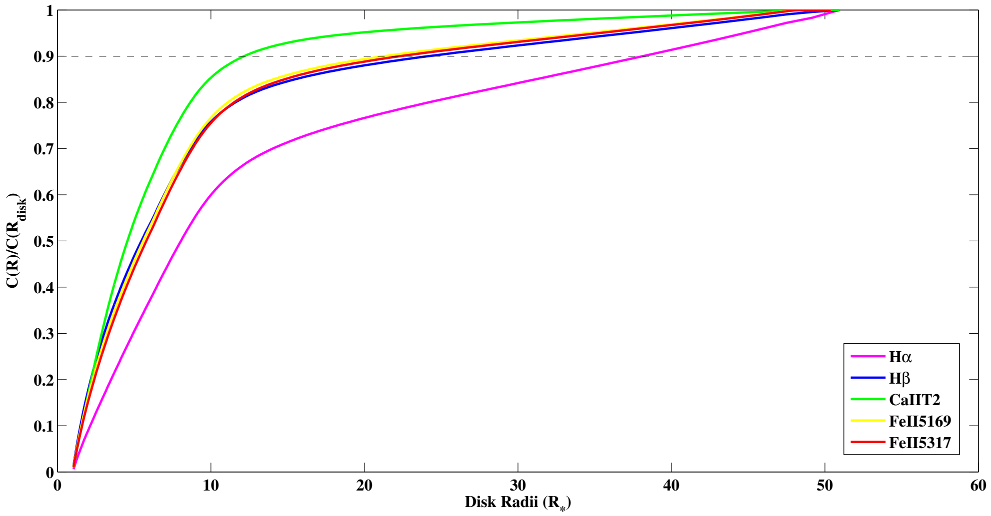

Figure 3.8: The cumulative line emission (Equation 3.2) as a function of distance from the star for each observed line using the global disk density model. The global model parameters can be found in Table 3.3. The black dashed line represents from where the 90% of the emission is coming from.

peaked shape. Both of the synthetic Fe II line profiles have approximately the same shape and strength when compared to each other; however the width of the wings are different: Fe II (42) (λ 5169) has a narrower spread of velocity in the wings when compared to Fe II (49) (λ 5317). Both synthetic Fe II line profiles are too strong compared to the observed profiles, suggesting that smaller regions may be required to reproduce the observed line (as seen in Section 3.2.1). Finally, He I shows absorption with some central emission, sometimes called a central quasi emission (CQE) feature (Hanuschik, 1995). Because the star and disk system is seen 45°, the CQE can be attributed to the disk partly blocking the direct stellar radiation.

Figure 3.8 illustrates where the intensity is produced by these lines for this single power-law model by plotting C(R), Equation 3.2, as a function of disk radius. It can be seen that, in all the cases, 90% of the emission now is coming from inside 40 R_* (or 1.25 AU). This figure also illustrates that the Ca II IR Triplet (λ 8542) is produced in the innermost 10 R_* of the disk; the Hβ (λ 4861) and the Fe II multiplets (λ 5169 and λ 5317) produce most of their emission within 20 R_*, and Hα emission is produced throughout the disk, with 90% coming from within 40 R_*. Comparison of Figures 3.6 and 3.8 shows that the Ca II IR triplet forms in the innermost part of the disk, while Hα forms throughout the disk. The emission from Hβ and Fe II multiplets are intermediate and emerge from the same region for the global model.

In addition to constraining the density distribution in the disk for a model that is consistent with the observations, the global model can be used to give insight to the temperature structure of the disk. Figure 3.9 illustrates the temperature distribution predicted by BEDISK in a thin disk for a model with the base disk density parameter ρ_0 of 1.0×10^{-10} g cm^{-3} and power-law index n of 2.0. The upper plot illustrates the temperature in the entire disk, which generally ranges from 5500 K to 10000 K. The bottom log-log plot shows the region close to the stellar surface where temperatures in the disk can reach as high as 14000 K. When combined with the density structure, this provides valuable information on the structure of the inner, gaseous disk. For example, even at 110 R_*, the coolest temperature predicted in the equatorial plane, $\simeq$5500 K, is still above the dust sublimation temperature.

Finally, the disk density parameters can be used to estimate the total mass of the inner gaseous disk. The mass is estimated to be 9.3×10^{26} g ($5.7 \times 10^{-8}\, M_*$ or 4.6×10^{-7} $M_\odot$), while the scale height H of the disk at the stellar surface was estimated to be 1.6×10^{10} cm ($3.5 \times 10^{-2}\, R_*$ or 0.23 $R_\odot$).

It was noticed in the fitting process that the metal lines, especially the Ca II IR Triplet, require a high disk density parameter ρ_0 with low value of the power-law index n. Ca II is generally not well reproduced by the models that otherwise are found to work reasonably well for a single power law. For this reason, we searched for global fits that exclude the Ca II line by setting $w_i = 0$ for $\mathcal{F}^{\mathrm{Ca\,II}}$ in Equation 3.3. The result can be seen in Figure 3.10. The details for this model can be found in Table 3.3, and this model is able to reproduce the emission in the two Fe II lines reasonably well. The Balmer lines are not strong enough to match the strength of the observed profile. However, they match well when the width of the lines is considered. The same is the case for He I line. The Ca II IR triplet for this model shows hardly any emission, and this indicates that Ca II is likely formed in a different region, while all the other lines can be reasonably produced by a disk with a single power law with n=3.0. The mass of this disk

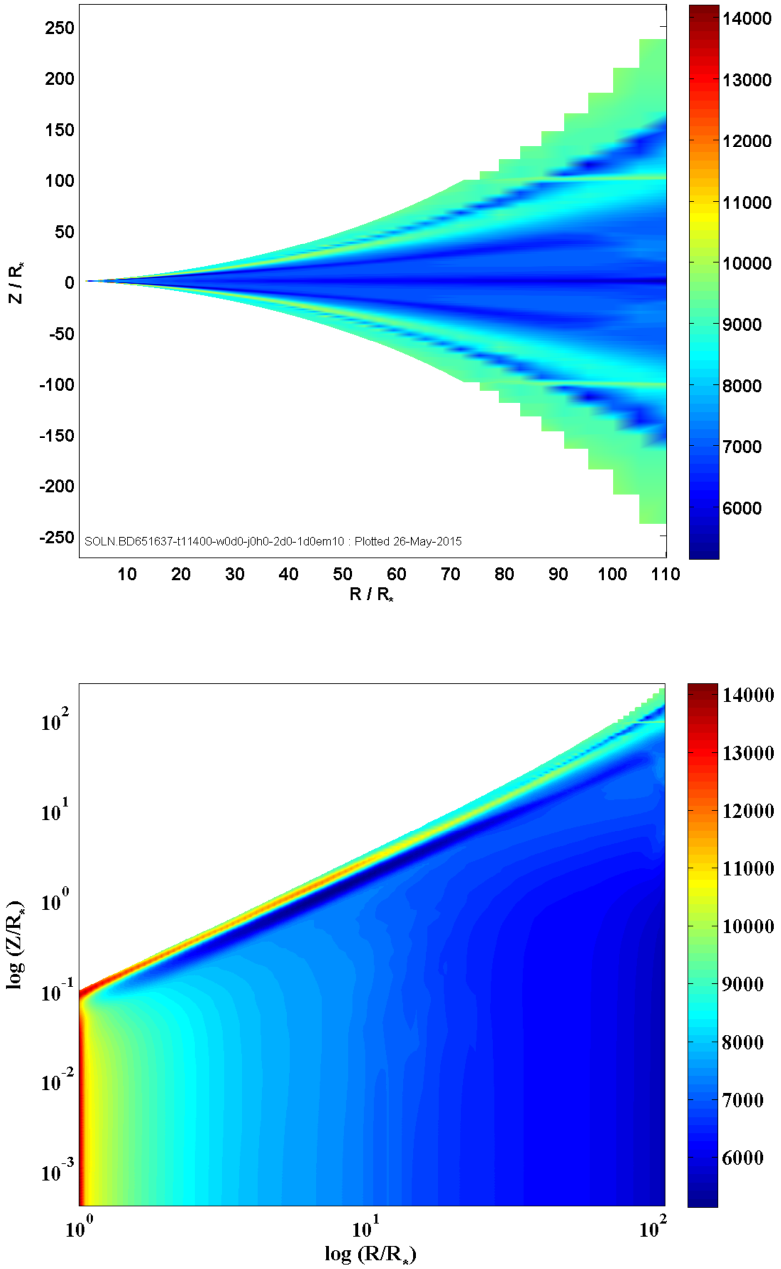

Figure 3.9: Temperature distribution in the disk for a model with the base disk density parameter ρ_0 of 1.0×10^{-10} g cm^{-3} and power-law index n of 2.0. On the top, the plot illustrates the temperature structure in the entire disk, while at the bottom, in a log-log plot, the temperature distribution in the region close to the stellar surface is illustrated. A color bar giving the temperature scale (in K) is to the right of each plot.

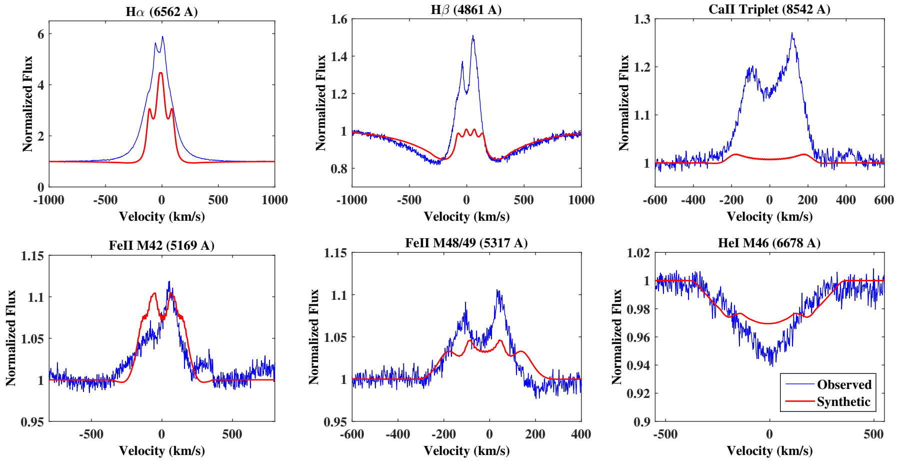

Figure 3.10: Synthetic profiles (red) for the global best-fit for the model that produces reasonable fits for all lines except Ca II IR Triplet (λ 8542) when compared to the observed spectral lines (blue). The global model used can be found in Table 3.3 (on the line "w/o Ca II").

was estimated to be 4.8×10^{25} gm ($2.3 \times 10^{-9}\ M_*$ or $4.6 \times 10^{-7}\ M_\odot$).

In order to illustrate where these lines are formed in this model that excludes Ca II, and if there is any similarity to the previous global model, Figure 3.11 was constructed. The plot shows Hα forming almost throughout the entire disk with the 90% of emission coming from inside the 30 R_*. Hβ, Fe II (λ 5169) and Fe II (λ 5317) can be seen forming within 15 R_*. When compared to the previous global fit model (Figure 3.8), all the emission lines except Hα in this model are produced within half the radius.

Thus, from the all three models considered, it can be concluded that the Hβ and the metal lines form in the innermost region of the disk, while the Hα forms in an extended region covering nearly the entire disk.

3.2.3 The Near-IR SED

As mentioned in Section 2, Beray can also calculate continuum SEDs of the star+disk system. In order to assess how comparable these models are to the available observations, a SED was produced for the global disk model of Table 3.3 and compared to the observed SED for BD+65 1637 found in Hillenbrand et al. (1992). This is illustrated in Figure 3.12. The star's

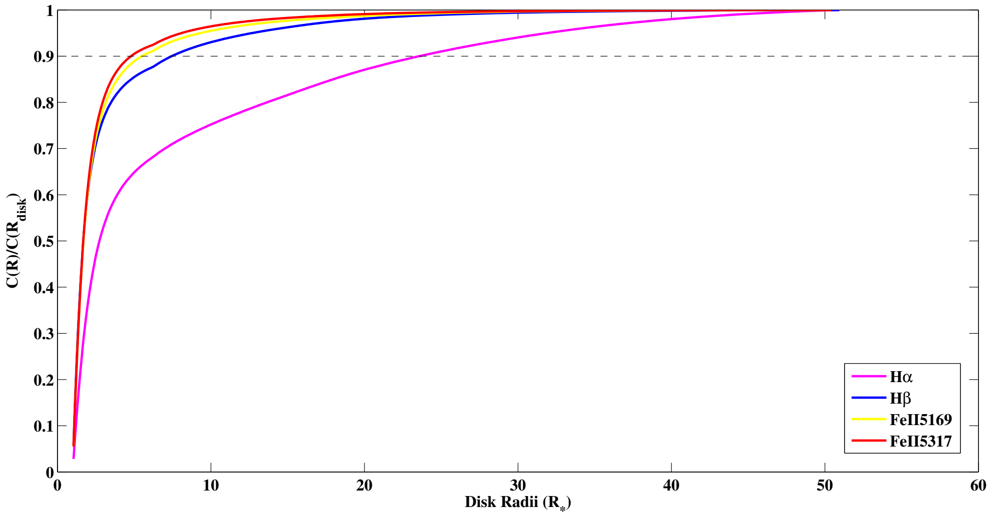

Figure 3.11: Cumulative line emission (Equation 3.2) as a function of distance from the star for each observed line using the global disk density model without Ca II. The model parameters used for this figure can be found in Table 3.3. The black dashed line represents where 90% of the emission is coming from.

continuum SED, i.e., in the absence of a disk, is also shown. As it can be seen in the figure, the global disk model produces a brighter SED at longer wavelengths compared to the observed SED. This suggests a thinner and less dense disk than those considered here is required in order to be comparable to the observed SED. However, it is important to note that the SED observations were taken more than 16 years prior to the observations of the emission lines used in the analysis here. Hα has been previously reported to be variable in EW (26 Å to 45 Å), so the comparison of the disks over a long period of time should be considered with caution.

3.3 Uniqueness of Disk Models

As described in the Section 3.2, the fitting procedure used the values of the figure of merit $\mathcal{F}$ for all the lines, found by using Equation 3.3, to build a set of the global, best-fit models. In Section 3.2.1, it was noted that although one model is the best-fit for each line profile, more than one model can fit a particular line profile within a certain range of $\mathcal{F}$. Table 3.4 gives the number of models for each emission line that have $\mathcal{F} < 1.25\mathcal{F}_{min}$ (the top 25% best fits). As

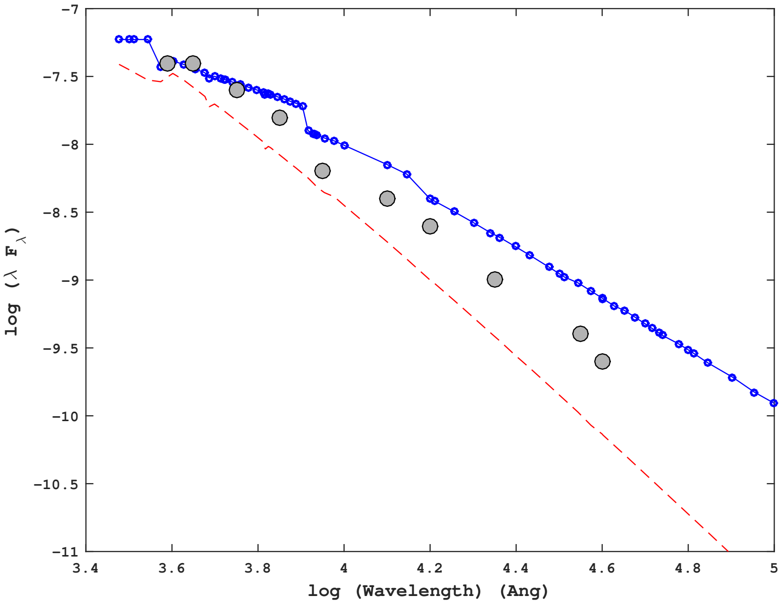

Figure 3.12: Continuum SED calculated using Beray for the global best-fit model (with Ca II) for the disk (blue circles; see Table 3.3 for the disk parameters). The photospheric spectrum of the star is shown as the red dashed line. These SED observations of Hillenbrand et al. (1992) are marked with gray filled circles.

can be seen from the table, the number of models within this range varies from one model for Ca II to seven models for He I. Figure 3.13 illustrates where all these models fall in the explored parameter space of base disk density ρ_0 and power-law index n. If a single model is found, it is represented by a point. For two models, a line connecting the two models is shown on the figure. For three models, a triangle is used. For more than three models, an ellipse is shown that encloses most of the models. For He I, a photospheric feature, the region that represents the models that reproduce no disk emission is shown with an arrow. It is important to keep in mind that this figure represents only the value of the power-law index n and disk density ρ_0; the rest of the parameters for the models (R_{disk} and i) are not distinguished. As the figure illustrates, some, but not all, of the models overlap, again illustrating that no common region is found where all of the lines can be well fit by a single power-law model. However, two general regions on the plot can be separated, one for the Balmer lines, which require relatively low densities and another region of higher densities, dominated by the metal lines Fe II and Ca II. This figure confirms the earlier observation that the metal lines require higher densities.

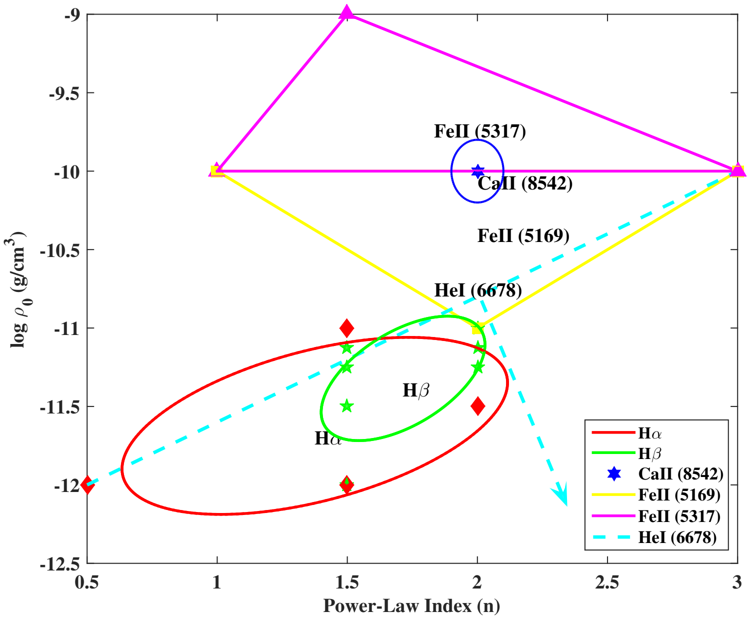

Figure 3.13: Regions of the $(n, log\,\rho_0)$ plane occupied by the top 25% of the profiles that match the observed profile of the indicated lines with figure-of-merit $\mathcal{F} \leq 1.25\,\mathcal{F}_{min}$. H$\alpha$ (λ 6562) in shown in red, Hβ (λ 4861) in green, Ca II (λ 8542) in blue, Fe II multiplet (42) (λ 5169) in yellow and multiplet (49) (λ 5317) in magenta, and He I (λ 6678) in cyan. The He I constraint is the region that results in no observable disk emission in the He I photospheric line.

Table 3.4: Number of Models within 25% of the Lowest Figure-of-merit $\mathcal{F}_{min} \leq \mathcal{F} \leq 1.25\,\mathcal{F}_{min}$ Using the Global Disk Density Model of Table 3.3.

Emission Line	Number of Models
Hα	4
Hβ	7
Ca II (λ 8542)	1
Fe II (λ 5169)	3
Fe II (λ 5317)	3

Given that a single model is not able to reproduce the observed line profiles, understanding how different power-law indices and disk densities for the disk affect the overall line strengths is important. To this end, the EW for each line as a function of disk density parameter ρ_0 was plotted for models with a 50 R$_*$ disk size seen at an inclination of 45°. Figures 3.14 and 3.15 show the results for the four disk types considered here: *thin, thick, thin and turbulent, and thick and turbulent*. Models with disk density parameter ρ_0 of 10^{-13}, 10^{-12}, 10^{-11}, 10^{-10} and 10^{-9} g cm^{-3}, and power-law indices n of 1.0, 2.0, and 3.0 are shown. In each figure, the black line indicates the observed EW for that particular emission line in the CFHT ESPaDOnS spectrum from 2006.

Even as no single (ρ_0,n) combination is able to match the observed EW of all the lines, some models match the observed EW for more than one line. For example, in Figure 3.14b for a thin and turbulent disk, the EW of two Fe II lines and He I line match the observed EW for the disk density ρ_0 of 10^{-10} g cm^{-3} and power-law index n of 3.0. The EW of Hα for the same model is very close to the observed EW. However, the EW of Hβ and Ca II (λ 8542) are weaker for the same model when compared to the observations.

In general, the EWs increase with disk density ρ_0 to a maximum value, and then decline as the lines become saturated while the continuum continues to increase, weakening the EW. A good example of this can be seen for the power-law index n of 1.0, where a sharp increase to a peak and than decline can be clearly seen for each line. In general, the maximum EW moves to a higher disk density ρ_0 as the power-law index n increases. Also illustrated in the plots, the addition of turbulence increases the strength of the lines. The thicker disk models generally show a large number of models with EW equal or greater than the observed EW for all the lines. For example, for a power-law index n of 2.0, the models with thicker disks show stronger EWs as the density increases.

3.4 Discussion

Good matches for all of the observed individual emission line profiles for BD+65 1637 have been found in the large library of synthetic models. However, the diversity of the models in Table 3.3, and the failure to find one global model that fits all the observed line profiles well, seems to indicate that the density distribution within the inner gaseous disk of BD+65 1637 cannot be of the simple form of a single power law (Equation 2.2) with power-law index $n > 0$. The differences between the best fits for individual lines and global fits suggest that the structure of the disk is more complex than a single power law. The idea that different density structures might be at play is supported by Figure 3.6 which illustrates how the variations in the structure of the disk can produce all the emission lines. In addition, the metal emission lines (Ca II and Fe II) seem to require a denser region for their formation as compared to the Balmer lines.

The SED of the best-fit, global model overpredicts the near-IR excess compared to the available observations. However, it is important to note that the SED is very sensitive to the underlying (assumed) stellar temperature in the optical/NIR, and hence should be viewed with caution. In general, the line modeling serves as a more powerful tool in inferring the structure of gaseous disk found close to the star. The comparison between the observed and computed SEDs was performed merely as a byproduct of the line modeling study performed here, and, perhaps most importantly, the SED and line spectra observations are separated by 16 years.

A general trend was noticed while manually searching for the best fit to the line profiles that

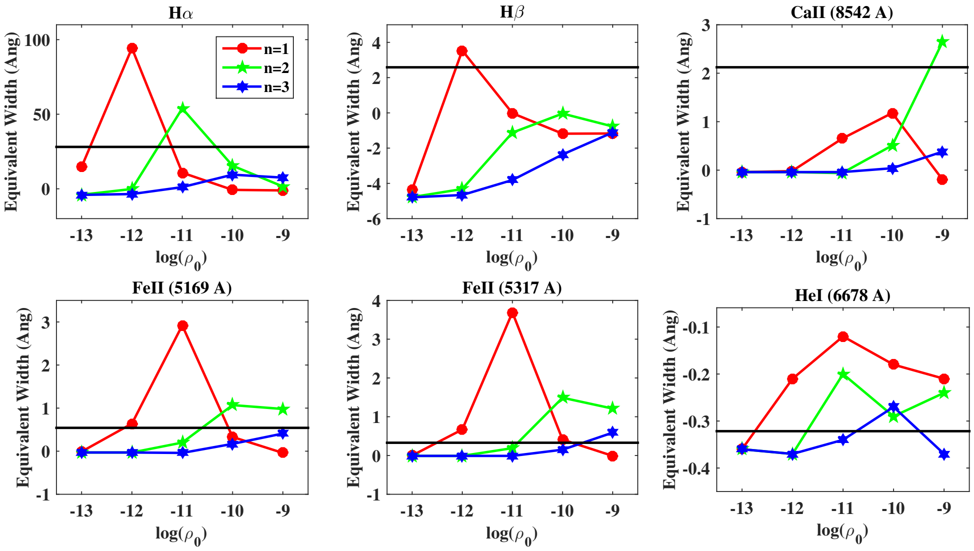

(a) *Thin* disk model

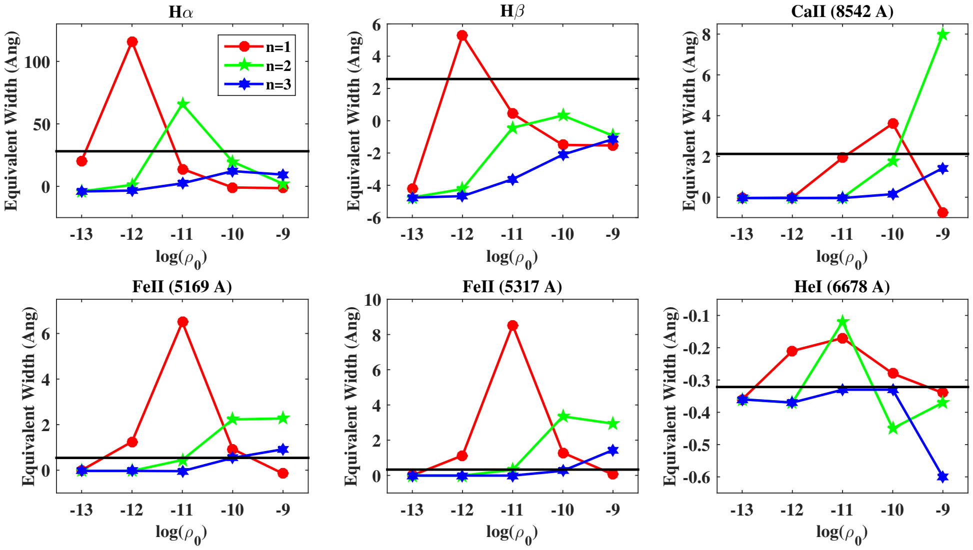

(b) *Thin & Turbulent* disk model

Figure 3.14: Equivalent width (Å) of each individual line as a function of disk density ($\log(\rho_0)$) for three different power-law indices n for models of radius $50\,R_*$ seen at 45° inclination angle. The solid black line in each panel is the observed equivalent width.

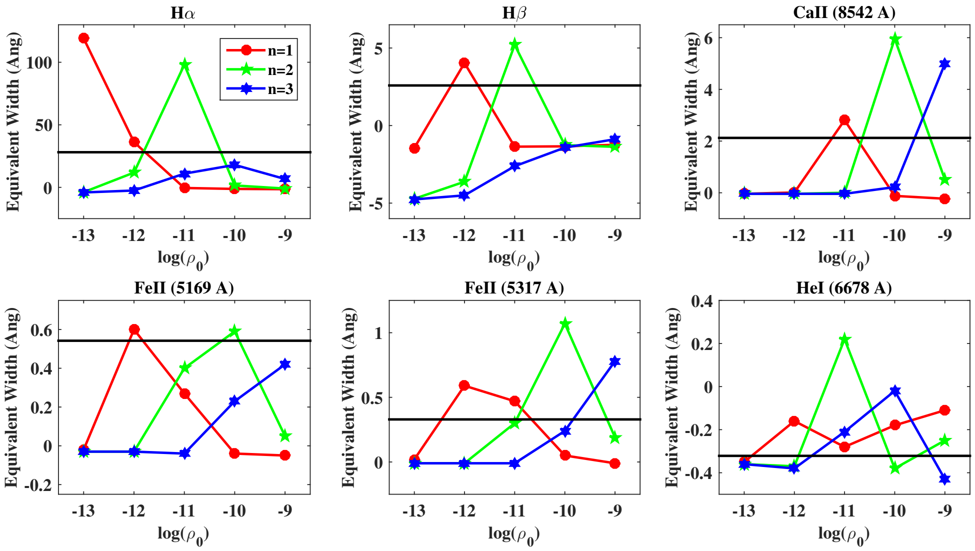

(a) *Thick* disk model

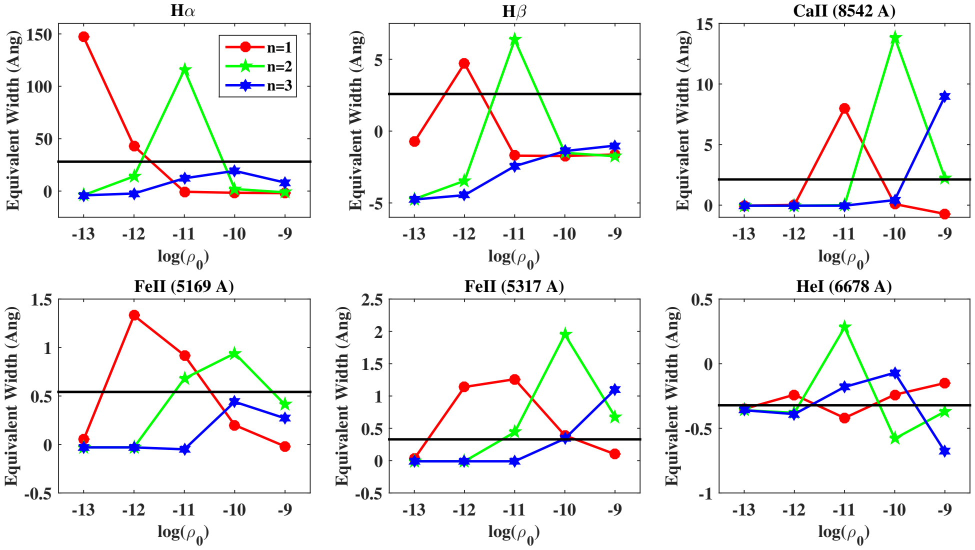

(b) *Thick & Turbulent* disk model

Figure 3.15: Equivalent width (Å) of each individual line as a function of disk density (log(ρ_0)) for three different power-law indices n for models of radius 50 R_* seen at 45° inclination angle. The solid black line in each panel is the observed equivalent width.

the metal lines required higher densities compared to the Balmer lines in order to reproduce the observed line profiles. The addition of turbulence to these models made the lines stronger and broader.

Finally, the analysis of observed and synthetic line profiles and their fits suggest that BD+65 1637 is seen at an angle between 45° and 60°.

Decretion disks around Classical Be stars are generally modeled with a single power law for the density structure, as mentioned in Section 2 and Sigut & Jones (2007). When hydrodynamic models are used, a more complex density structure is predicted (Carciofi, 2011). As shown by the current work, HAeBe stars do not seem to follow a single power law for their disk structure, perhaps as expected. Thus, a disk with density described by several different power laws in different radial zones might be able to provide a better global fit to all the lines considered. Finally, we assumed that the disk extends all the way to stellar photosphere, so another possible area of exploration would be to have the disk start further away from star. If the star is not actively accreting, or has sporadic events of accretion, the disk may not extend all the way to the star. Many recent studies such as Vink et al. (2005); Vink (2015) have suggested that it may be possible to constrain the presence of such an inner hole radius using polarimetry.

3.5 Conclusions

This study of inner gaseous disk of the Herbig B2e star, BD+65 1637, by modeling the optical and near-infrared emission lines, has led to three key findings:

- All of the observed emission lines considered in this study can be reproduced with models that use *photoionizing radiation of the central star* as the *sole* energy source for the disk.

- Despite being able to reproduce the observed emission lines individually, no model based on a single power law for the equatorial density was able to reproduce all of the emission lines simultaneously. More complex density models are required to generate a consistent disk structure for this star.

- The metal lines (Ca II, Fe II) require higher densities when compared to the Balmer lines.

Bibliography

Alecian, E., Wade, G. A., Catala, C., Grunhut, J. H., Landstreet, J. D., Bagnulo, S., Böhm, T., Folsom, C. P., Marsden, S. & Waite, I., 2013, MNRAS, 429, 1001.

Carciofi, A. C., 2011, IAUS, 272, 325C.

Dahm, S. E. & Hillenbrand, L. A., 2015, AJ, 149, 200D.

Finkenzeller, U., 1985, A&A, 151, 340.

Finkenzeller, U. & Mundt, R. 1984, A&AS, 55, 109.

Fernández, M., Ortiz, E., Eiroa, C. & Miranda, L. F., 1995, ApSS, 114, 439.

Garrison, L. M. & Anderson, C. M. 1977, ApJ, 218, 438.

Hanuschik, R. W., 1995, A&A, 295, 423H.

Hernández, J., Calvet, N., Briceño, C., Hartmann, L. & Berlind, P., 2004, AJ, 127, 1682H.

Herbig, G. H. 1960, ApJS, 4, 337H.

Hillenbrand, L. A. Strom, S. E. Vrba, F. J. & Keene, J. 1992, ApJ, 397, 613.

Hillenbrand, L. A. 1995, Ph.D. thesis, Univ. Massachusetts.

Rivinius, Thomas, Carciofi, Alex C. & Martayan, Christophe, 2013, A&ARv, 21, 69R.

Sigut, T. A. A. & Jones, C. E., 2007, ApJ 668, 481.

Straižys, V. et al 2013, MNRAS, 000, 18.

Strom, S. E., Strom, K. M., Yost, J., Carrasco, L., & Grasdalen, G. 1972, ApJ, 173, 353.

Vink, J. S., Drew, J. E., Harries, T. J. & Oudmaijer, R. D., 2005, ASPC, 343, 232V.

Vink, J., 2015, Ap&SS, 357, 98V.

Chapter 4

Herbig B2e Stars: HD 76534, HD 114981 & HD 216629

This chapter corresponds to the article: Patel, P., Sigut, T. A. A. & Landstreet, J. D., *'Photoionization Models of Inner Gaseous Disk of Herbig Be Star: HD 76534, HD 114981 & HD 216629'* (submitted).

4.1 Stars

Three HBe stars of spectral type B2 are considered in this study: HD 76534, HD 114981 and HD 216629. The stellar parameters, adopted from Alecian et al. (2013), can be found in Table 4.1. Alecian et al. (2013) derived the fundamental parameters, such as effective temperature, mass, radius and *v sini*, by using various methods; synthetic spectra, generated by TLUSTY and SYNSPEC codes (Hubeny, 1988; Hubeny & Lanz, 1992, 1995), were compared to the observed spectra and used to determine the stellar effective temperatures. The synthetic spectra were generated assuming $\log(g) = 4.0$ for all stars. The synthetic spectra were also used to determine *v sini* of the stars. Using the derived luminosities and effective temperatures, the stars were placed in the H-R diagram and compared to evolutionary tracks, calculated using the CESAM stellar evolutionary code version 2K (Morel, 1997), to determine the stellar

Table 4.1: Adopted Stellar Parameters.

Parameter	HD 76534	HD 114981	HD 216629
$T_{\rm eff}$ (K)	18000±2000	17000±2000	19000
log g (cgs)	4.0	4.0	4.0
Radius ($R_\odot$)	7.7±1.6	7.0±2.0	–
Mass ($M_\odot$)	9.0±0.6	$7.9^{+2.4}_{-1.3}$	–
Distance (pc)	870±80	550^{+260}_{-130}	720^{+190}_{-150}
$v\,sini$ (km s^{-1})	68±30	239±13	179±27

All parameters are adopted from Alecian et al. (2013).

masses and radii.

HD 76534 A (V* OU Vel) is of spectral type B2e with a visual magnitude of 8.35 located at a distance of 870 pc. It is a member of the Vela R2 association and illuminates the surrounding reflection nebula VdB 24 (Herst, 1975). This star is the brighter member of a visual binary. HD 76534 was first classified as a HBe star by Finkenzeller & Mundt (1984), and its small infrared excess led it to be classified as group III stars by Hillenbrand et al. (1992), HBe stars with small infrared excess, similar to those of classical Be stars. Large variations in equivalent width (EW) of Hα, ranging from 14.30 Å to -2.4 Å, have been noted in various studies, such as those of Oudmaijer & Drew (1997); Corcoran & Ray (1998); Oudmaijer & Drew (1999). Large scale variations are also seen in HD 76534's polarization over time scales of ~1 month (Jain & Bhatt, 1995).

HD 114981 (V* V958 Cen) is a 7.16 visual magnitude star found at the distance of 550 pc (Alecian et al., 2013). It is a B-type star that shows a small IR excess and has been suggested to be a classical Be star (Wilson Cauley & Johns-Krull, 2014), not a HBe star. Hill (1970) and Vieira et al. (2003) classified HD 114981 as a HAeBe candidate with spectral type B5 due to H α emission; however Alecian et al. (2013), used high resolution spectra to determine the temperature of the star and re-classified it as type B2. Mannings & Barlow (1998) identified HD 114981 as a candidate Vega-type star based on the IR excess, consistent with its HBe classification.

HD 216629 (V* IL Cep) is a B2e star of visual magnitude 9.31 magnitude located the distance of 720 pc (Alecian et al., 2013). Several studies, such as those of Peter et al. (2012); Garmany (1973), have associated HD 216629 with the Cep OB3 association; however, Alecian et al. (2013) argues against this based on its position in the H-R diagram. Wheelwright et al. (2010) studied HD 216629 with spectro-astrometry and found that it is a wide, double-lined spectroscopic binary. Alecian et al. (2013) also noted variation in He I lines from one observation to another and indicated that the binary companion might be causing the variations. A double-peaked emission Hα has been observed in emission in various studies with the EW ranging from +34.5Å to -4.5Å (Wheelwright et al., 2010; Harrington & Kuhn , 2009; Mottram et al., 2007; Acke et al., 2005; Vink et al., 2002). The EW of Hβ has been reported to be -3.4 Å previously (Mottram et al., 2007). Mottram et al. (2007) studied Balmer emission lines of HD 216629 and failed to detect any depolarization[1].

4.1.1 Observations

All observational data used in this study were obtained using the high-resolution ESPaDOnS spectropolarimeter at the Canadian-France-Hawaii Telescope (CFHT). This instrument covers the wavelength range 3700 to 10500 Å with a spectral resolution of 65,000.

The HD 76534 spectrum, obtained in 2005 (HJD 2453423), can be seen in Figure 4.1, with the peak SNR of per CCD pixel of 221 at 7080 Å. A high resolution version of spectrum is illustrated in Appendix A, Figure A.2. The spectrum contains not only a strong Hα emission (EW = +11 Å) but also weaker emission from Hβ and the Ca II IR triplet. Weak emission from several Fe II multiplets, common in the optical spectra of HBe stars, is also detected. The EWs of all the measured line profiles for HD 76534 can be found in Table 4.2.

For HD 114981, two different data sets are available, one from 2005 (HJD 2453422) with peak SNR per pixel of 329 at 5150 Å, and one from 2006 (HJD 2453748) with peak SNR per pixel of 633 at 5150 Å. The 2006 spectrum is shown in in Figure 4.2 and its high resolution

---

[1] Depolarization occurs when the continuum is much more polarized than the line photons.

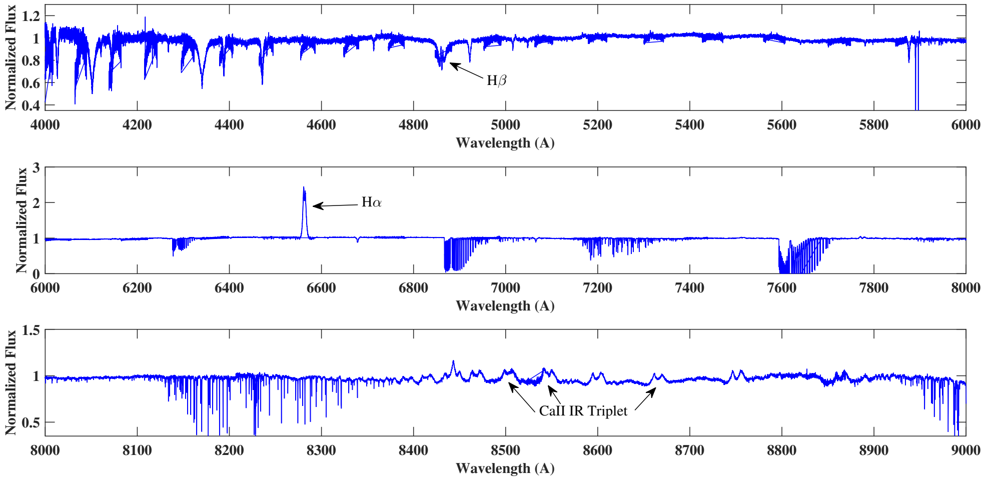

Figure 4.1: The 2005 (HJD 2453423) CFHT ESPaDOnS spectrum of HD 76534 from Alecian et al. (2013). The hydrogen Balmer lines, Hα (λ 6563) and Hβ (λ 4861), and the Ca II IR-triplet lines (λ 8498, λ 8542 and λ 8662) are indicated. Note that the strengths of the emission lines are quite diverse, particularly for Hα, as seen from the different vertical scale of each subplot.

version can be found in Appendix A, Figure A.3. Again, emission lines of Hα, Hβ, the Ca II IR triplet, and Fe II are detected. A comparison of the two spectra taken approximately a year apart can be seen in Figure 4.3; only small changes are seen in the spectrum. The Hα line is a bit stronger in the 2006 observations, and the Hβ line has shallower wings in the 2005 observations. For the Fe II lines, the 2005 profiles are slightly stronger. All the emission lines show symmetric, doubly-peaked profiles. He I λ6678 is seen in absorption and has a very broad profile. As the 2006 spectrum has a higher SNR, we analyze only the 2006 data. The EWs of all the line profile for HD 114981 can be found in Table 4.2.

The observed data for HD 216629 was obtained in 2006 (HJD 2454077) at peak SNR per pixel of 227 at 7080 Å and can be seen in Figure 4.4. Appendix A, Figure A.4 displays high resolution version. The spectrum shows Hα, Hβ, and Ca II IR triplet emission lines. The two Fe II lines, λ 5169 and λ 5317, are also present in emission, but very weak. The Hα is singly-peaked, while Hβ, the CaII IR triplet, and the FeII lines are doubly-peaked. Hβ and the two FeII lines show a stronger red (R) component in their doubly-peaked profile as compared to the blue (V) component. The EWs of all the line profiles for HD 216629 can be found in Table 4.2.

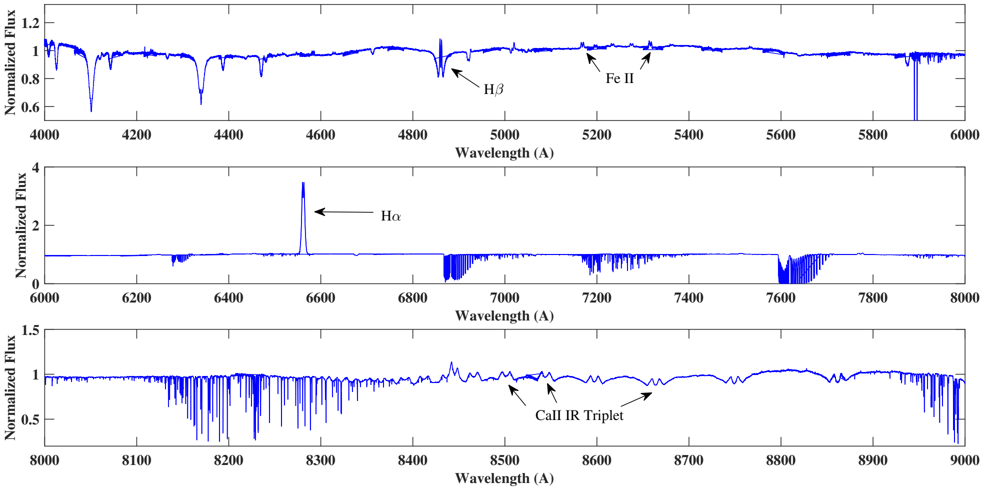

Figure 4.2: The 2006 CFHT ESPaDOnS spectrum of HD 114981 from Alecian et al. (2013). The emission lines Hα (λ 6563), Hβ (λ 4861), the Ca II IR-triplet lines (λ 8498, λ 8542 and λ 8662) and Fe II lines (λ 5169 and λ 5317) are indicated. Again, note the different scales on the y-axes.

4.1.2 Data Reduction

The spectra for all the stars were continuum normalized using IRAF[2] in order to be able to compare the observed line profiles to the synthetic spectra. The individual orders containing the emission lines of interest were normalized using various low order (2^{nd} or 3^{rd}) polynomials, using the 'Legendre' and 'cubic spline' functions available in IRAF.

Ca II Subtraction & Elimination

The three Ca II IR triplet lines, λ 8498, λ 8542, λ 8662, are blended with various high-n Paschen lines which need to be subtracted from the Ca II lines in order to extract unblended Ca II line profiles. In order to remove the contaminating Paschen emission, the two adjacent, and unblended Paschen, lines were averaged and subtracted from the Ca II profile. For example, to de-blend Ca II λ 8542 from Pa15 λ 8543, the average of the two adjacent Paschen lines, Pa14 λ 8596 and Pa17 λ 8465, was subtracted from the observed Ca II λ 8542 line.

---

[2] IRAF is distributed by the National Optical Astronomy Observatories, which are operated by the Association of Universities for Research in Astronomy, Inc., under cooperative agreement with the National Science Foundation.

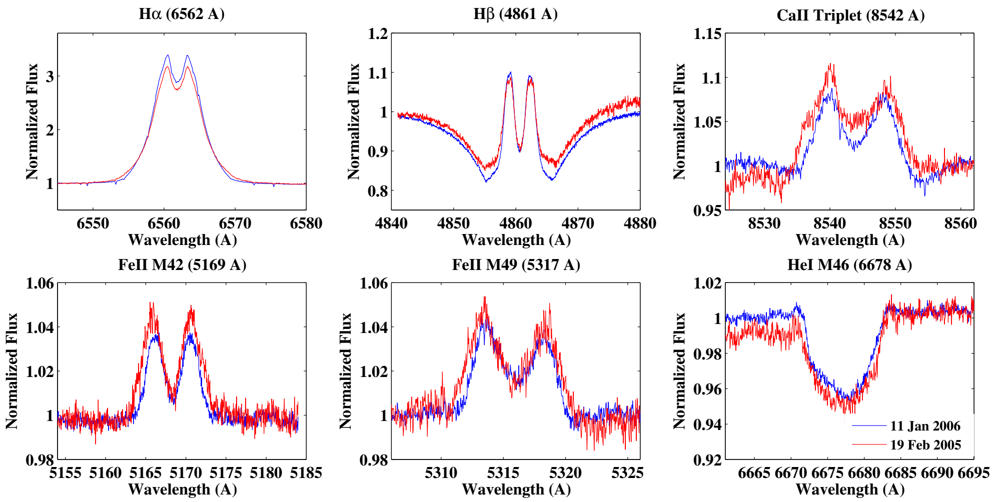

Figure 4.3: The 2005 (HJD 2453422) observations of HD 114981 are shown in red, overplotted in blue on the 2006 (HJD 2453748) observations, for lines modeled in this study.

Table 4.2: Measured Equivalent Widths.

Line (λ Å)	EW (Å)		
	HD 76534	HD 114981	HD 216629
H α (λ 6563)	10.93	18.63	19.74
H β (λ 4861)	-4.91	-4.45	-2.32
Ca II (λ 8542)	1.77	0.18	0.99
Fe II (λ 5169)	0.19	0.18	-0.36
Fe II (λ 5317)	0.60	-0.20	0.17
He I (λ 6678)	-0.51	-0.40	-0.66

This procedure was performed on all the three Ca II IR triplets lines for all three stars. An example of the subtraction process and results can be seen in Figure 4.5 using the Ca II λ 8542 emission line. This subtraction process did not yield a significant Ca II line profile compared to the continuum noise for two of the three stars, HD 76534 and HD 114981, and therefore, Ca II was not considered in the analysis of these stars. The Ca II line profile for HD 216629 however, shows a strong, double-peaked line profile after subtraction, and this profile was retained in the analysis.

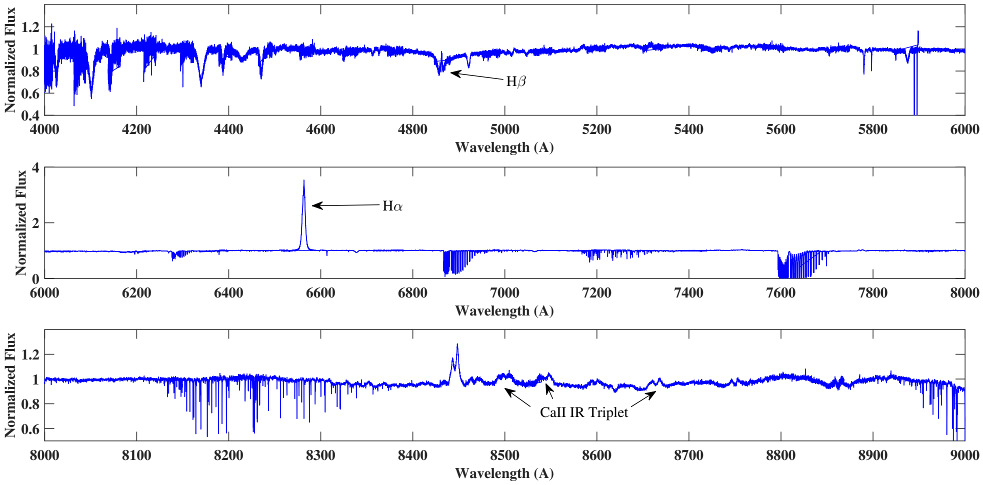

Figure 4.4: The spectrum of HD 216629 from Alecian et al. (2013). The emission lines Hα (λ 6563), Hβ (λ 4861) and the Ca II IR-triplet lines (λ 8498, λ 8542 and λ 8662) are as indicated. Again, note the different scale on the y-axes.

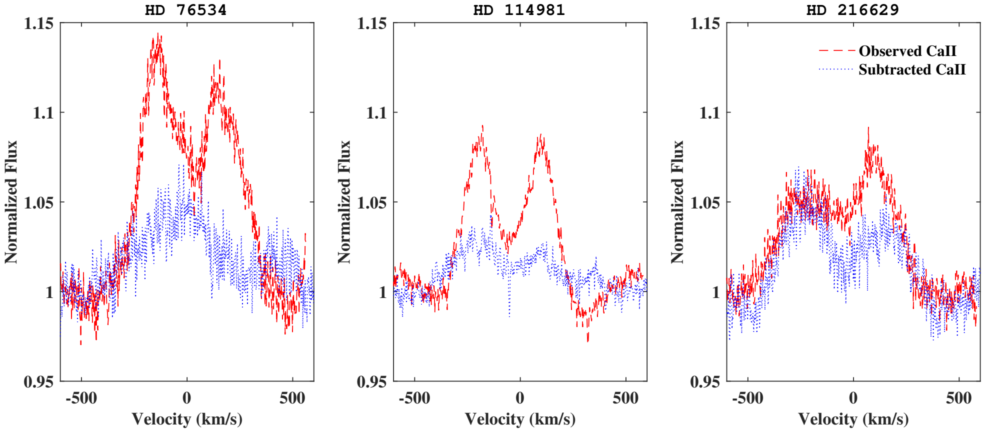

Figure 4.5: The Ca II IR triplet line λ 8542 before the subtraction process (i.e., blended with Paschen lines) is illustrated in red for all three stars: HD 76534, HD 114981, & HD 216629. The resultant subtracted profile for Ca II λ 8542 alone is seen in blue.

4.2 Results

To model the observed line profiles of the three HBe stars considered in this work, a large grid of synthetic line profiles for a disk surrounding a central B2 star were calculated using the parameters given in the Table 4.3. The adopted B2 parameters fall within the uncertainty of the stellar parameters given in Table 4.1 for all stars. A wide variety of disk parameters, listed in Table 4.4, were explored. Typical values of ρ_0 and n for classical Be stars fall in the range of $10^{-12}\,\mathrm{g\,cm^{-3}}$ to $10^{-10}\,\mathrm{g\,cm^{-3}}$, and 2 to 4 (peaking at 3.5), respectively (Rivinius et al., 2013). However, for HBe stars an expanded range of model parameters was considered in order to include more massive disks by calculating higher ρ_0 and/or lower n. Thus, the models were calculated with the disk base density parameter, ρ_0, ranging from 10^{-13} to $10^{-8}\,\mathrm{g\,cm^{-3}}$, and the power-law index, n, ranging from 0.5 to 3.0 . The size of the disk was chosen to be one of three values, R_{disk}=25, 50 and 100 R_*. All synthetic line profiles were calculated at four viewing inclinations, which represent the centers of the first four bins of five equal probability bins in a random $\sin i$ distribution: 18°, 45°, 60° and 75°. The fifth bin, $i = 84°$, was not considered as there is no evidence of shell absorption, i.e. deep central reversals in the line profiles originating from disk absorption, in any of the spectra.

To compare each synthetic profile in the computed library to an observed line profile, a

Table 4.3: Adopted stellar parameters for the B2 spectral type.

Parameter	Value
T_{eff} (K)	19000
log g (cgs)	4.1
Radius ($R_\odot$)	6.7
Mass ($M_\odot$)	8.11

Note: values were adopted from Alecian et al. (2013).

figure-of-merit, $\mathcal{F}$, was computed. This figure-of-merit was defined as

$$\mathcal{F} \equiv \frac{1}{N} \sum_{i=1}^{N} \frac{|F_i^{\mathrm{Mod}} - F_i^{\mathrm{Obs}}|}{F_i^{\mathrm{Obs}}}, \tag{4.1}$$

where F_i^{Obs} is the observed relative flux, F_i^{Mod} is the model relative flux, and the sum is over the N wavelength points spanning the line. A range of small shifts to the observed wavelength scale were also considered, within the errors of the star's radial velocity, in order to best match the observed profile. The smallest value of $\mathcal{F}$ was deemed to define the best-fit model for that feature, although the ten profiles with smallest $\mathcal{F}$ values were visually inspected in order to verify a best match. In cases of asymmetric line profiles, i.e. V/R ratios other than 1 (such as Hβ for HD 216629), the match was made to only one of the peaks, depending on the shape, strength and width of the line profile.

We will first discuss the best-fit models for each line of Table 4.2 individually for each star, and then consider the single, best global model for all the stars. Disk density parameters for the individual and global fits for all three stars are listed in Table 4.5. Section 4.4 discusses the uniqueness of the model fits.

Table 4.4: Explored model parameters for the disk of HB2e stars: HD 76534, HD 114981 & HD 216629.

Parameter	Range
Base Disk Density, ρ_0 (g cm^{-3})	10^{-8}...10^{-13}
Power Law Index, n	0.5...3.0
Inclination, i (°)	18...75
Disk Radius, R_{disk} (R_*)	25...100

4.2.1 Line Fits: HD 76534

The best-fit synthetic line profiles to the individual observed emission lines for HD 76534 are shown in Figure 4.6 and the top 9 best-fit lines and its corresponding model parameters can be found in Appendix B, from Figure B.11 to Figure B.18. All the observed emission lines are well matched in strength, shape, and width.

The model that best fits Hα line profile is from a $100\,R_*$, thin disk model with a base disk density (ρ_0) of $7.5 \times 10^{-12}\,\mathrm{g\,cm^{-3}}$ and power-law index (n) of 2.5 viewed at an inclination of $i = 45°$. The synthetic line profile is slightly weaker at the base when compared to the observed profile, indicating that either slightly more material is required closer to the star and/or the system is viewed at an inclination angle of somewhat more that 45°. However, the fit was not refined along these lines. For Hβ, the best-fit model profile is from a $100\,R_*$, thick disk model with base disk density (ρ_0) of $1.0 \times 10^{-11}\,\mathrm{g\,cm^{-3}}$ and the power-law index (n) of 3.0, seen at the same inclination as Hα, $i = 45°$. For the two Fe II lines, λ 5169 and λ 5317, the model that fits both observed line profiles is from a $25\,\mathrm{R}_*$, thin disk with a base disk density (ρ_0) of $1.0 \times 10^{-10}\,\mathrm{g\,cm^{-3}}$ and power-law index (n) of 3.0, again seen at $i = 45°$.

Except for the two Fe II lines, all of the optimal models for the individual lines differ. As noted before, these best fit models are those with the minimum value of $\mathcal{F}$. However, there is a range of other disk density models that fit each line profile nearly as well. The range of fitting models for each feature, and implications, will be discussed in Section 4.4.

As for HD 76534's He I absorption line, it presents a special problem. The observed line profile has a very wide base in the wings and a sharper, narrow absorption core. The synthetic profiles were found to well fit only either the wide wings or the narrow absorption core, depending upon the viewing inclination, with $i = 18°$ models matching the narrow core and $i = 45°$ models matching the broad wings. None of the models reproduced the observed line profile as whole. As He I λ 6678 Å is a transition in helium's singlet spin system, we do not expect a diffuse, forbidden component to the line's profile (as is the case for the triplet system). We have explored variations in the adopted stellar parameters; models were calculated for a

$T_{\rm eff}$ increased by 2000 K (in order to strengthen the helium lines), as well higher and lower values of log g. None of these variations were able to fit the observed He I profile. Finally, we investigated the possibility of binarity, postulating that the observed He I line is actually the sum of two stellar components of very similar spectral types. As mentioned earlier, HD 76534 is already known to be a visual binary, although the separation is too large for this to be the origin of the addition spectrum. We did manage to produce an acceptable match to the He I line by combining the two line profiles, i.e. a fit to the narrow absorption with a photospheric model with $v\,sini$ of 49 km/s and fit the wide base component of the line profile with a photospheric model with $v\,sini$ of 222 km/s. The two line profiles were combined assuming an equal flux contribution from each component, and the composite line profile is illustrated in Figure 4.7. Thus, there is evidence that the HD 76534 spectrum is actually a composite spectrum of two B stars of nearly the same spectral type. We note that we are unable to detect a systematic velocity offset between the two components, and therefore, the binary orbit must be either very wide or the orbital plane is in the plane of the sky. Despite this circumstantial evidence for a composite spectrum, we will retain the assumption that HD 76534's emission line spectrum is due to a single HBe star in the analysis.

From Table 4.5, we see that no single model was able to fit all the emission line profiles for HD 76534. It is likely that a disk density distribution more complex than an axisymmetric, single power law is necessary to explain the equatorial density variation of the inner, gaseous disk. To this end, and to investigate what range of disk radii contribute to the formation of each line, the cumulative emission for each line was calculated and plotted against the radius of the disk. To calculate this cumulative disk emission, $C(R)$, a face-on ($i = 0°$) synthetic image was produced in the integrated light of each emission line using the best-fit disk density model for that line. The intensity was then integrated over the total width of the line for each image, and then this integrated over disk radius as

$$C(R) = 2\pi \int_{R_*}^{R} I(R')\, R'\, dR' \,. \tag{4.2}$$

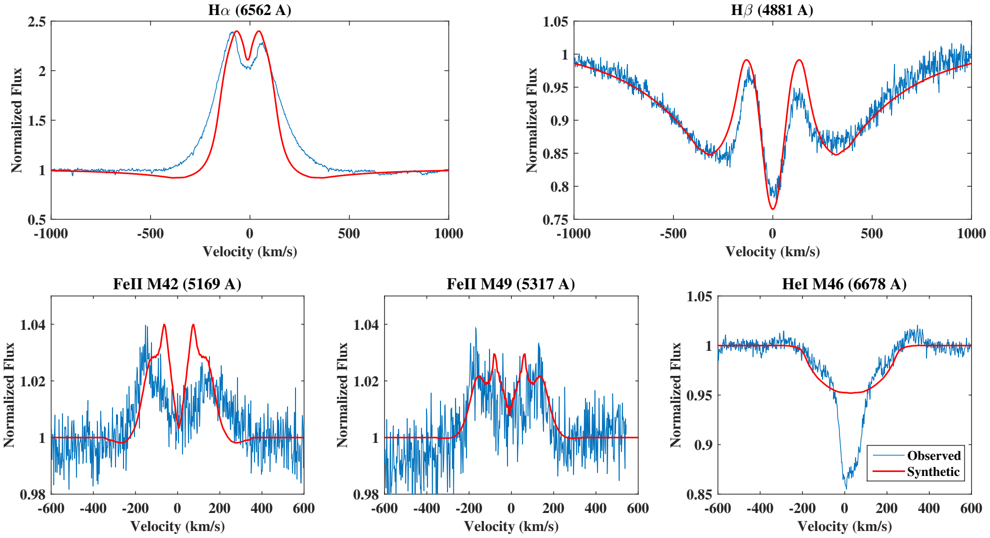

Figure 4.6: The best fit synthetic line profile (red) for each observed emission line of HD 76534 (blue): Hα (λ 6563), Hβ (λ 4861), Fe II multiplet (42) (λ 5169), Fe II multiplet (49) (λ 5317) and He I (λ 6678). The fit parameters for each model can be found in Table 4.5, with the exception of He I as it is fit by a pure photospheric profile.

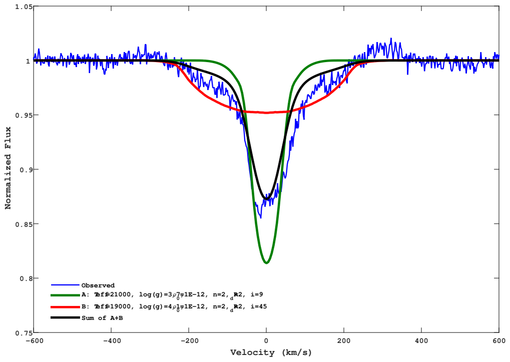

Figure 4.7: The two model fit for the observed He I line profile (seen in Blue) of HD 76534. The photospheric model with *v sini* of 222 km/s (red) is fit to the wide base and wings and the photospheric model with *v sini* of 49 km/s (green) is fit to the narrow absorption core. The sum of the two model lines (seen in Black) is matched to the observed.

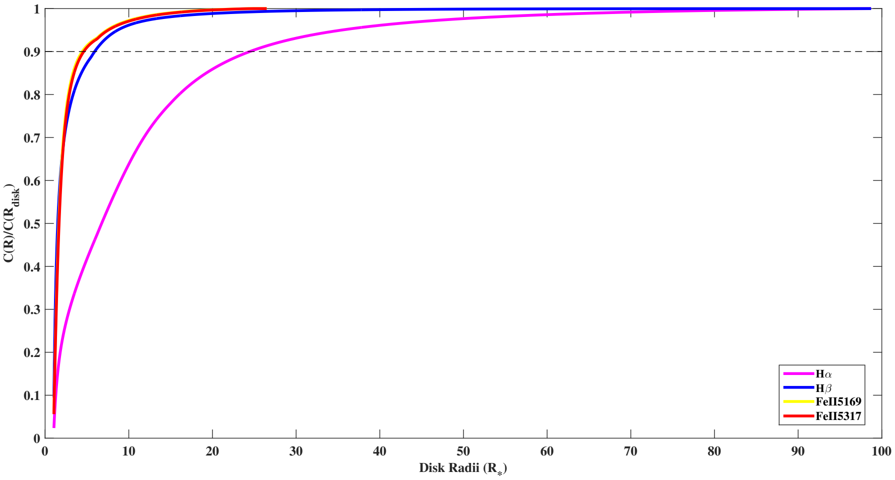

Figure 4.8: The cumulative line emission (Equation 4.2) as a function of distance from the central star of HD 76534 for each individual line using the best-fit disk density model. The model parameters that produced each individual line can be found in Table 4.5. The black dashed line represents a cumulative emission fraction of 0.9.

Here $I(R)$ is the wavelength integrated line intensity at distance R, and R_* is the stellar radius, assumed to be the inner edge of the disk. Then $C(R)/C(R_{disk})$ can be plotted versus R to determine the contribution to the total intensity of each line throughout the disk.

Figure 4.8 shows the cumulative emission $C(R)$ for each individual line. It is important to note that in this figure, the disk density model used to calculate the $C(R)$ for each line is the individual best fit model for that line given in Table 4.5. As a result, for example, $C(R)/C(R_{disk})$ reaches one at 100 R$_*$ for Hα and Hβ, but for Fe II, it is reached by 25 R$_*$. While Hβ requires a 100 R$_*$ disk to best reproduce the observed profile, most of the emission comes from the region very close to the star. Hα also requires extended disk, but 90% of the emission is produced in the 25 R$_*$ disk near the star. Both the Fe II lines on the other hand are mostly produced in the region less than 5 R$_*$.

4.2.2 Line Fits: HD 114981

For HD 114981, the best fit model parameters, both individual and global, can be found in Table 4.5, and the comparison between the model and observed profiles can be seen in Figure 4.9.

The top 9 best fit lines along with the corresponding models are illustrated in Appendix B, from Figure B.19 to Figure B.26. For this star, all of the observed lines were individually matched reasonably well in terms of strength and sample by synthetic library profiles.

The disk density model that best fits the observed Hα line profile is an 50 R_*, thick disk with base disk density (ρ_0) of 1.0×10^{-12} g cm^{-3} and power-law index (n) of 2.0 seen at an inclination of $i = 60°$. For Hβ, the model that best fits the observed line was a 100 R_*, thin disk with the base disk density (ρ_0) of 3.2×10^{-11} g cm^{-3} and power-law index (n) of 2.5 with again an $i = 60°$ inclination. For both the Balmer lines, the best-fit synthetic lines do show deeper central absorption compared to the observed line profile. A change in the inclination angle, intermediate between 45° and 60°, might improve the fit, but this was not attempted.

For the two Fe II lines, the model that fits both observed profiles well is a 25 R_*, base disk density (ρ_0) of 1.0×10^{-10} g cm^{-3} and power-law index (n) of 3.0 when seen at a $i = 45°$ inclination. The only difference between the two models used for the fits is that Fe II λ5169 requires a thin disk while Fe II λ5317 requires the thick disk. For He I, the photospheric model that best reproduces the observed line profile has a *v sini* of 222 km/s. The He I line is matched very well in strength.

The cumulative disk emission as a function of R_{disk} for HD 114981 is shown in Figure 4.10. Again it should be remembered that the individual disk density model for each line (Table 4.5) has been used to compute $C(R)/C(R_{disk})$. Hα requires an extended region to reproduce the observed line profile, with most of the emission for Hα is produced within 30 R_* of the disk. Hβ is produced throughout the 100 R_* disk; however, 90% of the emission comes from the inner 20 R_* of the disk. Finally, Fe II (λ5169) emits from region closer to the star, and most of the emission comes from within 5 R_*; Fe II (λ5317) emits from little further out in the disk, and 90% of the emission comes from within the first 10 R_* of the disk.

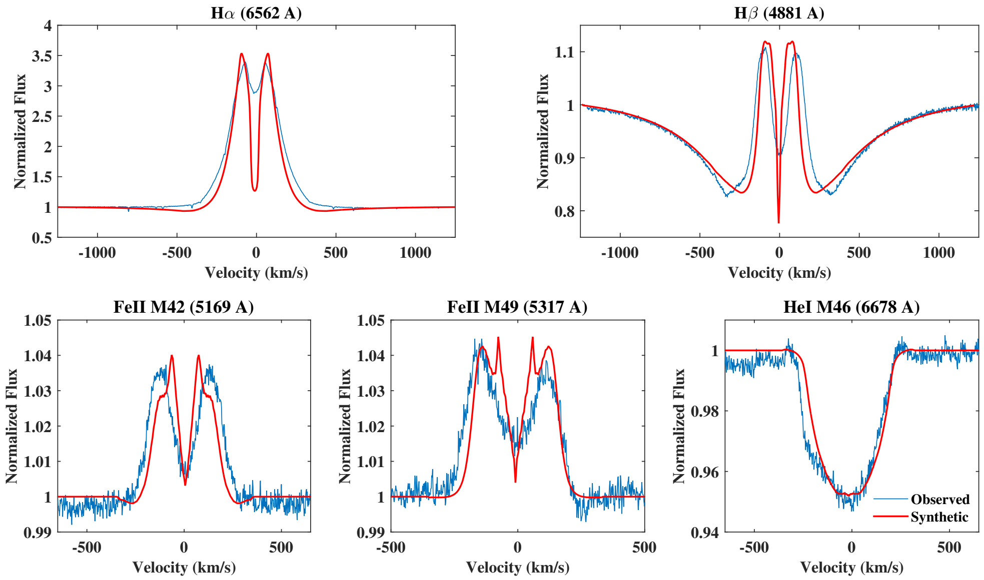

Figure 4.9: The best fitting synthetic emission line (blue) for each observed line (red) of HD 114981: Hα (λ 6563), Hβ (λ 4861), Fe II multiplet (42) (λ 5169), Fe II multiplet (49) (λ 5317) and He I (λ 6678) modeled using BERAY. The fit parameters for each model can be found in Table 4.5, with the exception of He I as it is fit by a photospheric profile.

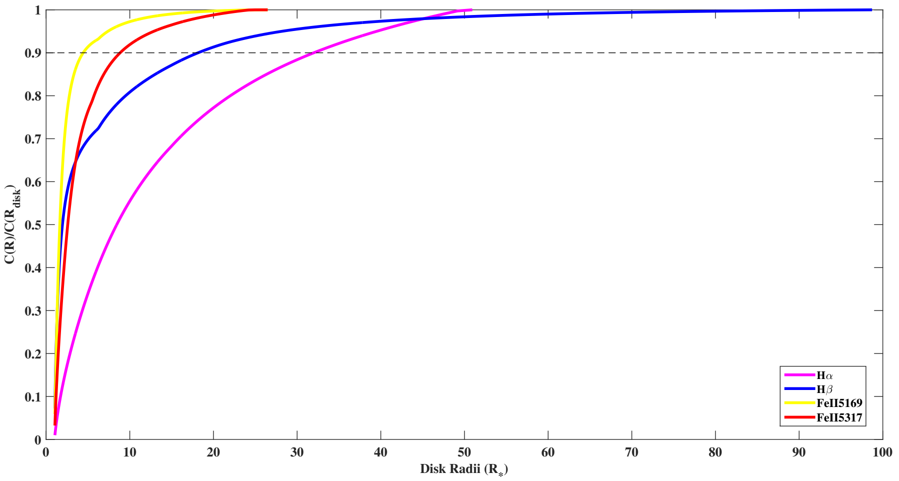

Figure 4.10: The cumulative line emission (Equation 4.2) as a function of distance from the central star of HD 114981 for each individual line using the best-fit disk density model. The model parameters that produced each individual line can be found in Table 4.5. The black dashed line represents a cumulative emission fraction of 0.9.

4.2.3 Line Fits: HD 216629

The individual, best-fit models for the emission lines of HD 216629 are illustrated in Figure 4.11, and the corresponding model parameters for each line can be found in Table 4.5. The top 9 best fit lines and its corresponding model parameters can be found in Appendix B, from Figure B.27 to Figure B.36. Unlike HD 76534 and 114981, the Ca II infrared-triplet is detected in emission in the spectrum of HD 216629, and the Paschen-subtracted profile for λ 8542 is available for the analysis. As can be seen from Figure 4.11, the hydrogen and iron emission lines are fit reasonably well, but not the Ca II IR triplet line where the model profile, while fitting the peak emission, is significantly narrower than the observed line profile.

The synthetic line profile that provides the best fit to Hα was a 25 R_* thin and turbulent disk with the a base disk density (ρ_*) of 1.0×10^{-11} g cm^{-3} and power-law index (n) of 2.5 seen at $i = 45°$. However, as can be seen in Figure 4.11, this model does not give a single-peaked line profile for Hα as observed and is too narrow at the base. The Hβ profile for this star shows asymmetric red and blue emission peaks, superimposed on a wide absorption trough. For modelling, the weaker, blue emission peak was chosen and a good fit to this emission peak and the absorption trough was found for a 25 R_*, thin and turbulent disk with the base disk density (ρ_*) of 1.0×10^{-11} g cm^{-3} and power-law index (n) of 2.5, seen at an inclination of $i = 45°$. Fitting the red peak instead (not shown) leads to a denser denser disk, (ρ_*) of 1.0×10^{-10} g cm^{-3} with a larger power-law index ($n = 3.0$) but seen at an inclination of $i = 60°$.

The observed Ca II IR triplet (λ 8542) emission line is very wide, with a full width of 870 km/s at the base of the profile from the apparent edge of one wing to the other. The best-fit synthetic model for Ca II is a 25 R_*, thick and turbulent disk with a base disk density (ρ_0) of 1.0×10^{-11} g cm^{-3} and power-law index (n) of 3.0 seen at an angle of $i = 60°$. The model reproduces the peak emission, but fails to match the overall width and strength of the line.

Fe II λ 5169 requires a 25 R_*, thin disk with a base disk density (ρ_*) of 1.0×10^{-10} g cm^{-3} and power-law index (n) of 3.0 seen at an inclination of $i = 60°$. Fe II λ 5317 line requires the same disk density parameters, but for a thin and turbulent disk seen at a higher inclination of

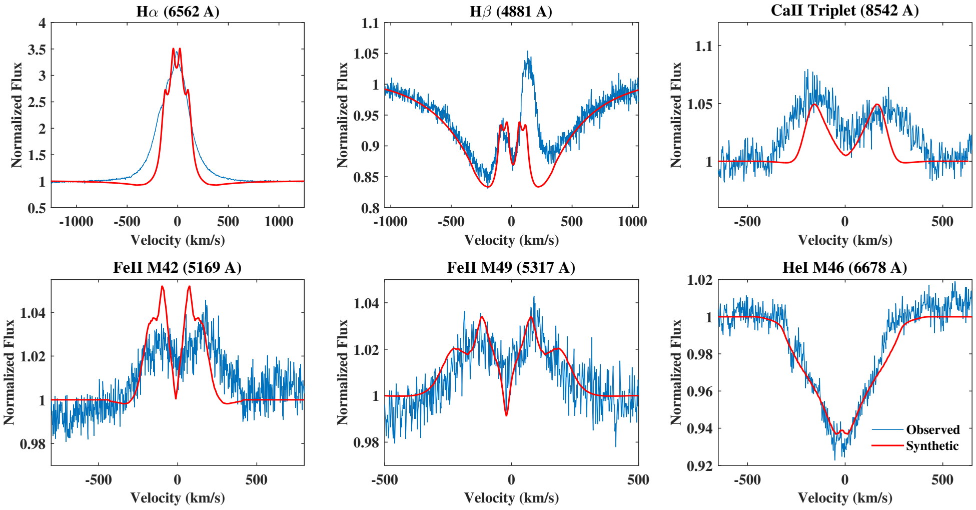

Figure 4.11: The best fit synthetic profiles (red) for HD 216629 compared to the observed emission lines (blue). The panels are Hα (λ 6563), Hβ (λ 4861), Ca II IR triplet (λ 8542), Fe II multiplet (42) (λ 5169), Fe II multiplet (49) (λ 5317) and He I (λ 6678) as indicated. The disk density parameters for each model can be found in Table 4.5, with the exception of He I as it is fit by a photospheric profile.

$i = 75°$. The synthetic profile for Fe II λ 5169 is narrower than the observed line profile but matches well in strength. The Fe II λ 5317 synthetic line profile matches well both the shape and strength of the observed line profile.

Finally, the He I λ 6678 can be fit to the observed line profile with a synthetic model that has a *v sini* of 303 km/s. The synthetic line profile shows some central emission, which can be attributed to a CQE feature arsing from stellar radiation being blocked by the disk as the system is seen at a higher inclination.

A plot of $C(R)/C(R_{disk})$ versus R_{disk} for HD 216629 can be found in Figure 4.12. Similar to HD 76534, most of the emission for the Fe II lines is produced in the inner most 5 R_* of the disk. 90% of the flux for Ca II IR triplet also comes from the inside the 5 R_*. For Hβ, 90% of the emission is produced within 7 R_* of the disk. Hα requires an extended region and is produced in the first 20 R_* of the disk.

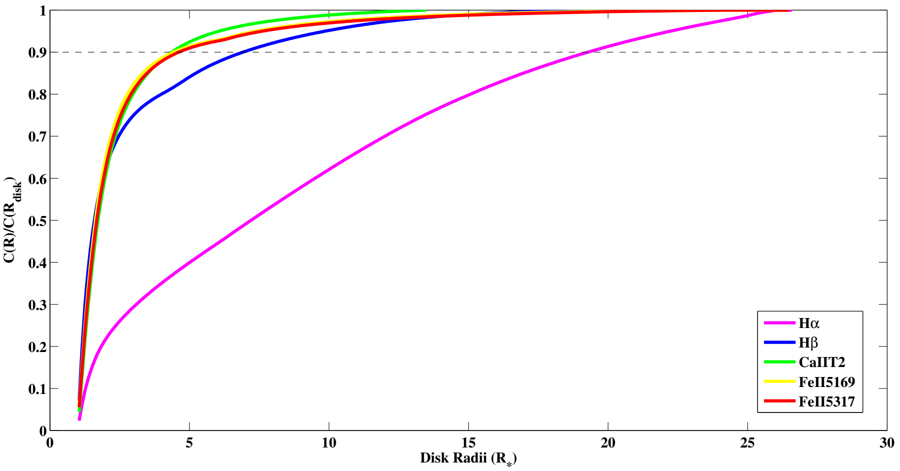

Figure 4.12: The cumulative line emission (Equation 4.2) as a function of distance from the central star of HD 216629 for each individual line using the best-fit disk density model. The model parameters that produced each individual line can be found in Table 4.5. The black dashed line represents a cumulative emission fraction of 0.9.

4.3 Global Fits

Given that the aim of this study was to determine a unique density structure for each star's innermost gaseous disk, the next step was to see how well a density model with a single set of parameters (ρ_0, n, i, R_d) and type (thin, thick, turbulent) could fit all of the observed line profiles. If a single density model is unable to reproduce all the emission line profiles satisfactorily, comparing the individual line fits to the best global model will assist in deciding how to generalize the density structure of the disk. To find the single best disk density model, a weighted sum of all the individual line profile figures-of-merit $\mathcal{F}$ was computed for each disk density model,

$$\mathcal{F}^{\mathrm{total}} = \sum_{i=1}^{N_l} w_i F^{\mathrm{i}} \ , \tag{4.3}$$

where i ranges over the lines available; $N_l = 6$ if the Ca II line is detected in the spectrum, but $N_l = 5$ otherwise. Initially, the weights w_i were set to one for all lines and such fits will be referred to as the *all-line fits*. However, additional weightings were also explored: *Balmer-line fits*, in which only the hydrogen Balmer lines Hα and Hβ were retained in the sum, or *metal-*

line fits, in which only the Fe II and Ca II (when available) metal lines were included in the sum. By examining the results of these various weightings, an adopted density model for the inner, gaseous disk for each star is suggested.

4.3.1 Global Fits: HD 76534

For HD 76534, a 25 R_*, thin and turbulent disk with the base disk density (ρ_0) of 1.0×10^{-9} g cm^{-3} and power-law index (n) of 3.0 seen at $i = 75°$ is the best global, all-line fit (Table 4.5). Figure 4.13 shows the synthetic line profiles for this single model compared to the observed lines.

The Hα synthetic line profile has the right strength and shape, but it is narrower at the base compared to the observed profile. As the selected model is seen close to edge-on, at angle of 75°, the center of the Hα profile shows a deep absorption feature in the core that is not observed. The synthetic line profile for Hβ produces the correct shape for the two peaks; however, it also shows a very deep central absorption core, that, like Hα, is not observed. Both Fe II lines produced by this model are stronger than the observed profiles and also show excessive central absorption. The He I synthetic line profile is a poor fit; however, the possible two-component nature of this line, illustrated in Figure 4.7, is not accounted for in this single, global model. The total disk mass associated with this global model is $\sim 1.2\times 10^{-8}\,M_*$ or 1.9×10^{26} g.

Figure 4.14 next shows the Balmer-line fit, where the metal lines are excluded, to the observations, while Figure 4.15 shows the metal-line fit in which the hydrogen lines were excluded. Comparing these two figures reveals that, overall, the metal-line fit seems to do the best job; while the fits to Hα and Hβ are formally worse, the differences are not compelling, and the metal-line fit hydrogen profiles now deep absorption cores that are not observed, owing to the $i = 45^o$ viewing angle that is now selected. In addition, the Fe II lines are now much better fit, while the wide base of the He I line is reproduced. For these reasons, we adopt this metal line fit as the best-fit, single disk model for HD 76534. The disk mass associated with this model is 1.9×10^{25} g or $10^{-9}\,M_*$, about ten times smaller than the mass associated with the best global model weighting all lines equally.

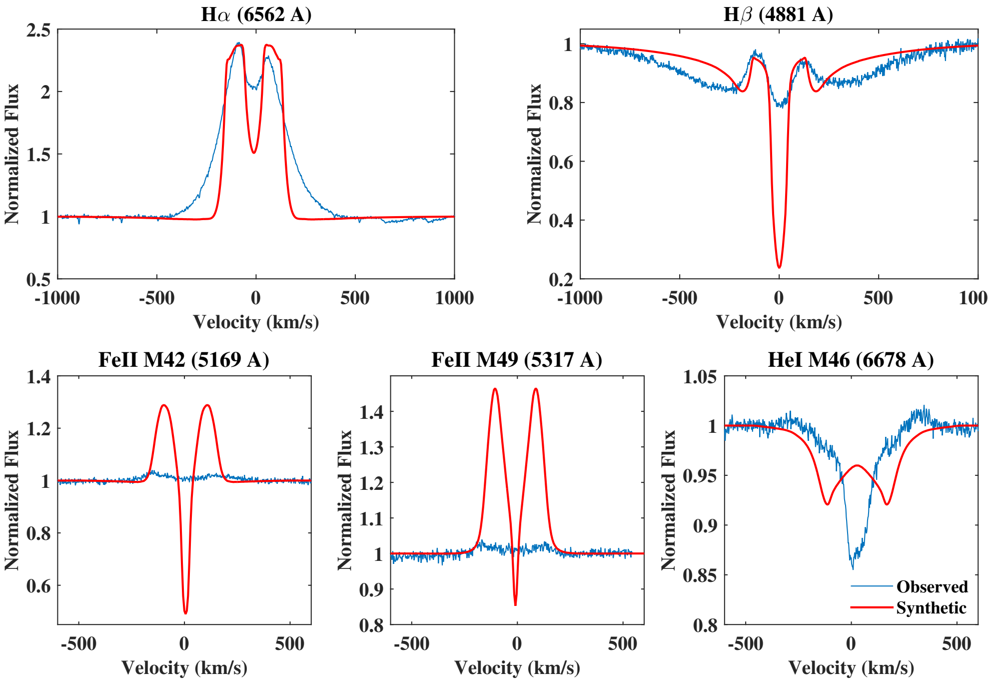

Figure 4.13: Global fits for HD 76534: model profiles (red) for the all-line fit compared to the observed emission lines (blue). The disk model parameters for this fit are $n = 3.0$, $\rho_0 = 1.0 \times 10^{-9}\ \mathrm{g\,cm^{-3}}$; further details can be found in Table 4.5.

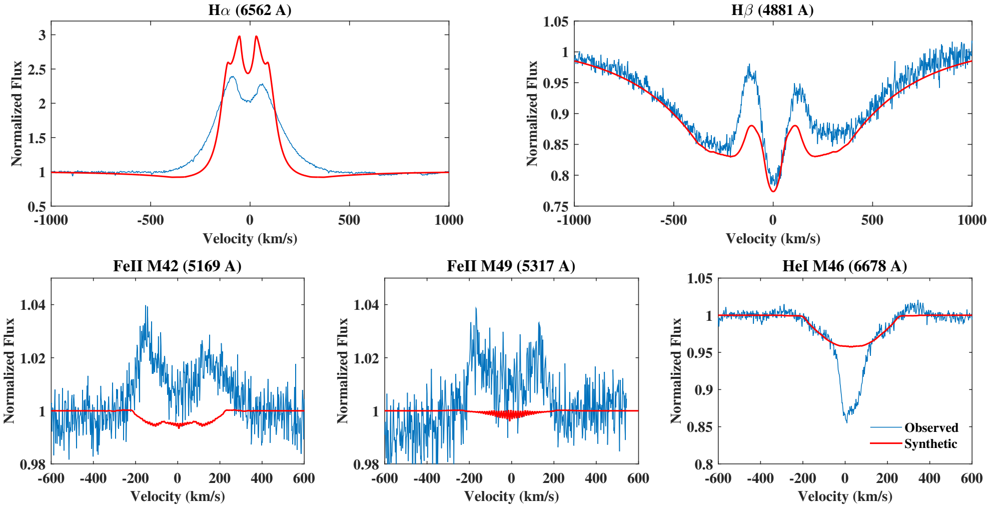

Figure 4.14: Global fits for HD 76534: model profiles (red) for the Balmer-line fit compared to the observed emission lines (blue). The disk model parameters for this fit are $n = 2.5$, $\rho_0 = 1.0 \times 10^{-11}\ \mathrm{g\,cm^{-3}}$.

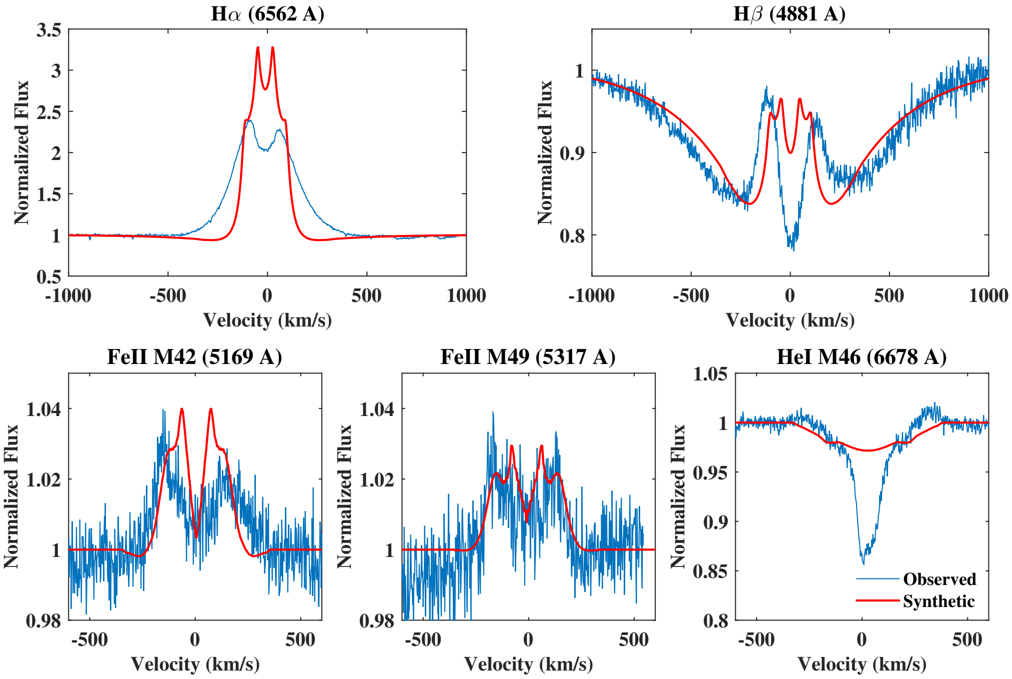

Figure 4.15: Global fits for HD 76534: model profiles (red) for the metal-line fit compared to the observed emission lines (blue). The disk model parameters for this fit are $n = 3.0$, $\rho_0 = 1.0 \times 10^{-10}\,\mathrm{g\,cm^{-3}}$.

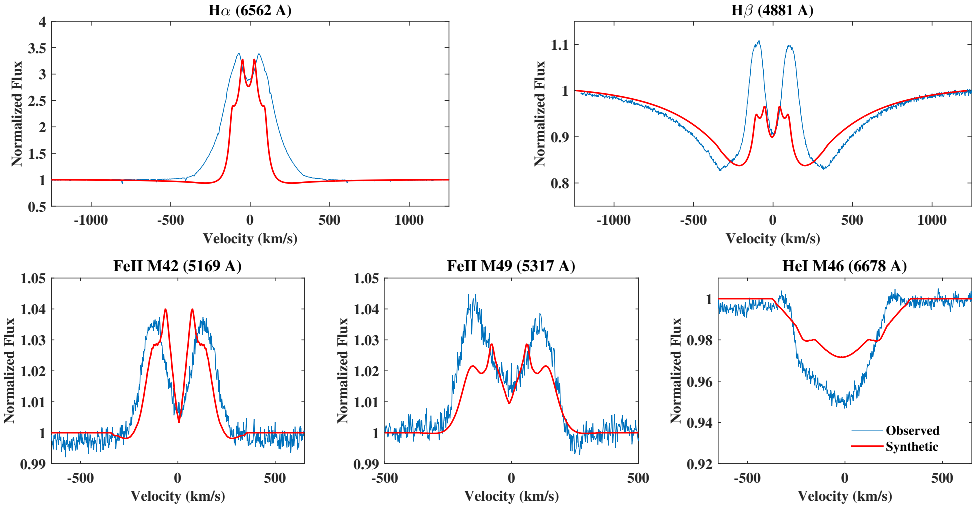

Figure 4.16: Global fits for HD 114981: model profiles (red) for the all-line and metal-line weightings (as both resulted in the same mode), compared to the observed emission lines (blue). The disk model parameters for this fit are $n = 3.0$, $\rho_0 = 1.0 \times 10^{-10}\,\mathrm{g\,cm^{-3}}$.

4.3.2 Global Fits: HD 114981

For HD 114981, a 25 R_* thin disk with a base disk density (ρ_0) of $1.0 \times 10^{-10}\,\mathrm{g\,cm^{-3}}$ and power law index $n = 3.0$ seen at an inclination of $i = 45°$ is the best global, all-line fit model. Figure 4.16 illustrates all-line fit model, and Table 4.5 lists the model parameters. As illustrated in the figure, the synthetic profile of Hα has the right strength and shape, but is narrower in width in comparison to the observed line profile. The wings of Hβ are reasonably well reproduced, and the line profile has two peaks and the right shape; however, the synthetic line profile is significantly weaker in the emission peaks. The synthetic line profile for Fe II λ 5169 matches to the observed the observed profile well, while for Fe II λ 5317, the shape of the observed line profile is well reproduced, but it is weaker in strength in the emission peaks. We note that λ 5317 shows an asymmetry in the emission peaks that is not seen in λ 5169. Lastly, the He I absorption line profile is weaker than the observed profile.

Figure 4.17 illustrates the Balmer-line fit for HD 114981, and the model parameters can be found in Table 4.5. The strength of the Hα, as well as its overall width, are better reproduced by this model, compared to the all-line fit previously discussed. For Hβ, the width of the line

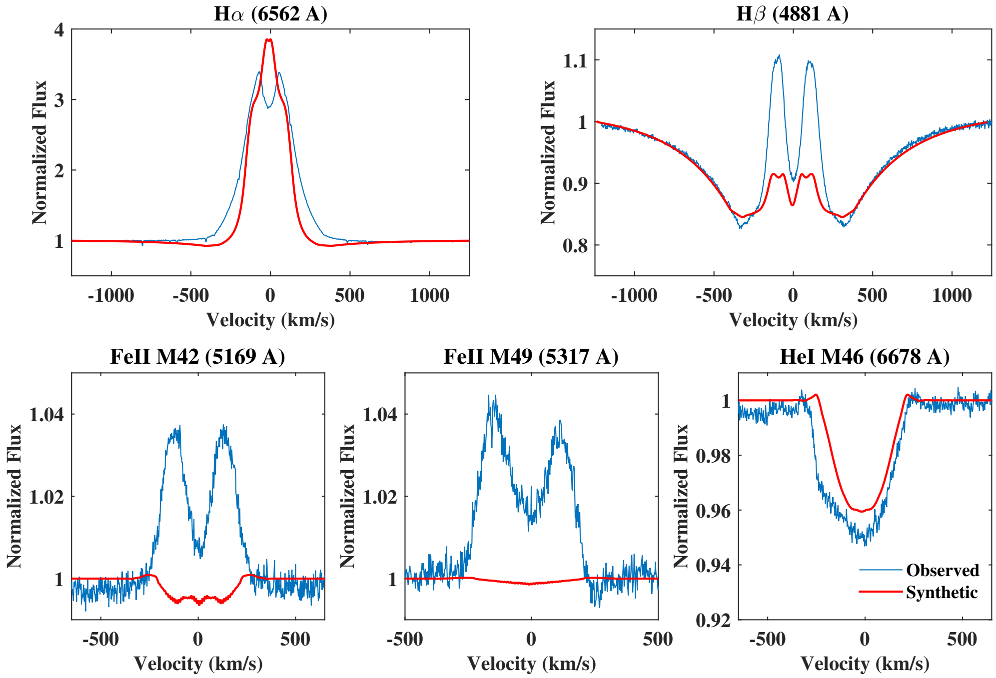

Figure 4.17: Global fits for HD 114981: model profiles (red) from the Balmer-line weighting compared to the observed emission lines (blue). The disk model parameters for this fit are $n = 2.5$, $\rho_0 = 1.0 \times 10^{-11}\,\mathrm{g\,cm^{-3}}$.

and the broad absorption trough is well reproduced, but again the strength of the emission peaks of the synthetic line profile does not match the observed. As for the two Fe II lines, the Balmer-line model is an extremely poor match, with this model predicting essentially no Fe II emission.

Finally, the metal-line fit based solely on the Fe II lines selects the same model as the global-fit model previously discussed. For this reason, we adopt the all-line fit model as the best single disk model for HD 114981. Note that this model is the same as that adopted for HD 76534, and thus the estimated disk mass is again $1.9\times\ 10^{25}$ g or $10^{-9}\ M_*$.

4.3.3 Global Fits: HD 216629

The best all-line fit model for the observed line profiles of HD 216629 is same model as the adopted models for both HD 76534 and HD 114981: a 25 R_*, thin disk with a base density ρ_0 of $1.0\times\ 10^{-10}\,\mathrm{g\,cm^{-3}}$ and power law index n of 3.0 seen at an inclination of $i = 45°$. Figure 4.18 illustrates this all-line weighted line profiles of HD 216629. This model reproduces the strength of Hα well; however, it is narrower at the base. The Hβ synthetic line profile reproduces the observed blue peak of the line very well; however, the red peak is a poorer match, with the model profile being too narrow and too weak. Unlike HD 76534 and HD 114981, the Ca II line is detected in the spectrum of HD 216629 and can be modelled. The synthetic Ca II line of the all-line model is much too weak compared to the observed line. The synthetic line profile for Fe II $\lambda\,5169$ is similar in shape and strength, but narrower compared to the observed line profile. On the other hand, the synthetic line for Fe II $\lambda\,5317$ matches the observed line quite well. The synthetic He I line matches the observed line well in width but produces emission in the core of the line that is not observed. Overall, with the exception of Ca II, all the line profiles match reasonably well.

Figure 4.19 shows the best Balmer-line fit model for HD 216629. This model has a lower ρ_0 and n, $1.0\times\ 10^{-11}\,\mathrm{g\,cm^{-3}}$ and 2.5 respectively, compared to the previous model. The Hα synthetic line profile is reasonably reproduced in strength; however, the width of the line at the

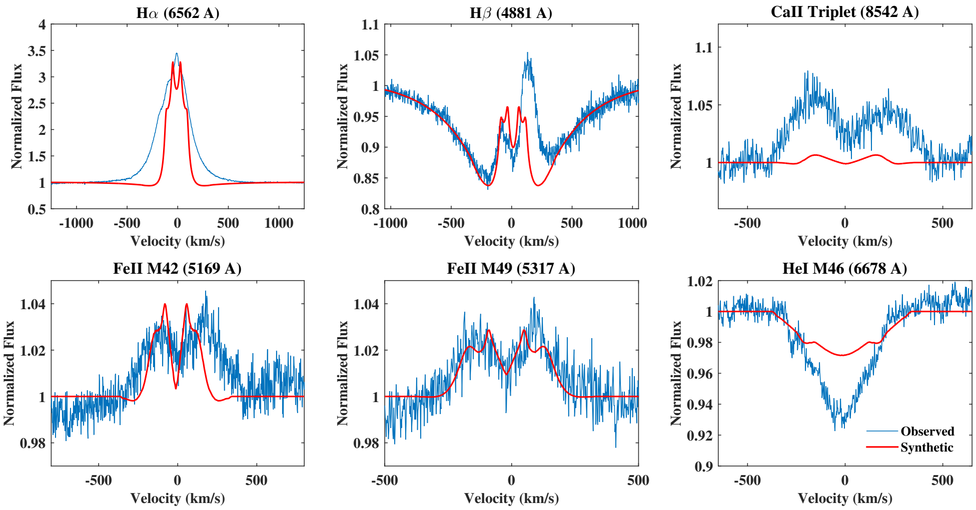

Figure 4.18: Global fits for HD 216629: model profiles (red) from the all-line and metal-line weighting (both resulted in the same model) compared to the observed emission lines (blue). The disk model parameters for this fit are $n = 3.0$ and $\rho_0 = 1.0 \times 10^{-10}\,\mathrm{g\,cm^{-3}}$.

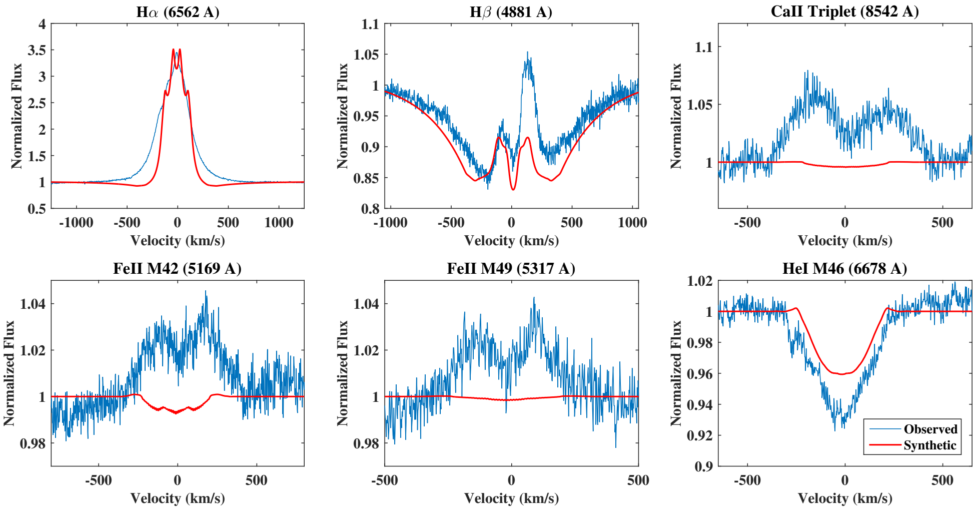

Figure 4.19: Global fits for HD 216629: model profiles (red) from the Balmer-line fit disk density model compared to the observed emission lines (blue). The disk model parameters for this fit are $n = 2.5$ and $\rho_0 = 1.0 \times 10^{-11}\,\mathrm{g\,cm^{-3}}$.

base is narrower when compared to the observed profile. For the Hβ, the strength of the blue peak is reproduced, but the overall the width of the synthetic line and the size of the red peak is not comparable to the observed profile. Essentially no Fe II or Ca II emission is predicted by this model.

The best fit for the metal-line weighting to HD 216629 is the same model as the all-line model above as illustrated in Figure 4.18. Hence, we adopt this model as the best single-power law model to represent the inner gaseous disk of HD 216629. The total disk mass of this model is 1.9×10^{25} g or $10^{-9}\,M_*$ and is the same as adopted global model for other two stars.

4.3.4 Summary of the Global Fits

Remarkably, the adopted, best-fit model based on a single set of density parameters for the inner disks of all three stars turns out to be the same: a thin disk with a base disk density of $\rho_0 = 1.0 \times 10^{-10}$ g cm^{-3}, a power index of $n = 3.0$, and an outer disk radius $R_d = 25\,R_*$, seen at an inclination of $i = 45°$. The disk mass associated with this model is $1.2 \times 10^{-9}\,M_*$ or 1.90×10^{25} gm. Recall that the only four inclination bins were considered, $i = 18$, 45, 60, and 75°, and some variation in the viewing inclinations is still consistent with the models. The finding of a similar disk model for all three B2 HBe stars is a result of the basic similarity of the strengths and shapes of their emission line spectra; this point is further discussed in Section 4.5.

To understand where the emission is produced in the disk by this single model, as well as to help in future work to decide how to better structure the disk in order to reproduce the line profiles, the cumulative line emission, $C(R)/C(R_{disk})$, is plotted as a function of disk radius, R_{disk}, for this adopted global model in the Figure 4.20. While this plot applies to all three stars considered, HD 76534, HD 114981 and HD 216629, one difference is that Ca II emission was detected only in HD 216629, despite the common model assigned to all three stars. Hα is produced in an extended region of the disk, with most of the emission produced within the inner 15 R_*. This is followed by Hβ, where 90% of the emission for the line is produced within the inner 7 R_* of the disk. Both the Fe II lines follow similar curve and are produced mostly

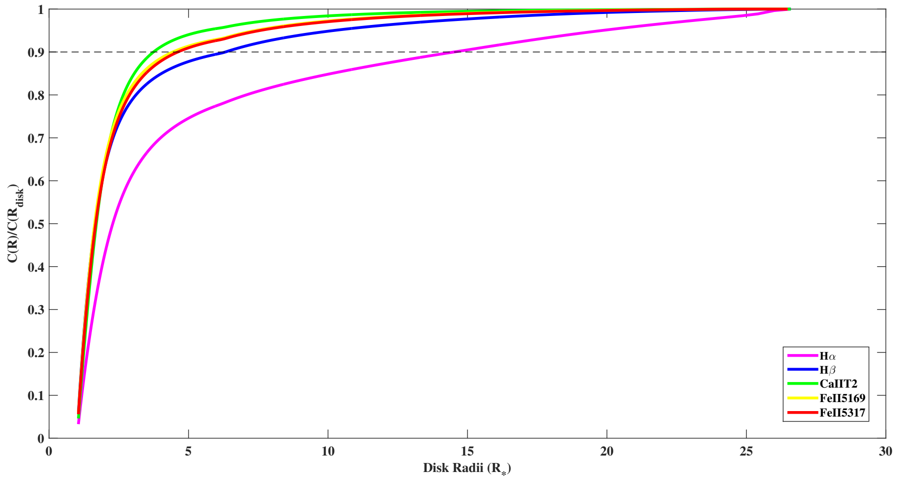

Figure 4.20: The cumulative line emission (Equation 3.2) as a function of distance from the star for each individual line using the best fit global disk density model for HD 76534, HD 114981 and HD 216629. The disk model parameters for this fit are $n = 3.0$, $\rho_0 = 1.0 \times 10^{-10}$ g cm^{-3}; further details can be found in Table 4.5. The black dashed line represents from where 90%.

in the inner region of the disk, confined to the 5 R$_*$. Given that hardly any emission was seen in the Ca II synthetic line profile, the little emission it produced was from the inner 4 R$_*$ of the disk.

4.4 Uniqueness of the Line Fits

As discussed in Section 4.2, a figure-of-merit is calculated whose minimum value, $\mathcal{F}_{min}$, defines the best fitting profiles. Nevertheless in the library of models, it is often the case that several models with different combinations of disk parameters ($\rho_0, n, i, R_{\rm disk}$) produce nearly as good fits to a given line. To quantify the range of models that come reasonably close to fitting each line, all the models that fall within 25% $\mathcal{F}_{min}$, i.e. those with figure-of-merit $\mathcal{F}$ satisfying $\mathcal{F}_{min} \leq \mathcal{F} \leq 1.25\,\mathcal{F}_{min}$, have been determined. Table 4.6 gives the number of such models found for each emission line for each star. The total number of matching models a given line is seen to vary from 1 to 17 depending on the line and the star.

In order to illustrate where the ensemble of best-fitting models for a given line falls in the explored parameter space, and how well the best fits for different lines agree, we have plotted the models satisfying $\mathcal{F} < 1.25\,\mathcal{F}_{\rm min}$ in the plane defined by the parameters ρ_0 and n. Note that the other model parameters, i and R_{disk}, and type of disk (thin, thick, turbulent, etc...) are not distinguished in such a plot. To illustrate ranges of satisfactory models in such a plot, a point is used to illustrate a single model. If there are two selected models, a line connects them, and if there are three models, a triangle is used. If there are more than three models satisfying the condition on $\mathcal{F}$, an ellipse is used to enclose the points. For He I, which generally has a photospheric origin and thus does not constrain the disk parameters, an arrow and line of the same color are used to represent the region of models that produce no disk emission. An example of such a plot is given in Figure 4.21 for HD 76534. As shown, only some of the models for different lines overlap in the (ρ_0, n) parameter space, illustrating the previous conclusion given in Table 4.5 that there is no single set of disk parameters, representing a single power-law for the disk's equatorial density, for which all of the lines can be well-fit. For HD 76354, two separate regions in parameter space can be seen, one in which the Fe II lines are best fit, and another where the fits to the hydrogen Balmer lines are found. The Fe II lines select a large region in parameter space that correspond to model profiles that fall withing within 25% of $\mathcal{F}_{min}$ that have high base disk densities and lower power law indices. The Balmer lines select similar to lower base disk densities and higher power law indices.

The plot illustrating the (ρ_o, n) plane for HD 216629 can be seen in Figure 4.22. There is a large set of models selected by Fe II $\lambda\,5169$. However, the Hα, Hβ, Ca II and Fe II $\lambda\,5317$ lines select only a few models satisfying the $\mathcal{F} \leq 1.25\,\mathcal{F}_{min}$ criteria. Again, no common region is found in the parameter space for all the lines.

Finally, Figure 4.23 illustrates the models for HD 114981. Unlike the previous two stars, HD 114981 has very few models in the range of 25% of the lowest $\mathcal{F}$ value for all the lines. The Balmer lines, as expected, are found in the lower base disk density (ρ_0) and higher power-law index (n) region. The two Fe II lines each have only one model that fits the criteria and they occupy the high base disk density and higher power law index region.

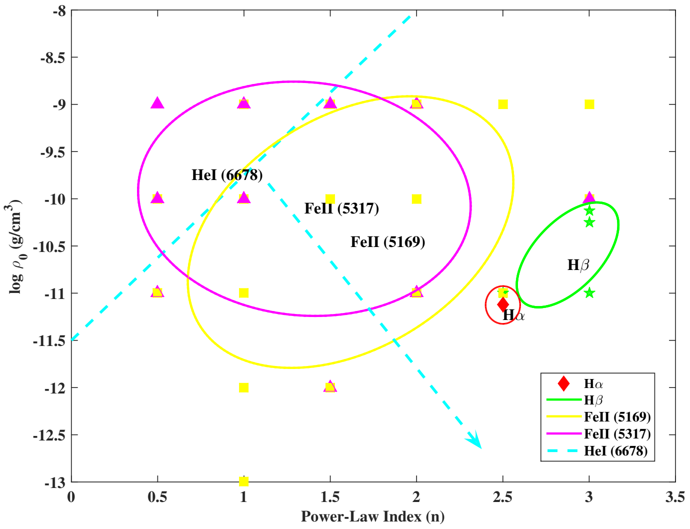

Figure 4.21: Regions of the $(n, log\,\rho_0)$ plane occupied by models with $\mathcal{F} \leq 1.25\mathcal{F}_{min}$ for the indicated lines for the star HD 76534. The He I constraint is the region indicated by the line and arrow below which there is no observable disk emission in the model He I line.

Finally note that the adopted global model for all three stars would fall at the point $\log\rho_0 = -10$ and $n = 3$. For all the three stars, no region in the explored parameter space leads to a unique model for the disk. This, along with the fact that individual line fits yielded good matches, suggests that a more complex model with various density variations amongst the disk is required in order to reproduce all the lines using a single model.

4.5 Discussion

While fitting the individual line profiles, it was interesting to see that all the models for HD 76534 that fit well to the emission lines were seen at inclination of 45°. For HD 216629, the observed Ca II IR triplet is wider than any of the line profiles in the database. The common parameter amongst all the lines is the smaller disk radii. Unlike HD 76534 and HD 216629, no common parameter or similarities were found amongst the Balmer and Fe II lines in HD 114981. While HD 76534 and HD 114981 required a thin or thick disk, HD 216629 required either thin, thin and turbulent or thick and turbulent disk to successfully reproduce all the individual line pro-

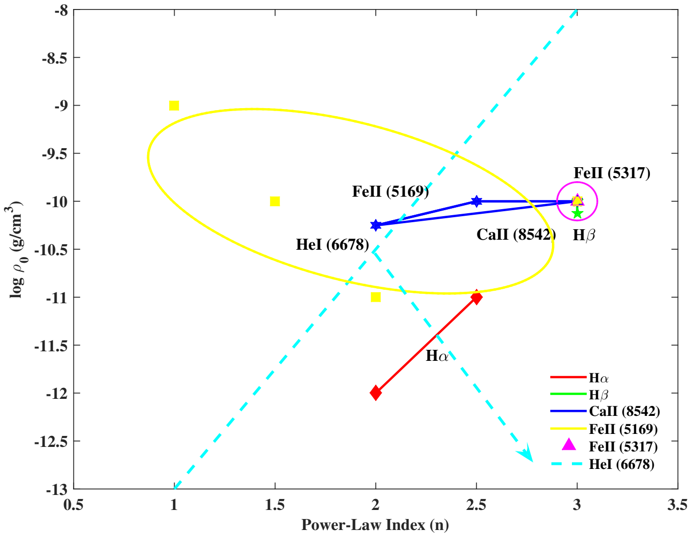

Figure 4.22: Regions of the $(n, log\,\rho_0)$ plane occupied by models with $\mathcal{F} \leq 1.25\,\mathcal{F}_{min}$ for the indicated lines for the star HD 216629. The He i constraint is the region indicated by the line and arrow below which there is no observable disk emission in the model He i line.

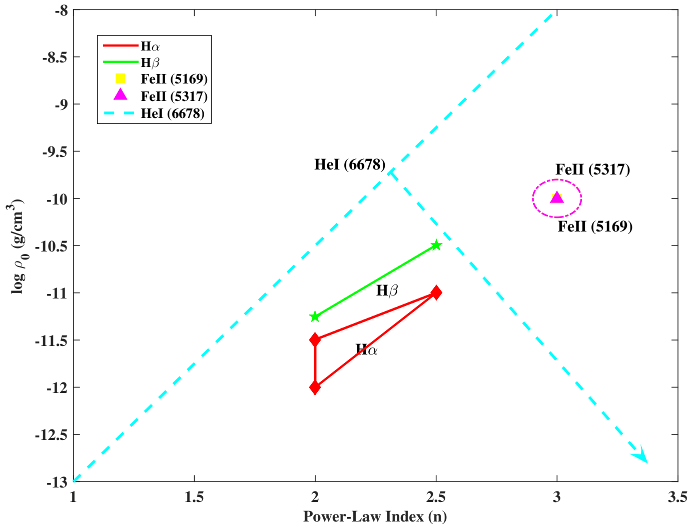

Figure 4.23: Regions of the $(n, log\,\rho_0)$ plane occupied by models with $\mathcal{F} \leq 1.25\,\mathcal{F}_{min}$ for the indicated lines for the star HD 114981. The He i constraint is the region indicated by the line and arrow below which there is no observable disk emission in the model He i line.

files. The two Fe II lines of all the three stars required the model with same base disk density (ρ_0), power law index (n) and disk radius (R_*) to match both λ 5169 as well λ 5317.

The parameters that are constant in the models for all the line profiles can help narrow the parameter space, making it easier to construct the complex single disk density model that can reproduce all the line profiles. Figures 4.8, 4.10 and 4.12 provide a wealth of information on the location of material in the disk. These figures show a complex density structure would be responsible in emitting the line profiles seen in the observed data. For all the three stars, it is evident from these figures that the lines of iron form in the inner-most region of the disk, while the Balmer lines require an extended region to form the emission lines with Hα being produced in almost the entire disk.

As discussed in Section 4.3, the best fit models selected for all the three stars are same, even with a wide variety of best fit models found for individual line profiles for all three stars. The similarities in the strength and shape of the Fe II lines for all the three is partly the reason why a similar model is found as the global best fit model.

Comparing to the work in previous chapter, there are some similarities and differences between the keys findings. Similar to BD+65 1637, the individual observed line profiles were found to match well with the synthetic line profiles. It was not possible for any of the three stars studied here to find a single global density distribution model that predicted emission line profiles in good accord with all lines observed. Like BD+65 1637 in Chapter 3, it was concluded that more complex models with density variations are required in order to be able to reproduce all the observed profiles. It was noted that BD+65 1637 required higher density and lower power law index models for metal (Ca II & Fe II) lines to fit the observed line profiles. In this work as well, similar models were required to fit the two Fe II lines. For the Ca II IR triplet however, conclusions were different. For two of the three stars in this work, HD 76534 and HD 114981, the Ca II line profiles were negligible after the Paschen subtraction process and were eliminated from the study. The Ca II line profile of HD 216629, as mentioned before, was too wide to be fit by any of our synthetic line profiles. This suggest more denser material

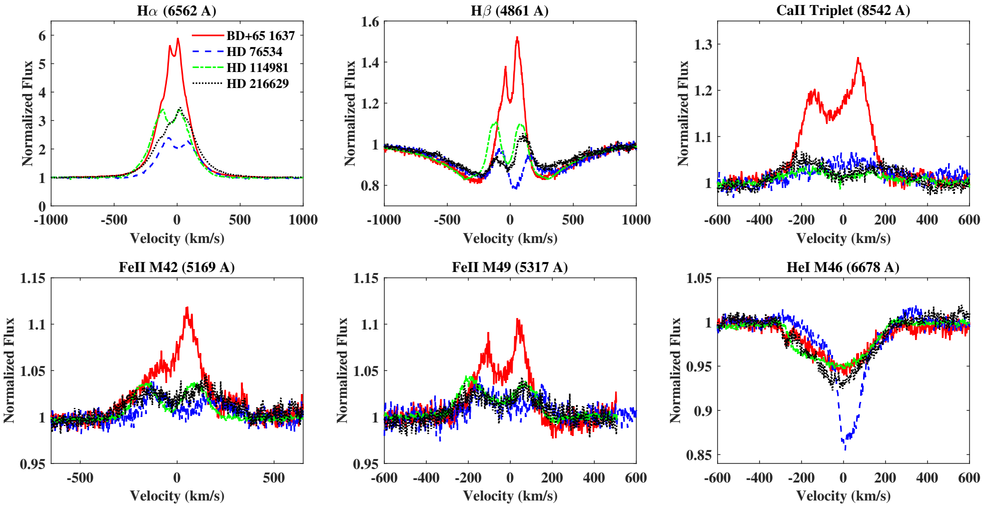

Figure 4.24: All the line profiles of all the stars considered in this chapter as well as in the previous chapter are overplotted. BD+65 1637 studied in the previous chapter is shown in red, while the three stars, HD 76534, HD 114981 and HD 216629, studied here are shown in blue, green and black respectively.

is required closer to the star than the model parameters considered in this study. Thus, models with density variations implemented by defining various power laws might be able to provide a better fit the line profiles and achieve a global model. For Classical Be stars, the disks are generally modeled with a single power law density structure (Sigut & Jones, 2007), however more complex structure is predicted using hydrodynamic models (Carciofi, 2011).

An over-plot of all the emission lines for all the four stars shows how similar these stars are to each other. This is illustrated in Figure 4.24. BD+65 1637 has stronger emission lines when compared to the other three stars, while still having a similar He I line profile to the other, with the exception of HD 76534. The similarity in the He I absorption lines of the three HB2e stars suggests the central stars are similar in nature, however the disks around them vary as seen due to the variety of their emission line profiles.

4.6 Conclusions

The key findings in the study of the inner gaseous disk of three HBe stars, HD 76534, HD 216629 and HD 114981, are:

- The line emission spectra of all three stars can be adequately reproduced, in terms of both line strength and shape, from a small, geometrically thin, gaseous circumstellar disk heated solely by the available photoionizing radiation field from the photosphere of central B star.
- The equatorial density in the disk varies roughly as $10^{-10}\,(R_*/R)^3\ \mathrm{g\,cm^{-3}}$.
- The size and mass of the emitting disk are $R_{\mathrm{disk}}/R_* \approx 25$ and $M_{\mathrm{disk}}/M_* \approx 10^{-9}$.
- The models, however, were not successful in reproducing the line profiles of H I, He I, Ca II and Fe II simultaneously based on an equatorial disk density varying as a single power-law with radius. A possible resolution is to consider equatorial density distributions that vary in a more complex way.
- The star HD 76534 has He I line profile which exhibits two distinct components: a wide base and a narrow, absorption core. This profile can be well fit by combining two equal photospheric B2V He I profiles that correspond to different $v\,\sin i$ values, suggesting that the spectrum is that of two equal-massed B stars as an unresolved binary.

A key limitation of the current study is that the three HBe stars analyzed are all Group III Herbig Ae/Be objects according to the Hillenbrand et al. (1992) classification, that is, objects with small infrared excesses resembling classical Be stars. We intend to extend our current analysis to Group I and II objects that show unambiguous signs of dust in their infrared spectral energy distributions.

Table 4.5: Individual line and global best-fit model parameters for all three stars. The adopted best-fit, global model for each star is indicated with a check-mark.

Star	Line	ρ_0 (g cm^{-3})	n	i (°)	R_{disk} (R_*)	Model Type
HD 76534	Hα (λ 6563)	7.5×10^{-12}	2.5	45	100	Thin
	Hβ (λ 4861)	1.0×10^{-11}	3.0	45	100	Thick
	Fe II (λ 5169)	1.0×10^{-10}	3.0	45	25	Thin
	Fe II (λ 5317)	1.0×10^{-10}	3.0	45	25	Thin
	Global Fit	1.0×10^{-9}	3.0	75	25	Thin & Turbulent
	Balmer Line Fit	1.0×10^{-11}	2.5	45	25	Thin
	Metal Line Fit √	1.0×10^{-10}	3.0	45	25	Thin
HD 114981	Hα (λ 6563)	1.0×10^{-12}	2.0	60	50	Thick
	Hβ (λ 4861)	3.2×10^{-11}	2.5	60	100	Thin
	Fe II (λ 5169)	1.0×10^{-10}	3.0	45	25	Thin
	Fe II (λ 5317)	1.0×10^{-10}	3.0	45	25	Thick
	Global Fit √	1.0×10^{-10}	3.0	45	25	Thin
	Balmer Line Fit	1.0×10^{-11}	2.5	45	100	Thin & Turbulent
	Metal Line Fit √	1.0×10^{-10}	3.0	45	25	Thin
HD 216629	Hα (λ 6563)	1.0×10^{-11}	2.5	45	25	Thin & Turbulent
	Hβ (λ 4861)	7.5×10^{-11}	3.0	45	25	Thin
	Ca II IR-triplet (λ 8542)	7.5×10^{-10}	3.0	60	25	Thick & Turbulent
	Fe II (λ 5169)	1.0×10^{-10}	3.0	60	25	Thin
	Fe II (λ 5317)	1.0×10^{-10}	3.0	75	25	Thin & Turbulent
	Global Fit √	1.0×10^{-10}	3.0	45	25	Thin
	Balmer Line Fit	1.0×10^{-11}	2.5	45	25	Thin & Turbulent
	Metal Line Fit √	1.0×10^{-10}	3.0	45	25	Thin

He I (λ 6678) is a photospheric line and is not used to constrain the disk models.

Table 4.6: Number of models satisfying $\mathcal{F}_{min} \leq \mathcal{F} \leq 1.25\,\mathcal{F}_{min}$.

Emission Line	HD 76534	HD 114981	HD 216629
Hα	1	3	2
Hβ	4	2	2
Ca II (λ 8542)	–	–	3
Fe II (λ 5169)	17	1	4
Fe II (λ 5317)	10	1	1

Bibliography

Acke, B., van den Ancker, M. E. & Dullemond, C. P., 2005, A&A, 436, 209

Alecian, E., Wade, G. A., Catala, C. et al. 2013, MNRAS, 429, 1001A.

Carciofi, A. C., 2011, IAUS, 272, 325C.

Corcoran, M. & Ray, T. P., 1997, A&A, 331, 147C.

Finkenzeller, U. & Mundt, R., 1984, A&AS, 55, 109.

Garmany, C. D., 1973, AJ, 78, 185.

Harrington, D. M. & Kuhn, J. R., 2009, ApJSS, 180, 138.

Herbst W., 1975, AJ 80, 683.

Hill, P. W., 1970, MNRAS, 150, 23.

Hillenbrand L. A., Strom S. E., Vrba F. J. & Keene J., 1992, ApJ, 397, 613.

Hubeny, I. 1988, CPC, 52, 103.

Hubeny, I. & Lanz, T. 1992, A&A, 262, 501.

Hubeny, I. & Lanz, T. 1995, ApJ, 439, 875.

Jain, S. K. & Bhatt, H. C., 1995, A&ASs, 111, 399.

Mannings, V. & Barlow, M. J., 1998, ApJ, 497, 330.

Morel, P. 1997, A&AS, 124, 597.

Mottram, J. C., Vink, J. S., Oudmaijer, R. D. & Patel, M., 2007, MNRAS, 377, 1363M.

Oudmaijer, R. D. & Drew, J. E., 1997, A&A, 318, 198.

Oudmaijer, R. D. & Drew, J. E., 1999, MNRAS, 305, 166.

Peter, D., Feldt, M., Henning, Th. & Hormuth, F., 2012, A&A, 538, A74.

Rivinius, Thomas, Carciofi, Alex C. & Martayan, Christophe, 2013, A&ARv, 21, 69R.

Sigut, T. A. A. & Jones, C. E., 2007, ApJ 668, 481.

Vieira, S. L. A., Corradi, W. J. B., Alencar, S. H. P., Mendes, L. T. S., Torres, C. A. O., Quast, G. R., Guimar£es, M. M., da Silva, L. 2003, AJ, 126, 2971.

Vink, J. S., Drew, J. E., Harries, T. J., Oudmaijer, R. D. 2002, MNRAS, 337, 356V.

Wheelwright, H. E., Oudmaijer, R. D. & Goodwin, S. P. 2010, MNRAS, 401, 1199.

Wilson Cauley, P. & Johns-Krull, C. M. 2014, ApJ, 797, 112C.

Chapter 5

Herbig B0e Star: MWC 137

This chapter corresponds to the article: Patel, P. Sigut, T. A. A. & Landstreet, J. D. *'Photoionization Models of Inner Gaseous Disk of the Herbig Be Star MWC 137'*, in preparation.

5.1 MWC 137

MWC 137 (V* V1308 Ori) is a 11.2 visual magnitude B0e star surrounded by the H II region SH 2-266 (Esteban & Fernandez (1998) and references therein). The spectral type and the evolutionary state of this star have long been a matter of debate: it has been labelled as everything from pre-main sequence to post-main sequence due to overlapping of features used in classification schemes. Several studies have classified it as an evolved B[e] supergiant (Esteban & Fernandez, 1998; Mehner et al., 2016; Muratore et al., 2015), and others as a HB0e star (Finkenzeller & Mundt, 1984; Hillenbrand et al., 1992; Thé et al., 1994; Hillenbrand, 1995; Fuente et al., 2003; Alonso-Albi et al., 2009; Verhoeff et al., 2012). It was even once mis-classified as a Planetary Nebula (Kohoutek, 2001; Frew et al., 2013)! As the majority of the spectral features in MWC 137's spectrum are emission lines, it has been called a continuum star (Heŕnandez et al. , 2004) or an emission line star.

Most recent studies, such as Muratore et al. (2015), have hinted at a post-main-sequence classification due to the enhanced $^{12}C/^{13}C$ ratio found in the circumstellar material around the star. Mehner et al. (2016) argues that the ^{12}C/^{13}C ratio should not alone be used as an indicator of a post-main-sequence phase and, employing color-color and color-magnitude diagrams, they provide additional evidence for a post-main-sequence phase. Nevertheless, they also observe a jet which is indicative of an accretion disk in the system.

Hillenbrand (1995) classified MWC 137 as Group I HBe star based on the shape of its infrared SED, and this SED is illustrated in Figure 5.1. Group I objects show a large IR excess for $\lambda > 2.2\,\mu m$. The stellar photosphere dominates until $1.2\,\mu m$ and the flux decreases between $1.2\,\mu m$ and $2.2\,\mu m$ for objects in this group. The change in the $1\mu m$ and $2\mu m$ window is attributed to a dust free zone by Hillenbrand (1995). The shape of this SED resembles that of T Tauri stars, and this hints to the young nature of the MWC 137. According to the criteria described by Lamers et al. (1998) for different B[e] stars, the primary criteria include log (L/L$_\odot$)≥4.0 for B[e] supergiants and log (L/L$_\odot$)≤5.0 for HAeBe stars. However, the log (L/L$_\odot$) value of MWC 137 depends on the distance used. Hillenbrand (1995) obtained the log (L/L$_\odot$)=4.4 assuming $d = 1300\,pc$, while Esteban & Fernandez (1998) dervied log (L/L$_\odot$)=5.37 assuming $d = 600\,pc$. Some of the conditions in the secondary criteria for a B[e] classification require that the star's spectrum shows indication of mass loss, either a P Cgyni profiles or a double peaked emission lines with violet shifted central absorption for Balmer lines; in addition, the B[e] criteria also require that the spectrum is a hybrid spectrum, containing the simultaneous presence of narrow, low excitation emission lines and of broad absorption features of higher-excitation lines. However, for MWC 137, all the Balmer lines are single-peaked, emission line profiles and most of the line profiles are fully in emission with hardly any absorption. In addition, MWC 137 is reported to be surround by interstellar dust and gas (Testi et al., 1997) further hinting at its young nature. In conclusion, most of the evidence points to a pre-, as opposed to post-main sequence evolutionary status for MCW 137, and in the analysis that follows, it is assumed that MWC 137 is a B0e HBe star whose optical and near-IR emission line spectrum comes from a gaseous circumstellar disk close to the star.

The stellar parameters for MWC 137 proposed by Hillenbrand (1995) can be found in Ta-

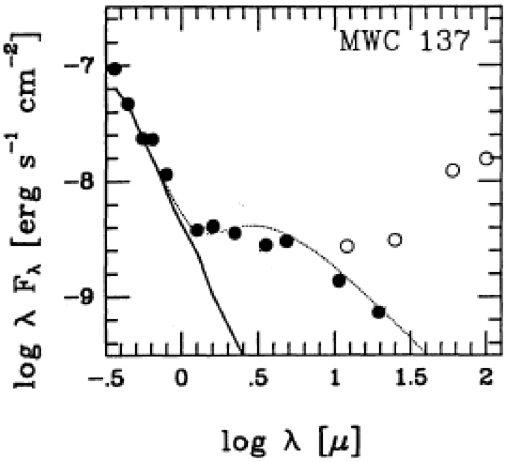

Figure 5.1: The SED of MWC 137, a Group I HBe star. Solid circles are ground based observations and open circles are IRAS observations. The solid line is a photospheric SED for a standard star of the same spectral type, and the dotted line is the 'best fit' model SED consisting of a central star with optically thick, circumstellar accretion disk (Hillenbrand, 1995).

ble 5.1.

5.1.1 Observations

The observational data for several B0e stars were obtained in 2014 and 2015 using the high-resolution spectropolarimeter ESPaDOnS at the CFHT.[1] MWC 137 was one of four B0e stars observed, and its spectrum was obtained in 2014 (HJD 2456972) and 2015 (HJD 2457031). The spectra cover the wavelength range from 3700 to 10500 Å with a spectral resolution of 65000. A detailed log of the observations can be found in Table 5.2.

MWC 137's 2015 spectrum can be seen in Figure 5.2 and a larger version of the spectrum can be seen in Appendix A, Figure A.5. The spectrum contains strong emission in the hydrogen Balmer lines, such as Hα, Hβ, and Hγ.[2] The spectrum also displays a very strong O I λ 8446 emission line. Other identified emission lines include the Ca II IR triplet, several multiplets of Fe II and lines of He I. It is important to note that the He I λ 6678 is typically a photospheric line and, hence, generally seen in absorption as is the case for the four HB2e stars discussed

---

[1] CFHT Program Number- 14BC25, PI- Patel, P.

[2] Hγ was not included in previous studies, however due to its strength, it has been included in this study.

Table 5.1: Stellar parameters for MWC 137

Parameter	Value
Spectral Type	B0e
$T_{\rm eff}$ (K)	31000
Radius ($R_\odot$)	6.0
Mass ($M_\odot$)	18.9
Distance (pc)	1300

All the values for the parameters are taken from Hillenbrand et al. (1992).

Table 5.2: Log of observations for MWC 137 obtained using ESPaDOnS spectropolarimeter at the Canada-France-Hawaii Telescope.

Star	Date (dd/mm/yyyy) Time (UT)	HJD	Total Exposure Time (sec)	Peak SNR	λ (nm)
MWC 137	10/11/2014 9:46:34	2456971.91118	3360	281	839
	8/1/2015 11:47:52	2457030.99629	3360	262	839

previously. However, for MWC 137, this He I line is in emission, both in the 2014 and 2015 spectra as illustrated in Figure 5.3.

The equivalent widths of individual lines for the 2014 and 2015 spectra are given in Table 5.3. The strengths of the emission lines are striking, with the EW of Hα being over 400 Å! This is more than an order of magnitude stronger than the previously studied HB2e stars considered in the previous chapters. Following the hydrogen lines, the O I line λ 8446 is the next strongest emission line in the spectrum, followed by the Ca II IR triplet lines. The spectrum does not display any sign of He II λ 4686, consistent with MWC 137 being of spectral type B and not of spectral type O.

The EW of Hα for MWC 137 has been observed to vary over time from +133 Å to +665 Å (Finkenzeller & Mundt, 1984; Esteban & Fernandez, 1998; Oudmaijer & Drew, 1999; Vink et al., 2002; Heŕnandez et al. , 2004; Baines et al., 2006; Kondratyeva, 2007; Wheelwright et al., 2010), and the shape of the line profile has always been singly-peaked. The variability of Hα

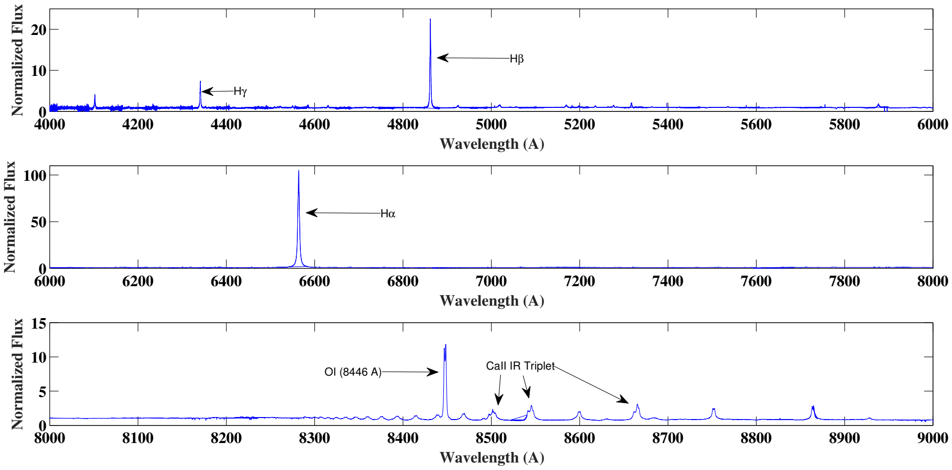

Figure 5.2: The 2015 (HJD-2457031) ESPaDoNS spectrum for MWC 137. The spectrum shows many emission lines, such as Hα, Hβ, Hγ, O I (λ 8446), and Ca II (λ 8498, λ 8542&λ 8662), as indicated. The strength of the emission lines varies over a large scale: note the vertical scale of each subplot.

and the entire spectrum is further shown by the two ESPaDoNS spectra obtain for this work, one in November 2014 and one in January 2015, barely two months apart. Variation is seen in all emission lines except He I. This is illustrated in Figure 5.3. For the analysis of the current study, only the 2015 spectrum will be used.

5.1.2 Reduction of Spectra

The observed ESPaDoNS spectra of MWC 137 were continuum normalized in order to compare the synthetic and observed line profiles. Each un-normalized spectrum was separated into wavelength-specific windows corresponding to the various echelle orders and then continuum normalized using IRAF[3] for individual emission lines of interest. ‘Legendre’ and ‘cubic spline’ functions, in combination with other low-order polynomials, were generally used to normalize the line profiles, and the mix varied from one spectral window to another.

The Ca II IR triplet lines (λ 8498, λ 8542 and λ 8662) are blended with several high-n

---

[3] IRAF is distributed by the National Optical Astronomy Observatories, which are operated by the Association of Universities for Research in Astronomy, Inc., under cooperative agreement with the National Science Foundation.

Table 5.3: Measured Equivalent Widths for MWC 137.

Line (λ Å)	EW (Å)	
	2014	2015
H α (λ 6563)	399.5	454.2
Hβ (λ 4861)	42.7	56.5
H γ (λ 4341)	15.5	19.6
O I (λ 8446)	51.1	51.1
Ca II (λ 8542)	15.8	18.7
Fe II (λ 5169)	1.9	2.8
Fe II (λ 5317)	2.1	2.9
He I (λ 6678)	1.5	1.4

Paschen lines of hydrogen. To de-blend the lines, an average Paschen line had to be subtracted from each of the individual lines of Ca II in order to be able to compare the Ca II lines to the calculated synthetic line profiles. The subtracted Ca II profile was obtained by taking the nearest two, unblended Paschen lines, averaging them, and then subtracting the average from the observed blend. Both the observed and un-blended Ca II lines are illustrated in Figure 5.4. For the rest of this study, only one of the triplet lines, λ 8542, has been modeled.

5.2 Preliminary Results

As discussed in Chapter 2, the BEDISK and BERAY codes were used to calculate synthetic line profiles for a disk around the B0 star for the lines of Hα, Hβ, Hγ, the Ca II λ 8542, Fe II λ 5169 and λ 5317, and He I λ 6678. The combination of disk density parameters used in the BEDISK calculations are noted in Table 5.4. The value of base disk density ranged between 10^{-9} and 10^{-13} g cm^{-3}, and the power law index ranged between 0.0 and 3.0. Four inclinations, 18°, 45°, 60° and 75°, were considered for the BERAY line profile computations. Due to the strengths of most of the emission lines being much larger than those encountered in the HB2e stars of the previous chapters, larger circumstellar disks were considered; disk radii of 25 R$_*$, 50 R$_*$, 100 R$_*$

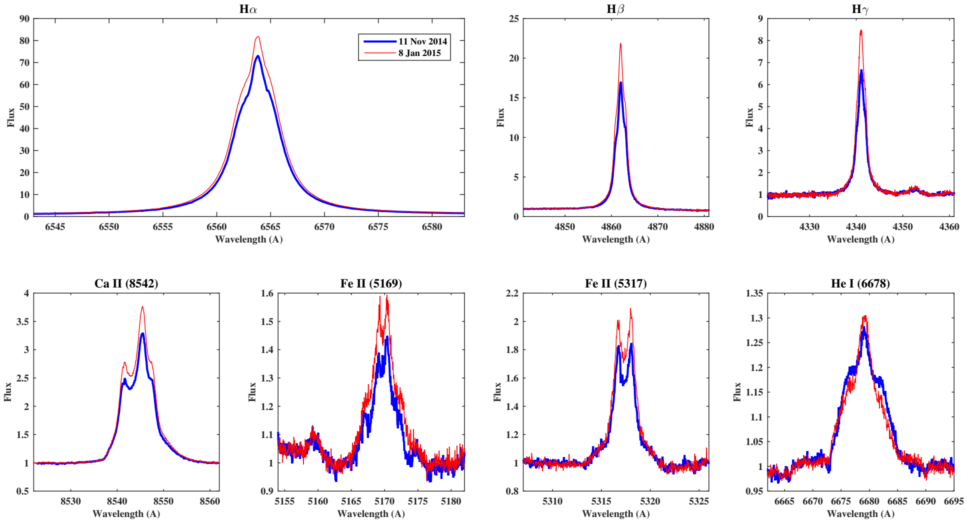

Figure 5.3: The 2014 (HJD 2456972) observations (blue) are over-plotted with 2015 (HJD 2457031) observations (red) for the indicated lines of MWC 137. Both observations were obtained using the ESPaDOnS spectropolarimeter at the Canada-France-Hawaii Telescope. Except for He I (λ 6678), all the lines show small variations with time.

and 200 R$_*$ were explored.[4] Only *thin* and *thin and turbulent* models have been computed for MWC 137.

Using the methods fully described in Section 3.2, each of the observed emission line profiles was compared to the library of synthetic line profiles. A figure-of-merit, $\mathcal{F}$, was calculated using Equation 3.1, with the smallest values defining the best fits. The top 9 synthetic lines with smallest $\mathcal{F}$ for each emission line were visually inspected for the best-fit lines. These top 9 best-fit lines, along with the model parameters illustrated using $\log_{10}\rho_0$ vs n plane for MWC 137, can be found in Appendix B, from Figure B.37 to Figure B.48. The best-fit model chosen from the top 9 models for each individual emission line is illustrated in Figure 5.5 along with the observed line profile; the respective model parameters can be found in Table 5.5.

A 100 R$_*$, thin disk with the base disk density (ρ_0) of $1.0 \times 10^{-13}\,\mathrm{g\,cm^{-3}}$ with the power-law index (n) of 0.5 and an $i = 18^\circ$ inclination angle is the best fit for Hα. As it can be seen in Figure 5.5, the synthetic line profile is lacking not only the strength of the observed line

---

[4] An attempt was made to model larger disks of 300 R$_*$ and 400 R$_*$; however, problems with BEDISK were encountered that could not be immediately solved.

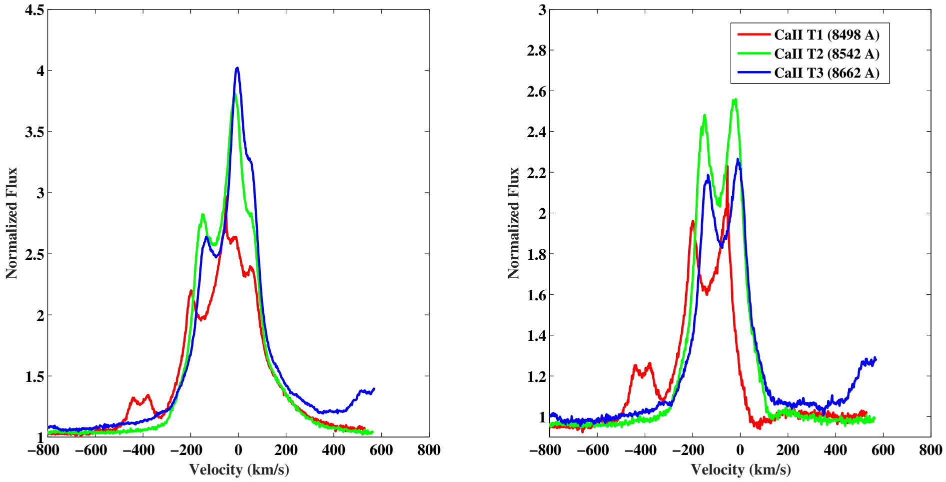

Figure 5.4: *Left*: All Ca II IR triplet lines before the subtraction process. *Right*: The Ca II IR triplet lines after subtraction of the average Paschen line. Note the different vertical scales.

Table 5.4: Range of model parameters considered for disk of MWC 137.

Parameter	Range
Base Disk Density, ρ_0 (g cm^{-3})	10^{-9}...10^{-13}
Power Law Index, n	0.0...3.0
Inclination, i (°)	18...75
Disk Radius, R_{disk} (R_*)	25...200

profile but also its width. The best fit model for Hβ is a 100 R$_*$ thin disk with the base disk density (ρ_0) of 1.0×10^{-12} g cm^{-3} with the power law index (n) of 1.0 seen at an angle of 18°. Like Hα, the synthetic line profile of Hβ also lacks strength and width when compared to the observed line profile. It is possible that our circumstellar disks did not extend to large enough radii to reproduce the strengths of these low-lying Balmer lines, but this would not increase the width of the computed lines. In addition, it is possible that the profiles are contaminated by the corresponding hydrogen recombination lines formed in the surrounding H II region SH-2-266, particular near line centre (or at low projected radial velocity). This is perhaps supported by the fact that the observed hydrogen lines Hα, Hβ and Hγ are all singly-peaked whereas the metal lines of Fe II and Ca II are doubly-peaked. Indeed some of the failure to match the widths of

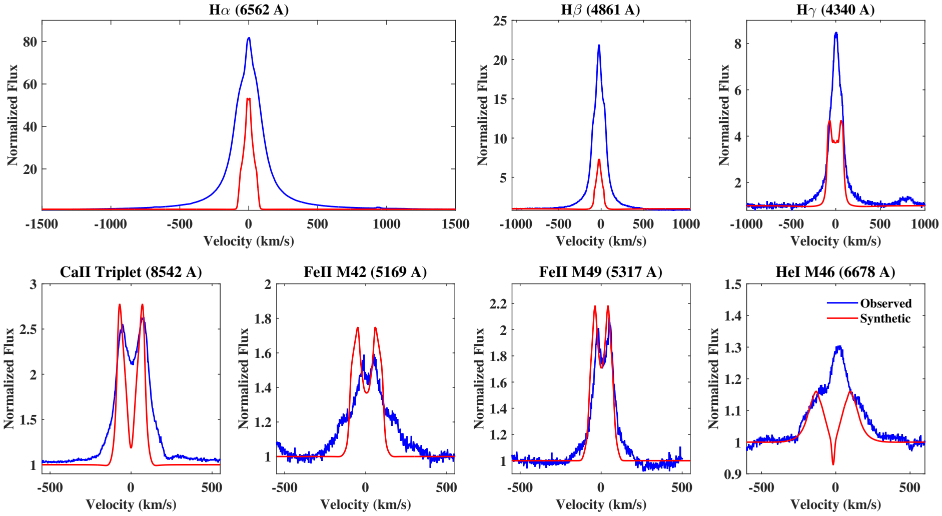

Figure 5.5: The best fit synthetic line profile (red) for each observed emission line (blue) for the indicated transition at the top of each panel. The fit parameters for each model can be found in Table 5.5.

the Balmer lines Hα and Hβ may have its origin in the selection of a low inclination, $i = 18°$, models in order to get singly-peaked lines.

For Hγ, however, a 200 R_*, thin disk with power-law index (n) of 1.0 and base disk density (ρ_0) of $1.0 \times 10^{-12}\,\mathrm{g\,cm^{-3}}$ seen at $i = 75°$ is the best fit found for the observed line profile, and the fit is better than for the two lower series members. Hγ is relatively well reproduced when it comes to the width of line; however, the synthetic model does fail to reproduce the strength. The fit of Hγ with an $i = 75°$ model also suggests that Hα and Hβ may be strongly contaminated near line centre by circumstellar emission away from the star and from the H II region.

For the Ca II IR triplet line $\lambda\,8542$, the best fit model is a thin disk with radius of 100 R_*, power-law index (n) of 2.0, base disk density (ρ_0) of $1.0 \times 10^{-9}\,\mathrm{g\,cm^{-3}}$ seen at an inclination angle of 75°. As illustrated in Figure 5.5, the synthetic line profile reproduces the strength and width of observed profile relatively well. However, the centre of the synthetic line profile shows a deeper absorption trough than the observed line profile. This is due to the disk being seen at a rather high inclination, i.e. closer to an edge-on view, for the synthetic line profile.

Table 5.5: Best-fit model parameters for individual emission lines for MWC 137.

Emission Line	Disk Density ρ_0 (g cm^{-3})	Power Law Index n	Inclination i (°)	Disk Radius R_{disk} (R_*)	Model Type
Hα (λ 6562)	1.0×10^{-13}	0.5	18	100	Thin
Hβ (λ 4861)	1.0×10^{-12}	1.0	18	100	Thin
Hγ (λ 4341)	1.0×10^{-12}	1.0	75	200	Thin
Ca II IR-triplet (λ 8542)	1.0×10^{-9}	2.0	75	100	Thin
Fe II (λ 5169)	1.0×10^{-11}	1.0	75	100	Thin & Turbulent
Fe II (λ 5317)	1.0×10^{-11}	1.0	45	100	Thin & Turbulent
He I (λ 6678)	1.0×10^{-10}	2.0	75	200	Thin

For the Fe II λ 5169, a thin and turbulent disk model of 100 R$_*$ with power-law index (n) of 1.0 and base disk density (ρ_0) of 1.0×10^{-11} g cm^{-3}, and a $i = 75°$ inclination angle gives the best fit. The observed profile for this line has an unusually wide base and narrow, double-peaked profile. The best synthetic line profile is stronger but lacks the broad wings when compared to the observed line profile. On the other hand, Fe II λ 5317 shows a double-peaked profile on a narrower base. The best synthetic model for this emission line is a thin and turbulent disk of 100 R$_*$ with power-law index (n) of 1.0 and base disk density (ρ_0) of 1.0×10^{-11} g cm^{-3} and inclination angle of 45°. The synthetic model fits well in terms of strength as well as width and overall shape when compared to the observed line profile.

For the B2e stars of previous chapters, the He I λ 6678 is generally reasonably well fit with a photospheric line profile for the central star. However for MWC 137, and as illustrated in Figure 5.5, its He I profile is in emission; thus, there is a contribution from the disk to this line profile. For this reason, He I profiles including the contribution of a disk were computed and included in the library. The best match was found to be a 200 R$_*$ thin disk with base disk density (ρ_0) of 1.0×10^{-10} g cm^{-3}, power-law index (n) of 2.0 and seen at 75° inclination angle. It may be significant to note that the shape of He I λ 6678 line is similar to that of Fe II λ 5169;

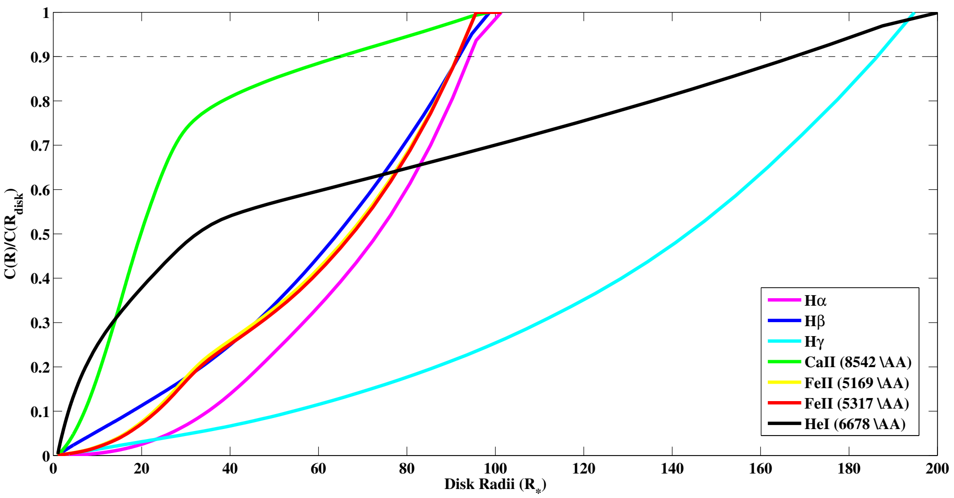

Figure 5.6: The cumulative line emission (Equation 3.2) as a function of distance from the star for each individual line using the best-fit disk density model for MWC 137. The model parameters that produced each individual line can be found in Table 5.5. The black dashed line represents a cumulative emission fraction of 0.9.

the He I emission line has very wide base with a narrow single peaked center.

In order to understand the flux contribution and formation of each line profile as a function of the disk radius, the cumulative flux as a function of radius was computed using the Equation 3.2 for the individual best-fit line models listed in Table 5.5. The results are shown in Figure 5.6. It is important to recall that because this plot represents the best-fit models for individual lines, the underlying disk density model and disk radius can vary for the features. Ca II (λ 8542) forms close to the star, with most of the emission coming from within 65 R$_*$, with the largest contribution to the flux from within 30 R$_*$. Hβ, the two Fe II lines λ 5169 and λ 5317 and the Hα produce 90% of their emission within 95 R$_*$ of the star. Finally, Hγ requires an extended region, with most emission being produced within 180 R$_*$ of the disk. Hγ also has a very gradual increase in emission as the radius increases. He I λ 6678 requires an extended disk of up to $\sim$ 200 R_*, but with most of the emission formed within $\sim$ 35 R_*. It should be kept in mind, however, that the Hα and Hβ lines were not matched at all with the models considered.

5.3 Discussion

From the results illustrated in Figure 5.3, larger disks with different disk density parameters are required to fit the individual line profiles of the Hγ and the lines of He I, Ca II and Fe II, when compared to the disks for B2e stars. The lower order Balmer lines Hα and Hβ were not fit at all with any of the models considered. In the previous studies of Herbig B2e stars, the best fits of individual models were used in order to narrow down the regions the metal and Balmer lines occupy in the disk density parameter space, namely a plot of base disk density ($\log_{10}\rho$) vs power law index (n), in search for a global model. The very poor fits in the case of MWC 137, and the large differences between the models found for individual lines, imply that a search for a global best-fit model is not warranted, and that more complex disk density models need to be considered in order to the fit individual line profile before a global fit for this star is attempted. This might also include much larger disks and/or constraints on nebular emission in the Balmer lines from the surrounding H II region. Note also that only a very crude grid of models has been computed for these lines so additional models with fine-tuned parameters may be able to fill in minor changes for the synthetic line profile such as the width of the Fe II (λ 5169) or central absorption feature of Ca II IR triplet (λ 8542).

The metal lines in the previous studies of HB2e stars have been fit with synthetic models with disk radii of typically 25 or 50 R_*, however for MWC 137, all the metal lines require at least a 100 R_* disk. The synthetic Balmer lines do not reproduce the observed lines at all and large disks may be required in order to have enough material in an outer portion of the disk to give significant emission near the line centre for these lines. Larger disks of size 200 R_* and 300 R_* were attempted for the Balmer lines; however, the very low densities so far out caused computational difficulties with the code that have yet to be rectified. Like HB2e stars, the metal lines for MWC 137 require denser disks compared to the Balmer lines, giving another indication that larger disks might be the solution to fit the Balmer lines. In addition, we note that the strengths of Hα and Hβ were maximized in disks of very low ρ_0, $\sim 10^{-12}$ or 10^{-13} g cm^3, compared to the metal lines, with a much lower power-law index (i.e. gradual density drop-off) in large disks. Hence a compound density structure of an inner, dense disk surrounded by a much larger, low density, nearly flat density drop-off disk may be a useful direction to explore for a global model.

The unusual structure of the Fe II λ 5169 and He I λ 6678, not seen in any of the other line profile, requires some material closer to the star along with large amounts away from the star. None of the computed synthetic lines show this structure; the models would either fit the wide base (as in the case of He I) or the narrow peak (as in the case of Fe II). This suggests that a disk with a change in the power law at some intermediate radius might be required in order to model these lines which have two components, as noted above in connection with the Balmer lines.

In addition to the considered emission lines of hydrogen and metals lines, MWC 137 hosts more emission lines which could be utilized to expand the number of emission lines in the database. One of the important and very strong emission lines, which can be seen in Figure 5.2, is that of O I λ 8446. A complication with this lines, and the reason it was not selected to model in this work, is that fluorescent excitation via pumping by hydrogen Lyβ may be an important excitation mechanism for this transition. Given the very poor match obtained for the hydrogen spectrum, it is unclear if the Lyβ source function would be computed accurately enough to represent this pumping effect.

5.4 Conclusions

The modelling of Balmer and metal emission lines of the inner gaseous regions of the Herbig B0e star, MWC 137, has led to a few preliminary key findings:

- No reasonable matches were found for the emission line profiles, with the exception of the Ca II IR triplet (λ 8542) and Fe II (λ 5317), using the small set of models computed for the disk of MWC 137.
- The metal lines require larger disk models, as opposed to denser disk models as the case

for HB2e stars, to reproduce the observed emission lines.

- The observed emission lines of MWC 137 are very strong, when compared to the HB2e stars studied previously, which led to the larger disk models to qualitatively fit the observed spectrum. Larger disk models, especially for the Balmer lines, are probably required to reproduce individual line fits.

Bibliography

Alonso-Albi, T., Fuente, A., Bachiller, R., Neri, R., Planesas, P., Testi, L., Berné, O., Joblin, C. 2009, A&A, 497, 117A.

Baines, D., Oudmaijer, R. D., Porter, J. M. & Pozzo, M. 2006, MNRAS, 367, 737.

Esteban, C. & Fernandez, M. 1998, MNRAS, 298, 185E.

Frew, David J., Bojičić, Ivan S., & Parker, Q. A. 2013, MNRAS, 431, 2F.

Finkenzeller, U. & Mundt, R. 1984, A&AS, 55, 109.

Fuente, A., Rodríguez-Franco, A., Testi, L., Natta, A., Bachiller, R. & Neri, R. 2003, ApJ, 598L, 39F.

Hernández, J., Calvet, N., Briceño, C., Hartmann, L. & Berlind, P. 2004, AJ, 127, 1682H.

Hillenbrand, L. A., Strom, S. E., Vrba, F. J. & Keene, J. 1992, ApJ, 397, 613.

Hillenbrand, L. A. 1995, Ph.D. thesis, Univ. Massachusetts

Kohoutek, L. 2001, A&A, 378, 843.

Kondratyeva, L. N. 2007, OAP, 20, 86K.

Lamers, H. J. G. L. M., Zickgraf, F., deWinter, D., Houziaux, L. & Zorec, J. 1998, A&A, 340, 117.

Mehner, A., de Wit, W. J., Groh, J. H., Oudmaijer, R. D., Baade, D., Rivinius, T., Selman, F., Boffin, H. M. J. & Martayan, C. 2016, A&A, 585A, 81M.

Muratore, M. F., Kraus, M., Oksala, M. E., Arias, M. L., Cidale, L., Borges Fernandes, M. & Liermann, A. 2015, AJ, 149, 13M.

Oudmaijer, R. D. & Drew, J. E. 1999, MNRAS, 305, 166.

Testi, L., Palla, F., Prusti, T., Natta, A. & Maltagliati, S. 1997, A&A, 320, 159.

Thé P. S., DeWinter D. & Perez M. R. 1994, A&AS, 104, 31539.

Verhoeff, A. P., Waters, L. B. F. M., van den Ancker, M. E., Min, M., Stap, F. A., Pantin, E., van Boekel, R., Acke, B., Tielens, A. G. G. M. & de Koter, A. 2012, A&A, 538A, 101V.

Vink, J. S., Drew, J. E., Harries, T. J. & Oudamijer, R. D. 2002, MNRAS, 337, 356.

Wheelwright, H. E, Oudmaijer, R. D. & Goodwin, S. P. 2010, MNRAS, 401, 1199.

Chapter 6

Conclusions & Future Work

6.1 Introduction

HAeBe stars are intermediate mass A- or B-type pre-main sequence stars with circumstellar disks of gas and dust. The dust and gas are inherited by the star during its formation phase and this circumstellar material settles into a disk as the star is forming. These stars show emission lines, particularly the hydrogen Balmer lines, in their optical and NIR spectra, and a strong IR-excess in their SED. These characteristics are indicative of circumstellar material (Waters & Waelkens, 1998).

Herbig (1960) was first to postulate that there exist higher mass analogs of T Tauri stars. He characterized 26 A- and B-type stars which showed the above mentioned peculiarities as possible pre-main sequence stars. After that, large surveys, such as those of Finkenzeller & Mundt (1984); Thé et al. (1994), were conducted in order to increase the dataset of HAeBe stars. These young stars are also thought to be the predecessors of Vega-type stars, stars with debris disks, making them ideal objects with which to study disks around stars to understand the formation of planetary systems (Thé et al., 1996; Pérez & Grady, 1997; Grady et al., 1997). Being bright, HBe stars provide a great testing bed for theories pertaining to stellar evolution and protoplanetary disks.

The structure of these disks has long been a matter of debate. The circumstellar dust and the gas, found in the extended region of the disk, is of a particular interest due to the region being the site of planet formation. Near the stellar surface, the temperatures are very high, evaporating the dust and creating a dust free zone. In the dust free zone, closer to the star, atomic gas is expected and as temperatures cool outward, molecular gas is expected. For the region closer to the star, however, information is scarce when compared to what is known about the dusty disk.

The understanding of the disk closer to the star not only improves our overall understanding of protoplanetary disks but also of the influence of the disk on the star's formation. Intermediate mass stars such as the HAeBe stars, bridge our understanding of low mass and high mass star formation processes. The inability to optically observe the formation of high mass stars, makes studying HAeBe star formation even more important (Zinnecker & Yorke, 2007).

Due to the above stated reasons, early-type HBe stars - four HB2e and one HB0e star - were selected in order to investigate the inner gaseous regions of their disks. Using optical and NIR emission lines, which are thought to form in regions close to the star, we studied the atomic gaseous region closer to the star, which experiences intense stellar radiation, in order to understand the disk properties such as the structure and kinematics of the disk. BEDISK and BERAY codes, which have been well tested for classical Be stars, provided an ideal set of initial models with which to test the disk physics by comparing the predictions of the computed models against the observed optical and NIR emission lines.

6.2 Summary

In Chapter 2 of this thesis, the circumstellar disk codes, BEDISK and BERAY, used for reproducing the observables for the star were summarized. They are non-LTE radiative transfer disk codes. The codes assume that the central star is the sole source of radiation in the system and that the disk is in radiative equilibrium and Keplerian motion. A user-defined density function is used to calculate the thermal structure of the disk in BEDISK. This thermal and density structure, along with the atomic level populations, obtained by solving equations of statistical equilibrium, are used by BERAY to calculate the emission line profiles and SEDs by solving the equation of radiative transfer. These codes have been successful in modeling the general structure of the gaseous decretion disk around classical Be stars, thus, making them an ideal starting point for modeling gaseous disks around HBe stars.

In Chapter 3, gaseous disk around one of the four HB2e stars, BD+65 1637, was investigated. Large libraries of synthetic models were generated for several emission line profiles of the Balmer series, such as Hα, Hβ, and of metal lines, such as Ca II IR triplet (λ 8542) and Fe II (λ 5169 and λ 5317). The synthetic line profiles were then compared to the high resolution observations of BD+65 1637 in order to constrain the physical properties of the disk. This was the first-ever attempt to understand the geometry, density structure and kinematics of the disk using radiative transfer codes such as those of BEDISK and BERAY by comparing synthetic line profiles of hydrogen, helium, iron and calcium with the observed line profiles.

Reasonable matches were found for all line profiles individually using the stellar radiation as the sole source of energy. However, no disk density model based on a single power-law for the equatorial density was able to simultaneously fit all of the observed emission lines. Amongst the emission lines, the metal lines, especially the Ca II IR triplet, required higher disk densities than the Balmer lines. Excluding the Ca II lines, the model in which the equatorial disk density falls as $10^{-10}\,(R_*/R)^3$ g cm^{-3} seen at an inclination of 45° for a 50 R_* disk provided a reasonable match to the overall line shapes and strengths of all the emission lines. The implied mass of the gaseous disk was estimated to be $5.7 \times 10^{-8}\,M_*$. The Ca II IR triplet (λ 8542) line required a shallower drop off as $10^{-10}\,(R_*/R)^2$ g cm^{-3} to match their strength and the mass of this disk was estimated to be $2.3 \times 10^{-9}\,M_*$. More complex disk density distribution models are likely required to refine the match to the BD+65 1637 spectrum.

In Chapter 4, the inner gaseous disk around three other HB2e stars, HD 76534, HD 114981 & HD216629 were studied. As these stars have similar spectral type as that of BD+65 1637, the same set of libraries of synthetic emission line profiles created for BD+65 1637, and similar methods as those discussed in Chapter 3, were used to analyze and compare the observed emission line profiles for each of these three stars to the synthetic profiles.

For the three stars, good matches were found for all emission line profiles individually. However, like BD+65 1637, no single disk density model based on a power law was able to reproduce all the observed emission lines simultaneously. Among the single power-law models considered, the model with a gas density varying as $\sim 10^{-10}\,(R_*/R)^3\,\mathrm{g\,cm^{-3}}$ in the equatorial plane, seen at a 45° inclination and assuming a disk extent of $25\,\mathrm{R}_*$, best represented all the spectral lines simultaneously of HD 76534, HD 114981 and HD 216629. This model implies a total mass of $\sim 1.2 \times 10^{-9}\,M_*$ for the inner gaseous disk. Similar to BD+65 1637, more complex models are likely required to fully reproduce the disk emission for these stars.

The He I line profile of HD 76534 was noticed to have a wide base and a sharp narrow component in the core. The modeling of this line suggests that it is a composite with a secondary component of approximately the same spectral type which contributes to the sharp, narrow absorption in the He I line profile.

In this chapter, the four HB2e stars studied are compared to gain an understanding of the overall structure of the disks found in HBe stars of this effective temperature. While BD+65 1637 has strong emission line profiles, hence possessing a larger disk, all the other three stars have very similar line profiles, especially in the Fe II line profiles, and they also followed the same density model.

In Chapter 5, the inner gaseous disk of a HB0e star, MWC 137 was investigated. By adding a HB0e star to the study, the similarities and differences of the structure of the disk as a function of effective temperature can be studied, allowing us to investigate and understand the influence of temperature on the disk structure. Using similar methods to those used in the previous studies, a small set of synthetic emission line profiles were generated specifically for B0 spectral type central star.

The MWC 137 spectrum is dominated by strong emission lines, especially that of the

Balmer series. The Balmer emission line profiles of MWC 137 are stronger and wider than those of any of the HB2e stars considered in the study. The metal lines, on the other hand, are not stronger but wider than those of HB2e stars. The preliminary results provided no reasonable matches for emission line profile of hydrogen and one of the Fe II lines, even as models with extended disk size of $200\,R_*$ were calculated. The metal lines, of Ca II and Fe II, were reproduced well by the synthetic models and required larger disk models, when compared to the HB2e stars. Thus, disks for MWC 137 requires larger disk models to reproduce the observed emission lines. It is possible that the observed hydrogen emission lines have significant contributions from the recombination emission of the surrounding H II region.

6.3 Future Work

Important progress has been made in understanding the physical properties of the inner gaseous disk around HBe stars with this first attempt by using high resolution spectra and non-LTE circumstellar disk models. Prior to this project, there was little or no information on this subject. However, there are still various avenues that need to be explored to further our understanding of the gaseous region and its implications on not only the formation of planets, but also on formation of the star. The overall results of individual line profiles from the study of these HBe stars have successfully shown that photoionizing radiation alone can reproduce the emission line profiles seen in these stars. This points to the possibility of classical disk accretion amongst early-type HBe stars. To further this understanding, it is important to understand the similarities and differences in the disks around early and late-type HBe stars.

More complex models with radial density variations are likely required to fully describe the disks of all HB2e stars. This modification can easily be achieved in the BEDISK and BERAY codes by setting different power law indices in different radial zones and should be the logical next step. Currently in the models, the disk extends all the way to the stellar surface; an attempt can therefore be made to model a disk that does not touch the surface of the star. This would be the case if the accretion is sporadic. In addition to the previously modeled emission lines, one of the other strong emission line profiles that has been noticed in the HBe stars is O I (λ 8446). This line profile can be added to the already existing set of line profiles. It is important to note that this line profile, like that of the Ca II IR triplet, is blended with the Paschen lines and should be corrected before being analyzed.

For the HB0e star, the preliminary results suggest that larger disk models along with finer grid models will be required in order to fit the line profiles. In addition, *thick* and *thick and turbulent* disk models should be included to encompass some of the obvious possibilities of disk models. The issue of calculating observables for much larger disks, with low densities at larger distances, needs to be addressed in order to account for the strong line center emission. The observing proposal that obtained the spectra of MWC137 also provided the spectra of three more HB0e stars, namely MWC 1080, MWC 166 and LkHα 101. As was the case for HB2e stars, having more than one star will provide a better overview of various possibilities of the disk as well as similarities and differences amongst them. Preliminary inspection of their spectra shows that the shape and strength of the emission lines of two of three HB0e stars are similar to that of MWC 137. This suggests similar larger disk models will be required for these stars and they should be analyzed along with that of MWC 137.

Once the modeling of the disks around HB0e stars has been attempted, a study of both models of the spectral type should be carried out. Studying these early type HBe stars and understanding the differences between the disks around these two spectral types will allow us to gain a more general understanding of the structure and the extent of the disk surrounding them.

Bibliography

Finkenzeller, U. & Mundt, R. 1984, A&AS, 55, 109.

Grady, C. A., Sitko, M. L., Bjorkman, K. S., Pérez, M. R., Lynch, D. K., Russell, R. W., Hanner, M. S. 1997, ApJ, 483, 449G.

Herbig, G. H. 1960, ApJS, 4, 337H.

Pérez, M. R. & Grady, C. A. 1997, SSR, 82, 407.

Thé P. S., DeWinter D., Perez M. R. 1994, A&AS, 104, 31539.

Thé, P. S., Perez, M. R., Voshchinnikov, N. V. & van den Ancker, M. E. 1996, A&A, 314, 233T.

Waters, L. B. F. M. & Waelkens, C. 1998, ARAA, 36, 233.

Zinnecker, H. & Yorke, H. W. 2007, ARAA, 45, 481.

Appendix A

High Resolution Observed Spectra

This Appendix gives larger, landscape figures for all of the CFHT ESPaDOnS spectra used in this thesis. The emission lines analyzed are labelled in each figure.

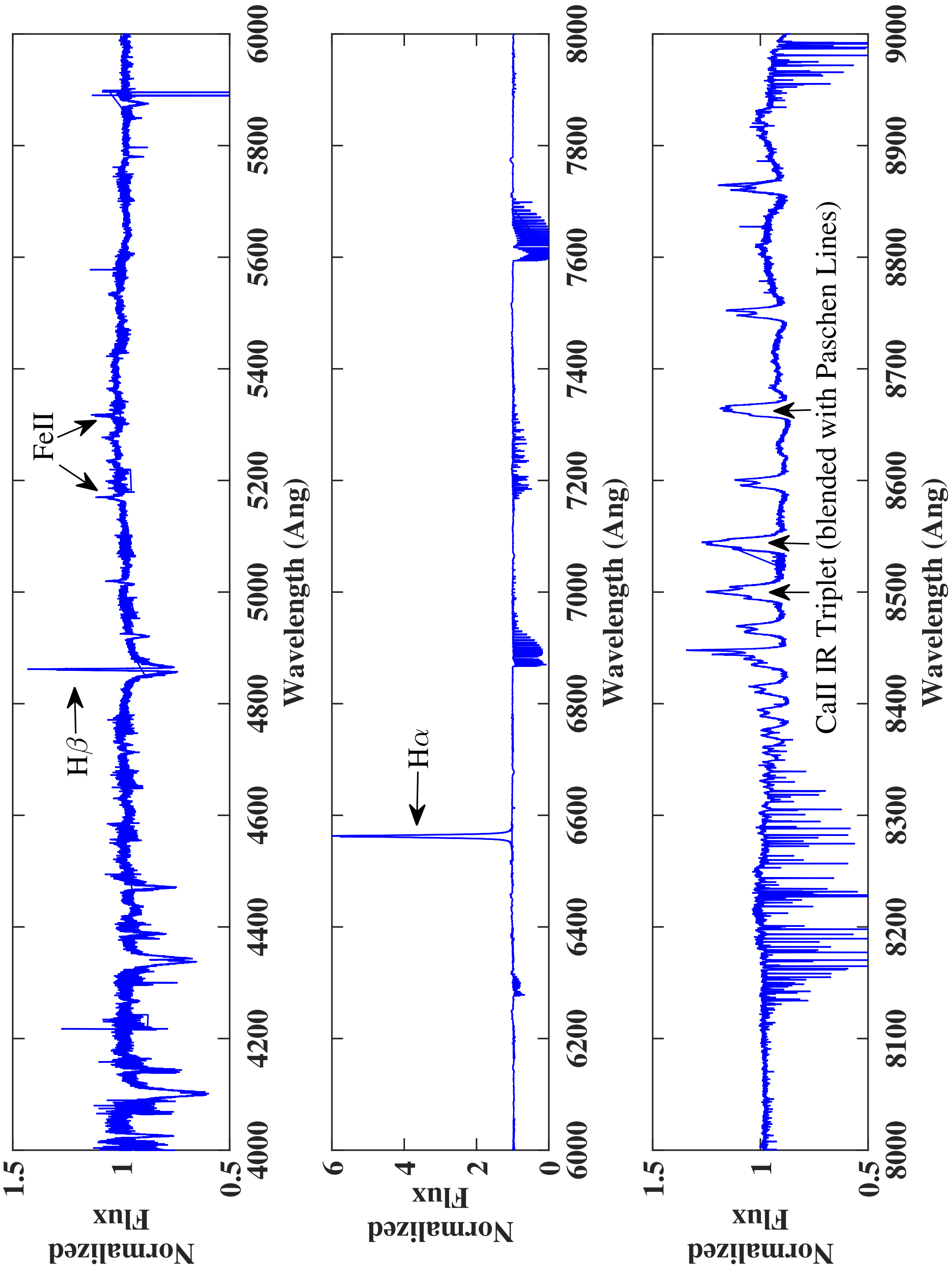

Figure A.1: High resolution 2006 CHFT ESPaDoNS spectrum of BD+65 1637.

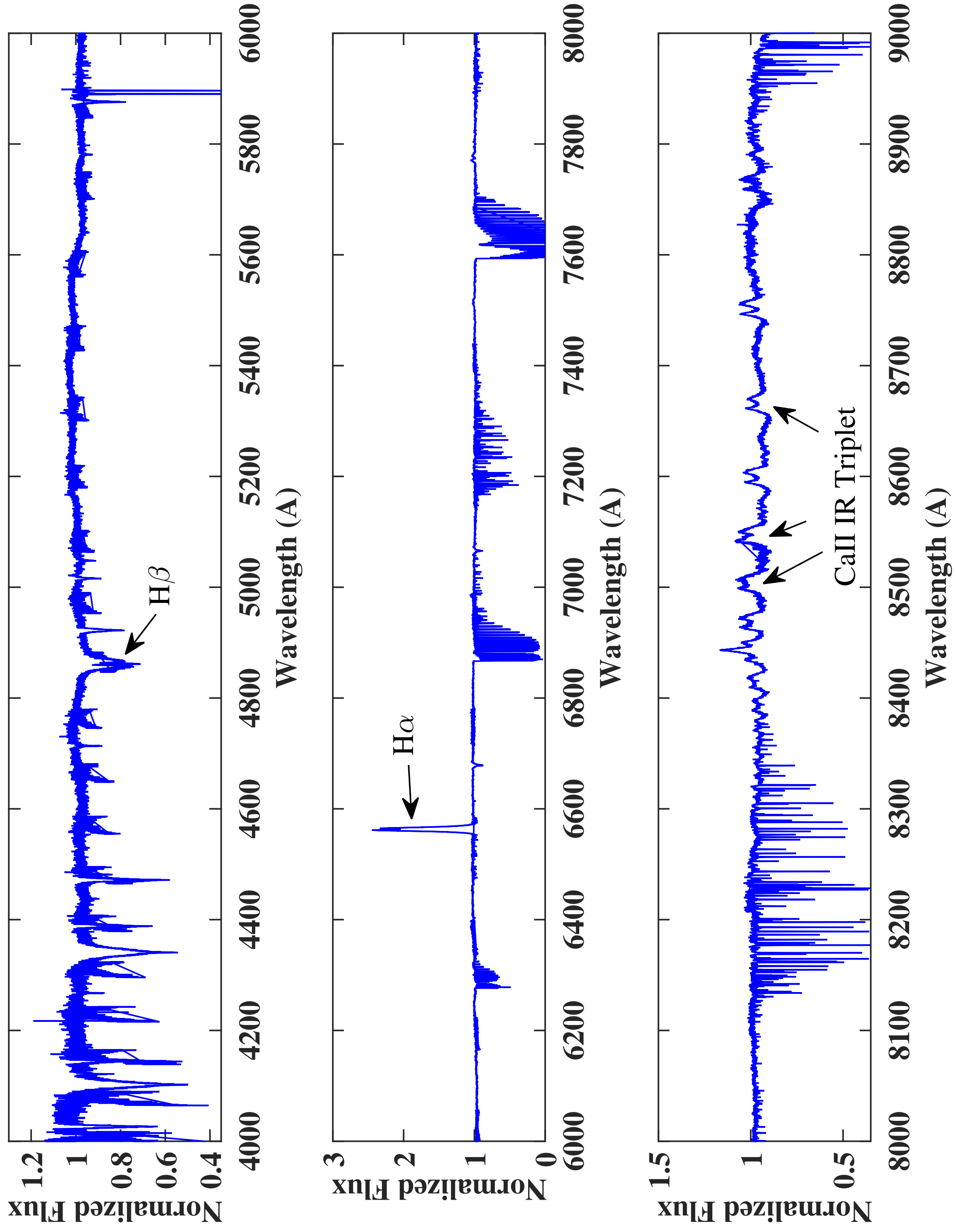

Figure A.2: High resolution 2006 CHFT ESPaDoNS spectrum of HD 76534.

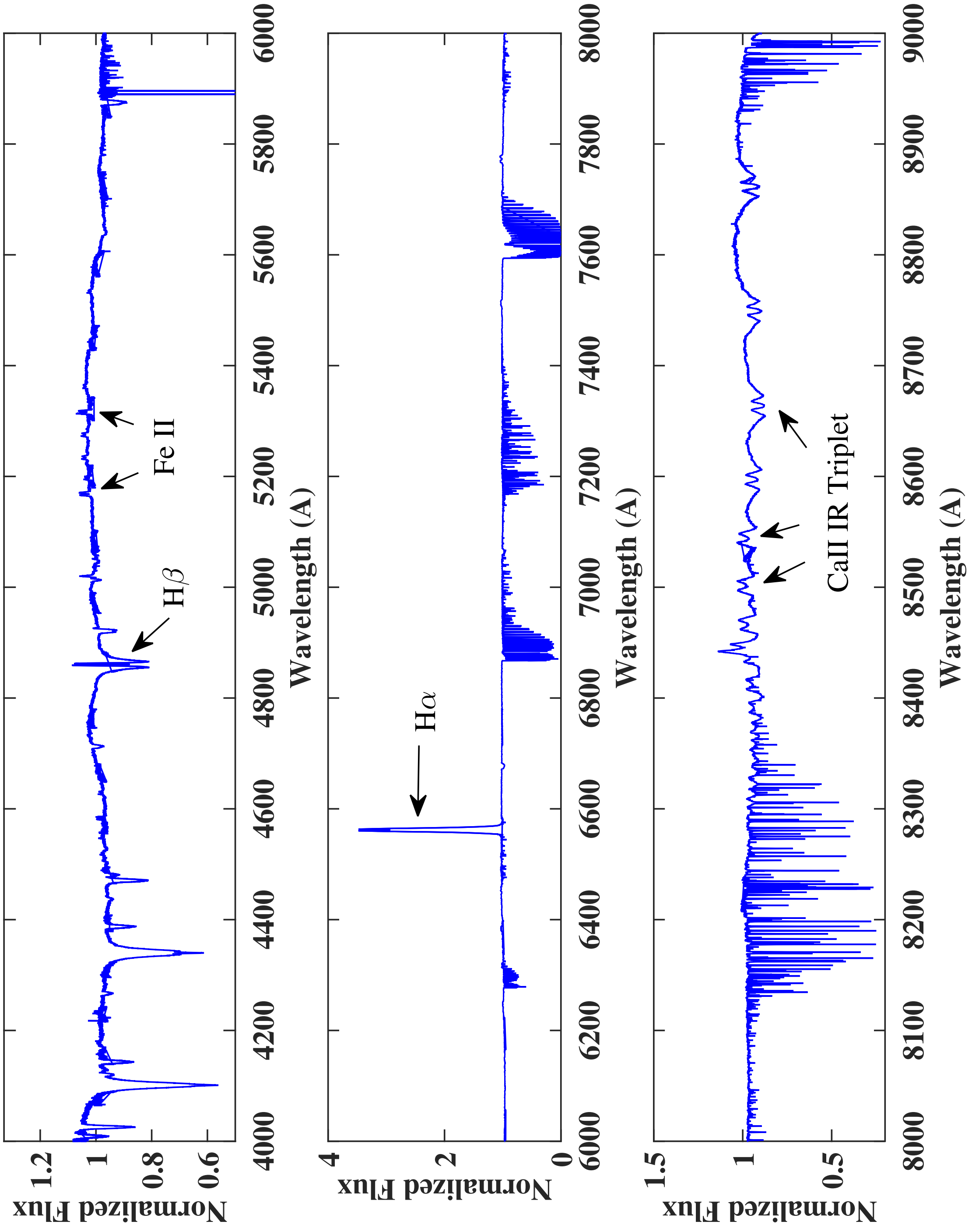

Figure A.3: High resolution 2006 CHFT ESPaDoNS spectrum of HD 114981.

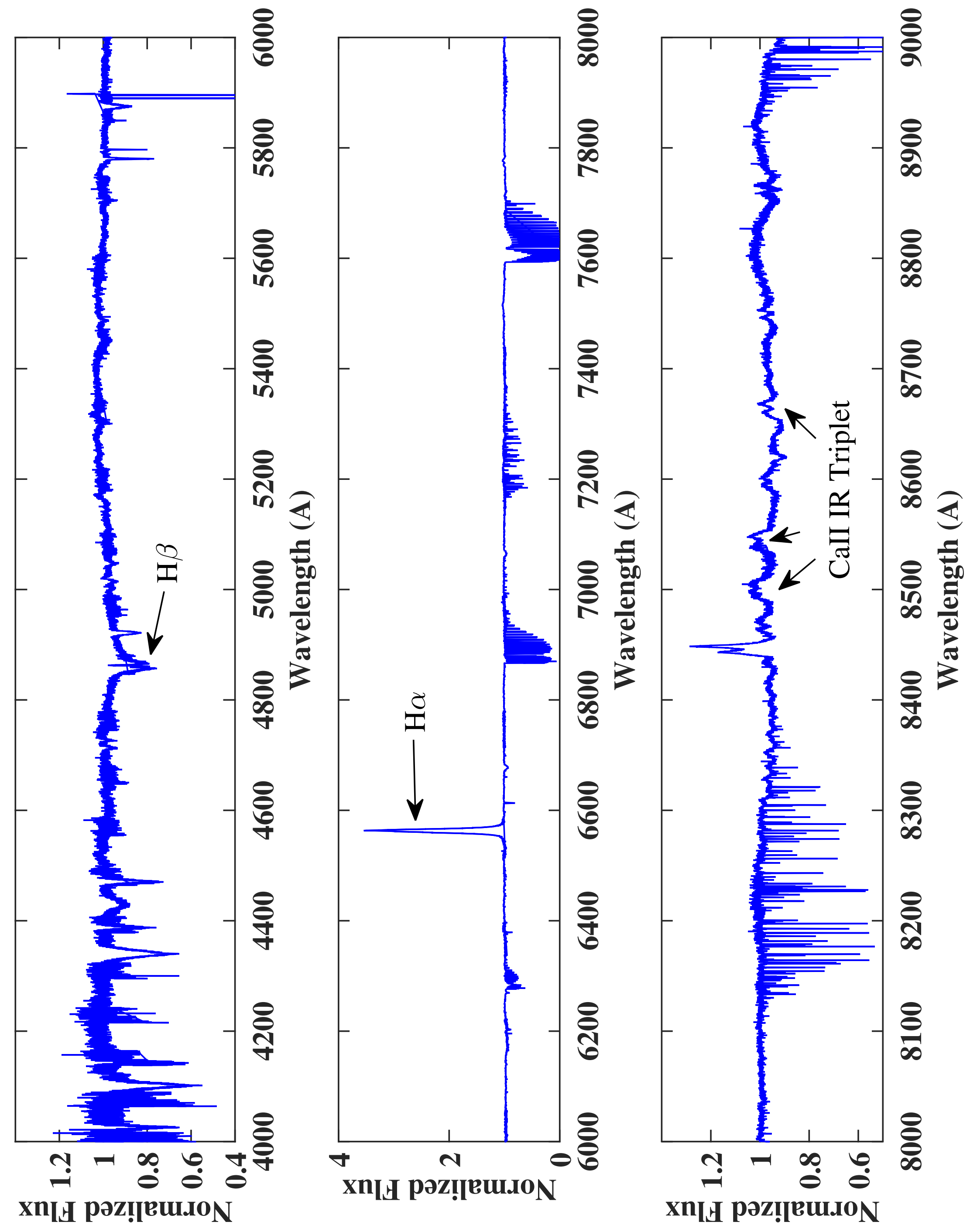

Figure A.4: High resolution 2006 CHFT ESPaDoNS spectrum of HD 216629.

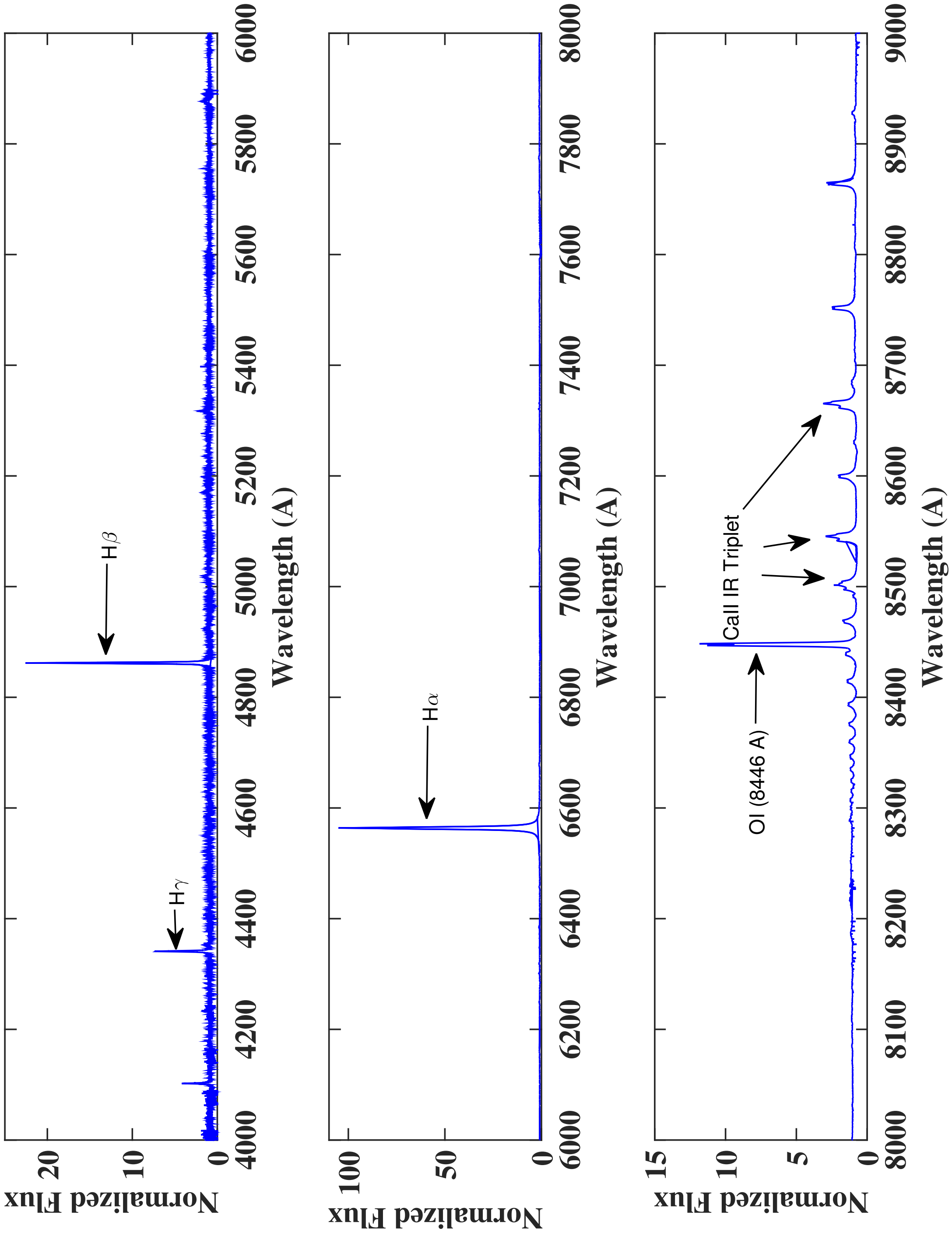

Figure A.5: High resolution 2015 CHFT ESPaDoNS spectrum of MWC 137.

Appendix B

Fits to Individual Lines Profiles

This Appendix illustrates the top nine individual line fits to all of the emission lines for all stars. Also given for each fit is the location of the models in the $(\log\rho_0, n)$ plane using the model number seen in the each panel of individual line fits as well as $(\log\rho_0, n)$ plot. These are the main parameters in the assumed single power-law density model. The viewing inclination and disk size for each fit can be found in the side panel of the latter plots. The title for both the individual line fits as well as $(\log\rho_0, n)$ plot represents the method used in the calculations of the $\mathcal{F}$ value, in this cases 2 represents the absolute percent difference test.

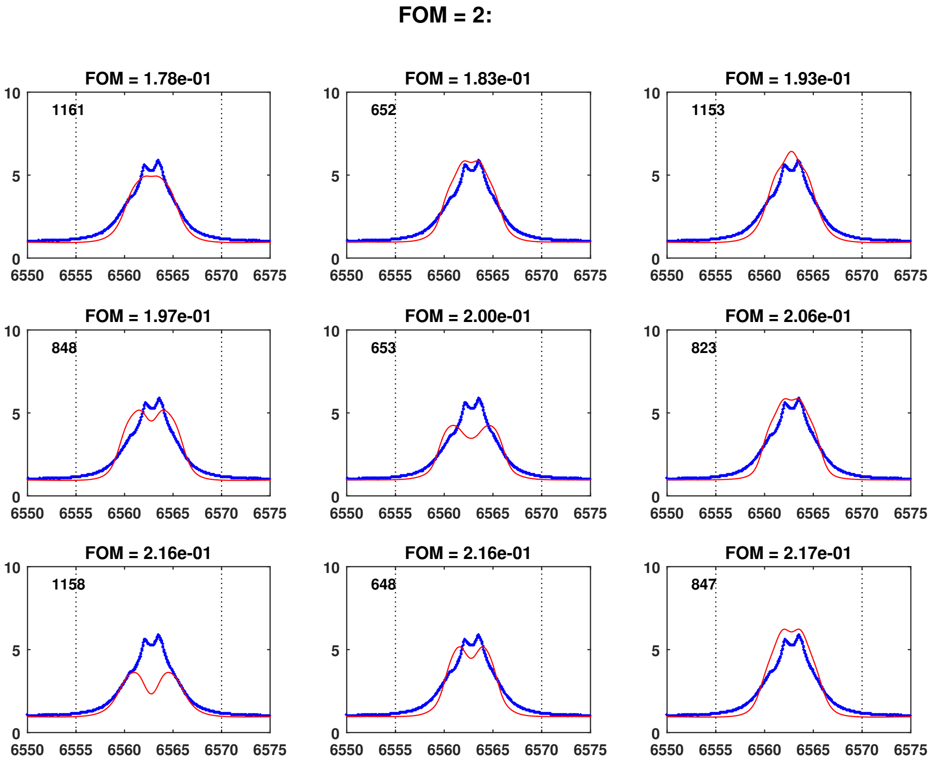

Figure B.1: Hα profiles for BD+65 1637: The top 9 best synthetic (red) line profiles, result of Equation 3.1, that best match the observed (blue) emission line. The FOM (figure-of-merit) value above each panel of best fit represents the $\mathcal{F}$ value calculated using equation 3.1.The top left panel represents the best-fit line profile.

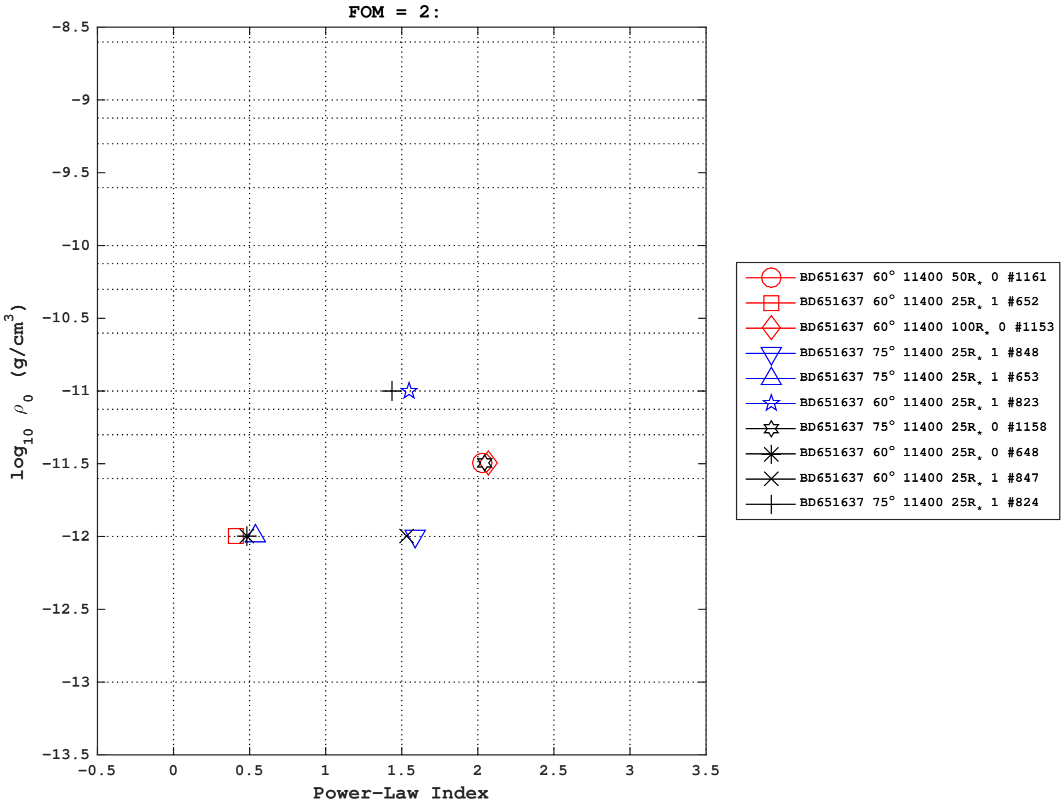

Figure B.2: Hα profiles for BD+65 1637: The top 9 best-fit models corresponding to the line fittings, seen in Figure B.1, in the $(n, log_{10}\,\rho)$ plane. The additional parameters of each model are noted in the legend in the following order: model name, inclination (i), disk temperature (T_{HE}), disk radius (R_*), turbulence (α) and model number (which corresponds to the individual line fits in the previous plot).

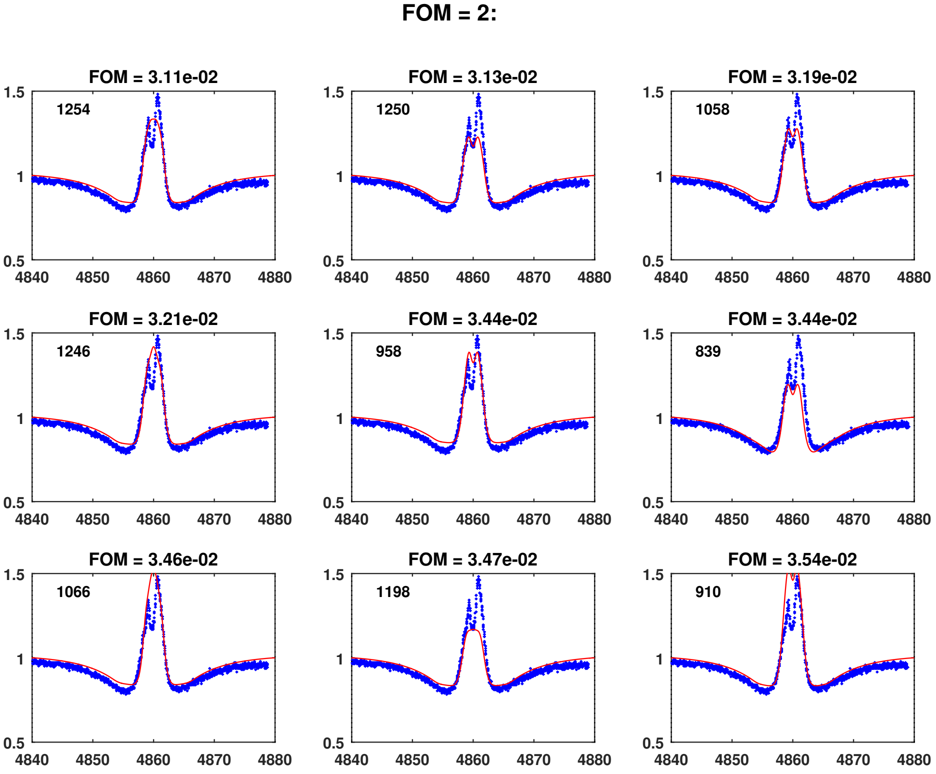

Figure B.3: Hβ profiles for BD+65 1637: The top 9 best synthetic (red) line profiles, result of Equation 3.1, that best match the observed (blue) emission line. The FOM (figure-of-merit) value above each panel of best fit represents the $\mathcal{F}$ value calculated using equation 3.1. The top left panel represents the best-fit line profile.

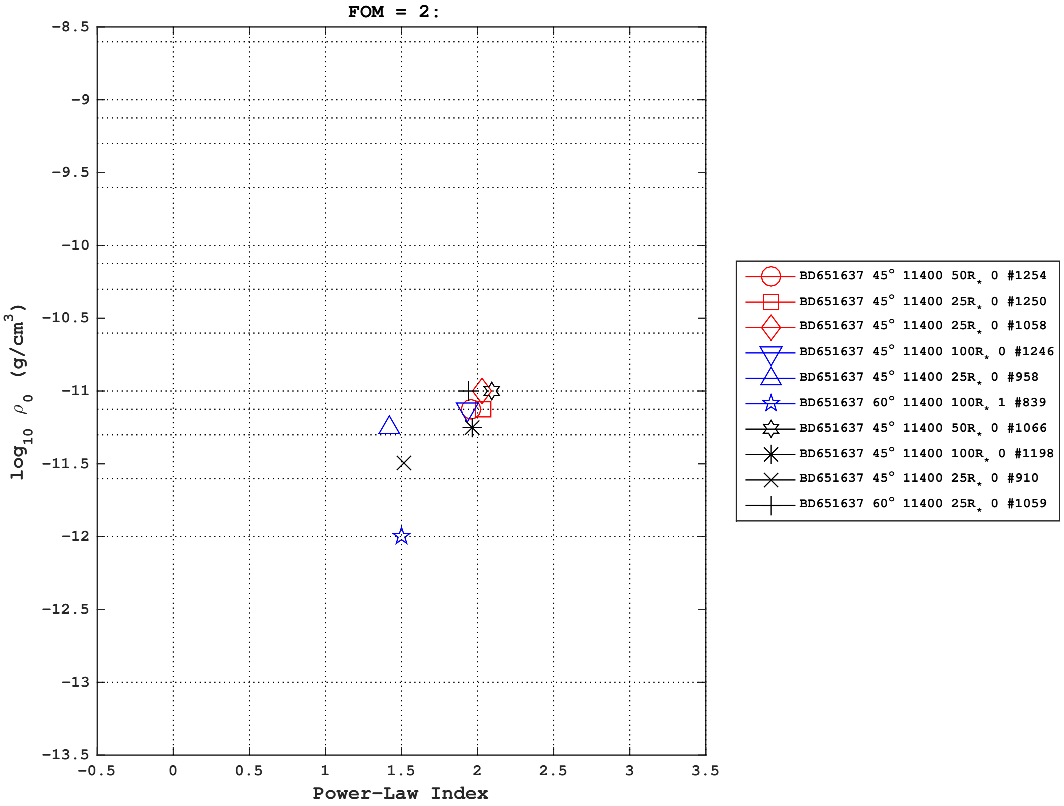

Figure B.4: Hβ profiles for BD+65 1637: The top 9 best-fit models corresponding to the line fittings, seen in Figure B.3, in the $(n, log_{10}\,\rho)$ plane. The additional parameters of each model are noted in the legend in the following order: model name, inclination (i), disk temperature (T_{HE}), disk radius (R_*), turbulence (α) and model number (which corresponds to the individual line fits in the previous plot).

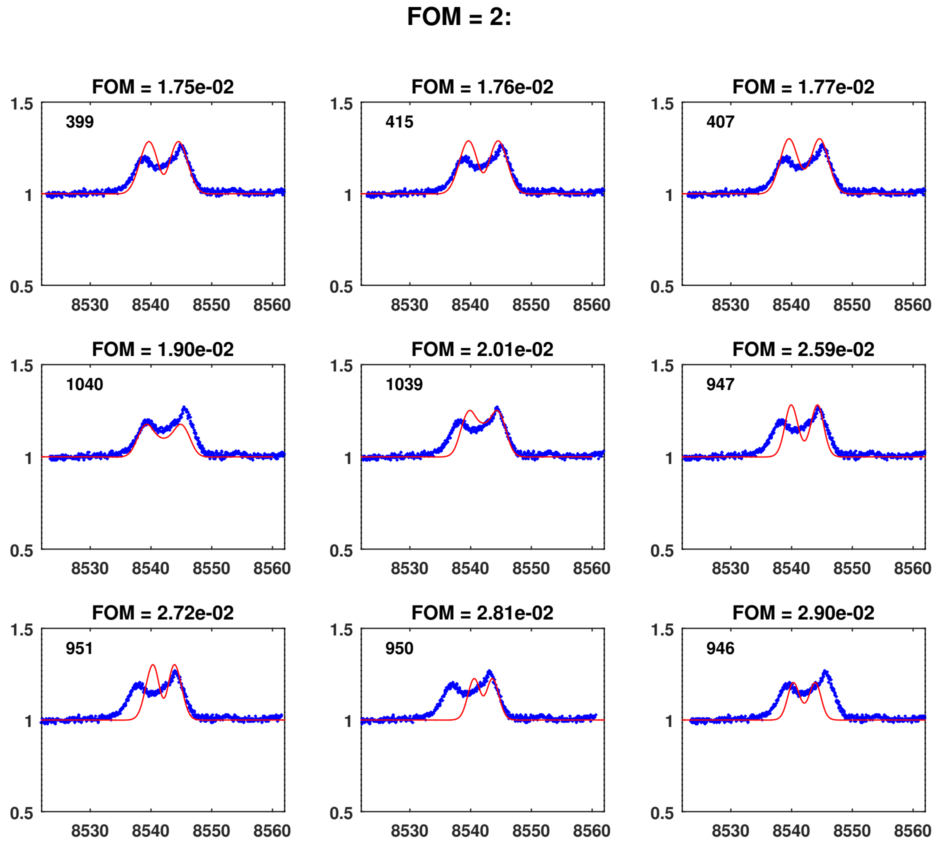

Figure B.5: Ca II profiles for BD+65 1637: The top 9 best synthetic (red) line profiles, result of Equation 3.1, that best match the observed (blue) emission line. The FOM (figure-of-merit) value above each panel of best fit represents the $\mathcal{F}$ value calculated using equation 3.1. The top left panel represents the best-fit line profile.

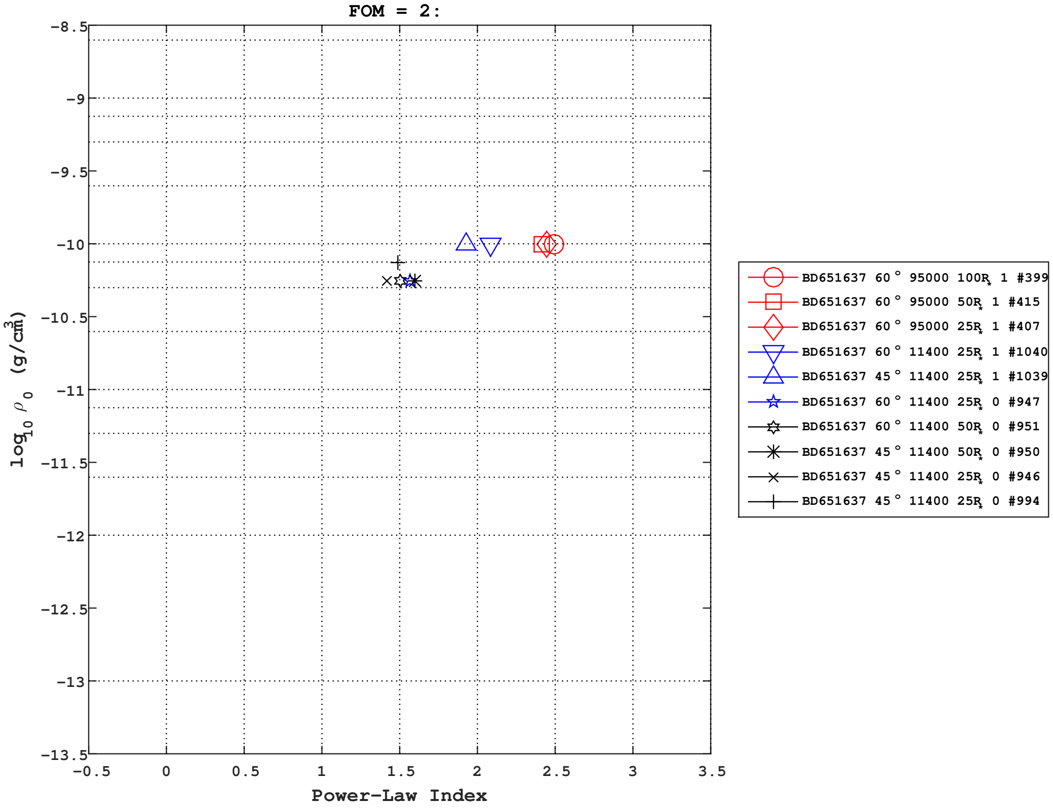

Figure B.6: Ca II profiles for BD+65 1637: The top 9 best-fit models corresponding to the line fittings, seen in Figure B.5, in the $(n, log_{10}\rho)$ plane. The additional parameters of each model are noted in the legend in the following order: model name, inclination (i), disk temperature (T_{HE}), disk radius (R_*), turbulence (α) and model number (which corresponds to the individual line fits in the previous plot).

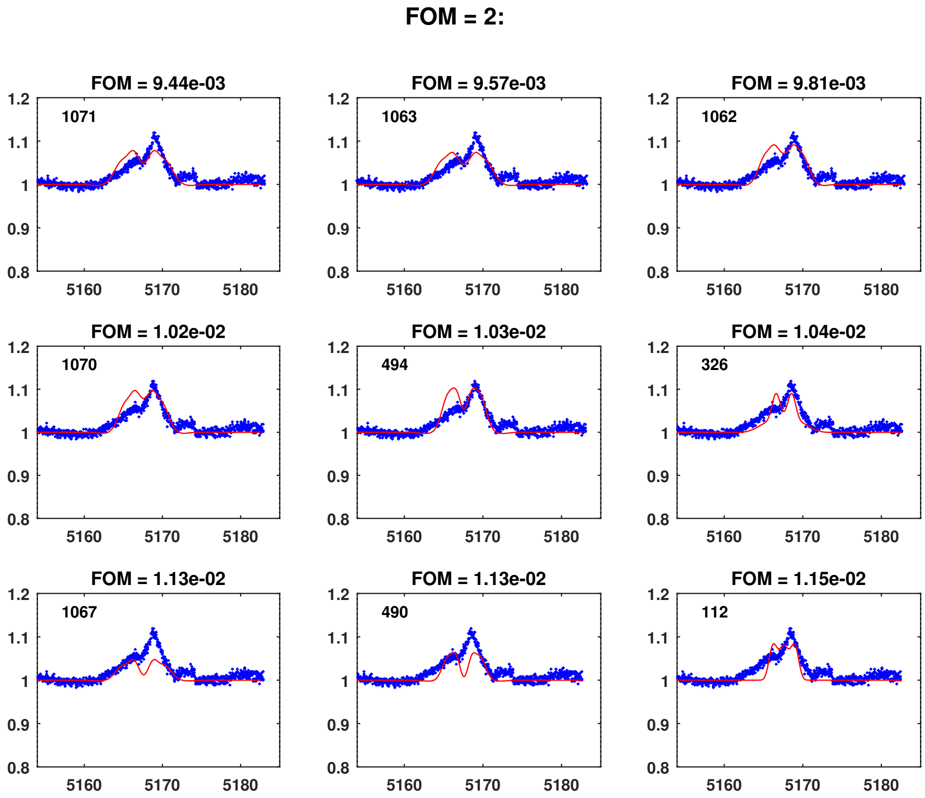

Figure B.7: Fe II (λ 5169) profiles for BD+65 1637: The top 9 best synthetic (red) line profiles, result of Equation 3.1, that best match the observed (blue) emission line. The FOM (figure-of-merit) value above each panel of best fit represents the $\mathscr{F}$ value calculated using equation 3.1. The top left panel represents the best-fit line profile.

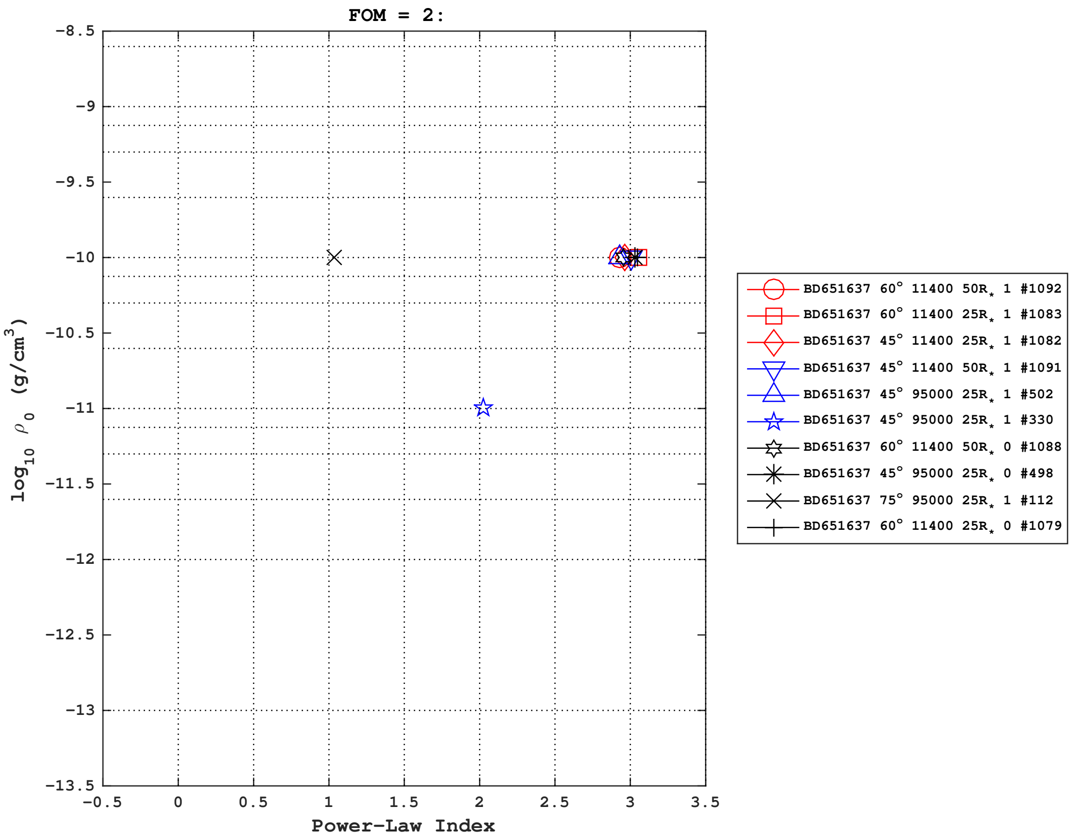

Figure B.8: Fe II (λ 5169) profiles for BD+65 1637: The top 9 best-fit models corresponding to the line fittings, seen in Figure B.7, in the $(n, log_{10}\rho)$ plane. The additional parameters of each model are noted in the legend in the following order: model name, inclination (i), disk temperature (T_{HE}), disk radius (R_*), turbulence (α) and model number (which corresponds to the individual line fits in the previous plot).

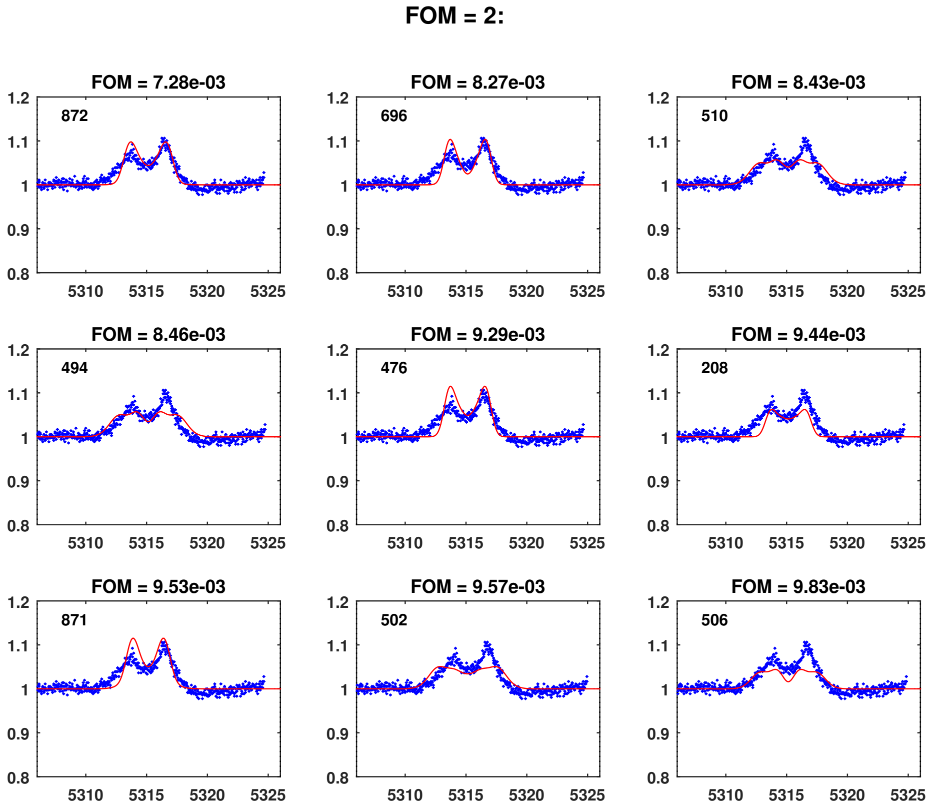

Figure B.9: Fe II (λ 5317) profiles for BD+65 1637: The top 9 best synthetic (red) line profiles, result of Equation 3.1, that best match the observed (blue) emission line. The FOM (figure-of-merit) value above each panel of best fit represents the $\mathcal{F}$ value calculated using equation 3.1. The top left panel represents the best-fit line profile.

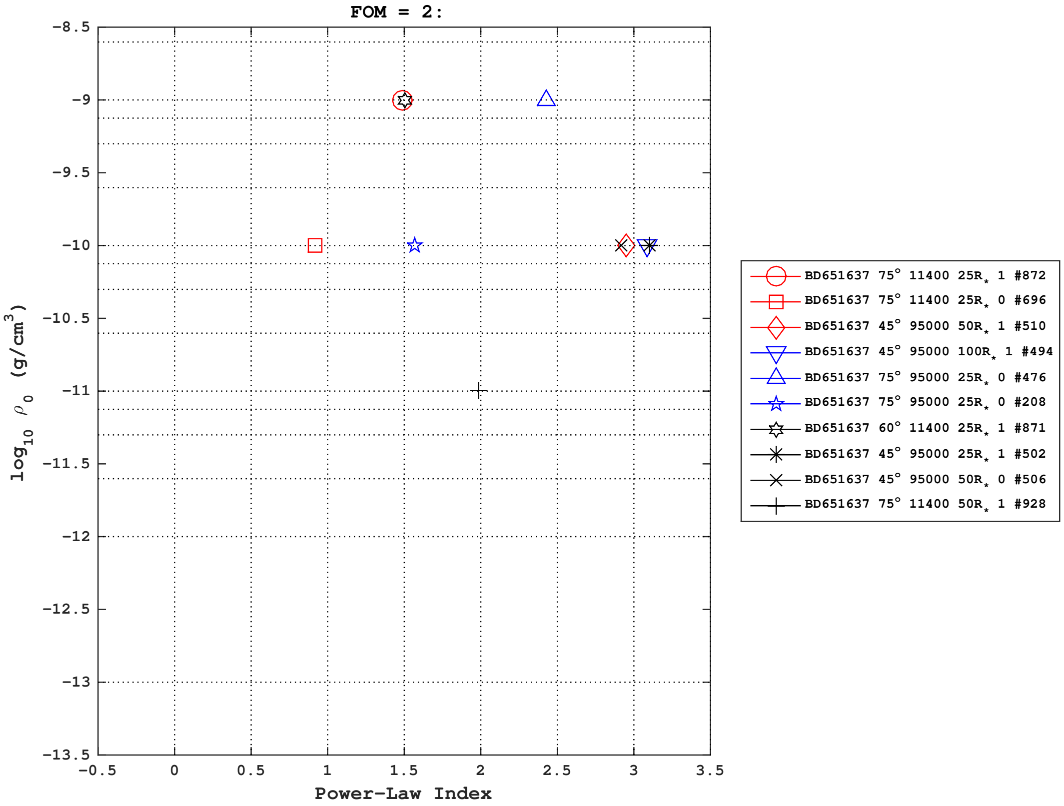

Figure B.10: Fe II (λ 5317) profiles for BD+65 1637: The top 9 best-fit models corresponding to the line fittings, seen in Figure B.9, in the $(n, log_{10}\,\rho)$ plane. The additional parameters of each model are noted in the legend in the following order: model name, inclination (i), disk temperature (T_{HE}), disk radius (R_*), turbulence (α) and model number (which corresponds to the individual line fits in the previous plot).

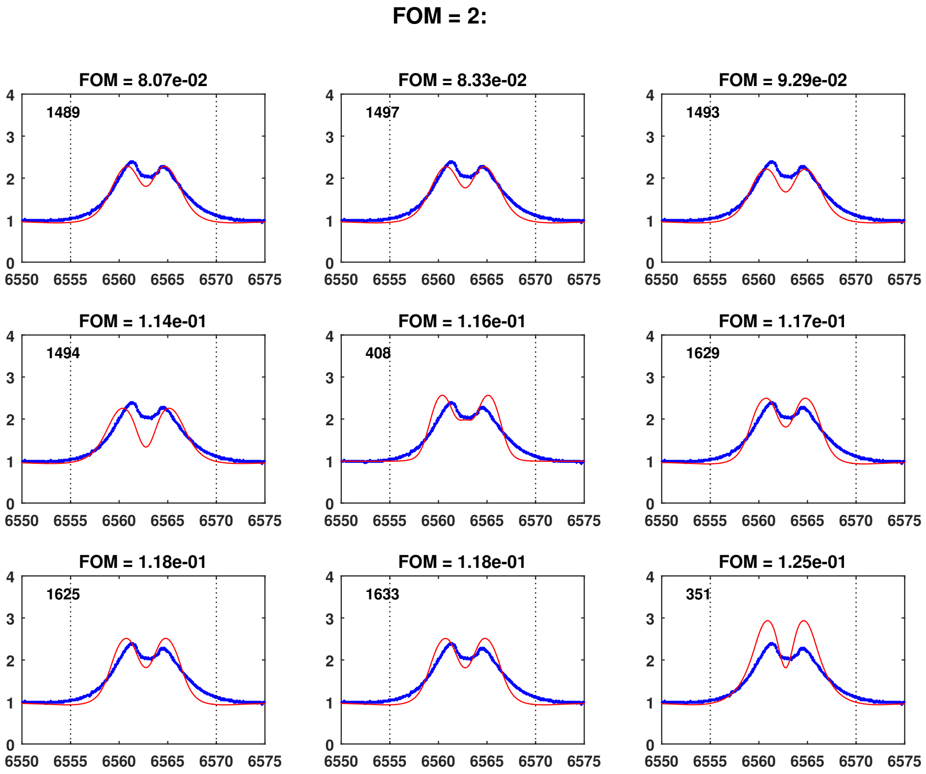

Figure B.11: Hα profiles for HD 76534: The top 9 best synthetic (red) line profiles, result of Equation 3.1, that best match the observed (blue) emission line. The FOM (figure-of-merit) value above each panel of best fit represents the $\mathcal{F}$ value calculated using equation 3.1. The top left panel represents the best-fit line profile.

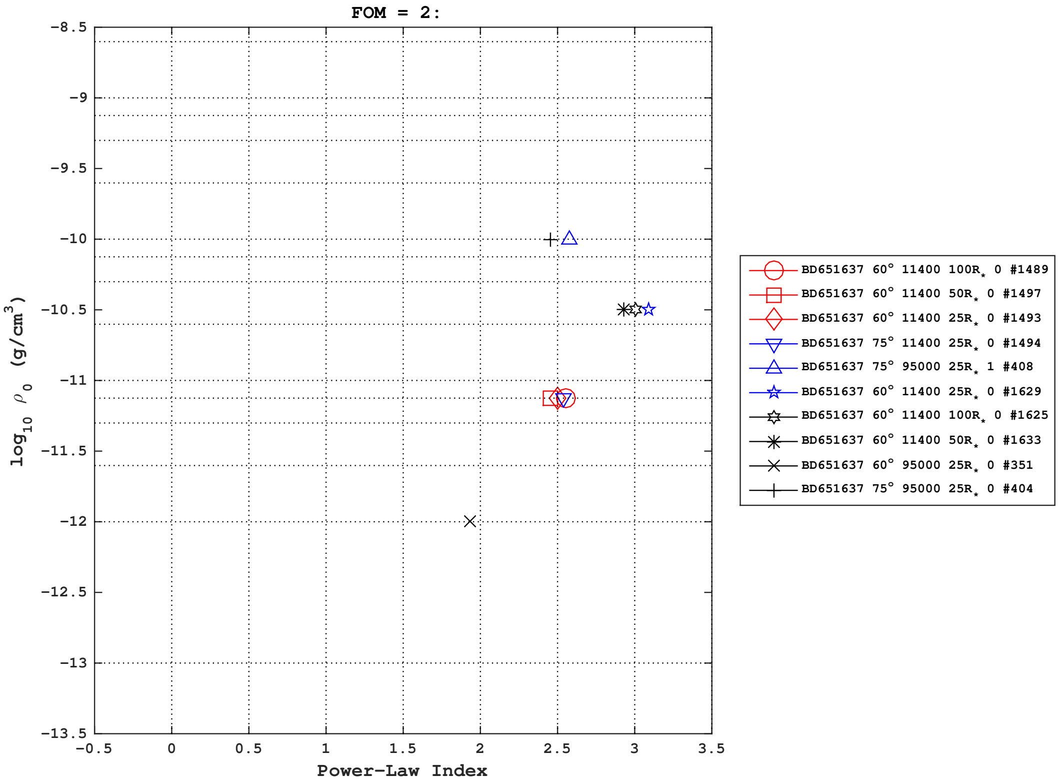

Figure B.12: Hα profiles for HD 76534: The top 9 best-fit models corresponding to the line fittings, seen in Figure B.11, in the $(n, log_{10}\rho)$ plane. The additional parameters of each model are noted in the legend in the following order: model name, inclination (i), disk temperature (T_{HE}), disk radius (R_*), turbulence (α) and model number (which corresponds to the individual line fits in the previous plot).

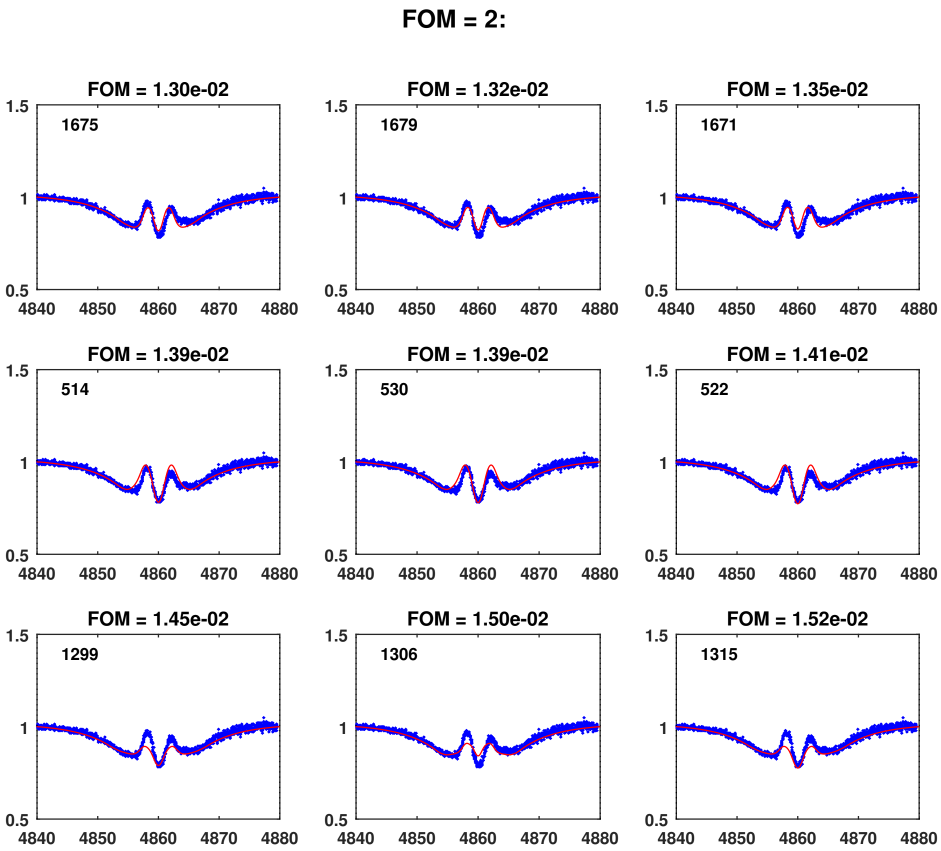

Figure B.13: Hβ profiles for HD 76534: The top 9 best synthetic (red) line profiles, result of Equation 3.1, that best match the observed (blue) emission line. The FOM (figure-of-merit) value above each panel of best fit represents the $\mathcal{F}$ value calculated using equation 3.1. The top left panel represents the best-fit line profile.

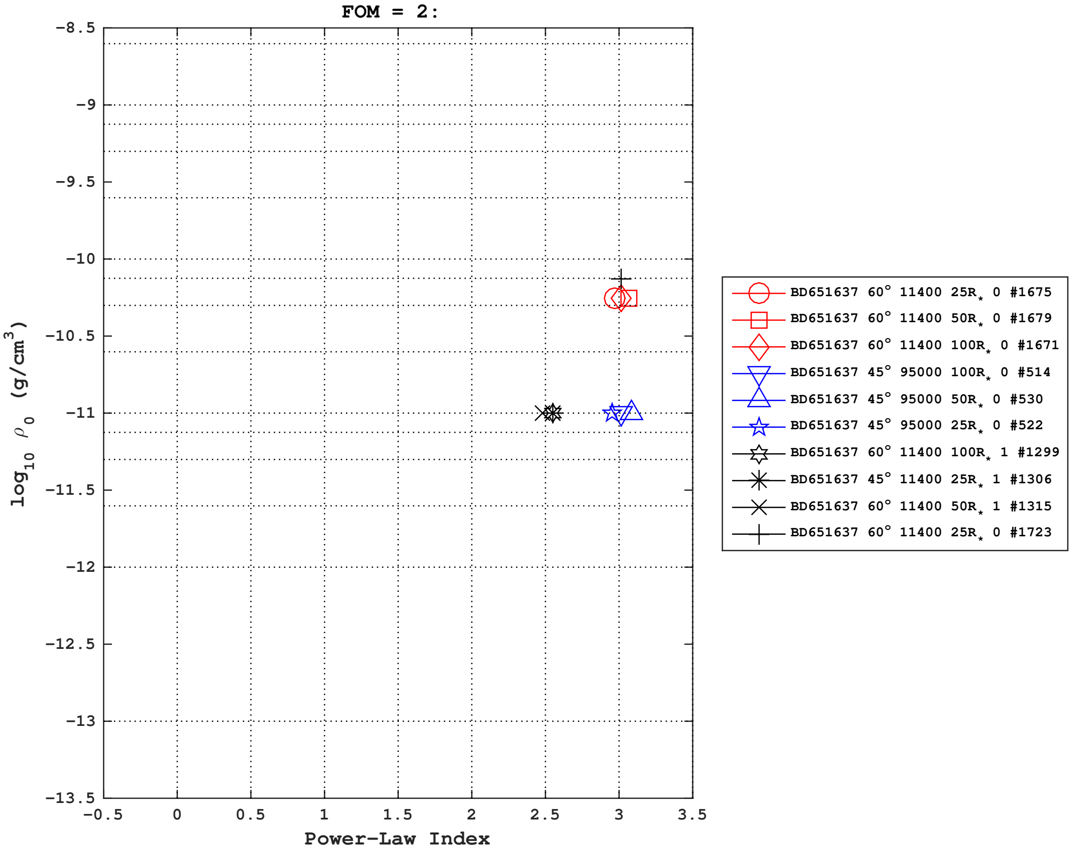

Figure B.14: Hβ profiles for HD 76534: The top 9 best-fit models corresponding to the line fittings, seen in Figure B.13, in the $(n, log_{10}\rho)$ plane. The additional parameters of each model are noted in the legend in the following order: model name, inclination (i), disk temperature (T_{HE}), disk radius (R_{*}), turbulence (α) and model number (which corresponds to the individual line fits in the previous plot).

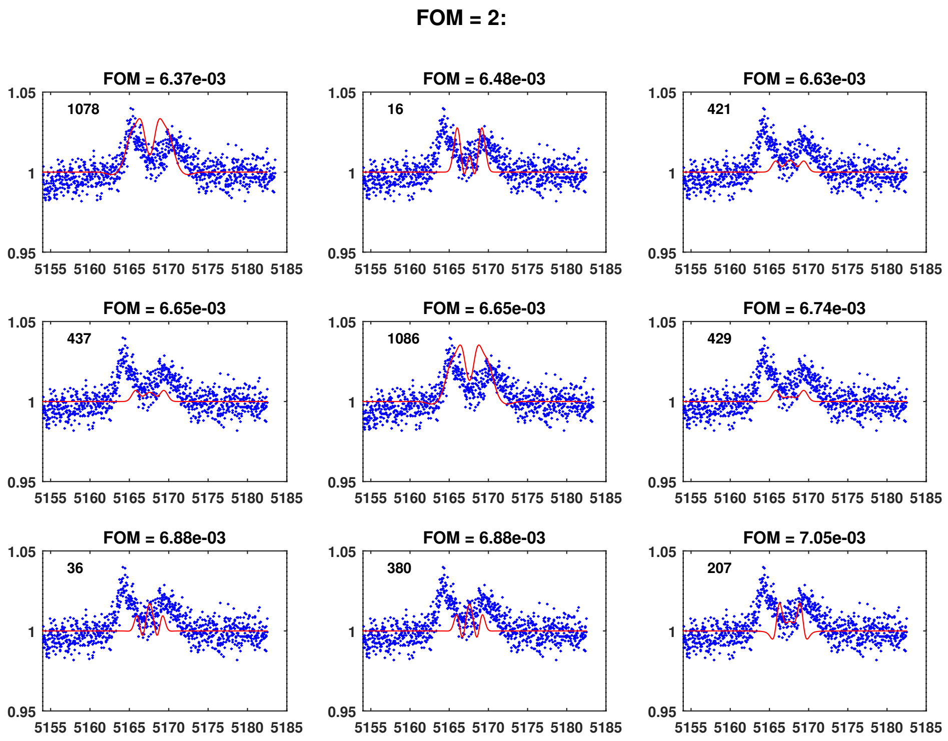

Figure B.15: Fe II (λ 5169) profiles for HD 76534: The top 9 best synthetic (red) line profiles, result of Equation 3.1, that best match the observed (blue) emission line. The FOM (figure-of-merit) value above each panel of best fit represents the $\mathcal{F}$ value calculated using equation 3.1. The top left panel represents the best-fit line profile.

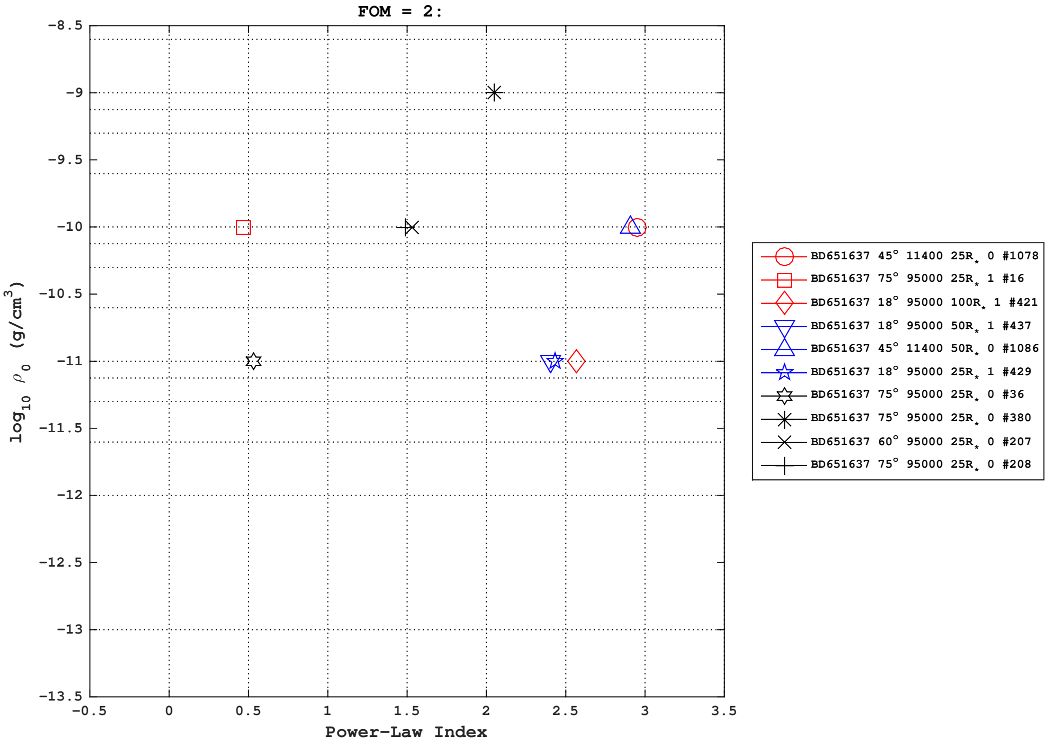

Figure B.16: Fe II (λ 5169) profiles for HD 76534: The top 9 best-fit models corresponding to the line fittings, seen in Figure B.15, in the $(n, log_{10}\,\rho)$ plane. The additional parameters of each model are noted in the legend in the following order: model name, inclination (i), disk temperature (T_{HE}), disk radius (R_*), turbulence (α) and model number (which corresponds to the individual line fits in the previous plot).

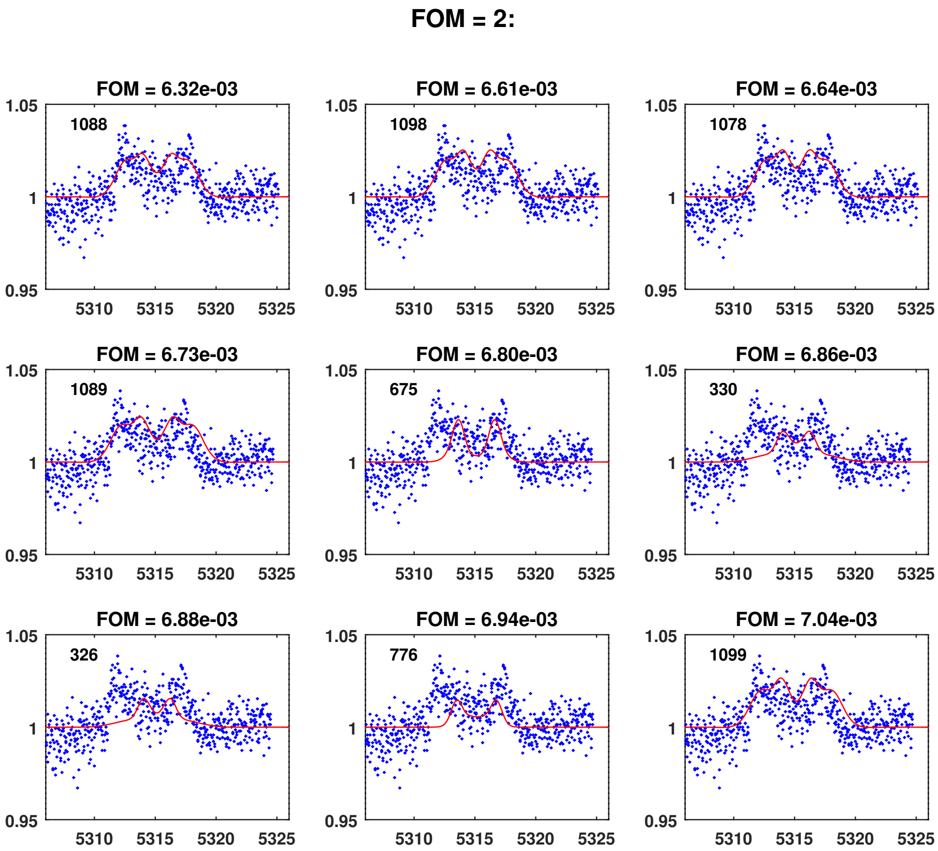

Figure B.17: Fe II (λ 5317) profiles for HD 76534: The top 9 best synthetic (red) line profiles, result of Equation 3.1, that best match the observed (blue) emission line. The FOM (figure-of-merit) value above each panel of best fit represents the $\mathcal{F}$ value calculated using equation 3.1. The top left panel represents the best-fit line profile.

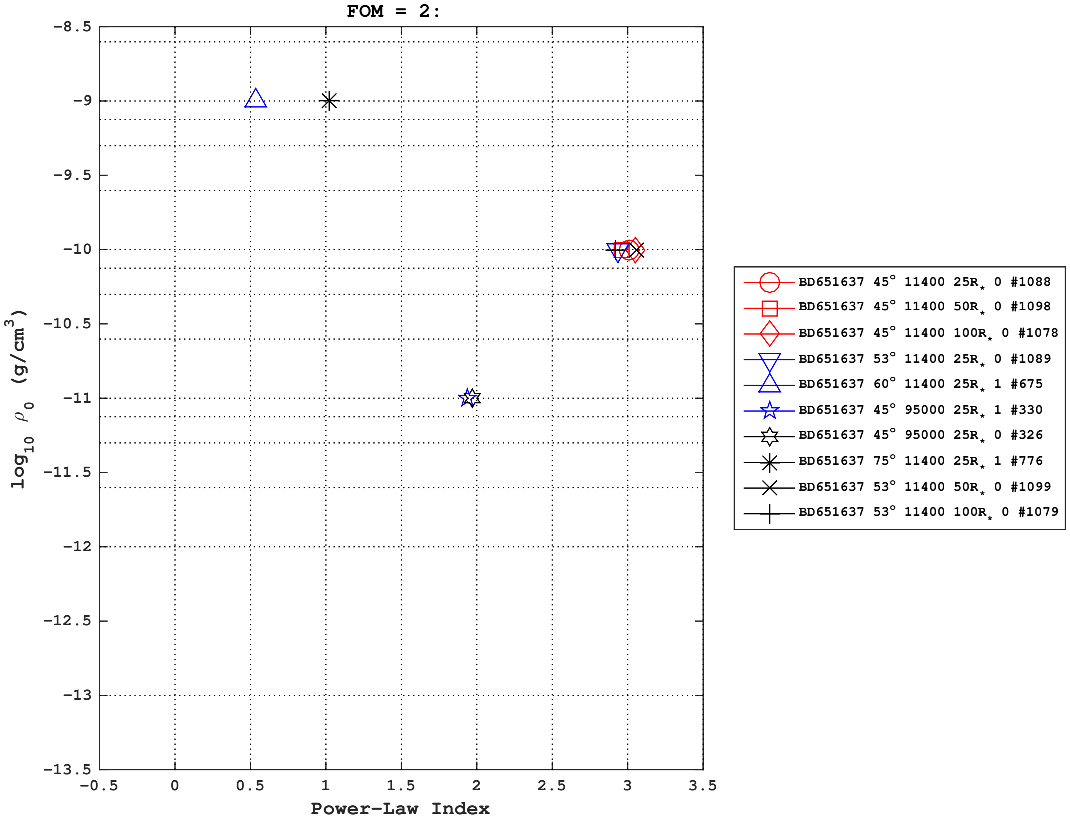

Figure B.18: Fe II (λ 5317) profiles for HD 76534: The top 9 best-fit models corresponding to the line fittings, seen in Figure B.17, in the ($n, log_{10}\,\rho$) plane. The additional parameters of each model are noted in the legend in the following order: model name, inclination (i), disk temperature (T_{HE}), disk radius (R_*), turbulence (α) and model number (which corresponds to the individual line fits in the previous plot).

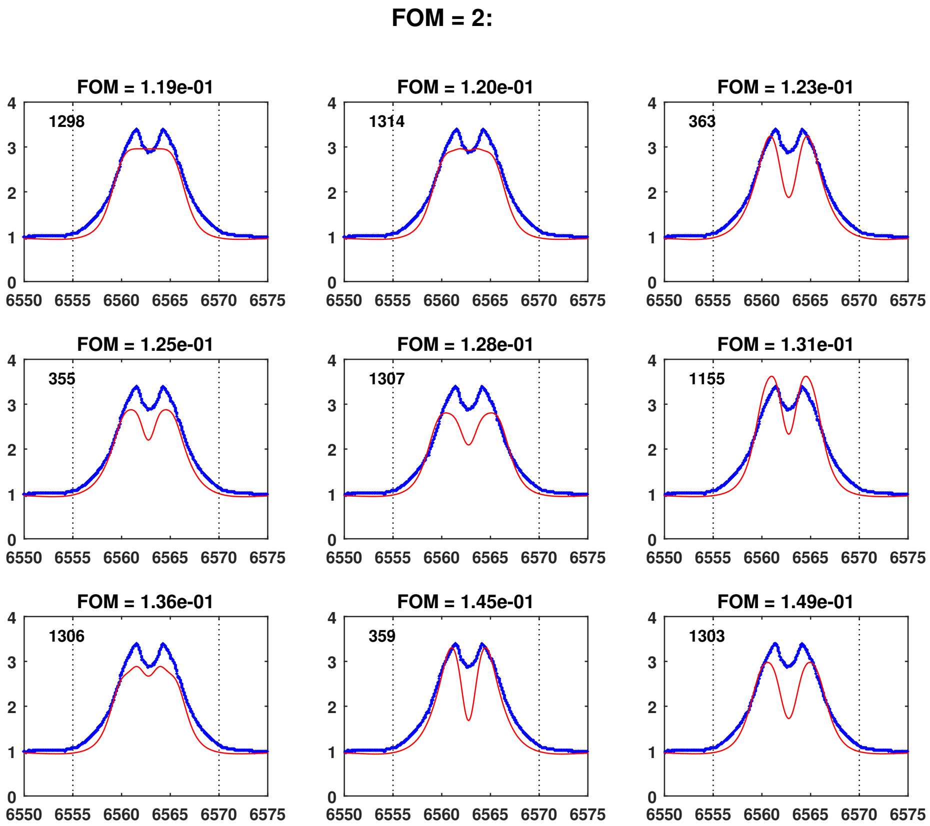

Figure B.19: Hα profiles for HD 114981: The top 9 best synthetic (red) line profiles, result of Equation 3.1, that best match the observed (blue) emission line. The FOM (figure-of-merit) value above each panel of best fit represents the $\mathcal{F}$ value calculated using equation 3.1. The top left panel represents the best-fit line profile.

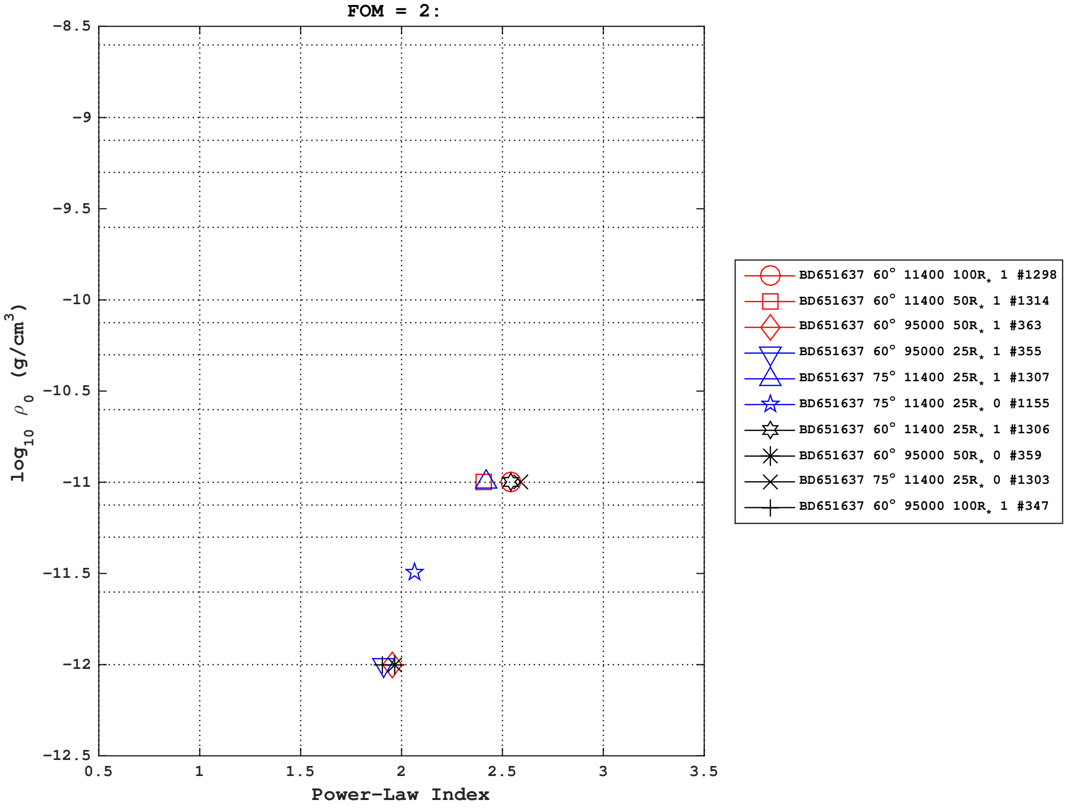

Figure B.20: Hα profiles for HD 114981: The top 9 best-fit models corresponding to the line fittings, seen in Figure B.19, in the $(n, log_{10}\,\rho)$ plane. The additional parameters of each model are noted in the legend in the following order: model name, inclination (i), disk temperature (T_{HE}), disk radius (R_*), turbulence (α) and model number (which corresponds to the individual line fits in the previous plot).

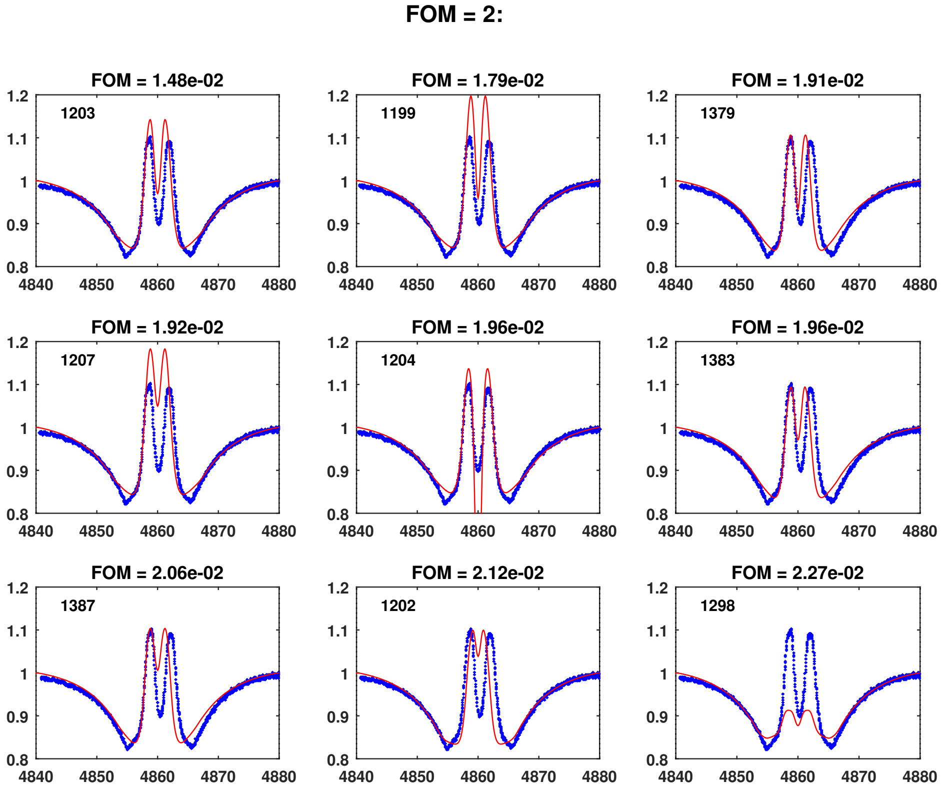

FOM = 2:

FOM = 1.48e-02

FOM = 1.79e-02

FOM = 1.91e-02

FOM = 1.92e-02

FOM = 1.96e-02

FOM = 1.96e-02

FOM = 2.06e-02

FOM = 2.12e-02

FOM = 2.27e-02

Figure B.21: Hβ profiles for HD 114981: The top 9 best synthetic (red) line profiles, result of Equation 3.1, that best match the observed (blue) emission line. The FOM (figure-of-merit) value above each panel of best fit represents the $\mathcal{F}$ value calculated using equation 3.1. The top left panel represents the best-fit line profile.

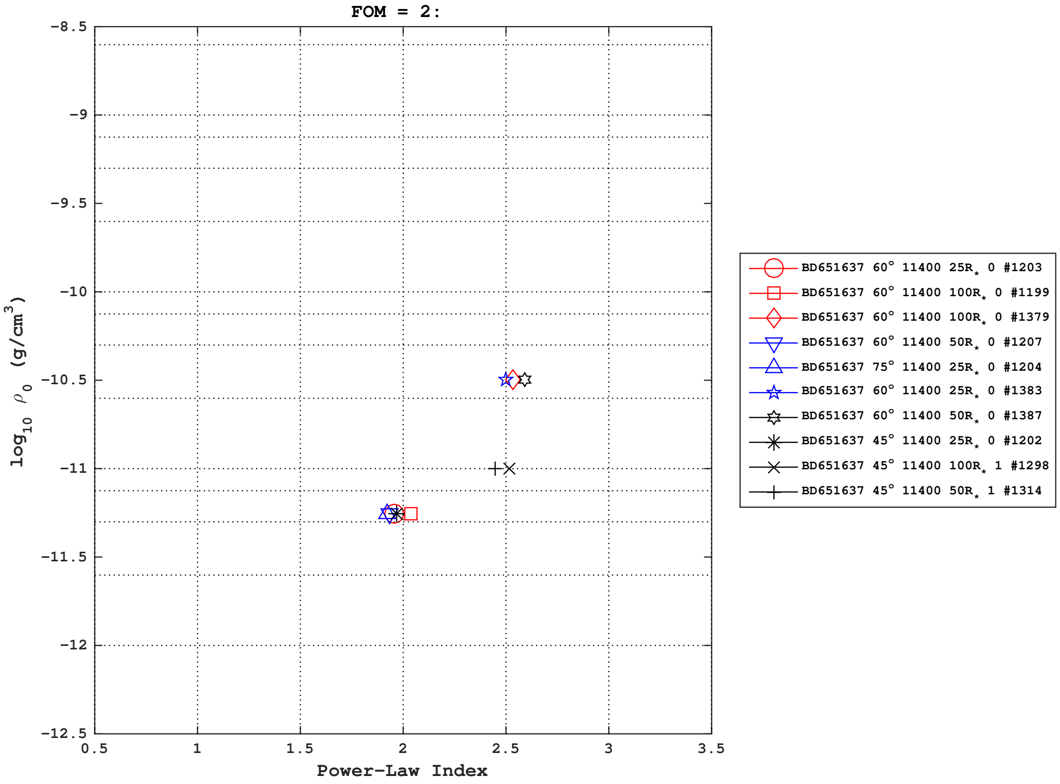

Figure B.22: Hβ profiles for HD 114981: The top 9 best-fit models corresponding to the line fittings, seen in Figure B.21, in the $(n, log_{10}\rho)$ plane. The additional parameters of each model are noted in the legend in the following order: model name, inclination (i), disk temperature (T_{HE}), disk radius (R_*), turbulence (α) and model number (which corresponds to the individual line fits in the previous plot).

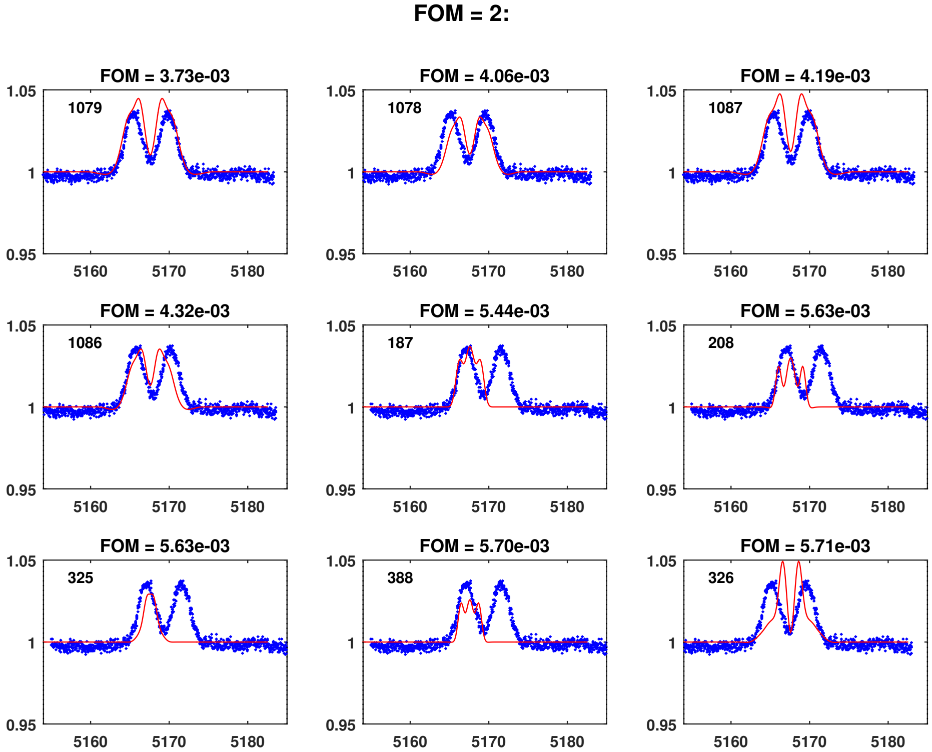

Figure B.23: Fe II (λ 5169) profiles for HD 114981: The top 9 best synthetic (red) line profiles, result of Equation 3.1, that best match the observed (blue) emission line. The FOM (figure-of-merit) value above each panel of best fit represents the $\mathcal{F}$ value calculated using equation 3.1. The top left panel represents the best-fit line profile.

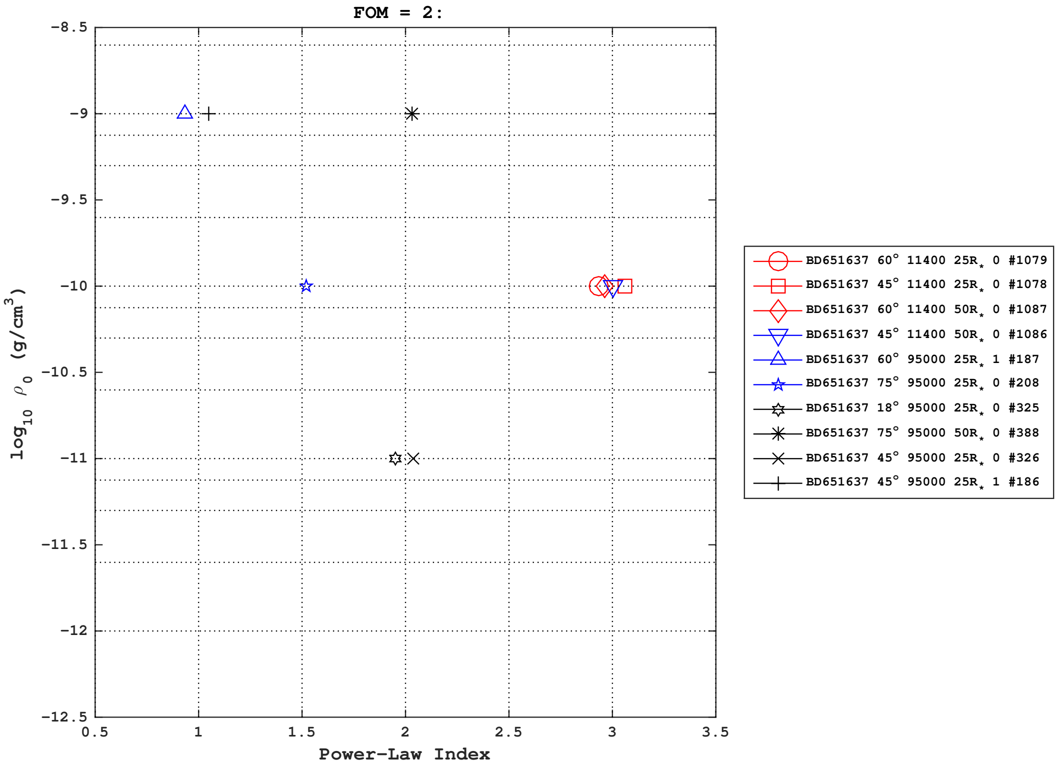

Figure B.24: Fe II (λ 5169) profiles for HD 114981: The top 9 best-fit models corresponding to the line fittings, seen in Figure B.23, in the $(n, log_{10}\,\rho)$ plane. The additional parameters of each model are noted in the legend in the following order: model name, inclination (i), disk temperature (T_{HE}), disk radius (R_*), turbulence (α) and model number (which corresponds to the individual line fits in the previous plot).

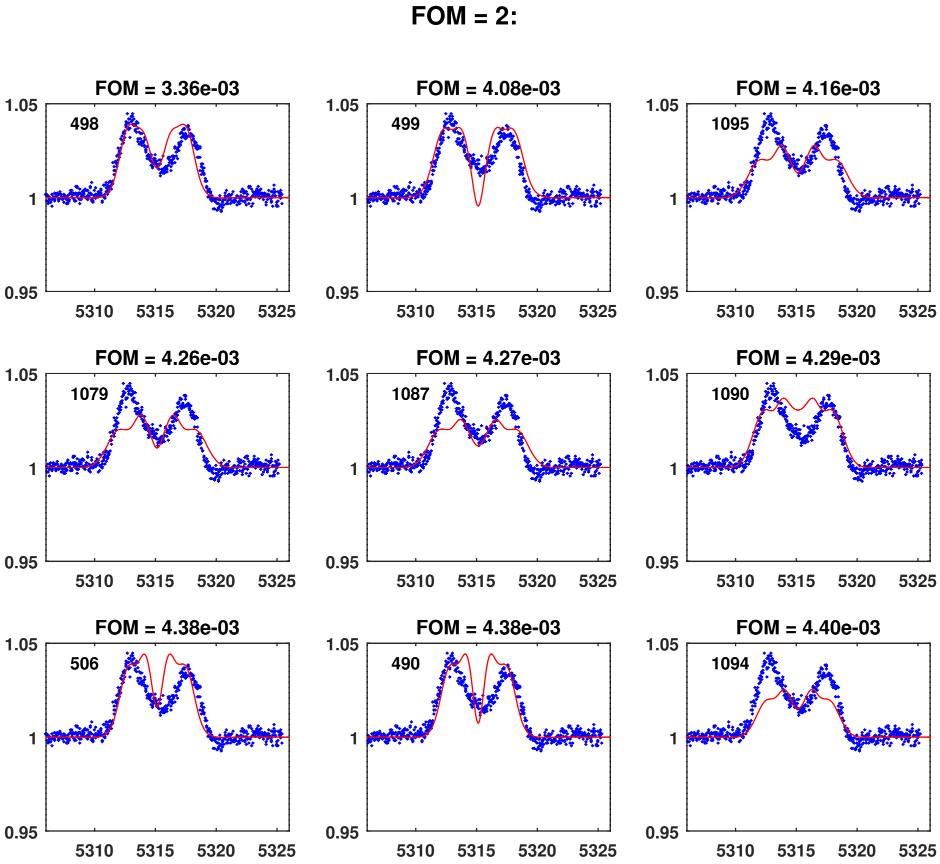

Figure B.25: Fe II (λ 5317) profiles for HD 114981: The top 9 best synthetic (red) line profiles, result of Equation 3.1, that best match the observed (blue) emission line. The FOM (figure-of-merit) value above each panel of best fit represents the $\mathcal{F}$ value calculated using equation 3.1. The top left panel represents the best-fit line profile.

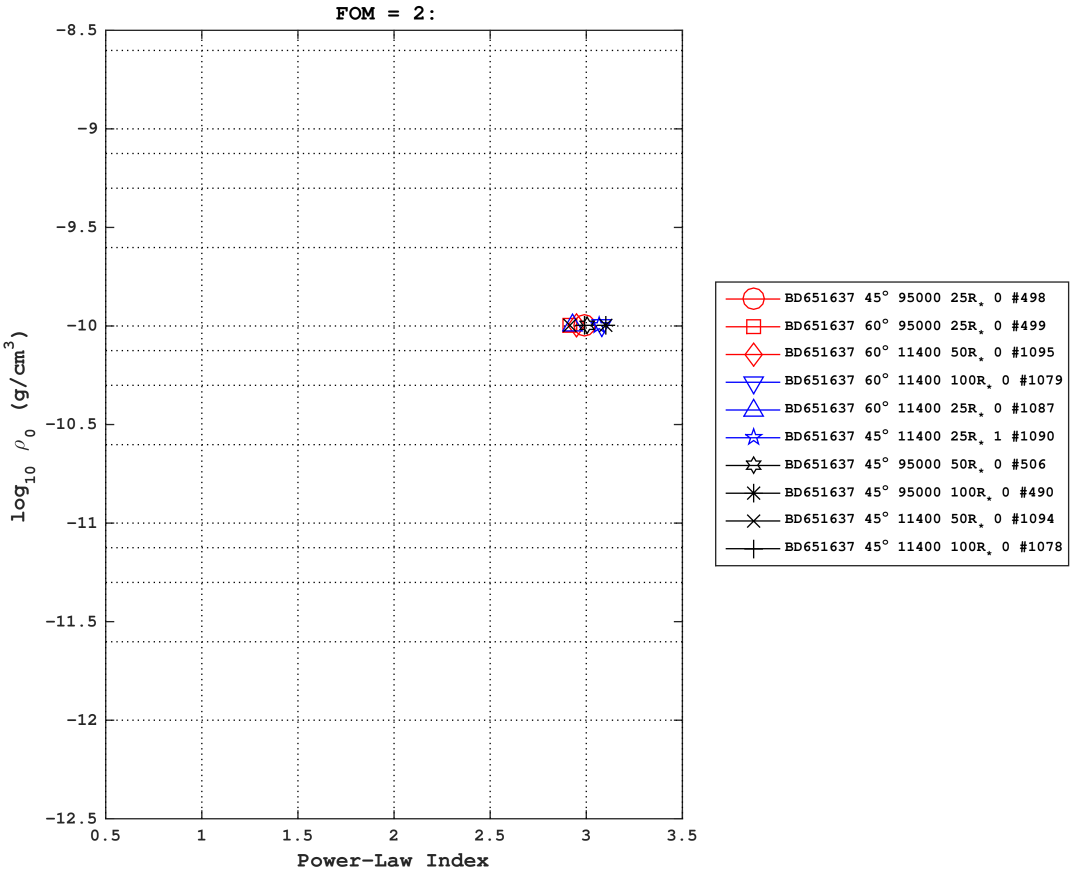

Figure B.26: Fe II (λ 5317) profiles for HD 114981: The top 9 best-fit models corresponding to the line fittings, seen in Figure B.25, in the $(n, log_{10}\,\rho)$ plane. The additional parameters of each model are noted in the legend in the following order: model name, inclination (i), disk temperature (T_{HE}), disk radius (R_*), turbulence (α) and model number (which corresponds to the individual line fits in the previous plot).

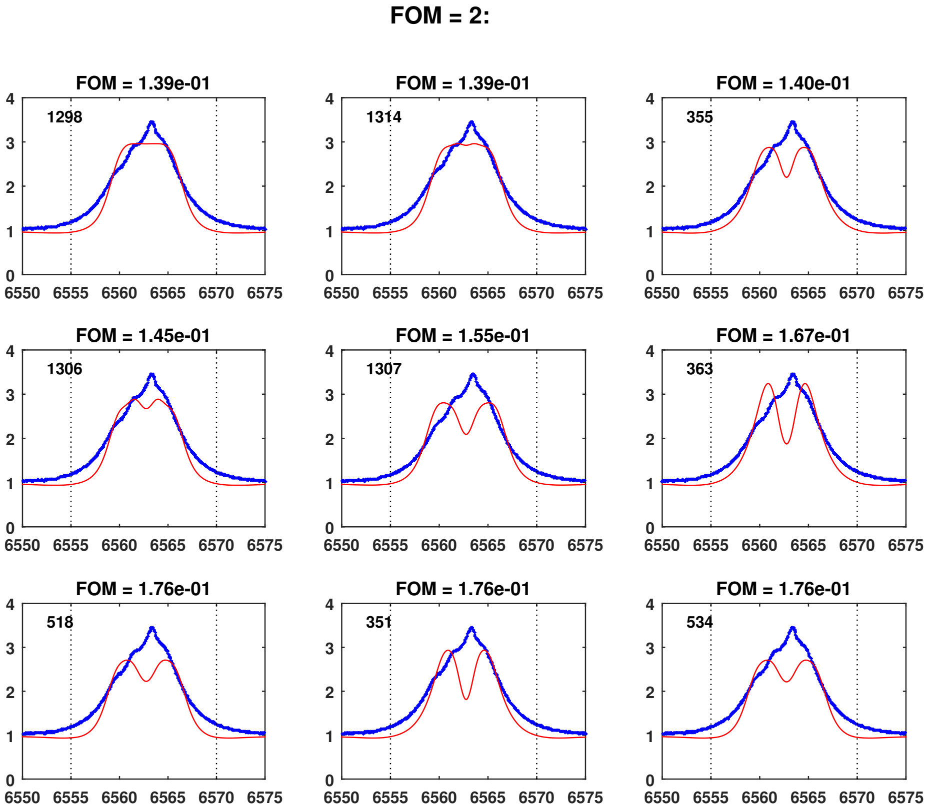

Figure B.27: Hα profiles for HD 216629: The top 9 best synthetic (red) line profiles, result of Equation 3.1, that best match the observed (blue) emission line. The FOM (figure-of-merit) value above each panel of best fit represents the $\mathcal{F}$ value calculated using equation 3.1. The top left panel represents the best-fit line profile.

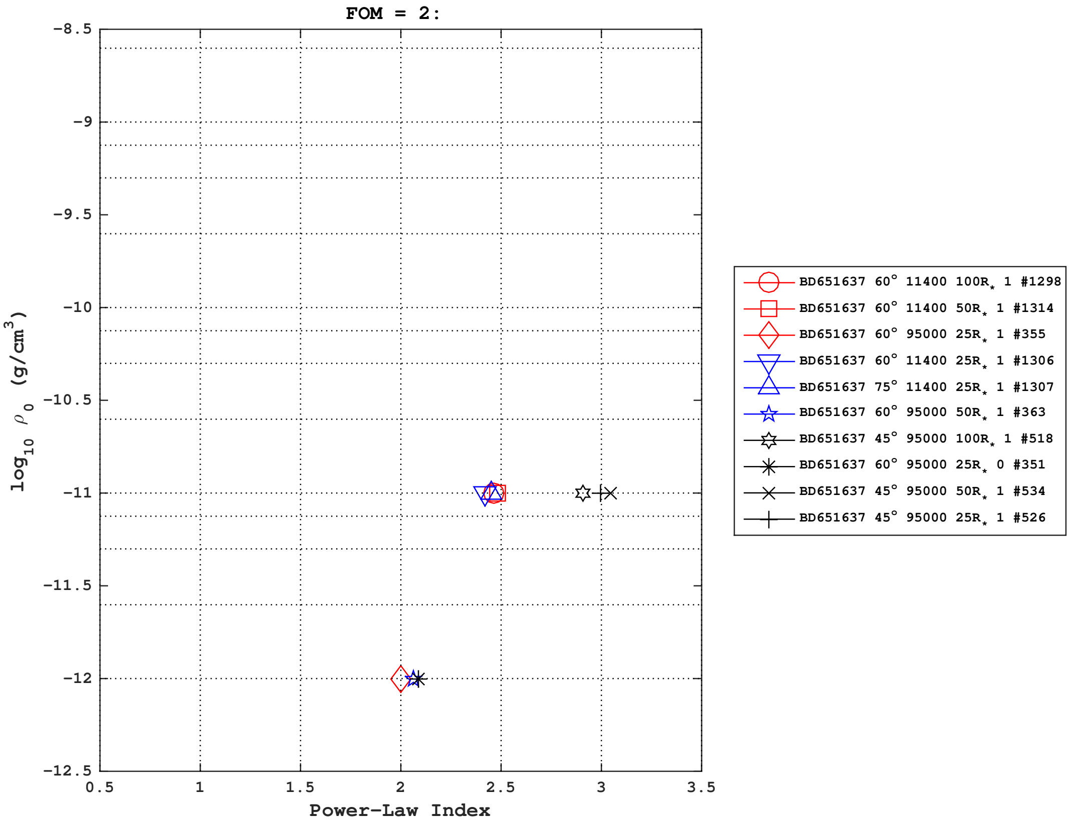

Figure B.28: Hα profiles for HD 216629: The top 9 best-fit models corresponding to the line fittings, seen in Figure B.27, in the $(n, log_{10}\,\rho)$ plane. The additional parameters of each model are noted in the legend in the following order: model name, inclination (i), disk temperature (T_{HE}), disk radius (R_*), turbulence (α) and model number (which corresponds to the individual line fits in the previous plot).

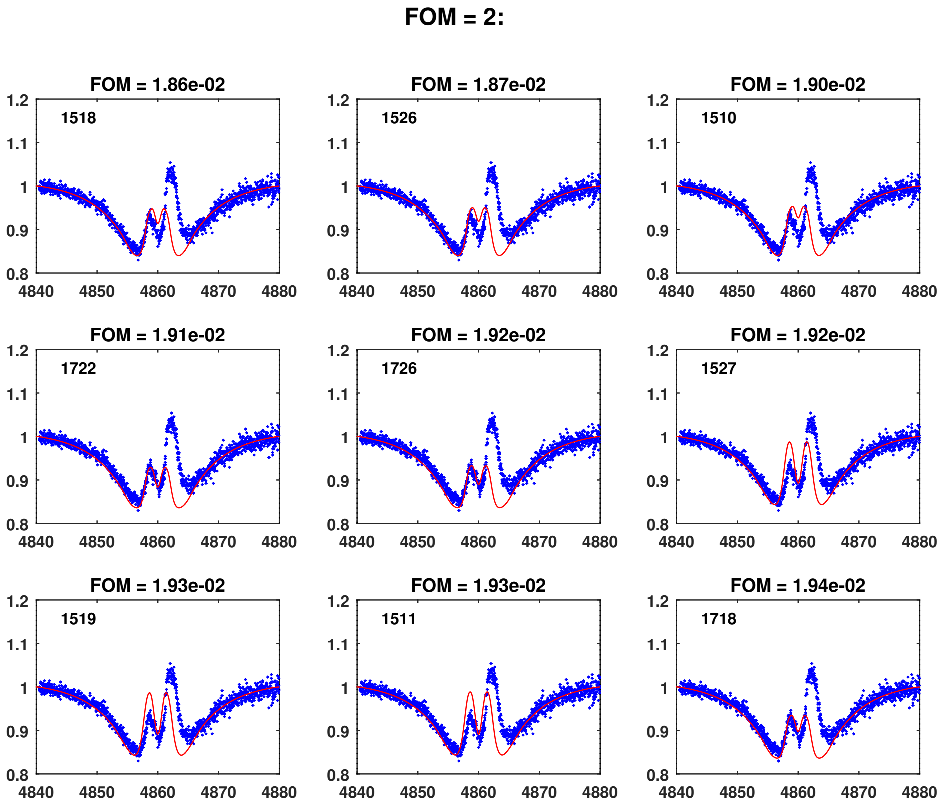

Figure B.29: Hβ profiles for HD 216629: The top 9 best synthetic (red) line profiles, result of Equation 3.1, that best match the observed (blue) emission line. The FOM (figure-of-merit) value above each panel of best fit represents the $\mathcal{F}$ value calculated using equation 3.1. The top left panel represents the best-fit line profile.

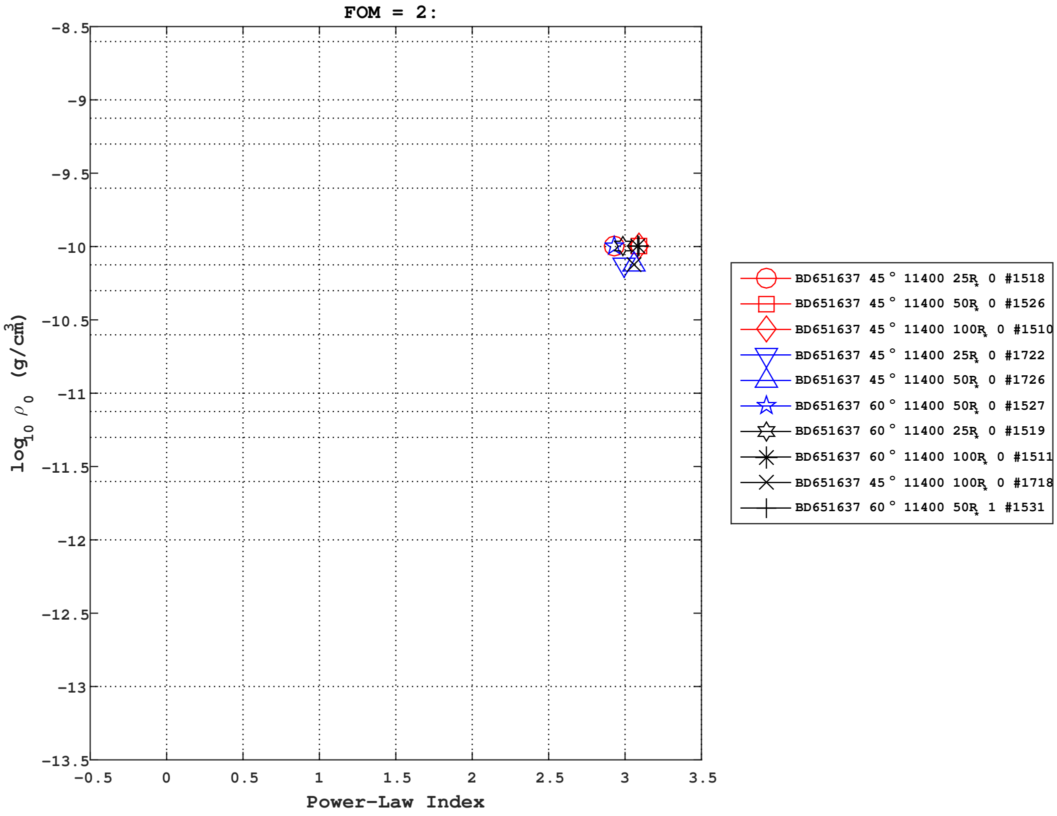

Figure B.30: Hβ profiles for HD 216629: The top 9 best-fit models corresponding to the line fittings, seen in Figure B.29, in the $(n, log_{10}\,\rho)$ plane. The additional parameters of each model are noted in the legend in the following order: model name, inclination (i), disk temperature (T_{HE}), disk radius (R_*), turbulence (α) and model number (which corresponds to the individual line fits in the previous plot).

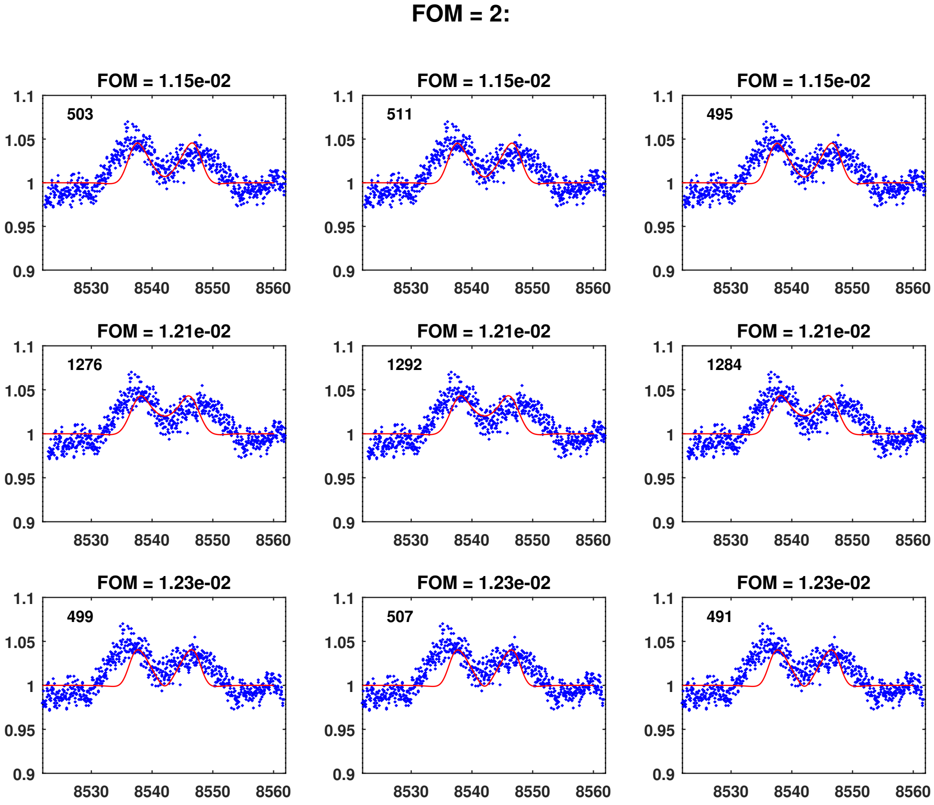

Figure B.31: Ca II profiles for HD 216629: The top 9 best synthetic (red) line profiles, result of Equation 3.1, that best match the observed (blue) emission line. The FOM (figure-of-merit) value above each panel of best fit represents the $\mathcal{F}$ value calculated using equation 3.1. The top left panel represents the best-fit line profile.

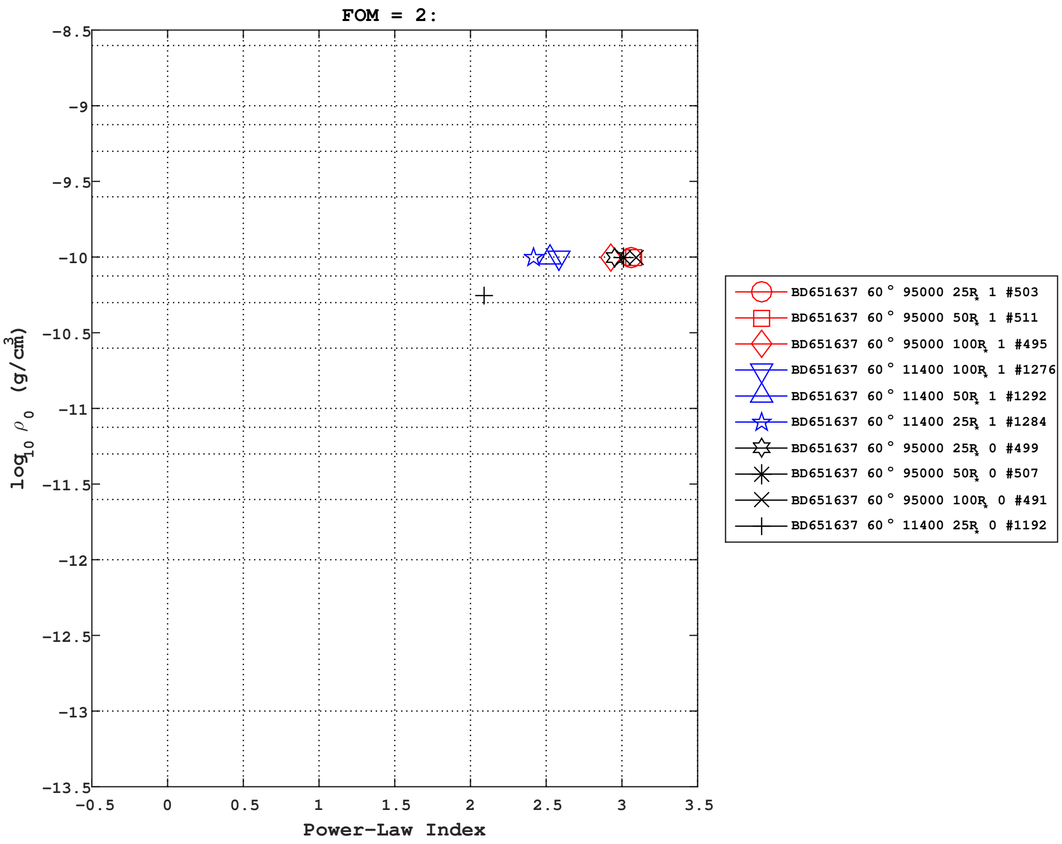

Figure B.32: Ca II profiles for HD 216629: The top 9 best-fit models corresponding to the line fittings, seen in Figure B.31, in the $(n, log_{10}\rho)$ plane. The additional parameters of each model are noted in the legend in the following order: model name, inclination (i), disk temperature (T_{HE}), disk radius (R_{*}), turbulence (α) and model number (which corresponds to the individual line fits in the previous plot).

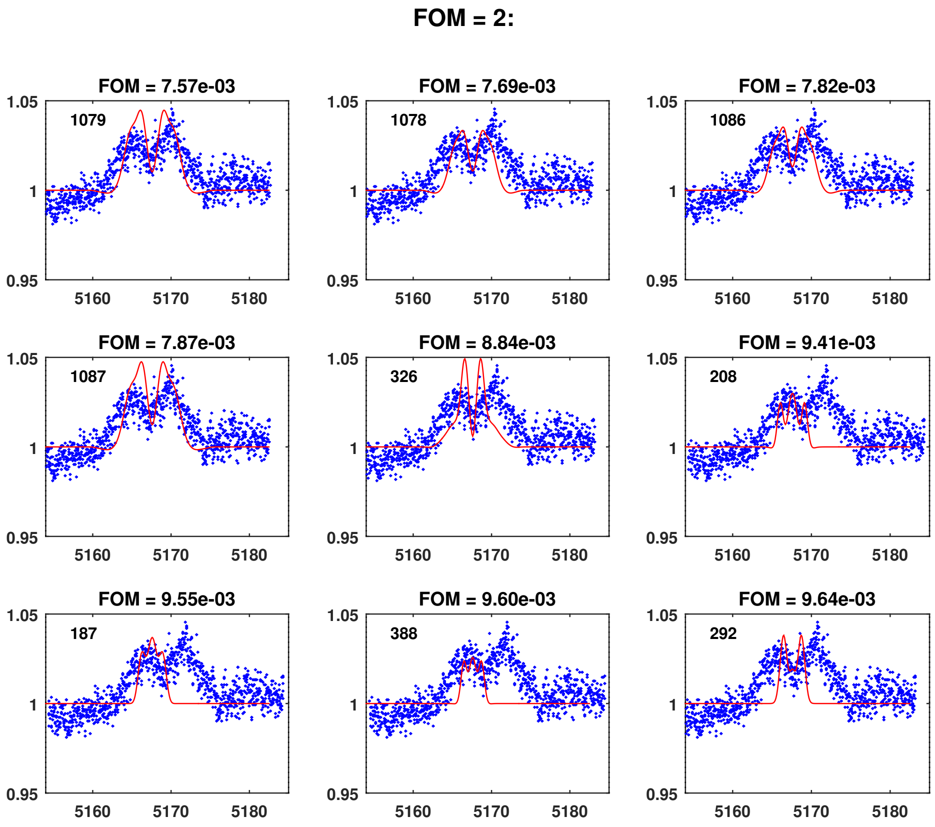

Figure B.33: Fe II (λ 5169) profiles for HD 216629: The top 9 best synthetic (red) line profiles, result of Equation 3.1, that best match the observed (blue) emission line. The FOM (figure-of-merit) value above each panel of best fit represents the $\mathcal{F}$ value calculated using equation 3.1. The top left panel represents the best-fit line profile.

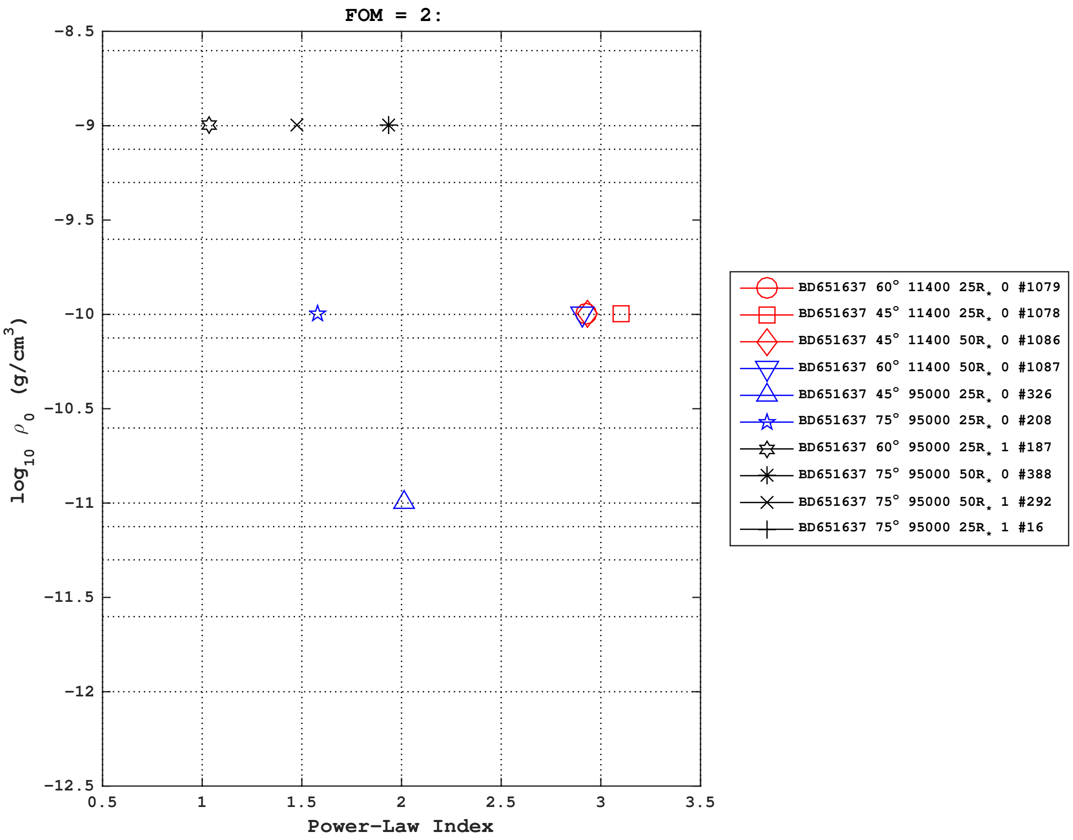

Figure B.34: Fe II (λ 5169) profiles for HD 216629: The top 9 best-fit models corresponding to the line fittings, seen in Figure B.33, in the $(n, log_{10}\,\rho)$ plane. The additional parameters of each model are noted in the legend in the following order: model name, inclination (i), disk temperature (T_{HE}), disk radius (R_*), turbulence (α) and model number (which corresponds to the individual line fits in the previous plot).

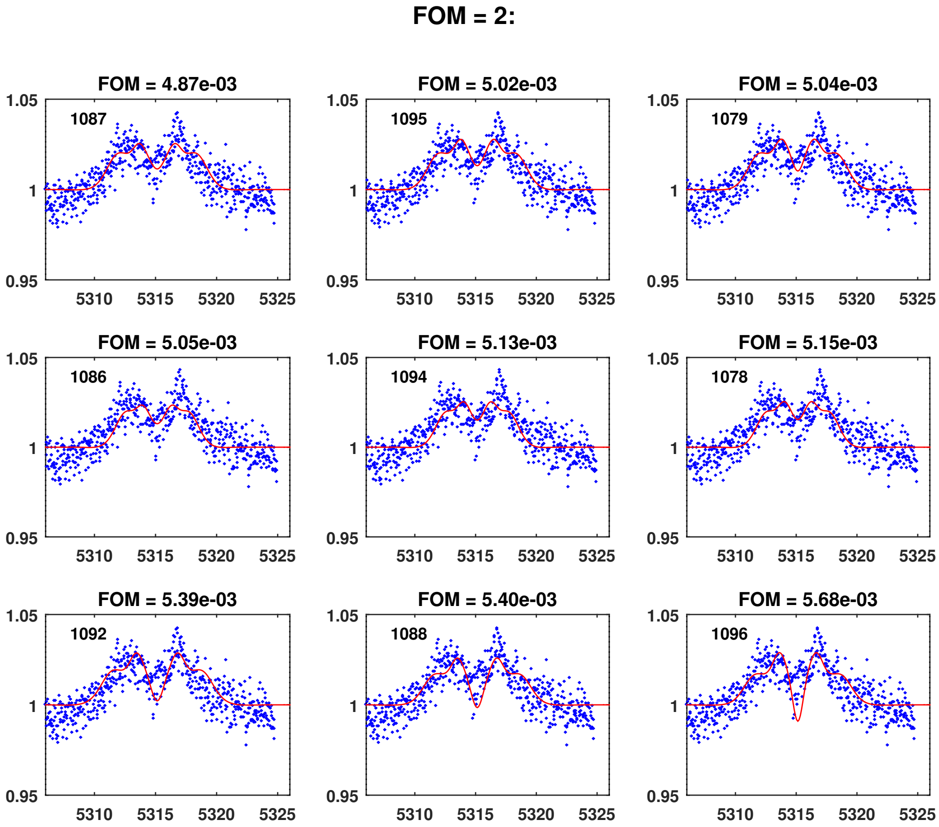

Figure B.35: Fe II (λ 5317) profiles for HD 216629: The top 9 best synthetic (red) line profiles, result of Equation 3.1, that best match the observed (blue) emission line. The FOM (figure-of-merit) value above each panel of best fit represents the $\mathcal{F}$ value calculated using equation 3.1. The top left panel represents the best-fit line profile.

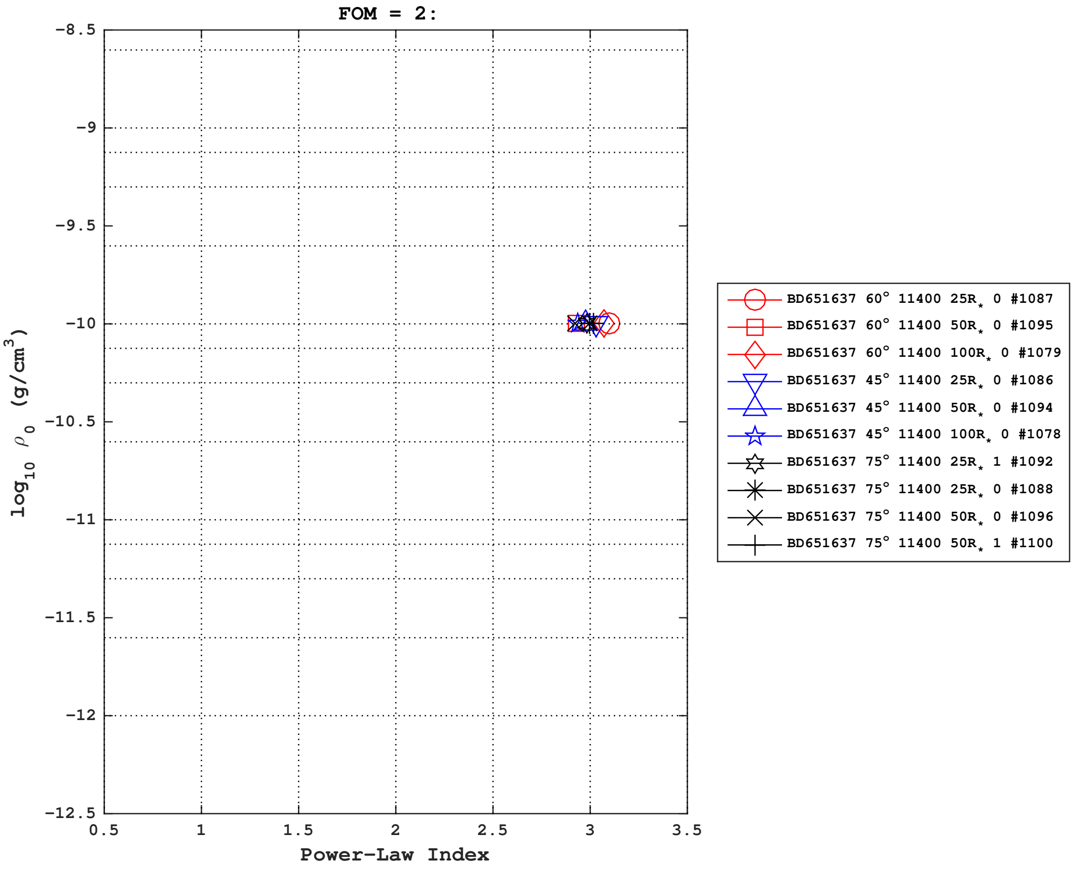

Figure B.36: Fe II (λ 5317) profiles for HD 216629: The top 9 best-fit models corresponding to the line fittings, seen in Figure B.35, in the $(n, log_{10}\,\rho)$ plane. The additional parameters of each model are noted in the legend in the following order: model name, inclination (i), disk temperature (T_{HE}), disk radius (R_*), turbulence (α) and model number (which corresponds to the individual line fits in the previous plot).

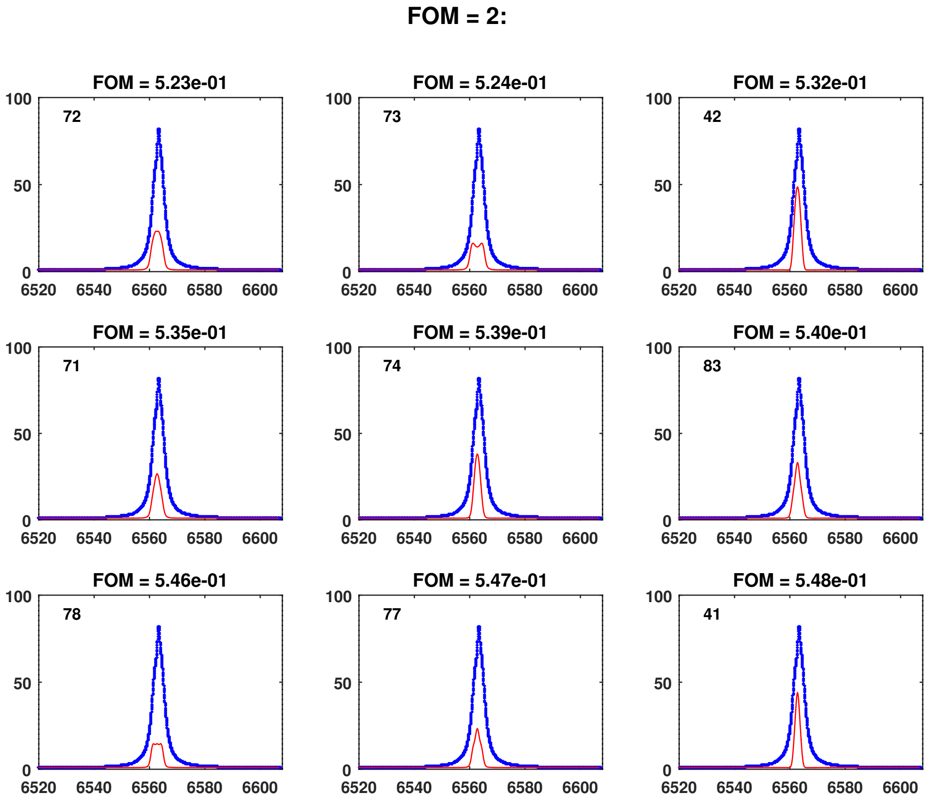

Figure B.37: Hα profiles for MWC 137: The top 9 best synthetic (red) line profiles, result of Equation 3.1, that best match the observed (blue) emission line. The FOM (figure-of-merit) value above each panel of best fit represents the $\mathcal{F}$ value calculated using equation 3.1. The top left panel represents the best-fit line profile.

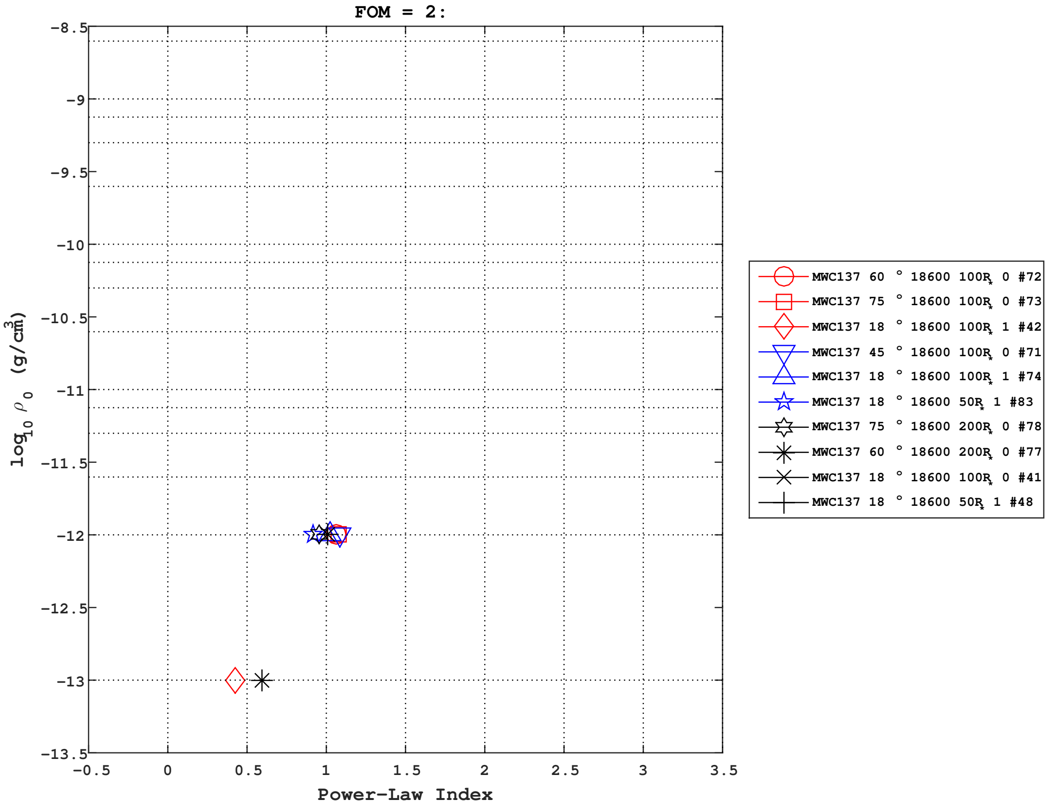

Figure B.38: Hα profiles for MWC 137: The top 9 best-fit models corresponding to the line fittings, seen in Figure B.37, in the $(n, log_{10}\,\rho)$ plane. The additional parameters of each model are noted in the legend in the following order: model name, inclination (i), disk temperature (T_{HE}), disk radius (R_*), turbulence (α) and model number (which corresponds to the individual line fits in the previous plot).

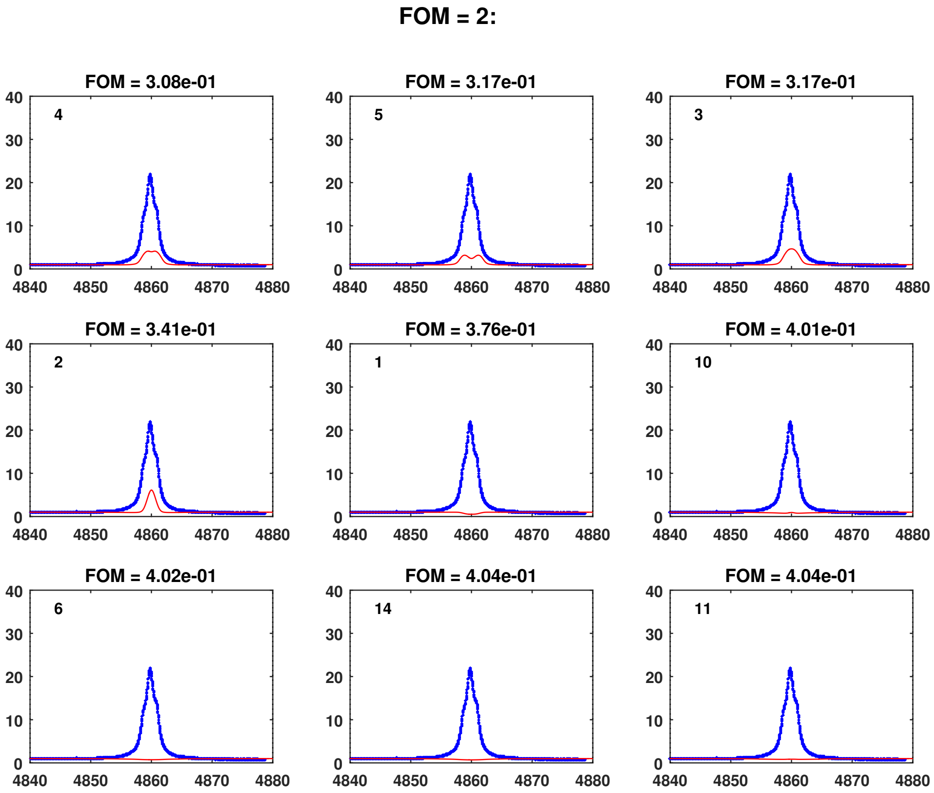

Figure B.39: Hβ profiles for MWC 137: The top 9 best synthetic (red) line profiles, result of Equation 3.1, that best match the observed (blue) emission line. The FOM (figure-of-merit) value above each panel of best fit represents the $\mathcal{F}$ value calculated using equation 3.1. The top left panel represents the best-fit line profile.

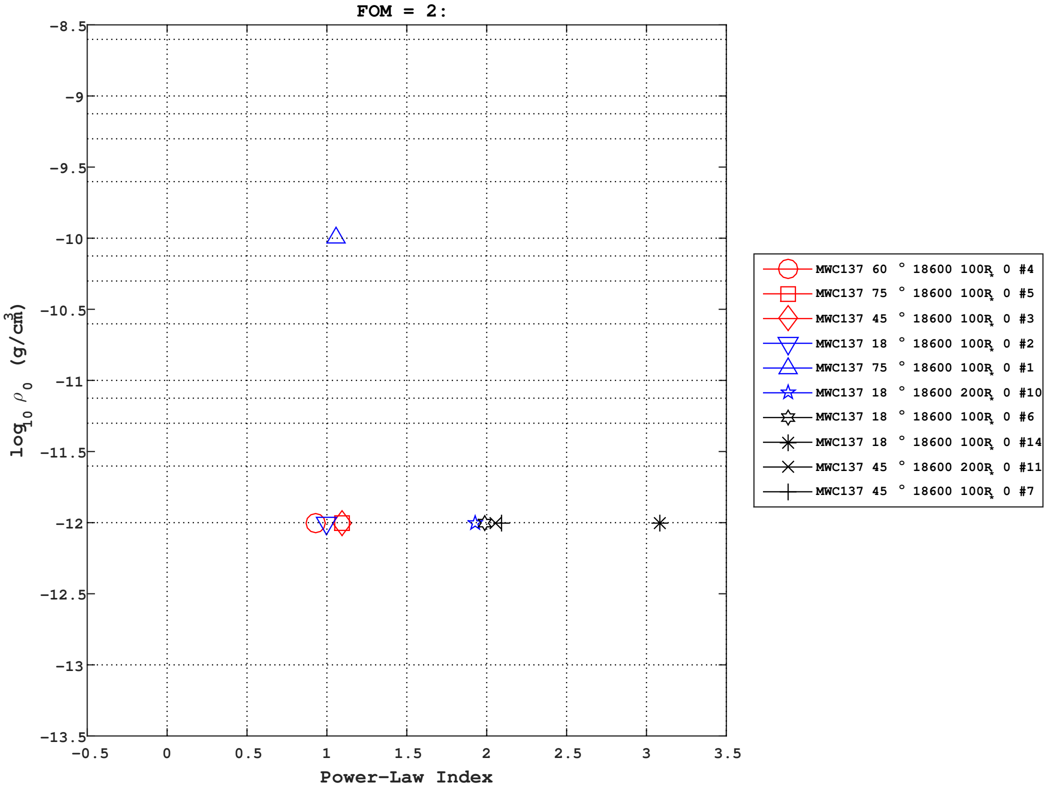

Figure B.40: Hβ profiles for MWC 137: The top 9 best-fit models corresponding to the line fittings, seen in Figure B.39, in the $(n, log_{10}\,\rho)$ plane. The additional parameters of each model are noted in the legend in the following order: model name, inclination (i), disk temperature (T_{HE}), disk radius (R_*), turbulence (α) and model number (which corresponds to the individual line fits in the previous plot).

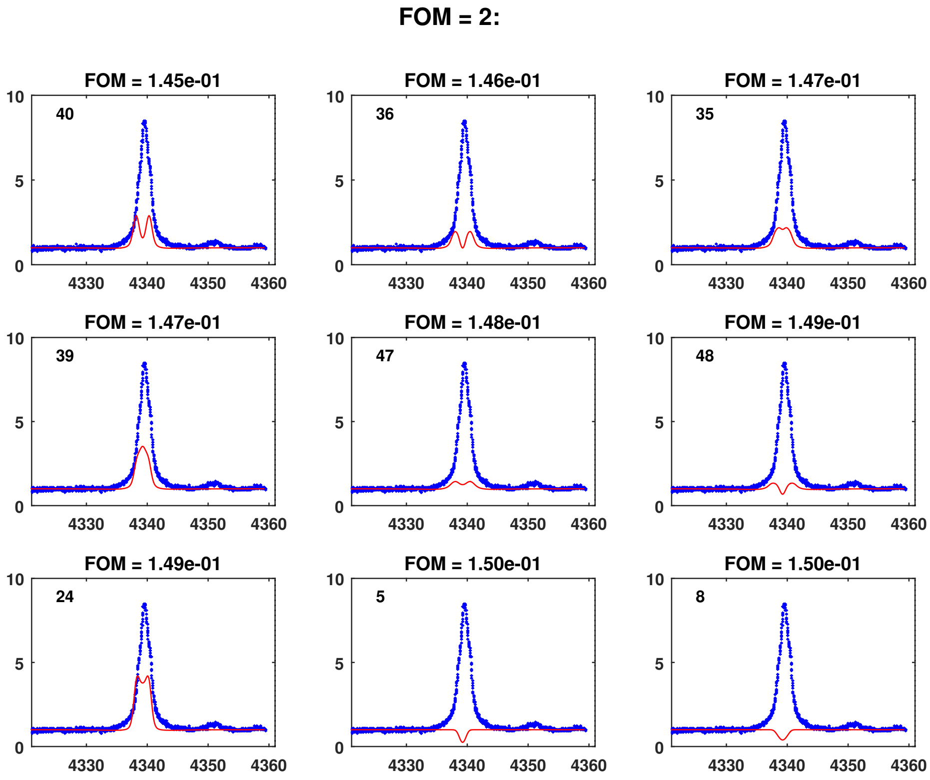

Figure B.41: Hγ profiles for MWC 137: The top 9 best synthetic (red) line profiles, result of Equation 3.1, that best match the observed (blue) emission line. The FOM (figure-of-merit) value above each panel of best fit represents the $\mathcal{F}$ value calculated using equation 3.1. The top left panel represents the best-fit line profile.

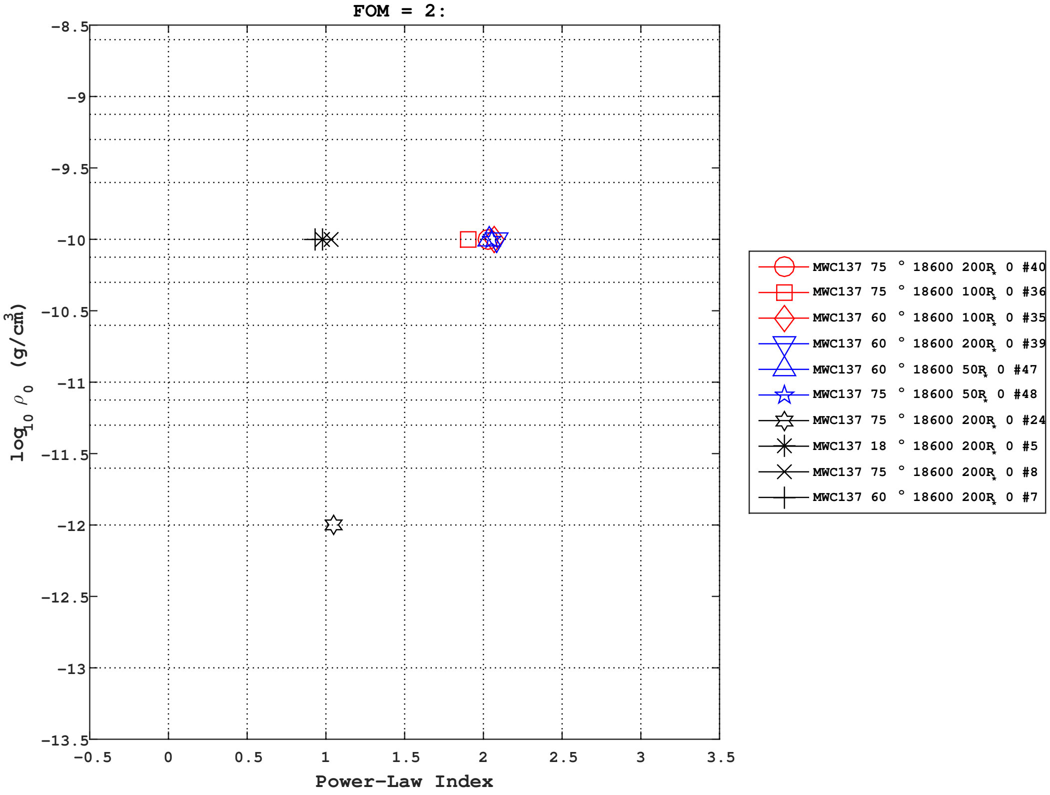

Figure B.42: Hγ profiles for MWC 137: The top 9 best-fit models corresponding to the line fittings, seen in Figure B.41, in the $(n, log_{10}\rho)$ plane. The additional parameters of each model are noted in the legend in the following order: model name, inclination (i), disk temperature (T_{HE}), disk radius (R_*), turbulence (α) and model number (which corresponds to the individual line fits in the previous plot).

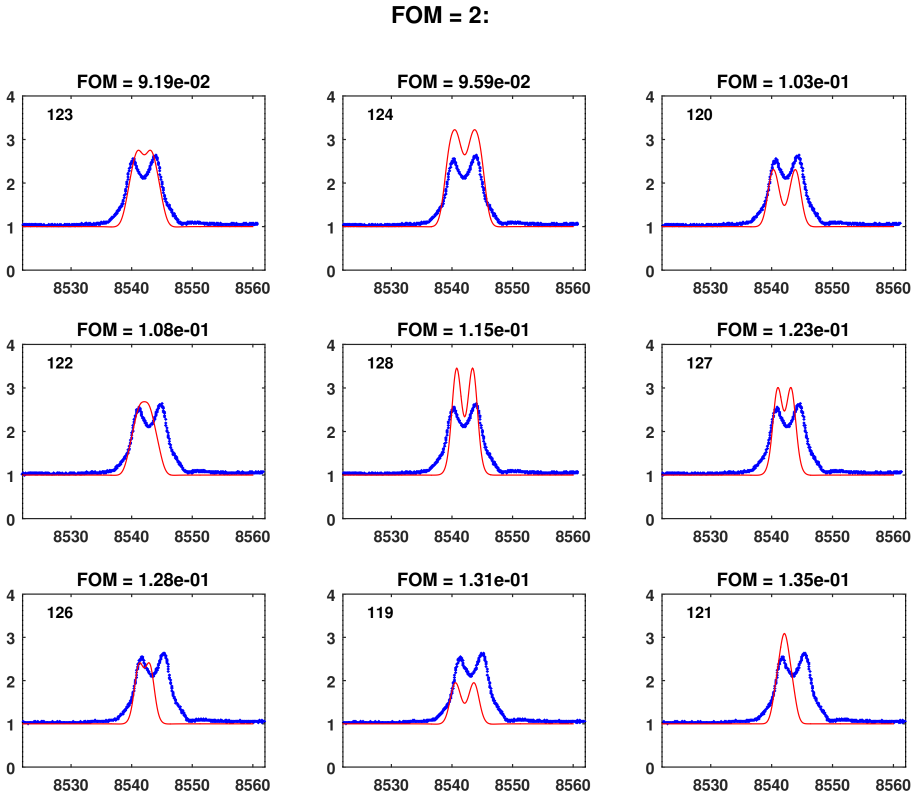

Figure B.43: Ca II profiles for MWC 137: The top 9 best synthetic (red) line profiles, result of Equation 3.1, that best match the observed (blue) emission line. The FOM (figure-of-merit) value above each panel of best fit represents the $\mathcal{F}$ value calculated using equation 3.1. The top left panel represents the best-fit line profile.

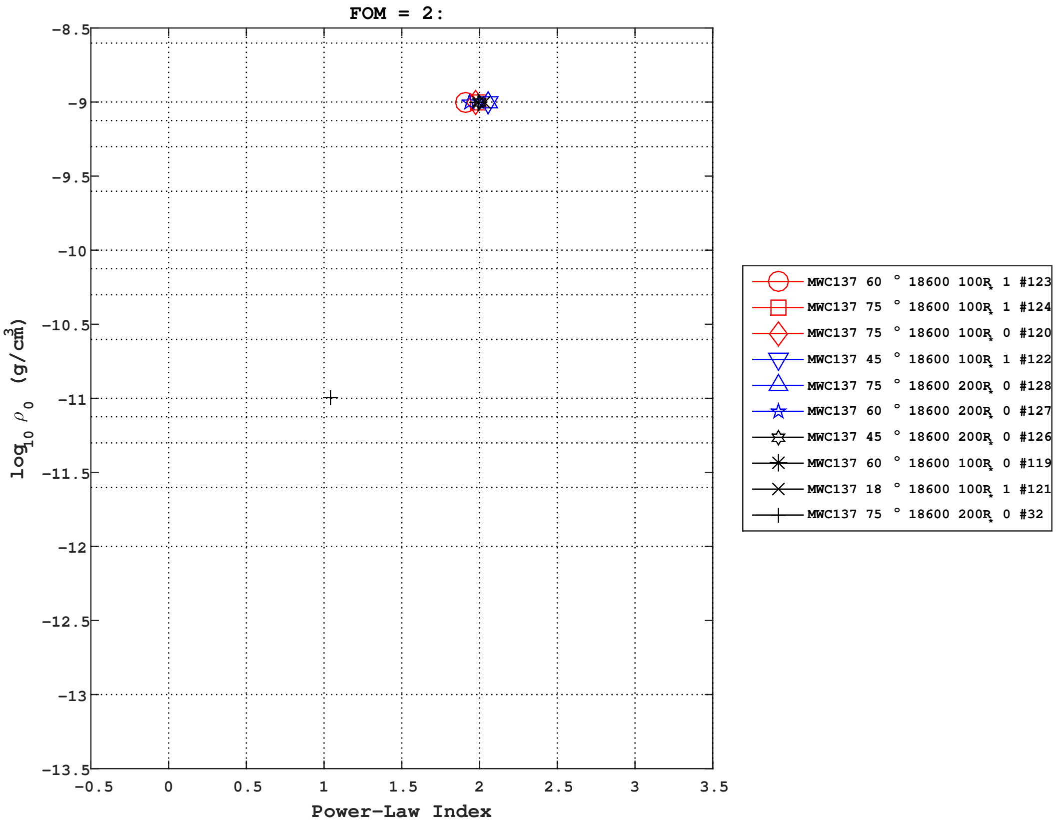

Figure B.44: Ca II profiles for MWC 137: The top 9 best-fit models corresponding to the line fittings, seen in Figure B.43, in the $(n, log_{10}\,\rho)$ plane. The additional parameters of each model are noted in the legend in the following order: model name, inclination (i), disk temperature (T_{HE}), disk radius (R_*), turbulence (α) and model number (which corresponds to the individual line fits in the previous plot).

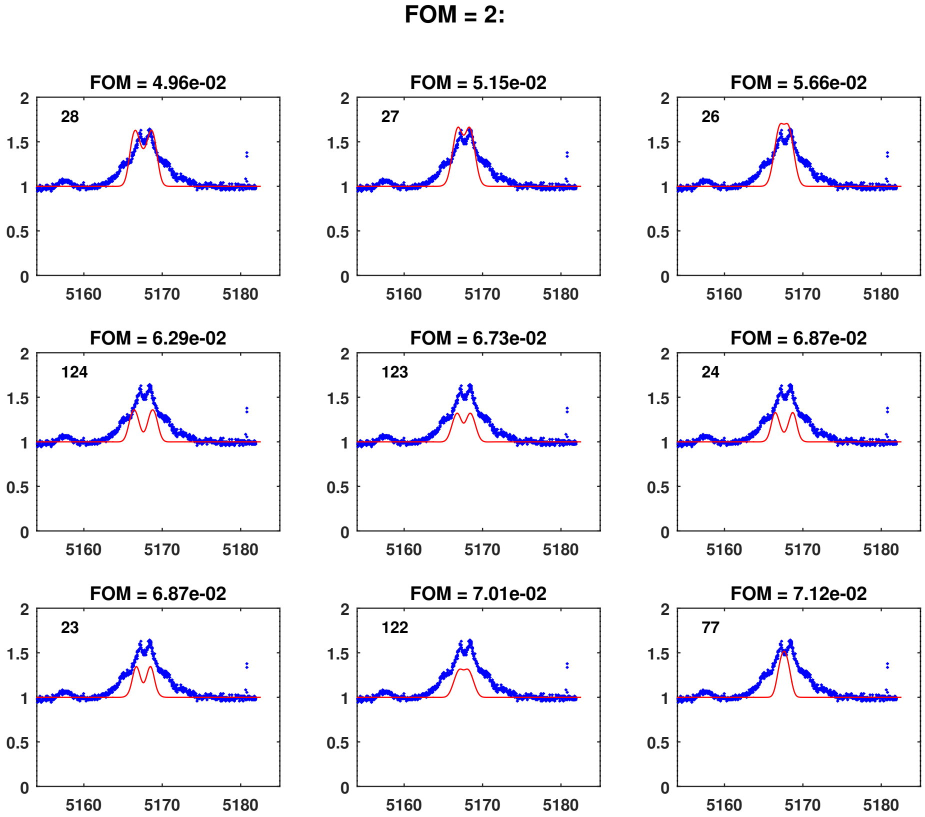

Figure B.45: Fe II (λ 5169) profiles for MWC 137: The top 9 best synthetic (red) line profiles, result of Equation 3.1, that best match the observed (blue) emission line. The FOM (figure-of-merit) value above each panel of best fit represents the $\mathcal{F}$ value calculated using equation 3.1. The top left panel represents the best-fit line profile.

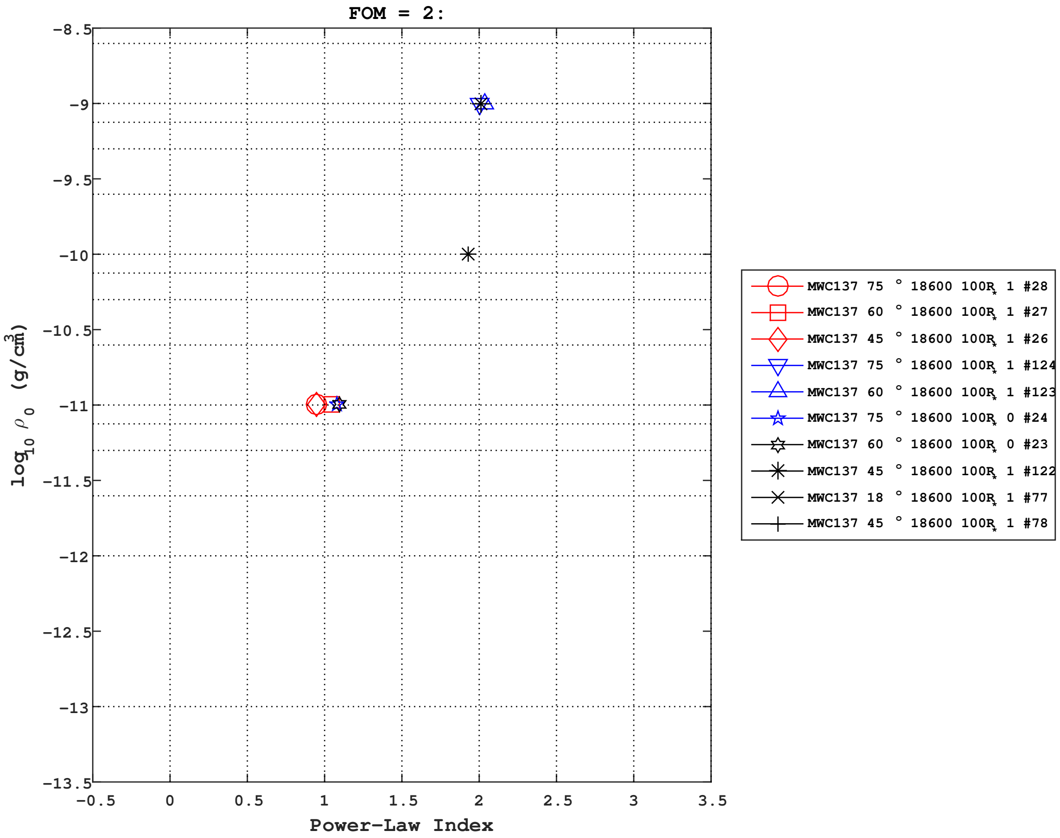

Figure B.46: Fe II (λ 5169) profiles for MWC 137: The top 9 best-fit models corresponding to the line fittings, seen in Figure B.45, in the $(n, log_{10}\,\rho)$ plane. The additional parameters of each model are noted in the legend in the following order: model name, inclination (i), disk temperature (T_{HE}), disk radius (R_*), turbulence (α) and model number (which corresponds to the individual line fits in the previous plot).

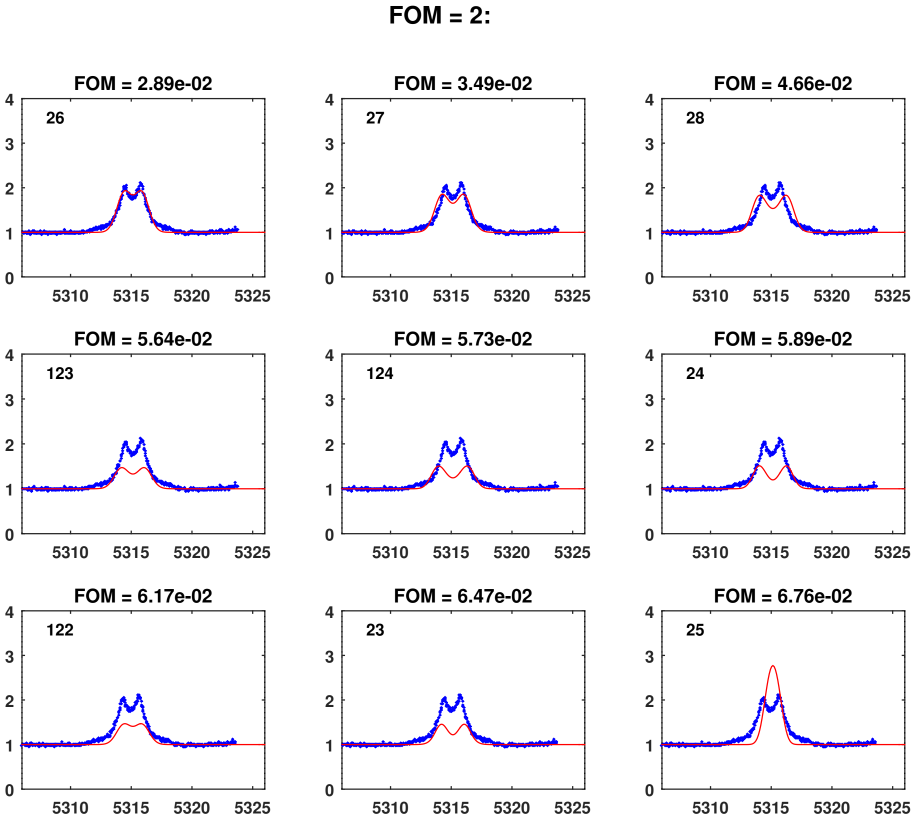

Figure B.47: Fe II (λ 5317) profiles for MWC 137: The top 9 best synthetic (red) line profiles, result of Equation 3.1, that best match the observed (blue) emission line. The FOM (figure-of-merit) value above each panel of best fit represents the $\mathcal{F}$ value calculated using equation 3.1. The top left panel represents the best-fit line profile.

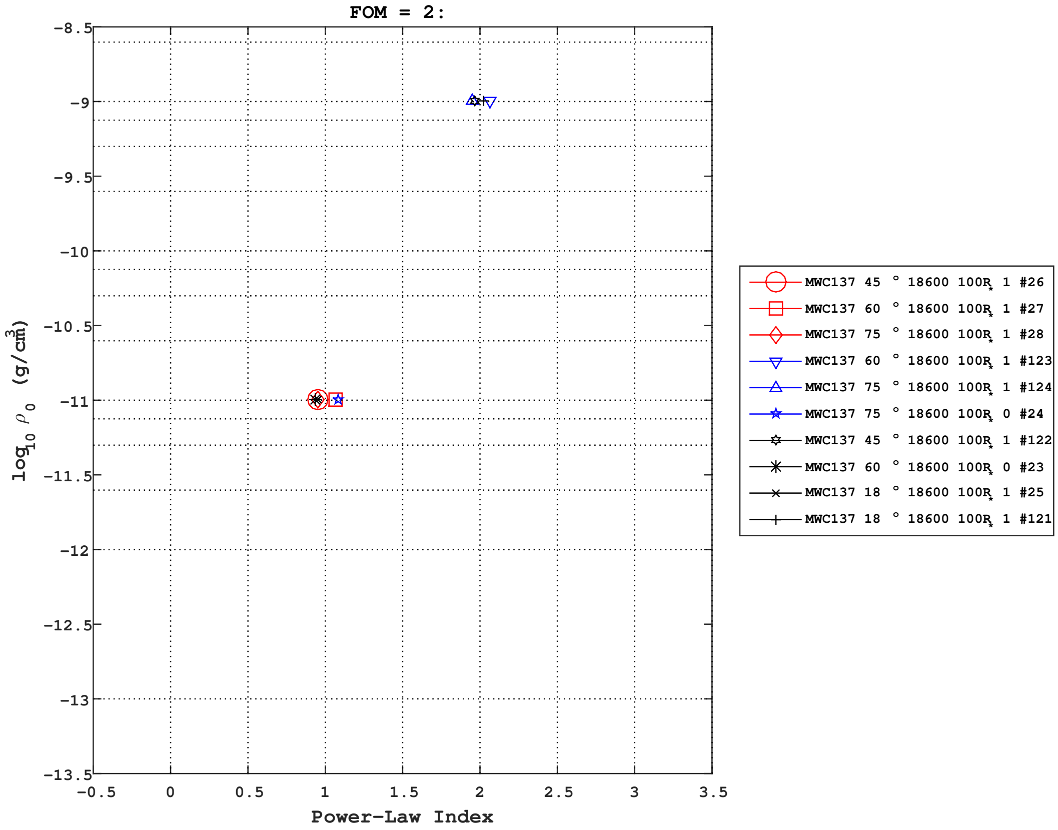

Figure B.48: Fe II (λ 5317) profiles for MWC 137: The top 9 best-fit models corresponding to the line fittings, seen in Figure B.47, in the $(n, log_{10}\rho)$ plane. The additional parameters of each model are noted in the legend in the following order: model name, inclination (i), disk temperature (T_{HE}), disk radius (R_*), turbulence (α) and model number (which corresponds to the individual line fits in the previous plot).

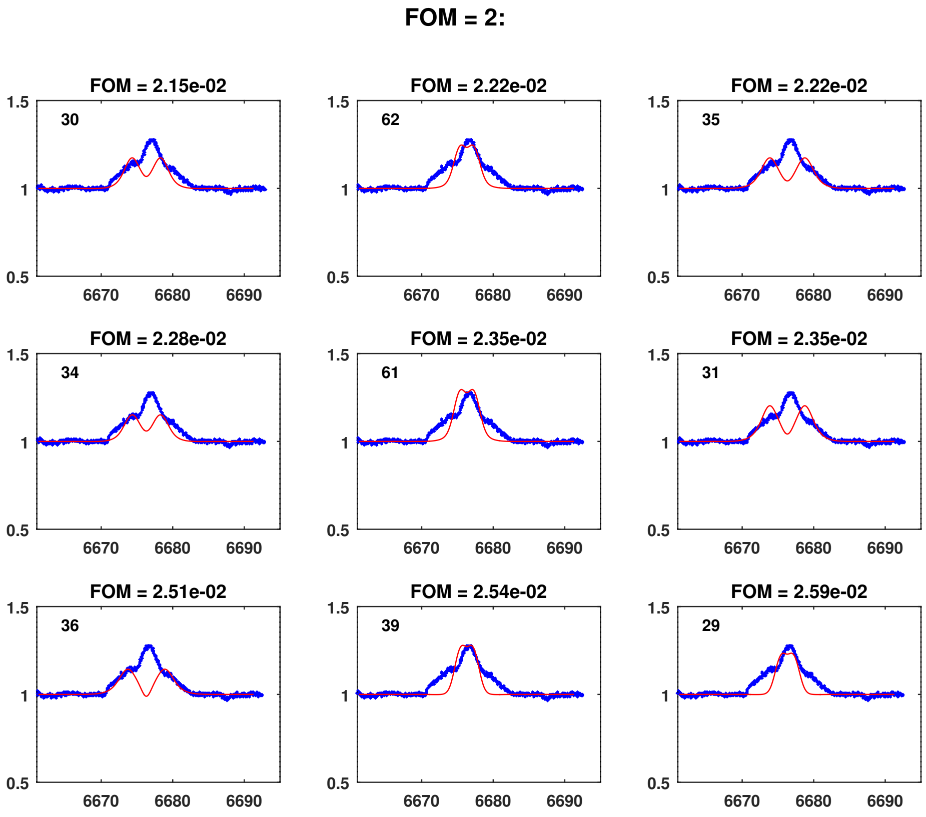

Figure B.49: He II profiles for MWC 137: The top 9 best synthetic (red) line profiles, result of Equation 3.1, that best match the observed (blue) emission line. The FOM (figure-of-merit) value above each panel of best fit represents the $\mathcal{F}$ value calculated using equation 3.1. The top left panel represents the best-fit line profile.

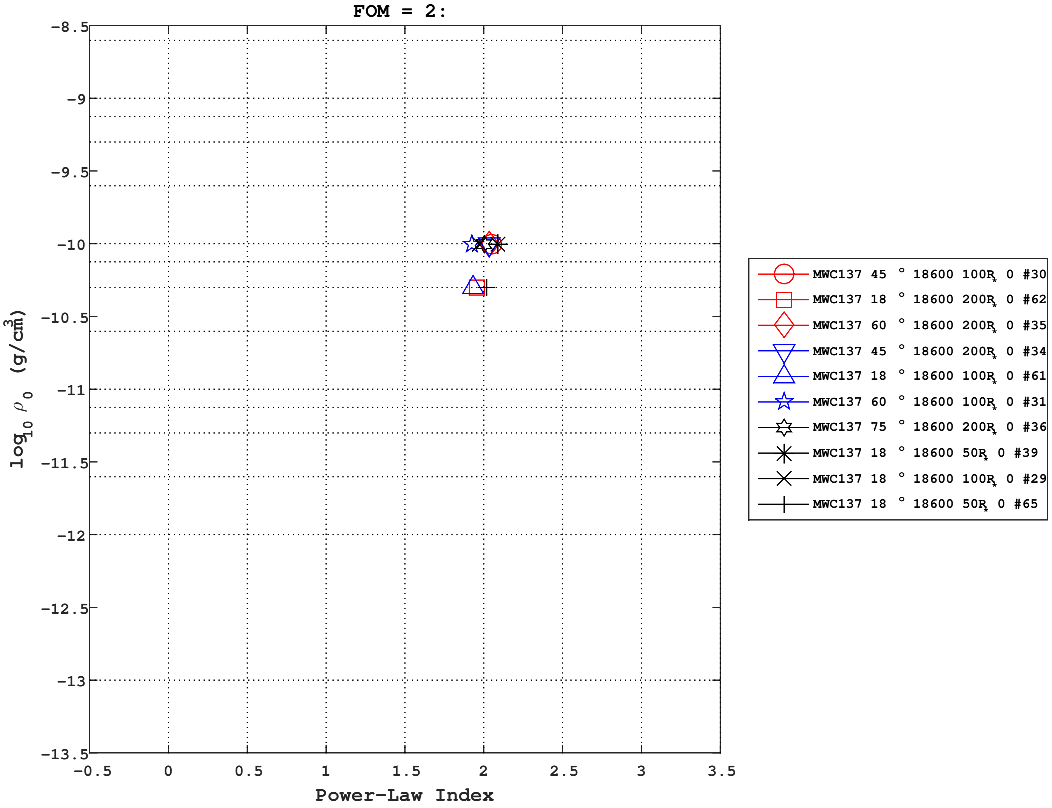

Figure B.50: He II profiles for MWC 137: The top 9 best-fit models corresponding to the line fittings, seen in Figure B.49, in the (n, $log_{10}\,\rho$) plane. The additional parameters of each model are noted in the legend in the following order: model name, inclination (i), disk temperature (T_{HE}), disk radius (R_*), turbulence (α) and model number (which corresponds to the individual line fits in the previous plot).

Curriculum Vitae

Name:	Parshati Patel
Post-Secondary Education and Degrees:	The University of Western Ontario London, Ontario 2012 - 2016 Ph.D. Astronomy & Planetary Science
	The University of Western Ontario London, Ontario 2010 - 2012 M.Sc. Astronomy & Planetary Science
	The University of Toronto Toronto, Ontario 2006 - 2010 Hons.B.Sc. Physics & Astronomy
Honours and Awards:	Western Graduate Research Scholarship 2010-2016
	Faculty of Science Outreach Award 2012 (Awarded to the entire Outreach team)
Related Work Experience:	Graduate Teaching Assistant The University of Western Ontario 2010 - 2016
	Teaching Assistant The University of Toronto 2009-2010

Publications:

Referred Publications:

P. Patel, T. A. A. Sigut & J. D. Landstreet. Photoionization Models of the Inner Gaseous Disk of the Herbig Be Star BD+65 1637. The Astrophysical Journal, 817, 29P (2016).

T. A. A. Sigut & **P. Patel**. The Correlation between H Emission and Visual Magnitude during Long-term Variations in Classical Be Stars. The Astrophysical Journal, 765, 41S (2013).

Conference Talks:

P. Patel, T. A. A. Sigut & J. D. Landstreet. Investigating Inner Gaseous Disks around Young, Massive Stars. Women in Physics Conference, 30 July-01 August 2015, Toronto, Ontario, Canada.

P. Patel, T. A. A. Sigut & J. D. Landstreet. Investigating Inner Gaseous Disks around Herbig Be Star BD+ 65 1637. Canadian Astronomical Society of Canada Annual Meeting, 24-27 May 2015, Hamilton, Ontario, Canada.

P. Patel & T. A. A. Sigut. The H- UBV Signatures of Disk Growth and Dissipation in Classical Be Stars. Canadian Astronomical Society of Canada Annual Meeting, 4-7 June 2012, Calgary, Alberta, Canada.

Conference Posters:

P. Patel, T. A. A. Sigut & J. D. Landstreet. Investigating Inner Gaseous Disk around Herbig Be Star BD+65 1637 by Modeling Emission Lines. Bright Emissaries Conference, 10-13 August 2014, London, Canada.

P. Patel, T. A. A. Sigut & J. D. Landstreet. Investigating Inner Gaseous Disks around Herbig Be Stars by Modeling Emission Lines. Herbig Ae/Be Stars Workshop, 7-11 April 2014, Santiago, Chile.